UNIVERSIDAD AUTÓNOMA DE NUEVO LEÓN

FACULTAD DE INGENIERÍA MECÁNICA Y ELÉCTRICA

“HYBRID NANOMATERIALS FOR PHOTODETECTORS WITH EXTENDED WAVELENGTH RANGE AND HIGH EFFICIENCY”

POR

AKSHANA PARAMESWARAN SREEKALA

1988527

COMO REQUISITO PARA OBTENER EL GRADO DE

DOCTOR EN INGINERIA DE MATERIALES

San Nicolás de los Garza, Nuevo León **Marzo 2023**

UNIVERSIDAD AUTÓNOMA DE NUEVO LEÓN
FACULTAD DE INGENIERÍA MECÁNICA Y ELÉCTRICA

“HYBRID NANOMATERIALS FOR PHOTODETECTORS WITH EXTENDED WAVELENGTH RANGE AND HIGH EFFICIENCY”

POR

AKSHANA PARAMESWARAN SREEKALA

1988527

COMO REQUISITO PARA OBTENER EL GRADO DE

DOCTOR EN INGINERIA DE MATERIALES

Supervisado por

Dr. SADASIVAN SHAJI

San Nicolás de los Garza, Nuevo León **Marzo 2023**

UNIVERSIDAD AUTÓNOMA DE NUEVO LEÓN
Facultad de Ingeniería Mecánica y Eléctrica
Posgrado

Los miembros del Comité de Evaluación de Tesis recomendamos que la Tesis "Hybrid nanomaterials for photodetectors with extended wavelength range and high efficiency", realizada por la estudiante Akshana Parameswaran Sreekala, con número de matrícula 1988527, sea aceptada para su defensa como requisito parcial para obtener el grado de Doctor en Ingeniería de Materiales.

El Comité de Evaluación de Tesis

Dra. Bindu Krishnan
Director

Dra. Selene Sepúlveda Guzmán
Revisor

Dr. Sadasivan Shaji
Revisor

Dr. Eduardo Gerardo Pérez Tijerina
Revisor

Dra. María Isabel Mendivil Palma
Revisor

Dr. Eduardo Martínez Guerra
Revisor

Vo.Bo.

Dr. Simón Martínez Martínez
Subdirector de Estudios de Posgrado

Institución 190001

Programa 122608

Acta Núm. 322

Ciudad Universitaria, a 29 de mayo de 2023.

ACKNOWLEDGEMENTS

I'm extremely grateful to:

CONACYT (Consejo Nacional de Ciencia y Tecnología) for providing me a doctoral research fellowship during the entirety of my Ph.D. program and supporting with project CB 2017-2018, No. A1-S-21684.

FIME (Facultad de Ingeniería Mecánica y Eléctrica), UANL for accepting me as a doctoral student and for offering all the resources for experiments and characterization.

CIIDIT (Centro de Innovación, Investigación y Desarrollo en Ingeniería y Tecnología) and **CIIIA** (Centro de Investigación e Innovación en Ingeniería Aeronáutica), UANL for granting access to characterization facilities.

I could not have undertaken this journey without the guidance of **Dr. Sadasivan Shaji**, my thesis advisor. I thank him for sharing his expertise, all the constructive criticism I received while working and most importantly, for continually inspiring me to learn all new things despite having a completely different academic background. Without a doubt, the information and experience gained throughout this research tenure were priceless.

I am deeply thankful to **Dra. Bindu Krishnan** for all her insightful comments made throughout the group meetings and manuscript corrections and you have always been a wonderful listener and provided support when needed.

I would like to express my deepest gratitude to **Dr. David Avellaneda Avellaneda** who has not only been there for help in the lab but has also helped me during times of emotional breakdown. He has never failed to offer positive affirmations when they were most needed.

I'd like to acknowledge my thesis revisors, **Dr. Eduardo Martínez Guerra**, **Dr. Eduardo Gerardo Perez Tijerina, Dra. Selene Sepulveda Guzmán** and **Dra. María Isabel Mendivil Palma** for spending time to review my thesis.

I would like to express my deepest appreciation to **Dr. Josué Amilcar Aguilar Martínez**, **Dr. Rene Fabian Cienfuegos Pelaes**, **Dr. Edgar Omar García Sánchez** and **Dr. Domingo Ixcóatl**

García Salazar for their timely help and support, especially with characterization techniques during my Ph.D.

Many thanks to **Dr. Marco Antonio Loudovic Hernández Rodríguez**, **Dr. Azael Martínez de la Cruz**, **Dra. Ana María Guzmán Hernández** and **Dr. Simón Martínez Martínez** for their support and it was great knowing **Dr. Tushar Kanti Das Roy** as well. Expressing my heartfelt thanks to all the faculty members who have taught classes of course work all the eight semesters.

This endeavor would not have been possible without the help of my parents, **Mr. S. Parameswaran Pillai** and **Mrs. Sreekala T.G**., who have supported and encouraged me to pursue what I am really interested in and letting me choose without any hesitation. I'm also appreciative of my sister, **Ms. Akshaja P.S.**, who has always embraced me more and more despite my absence.

Words are inadequate to explain how grateful I am to **Dr. Vasanth** for his patience with me throughout the years and acceptance of my decisions. Despite the fact that I have come to you with all of the world's troubles, you have listened to me and have supported me. I'm grateful that you were there for me when my health was poor and my emotions were up and down.

I would like to express my thanks to all my **family members** (Ammayi, Kochu and family). Also, **friends like family**, Appu, Stefz, Aathi, Sonimol, Sujithettan, Kuttanz, Hariettan who has never left my side. They have stood by me for years and have supported me selflessly. Special thanks to Alapatt and Sreed for helping me when I needed it most. Even though we don't always communicate, I'll never forget the time we spent in Monterrey and the wonderful experiences.

I'd like to recognize my **colleagues** Sebin, Joseph, Albert, Paulosutty, Katia and Pooja for their help and for making lab more exciting. We also share many great moments outside of the lab. And expressing my gratitude towards Aiswarya Nadukkandy for we have shared most of our time together and have been supportive of each other. The memories are worth cherishing. Thanks to Dra. Claudia, Diana, Varshika, Daniel as well. I would like to thank Angela Monserrat Garcia Olvera for her help with the experiments. I would like to thank my **friends** Fatima, Claudia Esmeralda, Jeidy and Ernesto for always being upbeat and cheery, even in stressful situations and for constantly saying encouraging things that gave me the motivation to move forward.

I would be remiss in not to mention my gratitude towards Dr. Sanal Kozhiparambil Chandran and Soorya Pushpan. They were always welcoming and treated me like family.

My gratitude goes out to all Mexicans for being kind, hospitable, and helpful, as well as I'm glad I got to know the Malayali community in Monterrey.

The next part of the acknowledgments will be in Spanish in consideration of the persons to whom it is directed.

Agradecer a mi familia mexicana, **Tía Maya**, **Tío Jaime**, Margot, Beto, Sol y Joel nunca sería suficiente. Me han mostrado un amor incondicional desde el principio y me han introducido a la cultura, la cocina y la gente mexicana. Constantemente recurro a Tia porque ella siempre ha sido una mama para mí. Tia y el tío siempre estuvieron ahí para mí cuando se hizo difícil estar lejos de mi familia en la India.

Gracias al dueño de mi casa, el Sr. Guillermo Sánchez y la Sra. Elizabeth Nájera, siempre han sido accesibles y flexibles con nuestras demandas. Han sido un gran apoyo en mis situaciones.

Not least, I thank God Almighty for giving me the strength to stay back and survive all these years, be it the good or difficult phases.

Dedicated to

My ammuma,

Smt. Maheswari Amma

who is no longer with us

&

To my parents and my sister

Mr. S. Parameswaran

Mrs. Sreekala T.G.

Ms. Akshaja P.S.

Abbreviations

AFM – Atomic Force Microscopy

Ag – Silver

Au – Gold

CFM – Chemical Force Microscopy

CIGS – Cu (In, Ga) Se_2

CNT – Carbon Nanotube

CVD – Chemical Vapor Deposition

DLS – Dynamic Light Scattering

EDX – Energy Dispersive X-ray Spectroscopy

EXAFS – Extended X-ray Absorption Fine Structure

FTO – Fluorine doped Tin Oxide

FESEM – Field Emission Scanning Electron Microscopy

GIXRD – Grazing Incidence XRD

HRTEM – High Resolution Transmission Electron Microscopy

ICDD – International Centre for Diffraction Data

IPA – Isopropyl Alcohol

ITO – Indium doped Tin Oxide

IR – Infra-Red

LMC – Layered Metal Chalcogenides

LML – Laser Melting in Liquids

LSPC – Laser Synthesis and Processing of Colloids

Nd:YAG – Neodymium-Doped Yttrium Aluminum Garnet

NCs – Nanocrystals

NPs – Nanoparticles

ns – nanosecond

PL – Photoluminescence

PLAL – Pulsed Laser Ablation in Liquid

PLFL – Pulsed Laser Fragmentation in Liquid

PLIL- Pulsed Laser Irradiation in Liquid

QDs – Quantum Dots

SAED – Selected Area Electron Diffraction

SAXS – Small Angle X-ray Scattering

SEM – Scanning Electron Microscopy

SMPs – Submicron-sized particles

SPM – Scanning Probe Microscopy

STM – Scanning Tunneling Microscopy

SnO_2 – Tin oxide

SnS –Tin sulfide

TEM – Transmission Electron Microscopy

UV-Vis-NIR – Ultraviolet-Visible-Near Infrared

WAXS – Wide-angle X-ray scattering

XANES – X-ray Absorption Near Edge Structure

XPS – X-ray Photoelectron Spectroscopy

XRD – X-ray Diffraction

XRF – X-ray Fluorescence Spectroscopy

ZTO – Zn_2SnO_4

TABLE OF CONTENTS

Abstract **10**

Resumen **12**

Chapter 1 ..... **14**

An introduction to hybrid nanomaterials, nanostructured thin films and devices using pulsed laser assisted techniques **14**

1.1 Nanomaterials **14**

1.1.1 Synthesis of nanomaterials 15

1.2 Hybrid Nanomaterials **16**

1.2.1 Introduction to hybrid nanomaterials 16

1.2.2 Characterization techniques for hybrid nanomaterials 18

1.2.3 Optical and Electrical Properties of Hybrid Nanomaterials 20

1.2.4 Applications of Hybrid Nanomaterials 23

1.3 Material Synthesis by LSPC techniques **23**

1.4 Thin films and devices from nanocolloids **30**

1.5 Photodetectors – Properties and devices **33**

1.5.1 Characterization of photodetectors 35

1.5.2 Parameters of photodetectors 36

1.6 UV-Vis-NIR semiconductor photodetectors **38**

1.7 Hypothesis **40**

1.8 General Objective **40**

1.9 Specific Objectives **40**

1.10 Justification **41**

Chapter 2 ..... **43**

SnS thin films for UV-Vis-NIR photodetection prepared by spin coating of laser ablated nanocolloids **43**

2.1 Introduction **43**

2.2 Experimental section **44**

2.2.1 Synthesis of nanocolloids 44

2.2.2 Fabrication of thin films of SnS by spin coating 44

2.2.3 Characterization techniques utilized in the work 45

2.3 Results and Discussion 46
2.3.1 Morphology and structure of SnS NPs by TEM 46
2.3.2 Morphology by SEM 49
2.3.3 Grazing Incidence X-ray Diffraction (GIXRD) of SnS films 52
2.3.4 Optical Studies of the SnS NPs 53
2.3.5 X-ray photoelectron spectroscopy 56
2.3.6 Current-voltage and photoresponse measurements 60
2.3.7 Photodetector parameters 67
2.4 Conclusions 70
Chapter 3 72
SnS-Si hybrids by pulsed laser irradiation/ablation in liquid for photodetector and photocatalytic applications 72
3.1 Introduction 72
3.2 Experimental Part 72
3.3 Results and Discussion 77
3.3.1 Transmission Electron Microscopy (TEM) 77
3.3.2 X-ray diffraction 81
3.3.3 UV-Vis-NIR Spectroscopy 84
3.3.4 Raman Spectroscopy 86
3.3.5 Scanning Electron Microscopy 87
3.3.6 X-ray photoelectron Spectroscopy 91
3.3.7 I-V characteristics and Photoresponse measurements 95
3.3.8 Photocatalysis 105
3.4 Conclusions 111
Chapter 4 113
Color insensitive UV-Vis-NIR photodetection using SnS:Graphene hybrid thin films 113
4.1 Introduction 113
4.2 Nanocolloid synthesis and SnS:Graphene photodetector fabrication 114
4.3 Results and Discussion 117
4.3.1 Optical Studies 117
4.3.2 Morphological Analyses 119

4.3.3 Structural, Phase and Compositional Analyses 127
4.3.4 Electrical Studies 133
4.4 Conclusions 145
Chapter 5 146
Hybrids of SnS with metal/bimetallic nanoparticles for visible photodetection 146
5.1 Introduction 146
5.2 Experimental 146
5.2.1 Metallic/Bimetallic and SnS nanocolloidal synthesis 146
5.2.2 SnS-metallic/bimetallic hybrid thin film fabrication 147
5.3 Results and Discussion 149
5.3.1 Transmission Electron Microscopy 149
5.3.2 UV-Vis Spectroscopic studies 153
5.3.3 X-ray diffraction studies 159
5.3.4 Scanning Electron Microscopy 160
5.3.5 X-ray photoelectron spectroscopy 161
5.3.6 I-V and Photoresponse studies 164
5.4 Conclusions 172
Chapter 6 174
General Conclusions and Outlook 174
References 178
Annexure -1 212
Pyrite (FeS_2) nanoparticles by pulsed laser ablation in liquid and its thin films for photodiodes 212
A.1 Introduction 212
A.2 Methodology 213
A.2.1 Synthesis of FeS_2 nanoparticles 213
A.2.2 Electrophoretic deposition of FeS_2 nanoparticles 214
A.2.3 Spin-coating of FeS_2 nanoparticles 214
A.3 Results 215
A.3.1 TEM and SEM analysis of NPs 215
A.3.2 X-ray Photoelectron Spectroscopy (XPS) of NPs 220

A.3.3 UV-Vis studies of NPs 222
A.3.4 X-ray Diffraction (XRD) of the films 222
A.3.5 SEM of FeS_2 films 225
A.3.6 Optical Studies of FeS_2 films 227
A.3.7 I-V characteristics and Photoresponse measurements 228
A.4 Conclusions 234
References 235
List of Figures 237
List of Table 245
Curriculum Vitae 246

Abstract

This Ph.D. dissertation is anticipated to be a significant step forward in the creation of novel hybrid nanostructures based on tin sulfide (SnS) for the fabrication of photodetectors operating in extended wavelength region with improved efficiency. This thesis work includes a thorough description of the synthesis of nanoparticles of high purity by laser synthesis and processing in liquids for hybrid nanostructured thin film fabrication by spin coating and spray deposition method for photodetection and photocatalytic applications. Tin sulfide nanoparticles (NPs) were synthesized using pulsed laser ablation in liquid (PLAL) and pulsed laser fragmentation in liquid (PLFL), two methods that are rapid, efficient, environment friendly and yield materials with clean surfaces without the use of surfactants. The generation of SnS NPs in isopropyl alcohol (IPA) at two different laser wavelengths (532 and 1064 nm) and the variations in its photodetection properties upon film fabrication using these nanocolloids were investigated first. Then, hybrid nanostructures of SnS with silicon NPs, graphene and metallic, bimetallic NPs were created to benefit from the synergistic characteristics of both materials in order to enhance their optoelectronic properties. Different fabrication techniques such as spin coating and spray deposition have been implemented to fabricate thin films of these materials followed by annealing. The NPs were either mixed physically, such as via ultrasonication, or during the fabrication of the films, by depositing one type of material over the other, resulting in chemical or interfacial interactions. The thin film fabrication parameters and the annealing conditions were optimized depending on the hybrids and the annealing temperature and time had an effect on the crystalline size of the resulting films. The combination of pulsed laser ablation and spin coating as well as the synthesis of SnS NPs by PLFL has never been reported earlier. Since Si NPs have a small bandgap, a high light-trapping capacity and a quick charge transfer nature, they were incorporated to SnS films with the intention of utilizing these properties. Due to its gapless/zero bandgap nature, ability to absorb a wider range of wavelengths, high carrier mobility and superior electrical conductivity, graphene was chosen to extend the wavelength of absorption of SnS to the entire UV-Vis-NIR region. Metallic NPs like silver (Ag), gold (Au) and bimetallic (Ag:Au) NPs were combined with SnS to make use of its plasmonic features for wavelength-specific detection. While SnS thin films were prepared by PLAL/spin-coating; SnS:graphene and SnS:Si were prepared by combining PLFL/spin-coating. SnS:Ag, Au, and Ag:Au were prepared by PLAL/spray deposition. The film

fabrication methods were effective in modifying their morphological, crystalline, optical and electrical characteristics. In comparison to all other combinations, the SnS:graphene hybrids showed improved photodetection characteristics with wavelength independent photodetection. In all the cases, XRD, Raman, XPS, TEM and SEM were used to examine the prepared nanoparticles and thin films for their structure, crystalline nature, composition and morphology. The SnS:Si photodetectors demonstrated a photoresponse of up to 1064 nm and its photocatalytic activities including its cyclic catalytic performance were also investigated. UV-Visible spectroscopy, I-V measurements under both dark and light illumination and photoresponse measurements, on the other hand, were used to identify the optical and electrical properties. The findings of this study demonstrate that highly sensitive SnS based hybrid photodetectors operating in extended wavelength region (UV-Vis-NIR) with promising semiconductor device architectures can be developed by effectively combining pulsed laser ablation/irradiation in liquid approach and facile film fabrication techniques.

Resumen

Esta disertación doctoral se prevé sea un importante paso hacia adelante en la creación de nuevas nanoestructuras híbridas basadas en sulfuro de estaño (SnS) para la fabricación de fotodetectores que funcionan en una región de longitud de onda extendida con una eficiencia mejorada. Este trabajo de tesis incluye una descripción detallada de la síntesis de nanopartículas de alta pureza mediante síntesis y procesamiento por láser en líquidos para la fabricación de películas delgadas híbridas nanoestructuradas mediante el método de recubrimiento por centrifugación (*spin coating*) y deposición por rocío (*spray)* para aplicaciones fotocatalíticas y de fotodetección. Las nanopartículas (NP) de sulfuro de estaño se sintetizaron mediante ablación por láser pulsado en líquido (PLAL) y fragmentación por láser pulsado en líquido (PLFL), dos métodos que son rápidos, eficientes, no contaminantes y producen materiales con superficies limpias sin el uso de surfactantes. En primer lugar, se investigó la generación de NPs de SnS en alcohol isopropílico (IPA) usando dos diferentes longitudes de onda (532 y 1064 nm) y las variaciones en sus propiedades de fotodetección tras la fabricación de películas con estos nanocoloides. Posteriormente, se crearon nanoestructuras híbridas de SnS con NPs de silicio, grafeno y NPs bimetálicas/metálicas (Au/Ag/Ag:Au) para aprovechar las características sinérgicas de los materiales involucrados y mejorar sus propiedades optoelectrónicas. Se han implementado diferentes técnicas de fabricación para la obtención de películas delgadas de estos materiales, como el recubrimiento por centrifugación y la deposición por rocío, además de su posterior tratamiento térmico. Los nanocoloides fueron mezclados físicamente mediante ultrasonido, o durante la fabricación de las películas, depositando un tipo de material sobre el otro, lo que resultó en interacciones químicas o interfaciales. Los parámetros de fabricación de películas delgadas y las condiciones de tratamiento térmico se optimizaron de acuerdo con los materiales híbridos; la temperatura y el tiempo del tratamiento térmico tuvieron un efecto sobre el tamaño de cristal de las películas resultantes. La combinación de ablación por láser pulsado y recubrimiento por centrifugación, así como la síntesis de NPs de SnS por PLFL, no se había reportado anteriormente. Dado que las NPs de Si tienen una banda prohibida pequeña, una alta capacidad de atrapar la luz y una naturaleza de transferencia de carga rápida, se incorporaron a las películas de SnS con la intención de utilizar estas propiedades. Debido a su banda prohibida cero, la capacidad de absorber una gama más amplia de longitudes de onda, la alta movilidad del portador y la conductividad

eléctrica superior, se eligió el grafeno para extender la longitud de onda de absorción del SnS a toda la región UV-Vis-NIR. Las NPs metálicas como la plata (Ag), el oro (Au) y las NPs bimetálicas (Ag:Au) se combinaron con SnS para hacer uso de sus características plasmónicas para la detección de longitudes de onda específicas. Mientras que las películas delgadas de SnS se prepararon mediante PLAL/recubrimiento por centrifugación; SnS:grafeno y SnS:Si se prepararon combinando PLFL/recubrimiento por centrifugación. SnS:Ag, Au, Ag:Au se prepararon mediante PLAL/deposición por rocío. Los métodos de fabricación de películas fueron efectivos para modificar sus características morfológicas, cristalinas, ópticas y eléctricas. En comparación con todas las demás combinaciones, los híbridos SnS:grafeno mostraron una característica de fotodetección mejorada e independiente de la longitud de onda. En todos los casos, se utilizaron las técnicas de XRD, Raman, XPS, TEM y SEM para examinar las nanopartículas preparadas y las películas delgadas en cuanto a su estructura cristalina, composición química y morfología. Los fotodetectores de SnS:Si mostraron fotorrespuesta hasta longitudes de onda de 1064 nm y también se investigaron sus actividades fotocatalíticas, incluido el rendimiento del ciclo del catalizador. Por otra parte, la espectroscopia UV-Visible, las mediciones de curvas I-V tanto en oscuridad como en iluminación, además de las mediciones de fotorrespuesta, se utilizaron para identificar las propiedades ópticas y eléctricas. Los hallazgos de este estudio demuestran que los fotodetectores híbridos basados en SnS altamente sensibles que operan en la región de longitud de onda extendida (UV-Vis-NIR) con arquitecturas de dispositivos semiconductores prometedores, pueden desarrollarse mediante la combinación efectiva de ablación/irradiación láser pulsada en enfoque líquido y técnicas sencillas de fabricación de películas delgadas.

Chapter 1

An introduction to hybrid nanomaterials, nanostructured thin films and devices using pulsed laser assisted techniques

1.1 Nanomaterials

Nanoparticles are found in nature and can be produced from a variety of materials, but by definition, a nanomaterial must have a minimum of one dimension that is less than or equal to 100 nanometers. According to ISO (2010), a material is considered a nanomaterial if any of its external dimensions are nanoscale (sizes between 1 and 100 nm) or if its internal or external structure is in the nanoscale. Some of the properties of materials in this size regime differ dramatically from those of the bulk material, which is why they are of such high interest in study and research. For instance, colored church windows and other antique-colored glasses with violet or red colors that come from gold nanoparticles distributed in them are some of the early examples where these various qualities were unknowingly employed. Over the past three decades, there has been a substantial impact on the optical and surface properties of nanomaterials due to the quantum confinement effect and extremely high surface-to-volume ratios that enable the stabilization of structures with novel physical properties and substantially size-dependent behavior. These elements have also fueled a tremendous amount of scientific interest in the unique characteristics of nanomaterials [1,2]. These materials have been used to address pressing issues that humanity is currently dealing with, like the increasing demand for green energy, the lack of access to clean water, the absence of effective personalized treatments for cancer and the rapidly deteriorating global environment, to name a few [3]. Some of the uses of nanomaterials are illustrated in Fig. 1.1. Boverhof et al. provide a comparative assessment of several regulatory and advisory definitions of nanomaterials [4].

The following could be part of a comprehensive evaluation of a nanomaterial [5]:

Physical properties	Chemical properties
• Size, shape, specific surface area, and height/width ratio • Whether they stick together • Number distribution by size • Their surface smoothness or bumpiness	• Molecular structure • Zeta potential/surface charge • Composition, including purity, and known impurities or additives • Hydrophilicity/hydrophobicity

• Their structure, including crystallinity and any defects • Solubility-How easily they dissolve	• Surface chemistry • Reactivity

1.1.1 Synthesis of nanomaterials

Generally, there are two types of nanomaterial synthesis: solution-based (mostly chemical) and gas- or vapor-based (chemical or physical). Precipitated hydrolysis, melting and rapid quenching, hydrothermal and thermal decomposition are examples of solution-based processes. Chemical vapor deposition (CVD) [6], metal-organic CVD (MOCVD) [7] and molecular beam epitaxy (MBE) [8] are examples of gas- or vapor-based methods. Initial nucleation and subsequent growth are two crucial processes in solution-based synthesis that are applicable to metal, semiconductor or insulator [9]. By regulating the nucleation and growth processes, it is possible to change the properties of the generated nanomaterials, such as their size, shape and crystal structure. The synthesis techniques for semiconductor nanomaterials (quantum dots (QDs) or nanocrystals (NCs)) differ depending on the semiconductor. As previously stated, the characteristics of nanomaterials depend heavily on their size, shape and other structural aspects (e.g., surface chemistry and porosity). As a result, a lot of work was first put on attaining fine structural control of single-component nanomaterials, figuring out how particular structures evolve, and explaining their features [10,11]. In the 1990s, there was a rapid advancement in the controlled synthesis of nanoparticles, such as the development of the organometallic method for the dependable synthesis of high-quality quantum dots by Murray et al. [10]. In theory, nanoscopic structures can be created either through so-called bottom-up approaches beginning with molecular precursors (such as sol-gel process, laser pyrolysis, molecular condensation, chemical vapor deposition etc.) or through top-down approaches beginning with bulk materials that are transformed into nanomaterials (such as ball milling, laser ablation, sputtering, electro-explosion, various lithographic techniques etc.). One might further differentiate between common physical methods (such as diverse vapor deposition techniques, molecular beam epitaxy and similar) and chemical ways among the numerous bottom-up approaches [12].

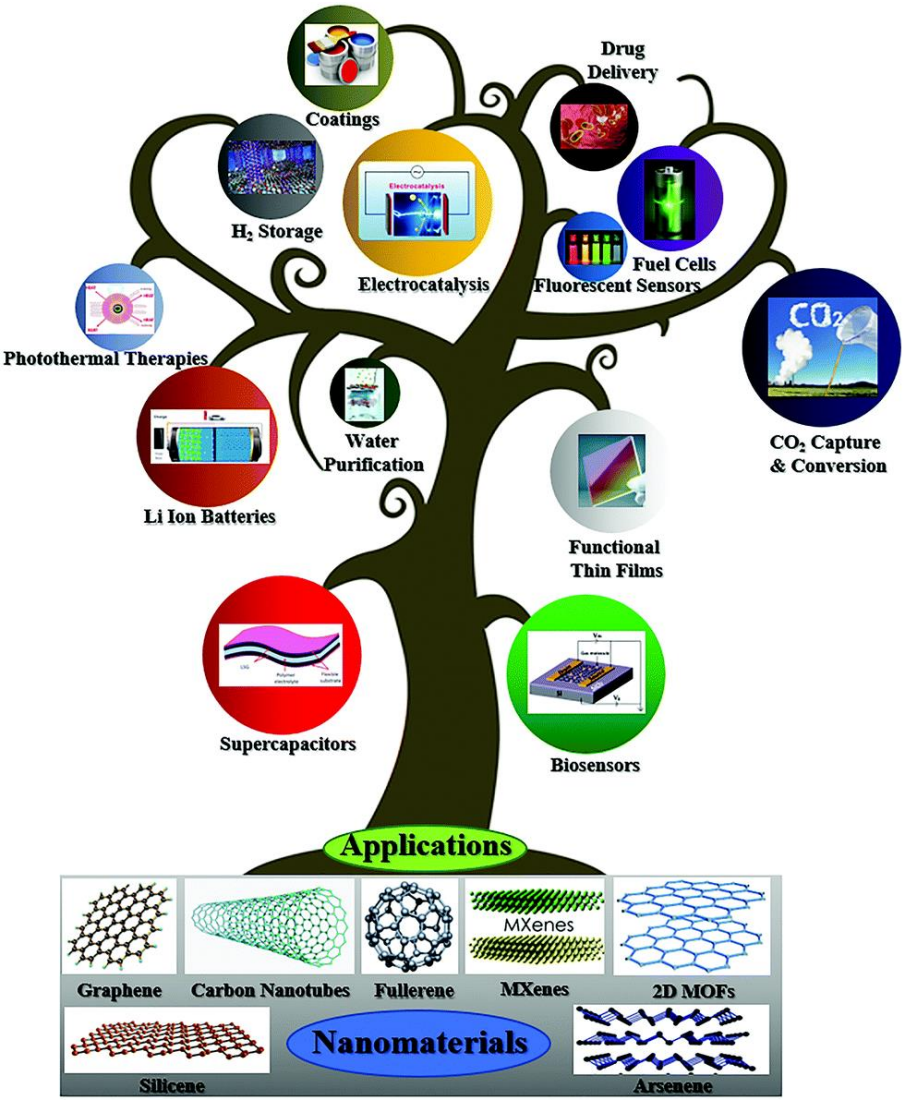


Fig. 1.1: A conceptual illustration of nanomaterials and their uses. *Reproduced with permission from RSC [12].*

1.2 Hybrid Nanomaterials

1.2.1 Introduction to hybrid nanomaterials

The paradigm of research has focused on the creation of hybrid nanostructures—which are made up of a minimum of two different materials. This is done to get beyond the restrictions of single components, to enhance properties, to create novel properties not feasible for single-component nanoparticles, and/or to achieve multiple functionalities for single nano-architectures. The synthesis of different hybrid nanomaterials [13–15] represents one of the most fascinating and rapidly developing areas in materials science in recent years. In order to synthesize hybrid

nanoparticles, two or more different materials must be combined onto one system [16]. Fig. 1.2 shows the numerous hybrid nanostructures, including single/multiple core-shell, yolk-shell, heterodimer NPs, Janus NPs, dot-in-nanotube, dot-on-nanorod, nano-branches etc., have been devised and produced [17–21]:

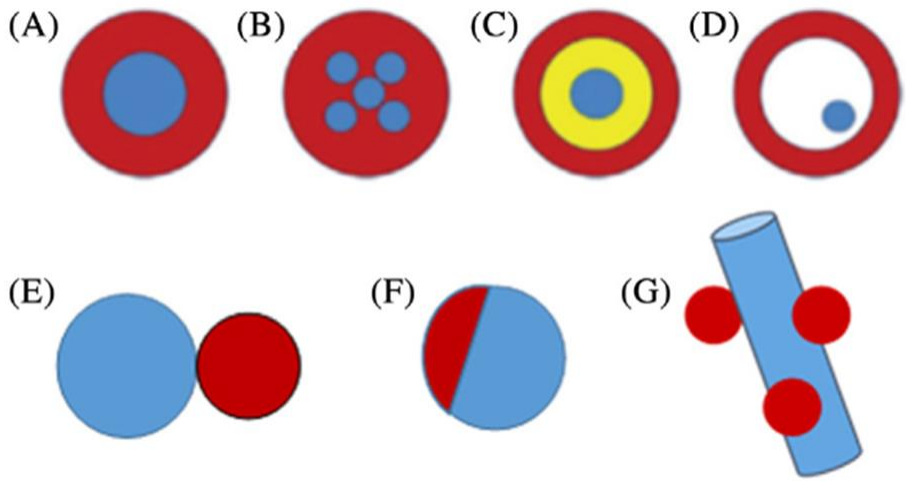


Fig. 1.2: Different kinds of hybrid nanostructures. *Reproduced with permission from [3].*

A "hybrid" colloidal nanocrystal created by combining various material domains provides an intriguing material platform for both understanding the fundamental behavior of connected nanocrystal systems and for producing particles with various functions [22]. Additionally known as "nano bioscience", hybrid nanomaterial science involves the combination of polymer science, biological science and material chemistry [23]. The need for complementary materials drives the development and deployment of hybrid nanomaterials, which enhances a number of features like the electrical, optical and stabilities [24]. According to the traditional categorization of materials as metal, semiconductor and insulator, it's possible to create hybrid nanostructures having components of metal-semiconductor, metal-insulator, semiconductor-insulator, and so on. They might also consist of two distinct metals, semiconductors or other materials. Of course, a hybrid system could potentially consist of several parts. The precise underlying enhancing mechanism is influenced by the structure, optical characteristic and assembly method of each particular nanocomponent. As a result, meticulous planning, careful synthesis, sophisticated characterizations, and a deep insight of structure-property correlations are all necessary to advance the research on highly functional hybrid nanomaterials and its practical implementation in the real

world. A combination of experimental and theoretical methodology is urgently needed to develop this field of study, which has the potential to fundamentally alter many facets of our society and way of life, including health, clean energy and the environment [3]. The statistical information on the status of year-by-year publications from 2000 to 2022 based on hybrid nanomaterials is shown below (Fig. 1.3). Over time, the area of hybrid nanomaterials has clearly received more scientific attention.

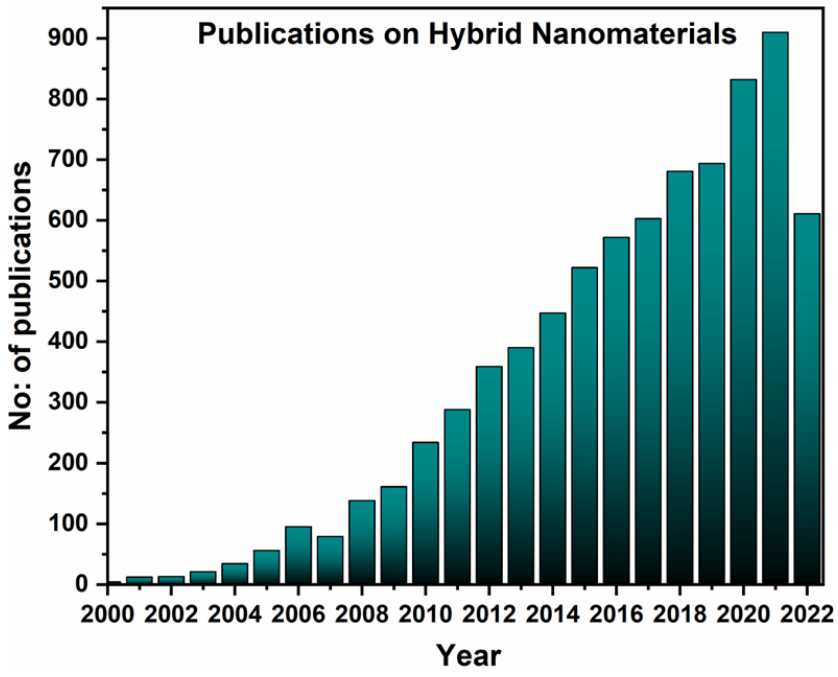


Fig. 1.3: Statistics information on the number of articles published on hybrid nanomaterials between 2000 and 2022 (September) *(Data Source: SciFinder).*

1.2.2 Characterization techniques for hybrid nanomaterials

Li et al. has summarized all important characterization techniques used for studying hybrid nanomaterials in a review article [25]. In this section, some of the methods most frequently used to characterize nanoparticles, particularly hybrid nanomaterials are described. Due to the complexity of hybrid nanomaterials compared to single component counterparts, their characterization frequently necessitates the use of multiple techniques or more advanced techniques. Spectroscopy, microscopy or X-ray techniques are used to base the characterizations. Various methods often rely on measuring light absorption, scattering or emission to gather data on the material properties. Electronic absorption (UV-Vis), photoluminescence (PL), infrared red (IR) absorption, Raman scattering, dynamic light scattering (DLS) and time-resolved techniques such

as transient absorption and time-resolved luminescence are examples of frequently used techniques. Single molecule spectroscopy and non-linear optical methods like up-conversion luminescence are two more specialized techniques. These methods can offer several details regarding the energy levels, surface and other molecular characteristics of interest. While IR and Raman are sensitive to vibration or phonon structures, UV-Vis and PL are sensitive probes of electronic transitions and structures. A measurement of the size of the particles in a solution from the scattered light is provided by DLS. Dynamic features like charge carrier lifetimes are ascertained using time-resolved methods.

In addition to optical spectroscopy, a variety of other experimental methods, including electron microscopy, electrochemistry, and X-ray-based approaches like X-ray diffraction (XRD), X-ray photoelectron spectroscopy (XPS), X-ray fluorescence spectroscopy (XRF), energy dispersive X-ray spectroscopy (EDX) and extended X-ray absorption fine structure (EXAFS), X-ray absorption near edge structure (XANES) are frequently employed to characterize nanomaterials. X-ray techniques are used to learn about structure, energy properties and surface characteristics, whereas microscopy techniques are typically employed to provide structural, morphological and topological information. With the exception of XPS, which analyzes electrons, these X-ray techniques are primarily based on detecting and analyzing radiation that is absorbed or emitted from a sample after being excited by X-rays. The spectroscopic characteristics can be employed for sample elemental analysis because they are distinctive to elements. Other comparable methods that are helpful for structural determination include small angle X-ray scattering (SAXS) and wide-angle X-ray scattering (WAXS). While WAXS predominantly results from regular, periodic fluctuations of electron density over length scales that are substantial compared to the repeat distance, SAXS is caused by inhomogeneous electron density on a variety of length scales ranging from angstroms to microns.

SPM stands for scanning probe microscopy, a collection of methods that have been widely used to analyze nanostructures. These methods include scanning tunneling microscopy (STM), atomic force microscopy (AFM), and chemical force microscopy (CFM). An atomically sharp tip is used in these techniques to scan across the specimen surface, and images are created by either detecting the force exerted on the tip or the current running through it. SPM allows for direct imaging of both organic molecules and inorganic surfaces and can be used in a variety of

environmental settings and liquids or gases. Nanoscale object manipulation is also possible. AFM is a superior option for imaging nanomaterials with any kind of surface (conducting or non-conducting). AFM functions similarly to STM, with the exception that the signal in AFM is the force exerted by the tip against the solid surface. At close range, the interaction between two atoms is repulsive, and at a distance, it is attracted. Images can be created by sensing the force when the tip is scanned across the specimen because the force acting on the tip reflects the distance from the tip atom(s) to the surface atom.

Electron microscopy is a more efficient way to collect high-resolution images in comparison to light microscopes and provides data that would be very challenging to obtain otherwise. A strong and well-liked method for visualizing the surfaces of practically any material with a resolution as low as 0.5 nm is scanning electron microscopy (SEM). The electron probe's characteristics as well as how it interacts with the material affect the image resolution that the SEM provides. Secondary electrons and backscattered electrons are created when an incident electron beam interacts with the specimen. Back-scattered electrons offer both topographic and compositional information, in contrast to secondary electrons observed in SEM, which predominantly offer topography information, such as surface texture and roughness. A method for high spatial resolution, structural and chemical characterization is transmission electron microscopy (TEM). In crystalline specimens, contemporary high-resolution TEMs (HRTEMs) have the ability to directly picture atoms at resolutions close to 0.2 nm, which is smaller than the interatomic distance. For materials at length scales ranging from atoms to hundreds of nanometers, this kind of characterization is crucial. Nanomaterials can be characterized using TEM to learn more about the size, shape, crystallinity and interparticle interactions etc.

1.2.3 Optical and Electrical Properties of Hybrid Nanomaterials

The incredible potential for combining several features in one material spurred an explosion of concepts for novel materials and applications. Investigations in this area, specifically to understand the relationship between structure and property, are vital because the fundamental science is occasionally still not fully known. There is a huge need for novel materials as a result of recent technical advancements and the desire for new functions. Early on, scientists and engineers discovered that materials in mixtures can exhibit better qualities than their pure counterparts [26]. Due to the synergistic qualities produced by the hybrids as well as the distinct characteristics of the individual components in the system, hybrid nanostructures have special

properties. Hybrid semiconductor nanomaterials have distinctive and intriguing optical capabilities that are useful in emerging technologies. In contrast to single component nanomaterials, hybrid nanomaterials provide the flexibility and opportunity to modify the material composition as well as associated factors like shape and interface to alter the properties of the material. When numerous materials are combined into a single particle at the nanoscale, changes in the optical and electrical properties that arise can essentially be separated into two groups:

(a) Multi-functional nanocrystals, wherein the hybrid particles largely maintain the original characteristics of both constituents while being merged into a single nanoparticle system; and, more intriguingly,

(b) Hybrid materials in which the addition of a second material causes a significant change in the properties of one material. The distinction between these two circumstances is not always clear-cut.

For the same combination of materials, the morphology of the particle (how one material domain is grown in relation to the other) and how they are connected together affect the attributes of the final hybrid nanomaterial in addition to the material properties of both components (whether the components are bonded chemically, brought close together by chemical linkers or assembled through self-assembly) [27].

Optical Properties

The resultant hybrid structures need not have their absorption spectra as linear addition of each component's absorbance, despite the fact that the overlap of the absorbance of the two materials making up the hybrid is unquestionably significant [28–30]. If we consider different combinations of hybrids, it has been proposed that for a metal-semiconductor hybrid generated by the combination of the two materials results from the mixing of the electronic states of the two materials, resulting in a changed density of states that alters the absorption spectrum [31]. In hybrid nanoparticles, the absorption of the semiconducting and metallic domains may also show notable alterations. In certain cases, the excitonic properties of a semiconductor often become "washed out" as metal domains build on top of it, making the excitonic peak and fine structure considerably less noticeable. When a wide-band-gap semiconductor is used, such as in the case of silver growth onto ZnO (the silver plasmon occurs at about 440 nm, whereas the ZnO absorption edge occurs

near 375 nm [32]) or gold growth onto CdS [29], this is most easily performed. At the resonance frequency, a typical anti-crossing and splitting of energy levels is seen in other circumstances where the excitation energy is shared and oscillates between the plasmonic and excitonic systems (Rabi oscillations) [33]. The combination of two semiconductors can be categorized as type I hybrids, consisting of a low band gap core and a wide band gap shell (such as CdSe/CdS), and they exhibit greater photooxidation stability, higher quantum yields and narrower emission peaks than one-component QDs. While type II semiconductor materials, such as CdSe/CdTe, which are made of materials with comparable band gaps, permit the localization of the electron and hole in various regions of the nanocrystal, resulting in spatially separated negative and positive charges as well as longer photoluminescence (PL) lifetimes [34]. Fluorescence is another aspect that influences optical properties, depending on how the two domains are chemically coupled. If it leads to a direct channel for charge separation, it will either quench luminescence or augment it due to the geometry of the hybrid structure, which effectively transfers energy from one component to another.

The chemistry of each component, as well as how two or more constituents interact with one another in a hybrid nanomaterial, plays a significant role in terms of optical properties. Interface, size, shape and structure are only a few examples of qualities that have a significant impact on how they interact. The optical properties of the composite should be like the straightforward summation of the optical characteristics of the constituent components in the utmost case of no or minimal interaction between the components. When the interaction between the materials is strong, the distinct properties of each of them are lost and new features are created and as a result additional absorption and emission bands might, for instance, develop in the absorption and emission spectra of hybrid nanomaterials.

Electrical properties

Combining two extremely different materials with complementary electrical properties might result in unique properties that are not seen in the separate materials. An intriguing feature is how the hybrid nanoparticles' nanoscale contact behaves when illuminated. An electron-hole pair is produced by the semiconductor component of the hybrid after it absorbs above-bandgap photons. Small molecules can act as a bridge to lower the activation potential for transport by being introduced at the junction of two grain boundaries [35]. The particular geometries and distinctive

characteristics of nanomaterials, such as their high surface-to-volume ratios, quick charge transport pathways and effective light scattering and trapping effects, offer an excellent platform for investigating how size reduction and low dimensionality affect electrical properties [36]. For pristine tin oxide (SnO_2), which has less conductivity, the electron-hole pairs tend to recombine, resulting in limited carrier lifetime and decreasing the photocurrent. Hybrids based on SnO_2/$SnSe_2$ were produced in which the addition of $SnSe_2$ has enhanced the photodetector's detection range while also assisting in the efficient separation of electron hole pairs produced in SnO_2 under UV light illumination. Additionally, $SnSe_2$ functioned as a transport layer generating a low resistive channel for the carriers due to its high conductivity [37]. Depending on the functionality, different combinations of hybrids can be tried out e.g.: QD/1D, nanoparticles/1D, 1D/1D nanostructures, 1D/2D nanostructures, organic semiconductor/Si, hybrid organic-inorganic semiconductor/Si, 0D/2D or 2D/2D nanostructures etc. [36,38].

1.2.4 Applications of Hybrid Nanomaterials

For hybrid materials, numerous combinations, including magnetic/luminescent, plasmonic/catalytic, and magnetic/catalytic, have been tried and achieved, greatly developing the repertoire of functional materials and even opening up new study fields. Examples include the development of two extremely promising sectors, plasmon-enhanced photovoltaics [39] and plasmon-enhanced photocatalysis [40], as a direct result of the fusion of plasmonic metal nanoparticles with semiconductor materials. Electronic, optoelectronic applications, environmental applications, biomedical applications, water purification [25,26,41,42] are some of the other areas of applications of hybrid nanomaterials.

1.3 Material Synthesis by LSPC techniques

Hybrid nanoparticles can be synthesized by physical or chemical methods. The synthesis of ligand/surfactant-free nanomaterials in natural environments is now made easier and more scalable by the use of laser synthesis and processing of colloids (LSPC) [43]. A variety of nanostructured materials can be synthesized at room temperature and pressure conditions and the final product is typically achieved without byproducts and requires no additional purification attributable to synthesis that is "simple and clean." The costs of production of the NMs will be lower than those of the wet chemical approach, despite the initial capital investment necessary to get the laser system. Based on the laser parameters, control over the nanoparticle size, shape and morphology is possible by this plug and play control technique [44]. Pulse duration, laser

wavelength, laser fluence and focusing, repetition rate and ablation/irradiation time are a few of the laser characteristics that affect the synthesis and processing of NPs. A comprehensive discussion on these parameters is beyond the scope of this thesis. Where necessary, the discussion is made in the corresponding thesis chapters.

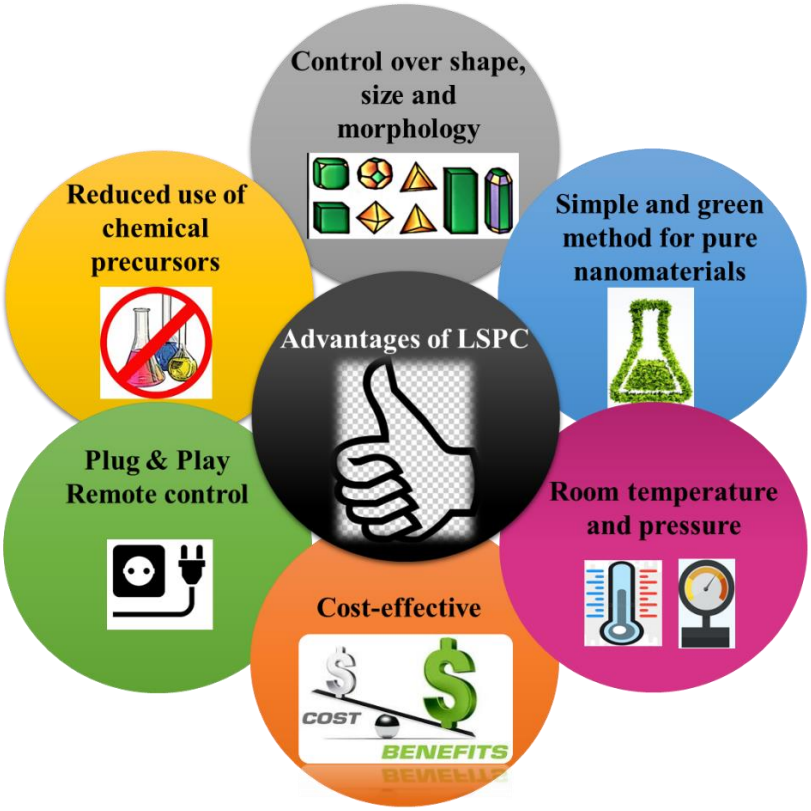


Fig. 1.4: Advantages of LSPC techniques.

The three methodologies of the LSPC techniques are i) laser ablation in liquids (LAL), ii) laser fragmentation in liquids (LFL) and iii) laser melting in liquids (LML). A brief synopsis of these techniques is described below. The two strategies used for the synthesis of different NPs in different works of this thesis are PLAL and PLFL. These topics are detailed and focused because of this.

Laser Ablation in Liquid (LAL)

The first-time laser ablation in liquid (also known as LAL) was used to create a colloidal solution of nanoparticles was less than two decades ago. In 1993, to create colloidal solutions

containing metal NPs, pure metal targets were pulsed laser ablated in several solvents [45]. Since then, LAL has evolved into a crucial technique for producing metals, semiconductors and even polymer NPs. Ablation is the process of removing surface atoms and includes both single photon process (breaking chemical bonds) and multiphoton excitation (thermal evaporation) [46]. The basic principle of LAL is the interaction of a laser beam with a bulk target (physical form of a substance) immersed in a thin layer of low-absorbing liquid. The experimental set-up for laser ablation in liquid method is given in Fig. 1.5. The liquid or solvent of choice must be transparent to the laser beam in order for the interaction to prevent liquid breakdown at the chosen fluence. Due to the filamentation and self-focusing effects, this problem also affects LAL, LFL and LML, and it is made more difficult when using ultrashort pulses [44]. Crucial milestone in the field of LAL includes the effective use of reliable Q-switching techniques, the creation of brand-new pulsed laser sources (such as nanosecond pulsed Nd-YAG and excimer lasers), and, more recently, the expansion of the availability of intense pico- and femto-second pulses. The great variety of applications for pulsed laser ablation technologies, however, has proven equally significant [47].

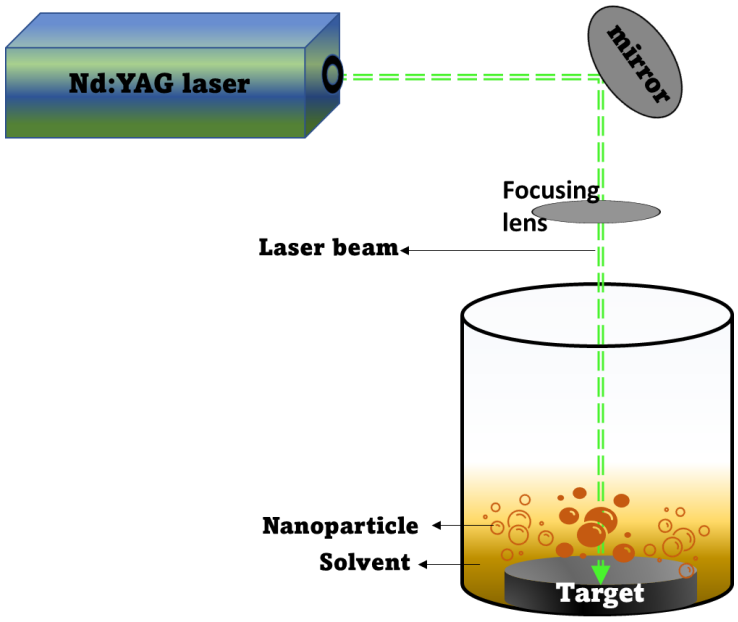


Fig. 1.5: Fundamental laser ablation in liquid laboratory setup.

Amendola et al. has explained some of the investigation techniques that can be employed to understand the mechanism of laser ablation as well as to characterize the products of ablation. This is shown in Fig. 1.6. The mechanism begins with the bulk target absorbing the laser pulse and forming a plasma plume. This is followed by the expansion of a plasma plume carrying the ablated

material into the surrounding liquid and the production of a shockwave. A shockwave is a pressure wave that moves through a medium and denotes a sudden change in temperature and density along its front. The breakdown-related expansion of plasma pushing the surrounding liquid results in a cavitation bubble which is a thin layer of vapor. The formation of the cavitation bubble is influenced by the liquid environment, a stronger confinement of the plasma and a quick energy transfer from the plasma to the surrounding liquid. The target and liquid are heated during shockwave propagation, which may aid in the separation of material from the crater. The plasma plume cools down and releases energy to the liquid solution as it expands. This event causes the release of a second shockwave, which causes the cavitation bubble to expand in the liquid before collapsing on a time period of hundreds of microseconds releasing NPs in the liquid resulting in stable colloidal solution [48,49].

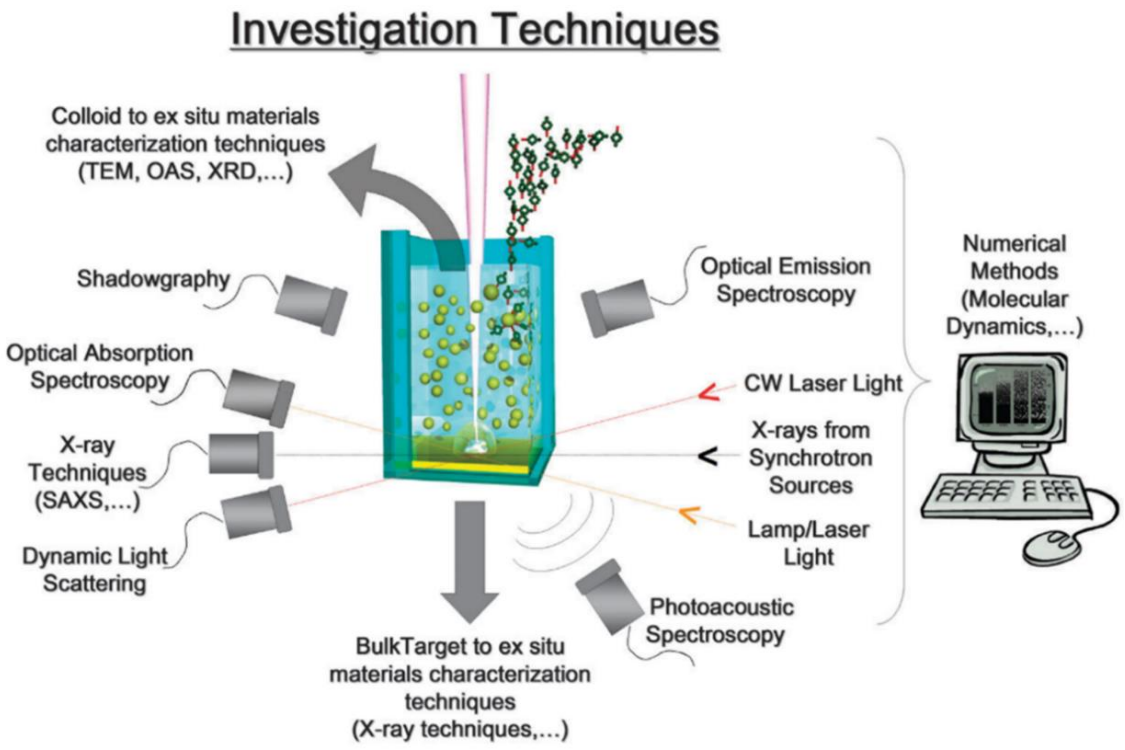


Fig. 1.6: Sketch of the techniques used so far for the investigation of LAL. *Reproduced with permission from* [48].

The pros of the techniques are organized below [50–57]:

- First, due to the high energy flux of the laser spot, almost any materials can be ablated for the synthesis purpose.
- The liquid medium in PLAL has a substantial impact on the morphology, enables some efficient parameter control during fabrication, and is widely applicable to the creation of micro- and nanostructures from virtually all forms of solid materials.
- Improved stoichiometry and phase composition control, which is highly helpful for the creation of complicated materials, including some high-quality nanomaterials that would be challenging to synthesize otherwise.
- Without the use of any chemical additives or precursors, the PLAL approach has the power to remove surface contamination; more crucially, it has the capacity to create new structures and metastable phases in a highly non-equilibrium synthetic environment.
- According to reports, the stability of nanoparticles against agglomeration is caused by a laser-induced surface charge that ensures extremely high colloid purity, negating the need for stabilizing ligands. A somewhat wide particle size dispersion and a poor production rate are the main limitations found.

Laser Fragmentation in Liquid (LFL)/Laser Melting in Liquid (LML)

It requires the use of short or ultra-short laser pulses to irradiate microparticle suspensions in transparent liquids. This method results in selective nanoparticles (NPs) absorption by interacting the electromagnetic wave with the electrons of the NPs, which generates collective mobility of the conductive electrons in metals or collective perturbations of electronic orbitals in non-metallic NPs [58,59]. Particle size modification and chemical conversion are made possible by laser irradiating educt particles in a liquid environment. If the solid output material is already in a particulate state, this method is simple. Pulsed laser processing of particles in liquids is a continuous process that meets conditions for upscaling, but it lacks mechanistic insight. There are two distinct processes that it can be divided into. One method involves the reduction of particle size through pulsed laser fragmentation in liquids (PLFL), and the other involves the transfer of particles into a molten state and subsequent re-solidification as spheres and is known as pulsed laser melting in liquids (PLML). The schematic representation of both the techniques is shown in

Fig. 1.7. When it comes to PLFL, these educt particles liberate the smaller ones that were trapped in the liquid. The educt particles melt, fuse, and then resolidify as spheres when they are exposed to laser parameters that result in PLML, with the particle size either increasing or remaining constant. The laser parameters and the material's response to incident light determine whether PLFL or PLML occurs during pulsed laser processing in liquid. PLFL falls within the category of wet comminution. However, PLML is distinct since an electromagnetic wave is used to irradiate the particle directly with the energy. In a liquid environment, the particle can therefore melt or fragment without the presence of any surfactants or impurities [60].

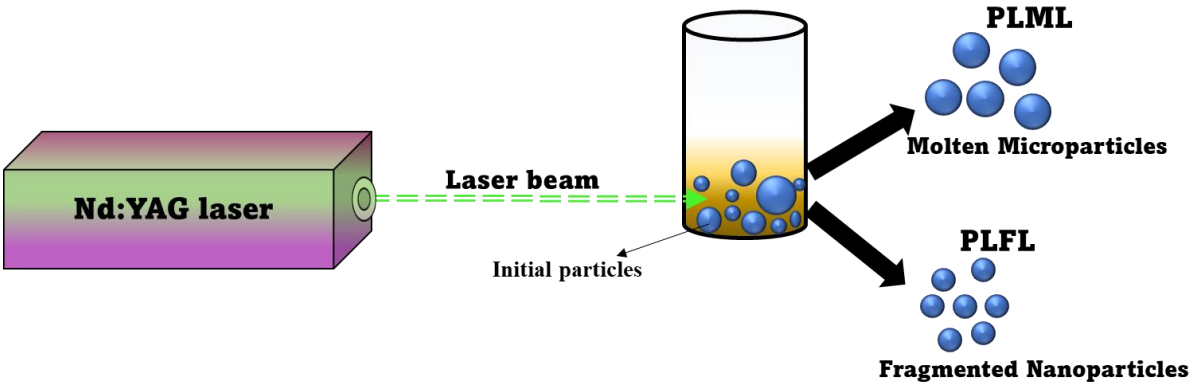


Fig. 1.7: Setup for laser melting and fragmentation experiments in liquid.

Mechanism of laser fragmentation

By irradiating suspended particles in a liquid, pulsed laser fragmentation is an efficient process of producing organic, metal, or semiconductor nanoparticles. Modeling and upscaling of this process, however, do not quantify the amount of laser energy needed for a certain NP product property, such as the colloid particle diameter or the bandgap energy of the synthesized nanoparticles. Typical difference in comparison to PLAL is that the flat surface of the bulk target material is exposed to irradiation during PLAL. Instead of using 2D geometry, PLAL from 1D thin wire-shaped targets releases nanoparticles at the wire's tip since the cavitation bubble is not contained by a flat surface [61]. In comparison to flat target geometries, this leads to much greater production rates [62]. In PLFL, 0D targets formed of suspended microparticles can be irradiated and disaggregated or fragmented into smaller particles to increase the degree of freedom for cavitation and nanoparticle release. In order to achieve the requisite fluences and intensities for adequate fragmentation, the pulsed laser beam utilized in PLFL technique is typically focused into

a suspension of micro- and/or nanoparticles. Even though the pioneering studies included PLFL, there is still little known about the mechanisms that occur when these particles are exposed to radiation and nanoparticles are created. Mechanisms that have been proposed include atom disruption from within the particle, mechanical eruption, or shock waves [63,64]. Particles suspended in liquids can change in size and structure when excited by intense laser light. If the target particles are exposed to an energy dose high enough, one of the mechanisms listed below may cause the size of the particles to decrease, resulting in the production of nanoparticles. The two main processes that PLFL can use are vaporization-induced nanoparticle formation and shock wave-induced particle disintegration. A fundamental mechanism can be hypothesized based on the nanosecond (ns) laser that is utilized in our work. The photons from the ns laser are absorbed, which results in electron-electron coupling, lattice energy transfer and an abrupt thermalization of the electrons. An increase in the lattice energy of the particle as a result of the entire process will result in fragmentation [65].

The process of laser ablation in liquids has a limitation in terms of its poor productivity, which is often only a few milligrams per hour [66,67]. However, research has led us to believe that the process of transformation of nanoparticles into sub-micrometer spheres might be completed in a shorter amount of time. As a result, sub-micrometer sphere production can be around two orders of magnitude more productive than LAL. Because of the reduction in size from bulk materials to nanoparticles and the resulting rise in the laser beam's absorption efficiency, productivity has significantly enhanced and reaction times have decreased [59]. The synthesis of Ag nanoparticles reported by Pyatenko et al. [68] in 2007 was a groundbreaking study on laser irradiation. They claimed that one-step or multistep synthesis can produce spherical particles of various sizes, with the final product or the intermediate colloids being soft laser treated. The highest amount of fluence for heating and melting that does not evaporate the spherical particles and, thus, does not change their sizes was defined as the soft laser fluence used in their method. The particle heating-melting-evaporation model, whose applicability was confirmed by the experiment findings, was used to determine this soft laser fluence. In 2010, Koshizaki's group [59,69–74] performed laser irradiation for colloidal NPs using a non-focused laser beam of moderate fluence as other research groups gradually began investigating the potentials of pulsed laser irradiation (fluence lower than the ablation threshold). Their findings demonstrated that under these laser irradiation settings, NP fusion was induced, resulting in submicron-sized particles (SMPs). This discovery was noteworthy

since there had never before been documented a straightforward, controllable approach to increase particle size. In Fig. 1.8, some of the most important applications of LSPC techniques in general are shown.

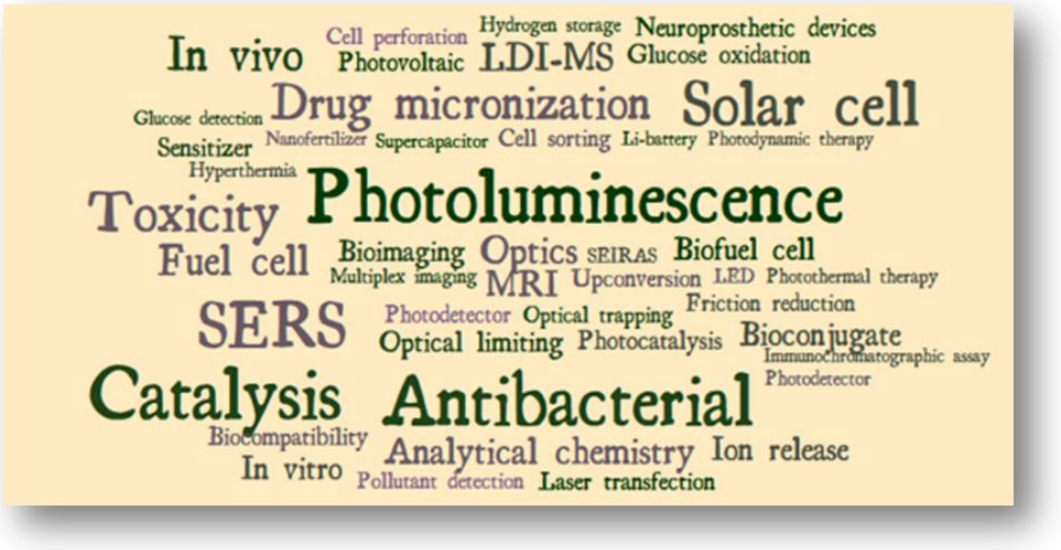


Fig. 1.8: Word cloud illustrating LSPC-NP uses mentioned in the literature. The word size in the figure is proportional to its mentions in the literature. *Reproduced with permission from* [43].

1.4 Thin films and devices from nanocolloids

Numerous methods, including hydrolysis [75], microwave irradiation approach [76], pulsed laser ablation [77], sonication-assisted layer-by-layer encapsulation [78], co-precipitation [79], etc., have been reported for the synthesis of nanocolloids. Rane et al. [79] reported the methods of synthesis for the fabrication of nanoparticles and described some of these methods stated above as well as others in detail. Utilizing NPs in colloidal form has several benefits, including the ability to manage NP size distribution, particle shape and composition suitable for synthesis at a laboratory scale [80]. In contrast to chemical synthesis methods, which need time-consuming processes or high temperature processing, the methodologies for producing thin films from nanocolloids are much simpler and would significantly reduce the amount of time required to deposit thin films. Additionally, the use of colloidal NPs simplifies the process of film formation and enables better control of the film morphology and properties since these elements are mostly determined by the properties of the NPs in the colloid [81]. Due to the utilization of the desired material's NPs as the source material, the film composition may not change at all until significant

alterations are made to the deposition conditions. Since in this thesis work, we focus on NPs synthesized by LSPC techniques, some of the most pertinent and intriguing reports on thin films and devices made from nanocolloids by laser assisted techniques are reviewed.

Monometallic and bimetallic Pt and Pd NPs were synthesized by PLAL followed by spin-coating of these NPs onto graphene layers for nanofabrication of NPs/graphene composites [56]. Even more potential possibilities for these nanocomposites in catalysis and electronic devices were mentioned. The **Spin-coating** method is a straightforward, simple, and room-temperature technique for producing thin films. Uniform coatings are produced by evenly casting a solution of the required substance in a solvent ("ink") across the substrate's surface while it is spinning [82]. To create colloidal metallic nanoparticles of Cu (In, Ga) Se_2 (CIGS) for thin film solar cells, Guo et al. reported a ligand-free synthesis employing liquid-phase pulsed laser ablation and electrophoretic deposition (EPD) [57]. Without switching to a different solvent or utilizing binders, EPD of the colloids produced the corresponding metallic precursor thin films with high purity and exact composition. Thin film chalcopyrite solar cells ($CuInSe_2$) based on EPD of colloidal nanoparticles has been reported [83]. **Electrophoretic deposition** relies on the colloidal particles' electrokinetic mobility when it is measured in the presence of an external electric field [84]. The increasing applications and interests in depositing nanoparticles have been widely studied and published in the book 'Electrophoretic Deposition of Nanomaterials' by Dickerson et al. [85]. The main benefit of EPD is the elimination of the need for binders and adhesives because of the film densification caused by a strong electrical force close to the electrode (substrate) surface. It can also be used for flexible substrates or substrates with complicated surface shapes. The surface charge of the particles, the electrical and fluidic properties of the solvents, the material of the electrode and the current-voltage characteristics must all be carefully considered in order to deposit a smooth and crack-free thin film. Our group has reported two-step process of **spin-dip coating** of $CH_3NH_3PbI_3$ to which PbS nanoparticles synthesized by PLAL were incorporated by dipping [86]. Synthesis and characterization of thin film solar cells based on the structure were reported. To generate homogeneous coatings on a substrate, the **spray deposition** technique involves directing an atomized stream of molten material droplets onto the substrate [87]. The fabrication of thin films of tin sulfide (SnS) by spray-deposition of SnS nanocolloids prepared by PLAL was reported [88]. The photodetector characteristics and cyclic voltammetry studies were also presented. While the film thickness is primarily influenced by the distance between the substrate

and spray nozzle, substrate temperature and precursor solution concentration; the properties of the films deposited using this technique depend on the spray rate, ambient atmosphere, substrate temperature, droplet size, carrier gas and cooling after deposition. Moreover, this method has the benefit of depositing high-quality films with practically no thickness restrictions. CuO NPs/Si heterojunction photodiode fabricated by **drop-casting** CuO NPs onto Si wafer were reported [89]. The fabrication of a colloidal In_2O_3 NPs drop-casted over an n-type single crystal silicon wafer is used to demonstrate a solution-processed silicon heterojunction photodetector [90]. The rectifying behavior and the good photoresponse were validated by the I-V characteristics and from the C-V readings, which showed an abrupt junction, the built-in voltage was calculated. The above-mentioned works demonstrate that thin films made from laser processed colloids are suitable for device applications such as solar cells, photodiodes, photodetectors, LEDs etc. due to their unique morphology, properties and low temperature processability.

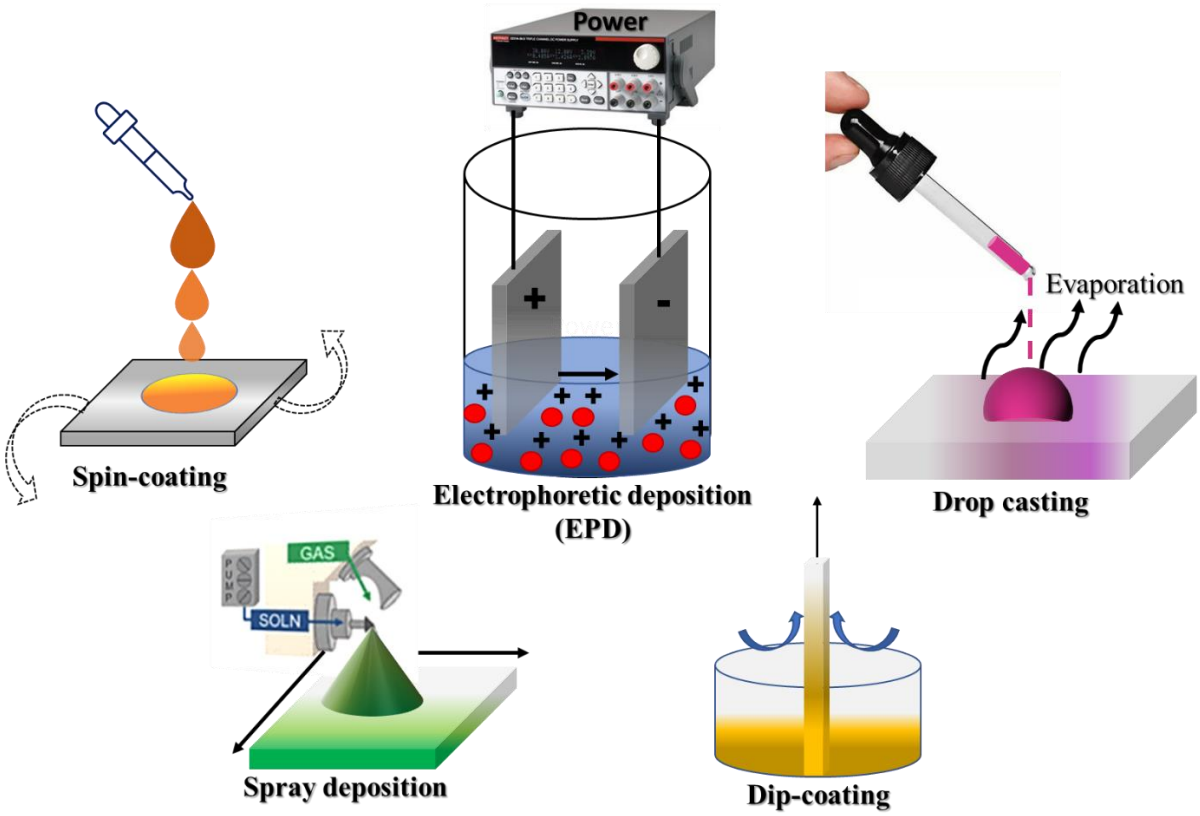


Fig. 1.9: Schematic of the most used techniques for thin film fabrication from nanocolloids.

1.5 Photodetectors – Properties and devices

The general idea behind photodetection in semiconductors is the generation of electron-hole pairs in response to light (photons). When a semiconductor material is exposed to photons with energies larger than or equal to that of its bandgap, it drives the electrons from the valence band into excited states in the conduction band, where they behave like free electrons and can move across the crystal structure over great distances when subjected to an internal or external electric field [91]. The positively charged holes that are still present in the valence band also aid in electrical conduction by shifting from one atomic site to another as a result of the electric field. Accordingly, the separation of electron-hole pairs produced by light absorption results in the generation of a photocurrent, which is defined as the fraction of photogenerated free charge-carriers that are collected at the material's edges by the electrodes of the photodetecting structure and whose current density at a given wavelength is an increasing function of the incident light intensity. Based on the type of electric field that causes the charge separation of photogenerated electron-hole pairs, we may distinguish between two major groups of photodetectors at this level:

★ **Photoconductors**, that are composed of a simple semiconductor layer with just two ohmic connections, and where the electric field resulting in the collection of the charge-carriers is generated by applying a bias voltage between the contacts at either end. It functions by utilizing the improvement in electrical conductivity brought about by the photogeneration of free carriers [92].

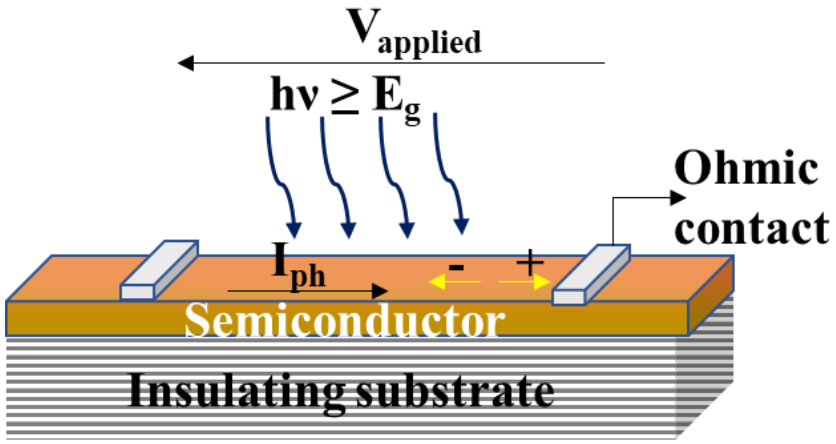


Fig. 1.10: Structure of photoconductive photodetector

★ **Photovoltaic** photodetectors, which separate the charge using the internal electric field of a p-n or Schottky (metal- semiconductor) junction.

In a p-n junction photodiode configuration, shallow diffused region is present. Then through diffusion, the carriers created within the junction's diffusion length migrate to the space charge region, where an electric field is used to separate them (minority carriers become majority carriers on the other side). This results in the generation of a photocurrent, which alters the voltage across the open-circuit cell or, in the case of a short circuit, causes current to flow [93].

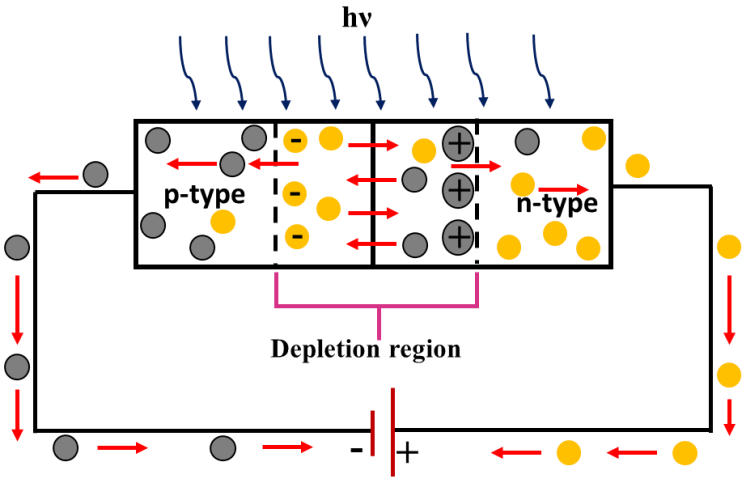


Fig. 1.11: Structure of photodiode

A metal-semiconductor (m-s) junction produces a majority carrier device known as a Schottky barrier photodiode. The m-s interface offers a potential barrier that might keep the optically created electron-hole pairs apart, just like the p-n junction diodes. At the m-s interface, carriers can be generated in both the space charge area and the neutral semiconductor region.

The technique used for detection is frequently used to categorize photodetectors. The effects of the light-matter interaction used for photon-carrier propagation in photodetectors are generally photoemission or photoelectric effect, thermal effect, photochemical effect, polarization effect, or weak interaction effect [94].

The standard specifications of a good photodetector are [95]:

- A **high sensitivity** to the signal's emission wavelength range
- A **minimum** addition of **noise** to the signal

- A **fast response speed** to handle the desired rate
- Be **insensitive to temperature** variations
- Have a **reasonable cost** compared to other system components
- Have a long **operating lifetime**

A wide range of applications for photodetectors include monitoring, remote sensing, telecommunication, astrophysics, high energy physics experiments, aerospace, nuclear safety guards, medical imaging, and photonics. Because of this, there is a lot of interest in creating high-performance, inexpensive and compact light sensor devices [94,96].

1.5.1 Characterization of photodetectors

In this section, we present cutting-edge micro and nano characterization methods that span every step of the fabrication of photodetectors, from material synthesis through construction to photoresponse mechanism analysis. Photodetectors can be characterized for increased efficiency and extended wavelength absorption by combing these with some complementary technologies as well. Only a brief discussion of the methods is made here but Zhong et al. has already explained in great depth [96].

Due to their atomic thickness and quantum confinement, nanomaterials of different dimensions are prone to hetero- and metal-semiconductor interfaces (heterojunction). The characteristics of the nanomaterials will be drastically altered, if not completely destroyed, by the interactions. Creating a clear and precise interface is crucial for producing high-performance photodetectors. **Transmission electron microscopy (TEM)** is an effective instrument for examining crystal structures. Impact of interface quality on a photodetector for 2D materials can be understood from STEM and HRTEM. **Raman Spectroscopy** is connected to vibrational modes and offers a wide range of information about crystal orientation, defects and doping concentration. It is a very practical and non-destructive method when compared to TEM. The trap center defects, which drastically slows response time, should be taken into account while building high-performance photodetectors. Carrier mobility for anisotropic 2D materials varies with different directions, which has an impact on photoresponse, transient response, operating speed and drift velocity. The mobility is further impacted by the layer number and crystal orientation, which likewise places restrictions on the on/off ratio. High-performance photodetectors and functional electronics can both benefit from knowing the crystalline growth direction. The Raman spectra for

the anisotropic structure exhibits a strong polarization dependence, which enables it to distinguish the ideal direction. Additionally, the stacking between various layers is crucial for electrical and optical properties. The aforementioned problems can be found via Raman spectroscopy. **Photoluminescence spectroscopy (PL)** can be used to determine the bandgap, which is a crucial parameter for identifying the range of the response wavelength and the properties of the photodetectors. The bandgap of the material can be altered using a variety of techniques because of the atomic thickness and van der Waals interaction. The PL spectrum, which provides direct proof for bandgap, can be used to study electron transition path.

1.5.2 Parameters of photodetectors

Quantum efficiency (η): is described as the quantity of charge carriers produced by a photodetector for each incident photon.

In purely defect-free materials, the internal quantum efficiency—defined as the number of pairs generated divided by the number of photons absorbed—is typically quite high. Only the photon-generated carriers that are collected as a result of light absorption are taken into consideration by the external quantum efficiency. External quantum efficiency is a more useful metric than internal quantum efficiency for photodetector measurements because it shows the useful fraction of signal produced by interaction between light and photodetector. The number of carriers captured divided by the number of incident photons is how external quantum efficiency is calculated [97].

$$\eta = \frac{\frac{I_\lambda}{e}}{\frac{P_{opt}}{h\nu}} \qquad (1.1)$$

where I_λ is the difference between current upon illumination and the current in dark ($I_\lambda = I_{light} - I_{dark}$) at a given wavelength (λ), e is the electron charge and P_{opt} is the incident optical power in Watt. The quantity, $h\nu$, is the energy per photon in Joules, where h is Planck's constant and ν is the frequency.

Sensitivity (S): Sensitivity, or the ability of the device to detect weak signals, is one of the most critical factors that affects the quality of a photodetector. Sensitivity is measured by the sample's altered conductivity in response to illumination. It is determined by the photocurrent to dark current ratio [98,99].

$$S = \frac{I_\lambda}{I_{dark}} \times 100\% \qquad (1.2)$$

Spectral Responsivity (R): is defined as the quantity of photocurrent produced per unit of incoming light output on an effective area [100].

$$R = \frac{I_\lambda}{PA} \qquad (1.3)$$

R is the spectral responsivity, P is the optical power density (optical power density is the laser power by the area of the beam), A is the active area of illumination.

Noise equivalent power (NEP): is the smallest amount of light required to differentiate between the photocurrent and noise current, with the input optical power at a signal-to-noise ratio (S/N) of 1. The minimum amount of light that a photodetector can detect is defined by NEP [101]. Thus, the following expression can be used to calculate a photodetector's NEP:

$$NEP = \frac{\sqrt{2eI_{dark}}}{R} \qquad (1.4)$$

Specific Detectivity (D*): The least discernible radiant power is measured by the normalized specific detectivity [102].

$$D^* = \frac{R\sqrt{S}}{\sqrt{2eI_{dark}}} \qquad (1.5)$$

Spectral response (SR): explains how a photodetectors responsivity changes with photon frequency [94]. The quantum efficiency and the spectral response are conceptually identical and the choice is made based on the application. The quantum efficiency employs the photon flux, whereas the spectral response uses the power of the light at each wavelength. The formula below is used to convert quantum efficiency to spectral response:

$$SR = \frac{e}{h\nu} \times \eta \qquad (1.6)$$

Response time (Rise time/Decay time): The photocurrent's rise time and decay time are measured in terms of how long it takes for the photocurrent to go from 10% to 90% of its maximum value and back down to 10% of its maximum value, respectively [103].

Linear dynamic range: To determine whether the devices' responsivity remains steady under different light conditions [104].

$$LDR = 10 \log \frac{P_{sat}}{NEP} \qquad (1.7)$$

where P_{sat} is the light intensity causing the signal saturation.

1.6 UV-Vis-NIR semiconductor photodetectors

Broadband photodetectors have been utilized and researched in numerous fields. The development of hybrid high-performance flexible broadband detectors based on chalcogenides, perovskites etc. are explained. Norton et al. published a review on the synthesis, properties and applications of bulk and two-dimensional SnS in which the photodetectors fabricated by different synthesis methods and photodetector parameters are mentioned [105]. Li et al. synthesized colloidal SnS nanosheets with the aid of surfactants to modify their size and shape. The device had a sensitivity of 0.95, a spectral response of 10^3 A/W and a detectivity in the order of 10^9 Jones [106]. Broadband image sensors using a two-step vapor deposition technique, with SnS QDs/Zn_2SnO_4 (ZTO) nanowire hybrid nanostructures were developed as sensing components. The hybrid QDs/NWs displayed substantially greater photoconductive gain and specific detectivity in the UV area as well as prolonged photoresponse stretching from UV to NIR region (300-900) when compared to pure ZTO nanowires. The photodetector showed increased photoconductive gain (up to 1.6×10^6) and specific detectivity (up to 3.8×10^{16} Jones) [107]. Other chalcogenides with some of excellent properties are as follows. A monolayer MoS_2 photodetector with a broad photoresponse (375-808 nm), detectivity of 10^{10} Jones and superior responsivity of 0.0084 A/W was developed by chemical vapor deposition [108]. Jiang et al. reported self-powered photodetectors of $SnS_2/ZnO_{1-x}S_x$ heterojunctions produced by a simple sputtering technique operating in the range of 365-850 nm. It demonstrated a responsivity of 8.28 mA/W, photodetectivity of 5.09×10^{10} Jones and the device had a fast response speed with a rise time of 49.51 ms and a decay time of 25.93 ms [109]. The fabrication of UV-Vis-NIR photodetectors on mica based on ZnO nanowire array and PbS QD heterostructures using electrospinning and exchanging procedure were reported to have a steady photoresponse between 350 and 900 nm even after 200 cycles of 180 bending [110].

The review article by Wu et al. highlights current developments in using novel optoelectronic nanohybrids and comprehending the underlying physics toward high-performance optoelectronic nanohybrids that are competitive in the commercialization of diverse optoelectronic devices. Due to their exceptional optical absorption in the IR spectrum, which is ascribed to the

1D electronic structure and improved ballistic carrier transport along the carbon nanotube (CNT) axial direction, CNT-based nanohybrid photodetectors are arguably the ones that have received the most research attention among other optoelectronics. The review also covers details about graphene based nanohybrids, implementation of plasmonic structures in nanohybrids, 2D based detectors and flexible photodetectors [111]. Another review on perovskite-based materials [112] describes performance characterization in photodetectors and charge photo-generation in perovskites and/or its hybrids. Perovskite-based photodetectors are examined and detailed in terms of their various compositions, constituent materials' structures and morphologies, different device geometries and interfacial engineering. These include a variety of photodetecting devices such as photoconductive, photodiodes and phototransistors. The difficulties that perovskite solar cells encounter is primarily those of stability, toxicity and in addition, the currently available halide perovskites exhibit a poor photoresponse to NIR light. A novel hybrid planar $CH_3NH_3PbI_3$/SnS broadband (365 to 850 nm) photodetector was suggested by Kumar et al. [113]. The $CH_3NH_3PbI_3$ embedded SnS device produced 0.05 µA photocurrent at 365 nm, which was noticeably increased by 140 times than bare SnS. The maximal detectivity was calculated to be 2.7×10^9 Jones and the peak responsivity was 5.62 mA/W. Optoelectronics has recently shown great promise for hybrid organic-inorganic devices based on perovskites. A tabulation of the important key parameters of different hybrid nanostructure-based photodetectors is given in Table 1.1.

Table 1.1: Comparison of key parameters of different hybrid nanostructure-based photodetectors.

Photodetectors	**Operating range (nm)**	**Spectral responsivity (A/W)**	**Detectivity (Jones)**	**Rise/decay time**	**Ref.**
SnS QDs/ZTO	300-900	10^{-1}-10^5	10^{16}	-	[107]
$SnS_2/ZnO_{1-x}S_x$	365-850	8.28×10^{-3}	10^{10}	49.51 ms, 25.93 ms	[109]
$SnS/CH_3NH_3PbI_3$	365-850	5.62×10^{-3}	10^9	-	[113]
SnS nanosheets/Au	808	635	10^9	350 ms, 350 ms	[114]
SnS nanoflakes/Graphene	375-1500	10^3	10^{12}	24 ms,	[115]

				19 ms	
MoS_2/PbS	400-1500	10^5	10^{14}	− , 350 ms	[116]

It is necessary to develop low-cost photodetectors operating in the broadband UV-Vis-NIR region with high sensitivity and detectivity as the generally reported materials like Si, Ge and GaAs are slightly expensive, complex, less flexible and require a high applied voltage for use. For better performance, it is crucial to manage optoelectronic phenomena such as light absorption, electron - hole dissociation and transfer/transport of charge carriers. Among the most researched optoelectronic applications are nanohybrid photodetectors. This is not unexpected given the existence of quantum confinement in optoelectronic nanostructures and future advancements in device performance are anticipated. Defects, charge traps that can form on surfaces and low-dimensional sensitizer quality issues can all impact uniformity of devices. The goal of future research in optoelectronic nanohybrids will therefore continue to be to better understand and manage the optoelectronic process from atomic to nanoscale, on low-dimensional nanostructures and their heterojunction interfaces for charge transport with reduced charge recombination in optoelectronic nanohybrids.

1.7 Hypothesis

Fabrication and characterization of photodetectors based on hybrid nanomaterials (SnS with graphene/Si/metal/bimetals) using their nanocolloids prepared by Liquid-phase Pulsed Laser irradiation techniques can lead to photodetection in enhanced wavelength ranges with improved efficiency (responsivity or detectivity).

1.8 General Objective

To synthesize and characterize hybrid nanomaterials for photodetectors with extended wavelength range and high efficiency.

1.9 Specific Objectives

- Synthesis of nanocolloids of tin sulphide (SnS) and Si/Graphene/noble metallic and bimetallic nanoparticles by LSPC techniques.

- Studying the effect of parameters such as laser wavelength, time of irradiation, effect of solvents etc.
- Characterization of these synthesized nanomaterials for structural, compositional and morphological studies.
- Hybrid nanomaterial synthesis – Combining the two prepared materials using chemical methods or irradiation techniques.
- Utilizing these nanohybrids for the fabrication of thin films by Spin coating / Spray deposition techniques.
- Investigating the effects of changing deposition time, annealing temperature, annealing time and other factors on the morphological, optical and electrical properties of thin films.
- Characterization of these films by techniques such as SEM, XRD, Raman and XPS for morphology, structure, phase and chemical compositional analysis.
- Fabrication of photodetectors.
- Characterization of photodetectors – optical, electrical and photodetection studies.

1.10 Justification

Most of the commercially available photodetectors are either of UV-Visible range with limiting detection below 1000 nm or NIR range from 1100 to 3000 nm. For all these materials, poor detectivity and sensitivity is reported as the wavelength nears both the ends of their detection ranges. So, there is a high priority for hybrid photodetectors with enhanced detection wavelength and sensitivity. The poor transport qualities of the film generated from nanocrystals are one of the biggest challenges to the integration of colloidal nanocrystals into effective photodetectors so far described [117]. The majority of photodetectors benefit from better carrier separation or greater carrier mobility, exhibiting excellent sensitivity, rapid photoresponse, and superior stability. We think that continued work in this direction with the hybrid material (SnS-Si/ SnS-Graphene/ SnS-Ag, Au and Ag:Au bimetallic) we proposed will result in viable and promising photodetectors and could provide fresh perspectives on the development of controlled photodetectors [118] and their possible use in new fields.

Developing flexible, non-toxic, affordable, high-performance photodetectors that can work at room temperature is still difficult [119]. SnS is an emerging 2D semiconductor that is economical, less-toxic, abundant naturally, heavy-metal free (i.e., free of Pb, Hg, and Cd), has stable properties under ambient conditions, and has a suitable band gap for the absorption of visible

light (ranging from 1.5 eV to 2.2 eV depending on crystal size). It also has a high absorption coefficient ($\alpha > 5\times10^4$ cm^{-1}) near the fundamental absorption edge, allowing light absorption at narrow thickness [120]. Silicon (Si) is another semiconductor material that possesses unique properties and is optically transparent at photon energies below its 1.12 eV band gap, making the sub-band gap optoelectronic response extremely difficult. Unfortunately, it is reported that Si's indirect bandgap severely limits the effectiveness and practicality of Si-based photodetectors. Graphene has exceptional photonic qualities, including strong interband transitions in comparison to other materials and photon absorption over a broad wavelength range (visible to IR). The metallic and bimetallic nanoparticles have features of plasmonic peaks. In the annexure, we also propose the photodiodes fabricated using nanoparticles of iron sulfide (FeS_2). The material was chosen due to its outstanding photoelectric conversion capabilities, low band gap and high light absorption coefficient [121]. All these opens our possibility in tuning the material for various applications using nanostructures and thin films.

By combining laser assisted techniques like pulsed laser ablation in liquid/pulsed laser fragmentation in liquid for the preparation of nanocolloids followed by the film fabrication by spin coating or spray deposition can assist tuning the properties of these materials for photodetection in the extended wavelength region.

Chapter 2

SnS thin films for UV-Vis-NIR photodetection prepared by spin coating of laser ablated nanocolloids

2.1 Introduction

In the realm of layered metal chalcogenides (LMCs), tin sulfide (SnS) has become one of the most popular semiconductors due to its outstanding optical characteristics (energy band gap of 1.35 eV) and high absorption coefficient (~ 10^5 cm^{-1}) [122]. Because of the two layers of tightly connected Sn-S atoms in SnS, which typically has an orthorhombic crystal structure, and the weak van der Waal type of bonds that separate the layers, SnS is regarded as an extraordinary material for its semiconducting capabilities [123]. Additionally, SnS has shown interesting applications in the field of optoelectronic devices because it is inexpensive, less toxic, earth abundant and free of heavy metals nature [124]. This chapter will focus primarily on photodetectors of SnS, while the subsequent chapters of this thesis will focus on hybrids of SnS.

In this study, SnS nanocolloids were obtained by PLAL utilizing 532 and 1064 nm laser wavelengths from a Nd:YAG laser. The majority of the literatures [125–127] reporting various nanoforms of SnS by different methods require complex reaction environments/experimental settings and time-consuming procedures involving a lot of chemicals. The capacity to eliminate surface impurities without the need of chemical precursors or additives is achieved by using PLAL, a novel and distinctive technique for the synthesis of pure stable nanocolloids. There have been noticeable attempts in this field to use laser ablation to create SnS nanoparticles. A two-step process that involves laser ablation of a Sn target in solution and chemical etching to remove the Sn core was reported in 2012 for the synthesis of SnS hollow NPs [128]. Dimethyl sulphoxide (DMSO) was employed as the sulfur source in a recently reported one-pot synthesis of SnS for antibacterial activity [129]. To create pure crystalline SnS nanoparticles, our group has reported the direct ablation of SnS target, without the need of stabilizers or precursors and we have investigated several synthesis conditions by modifying experimental variables including laser parameters and liquid media [77,130].

Additionally, these nanocolloids were used to spin-coat thin films of SnS, which were then annealed in vacuum at 350 and 450 °C. The reports available on SnS films prepared by spin-coating are based on liquid/solution-phase deposition [131–133] and other methods. These

methods either involve chemical processes or require time-consuming synthesis pathways. Our study uses spin-coating to fabricate films and the laser aided synthesis process to create nanocolloids, which overcome these shortcomings.

In this chapter, nanoparticle and thin film characterization and photodetector parameters are presented. The photodetection properties of the films show response in the UV-Visible and NIR (785, 840, and 980 nm) regions. Results of this chapter were published in reference [82].

2.2 Experimental section

2.2.1 Synthesis of nanocolloids

Tin sulfide (SnS) nanocolloids were synthesized using the PLAL process. The schematic of the setup is given in Fig.2.1. In a 250 mL beaker, SnS target (99.9% purity, Beijing Goodwill Metals, China) was placed and filled with 25 mL of isopropyl alcohol (IPA) (Fermont; analytical grade, 99.9% purity). Each time, the SnS target surface was polished and washed with IPA to get rid of any impurities. Two distinct laser wavelengths were employed to irradiate the SnS target positioned in the beaker in a vertical configuration of the experiment. For the ablation, a pulsed Nd:YAG laser (Model LQ 929, Solar laser system) with pulse width 10 ns and frequency 10 Hz was used. Its fundamental output was at 1064 nm, while its second harmonic output was at 532 nm. Using an energy meter (Thorlabs PM100D with ES245C pyroelectric energy sensor), the output laser energies of laser incident on the target surface (without taking into account the liquid medium) were measured as 330 and 280 mJ for 1064 and 532 nm, respectively. In each instance, a 5-minute laser ablation was carried out without the aid of a focusing lens. For ablation at 1064 and 532 nm, the measured laser fluence was 0.84 and 0.71 J/cm^2, respectively. In order to avoid the ablation cavity depth on the target, different spots on the target were manually moved during the experiment and exposed to laser light at different times. For the 1064 nm ablated colloid (S1064), a stable brown nanocolloid was produced and for the 532 nm wavelength, a light golden-brown colloid (S532) was obtained and is depicted in Fig. 2.1 (a).

2.2.2 Fabrication of thin films of SnS by spin coating

The colloids (S532 and S1064) were spin coated for film fabrication using a portable spin coater (Model CY-SP4). Since the concentration of NPs created in PLAL is quite low, it is a challenge to produce thin films using spin-coating of laser-ablated nanocolloids compared to other methods. Multiple nanocolloid deposition in spin coating outperforms this. To produce better film thickness, the SnS colloids in IPA were multideposited (total of 50 mL SnS) on glass substrates

(spin speed: 1000 rpm; accelerated speed: 100 rpm/s; spin time for single coating/deposition: 30 s). We used a solvent with a low boiling point (IPA-82.5 °C) that evaporates rapidly so that the spin-coating of the films could be done with little solvent waste. These films were vacuum annealed for 1 hour at 350 and 450 °C. In the rest of the discussion, the colloids and the films made using 532 and 1064 nm lasers are referred to as S532 and S1064 correspondingly. For comparison experiments, SnS nanocolloids and their thin films were also prepared. The images of the SnS thin films are shown in Fig. 2.1 (b). The size, shape and distribution of nanoparticles as well as their formation affect the color of the colloids [134,135]. When it comes to thin films, the annealed films change more physically than the as-prepared films. With an increase in annealing temperature, the films became darker.

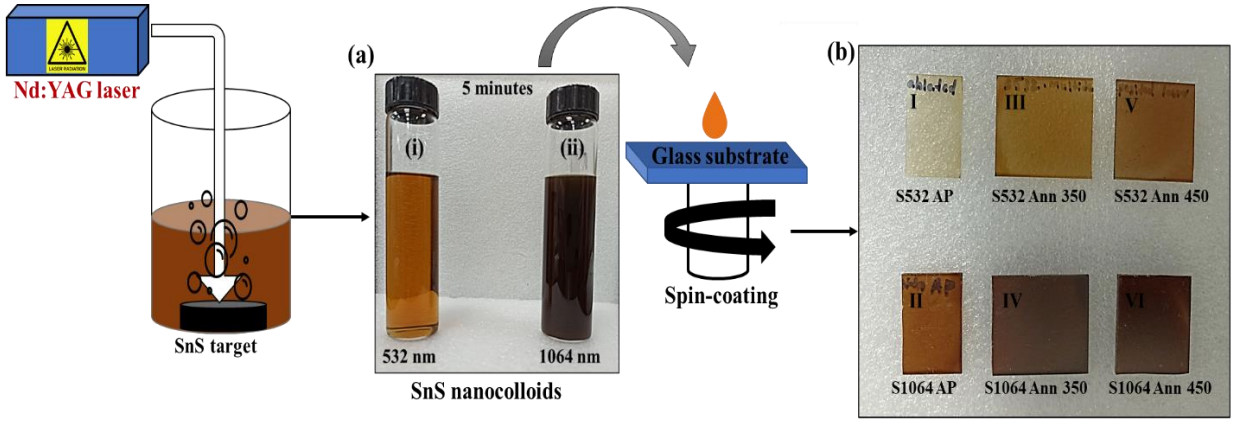


Fig. 2.1: Images of the (a) SnS nanocolloids produced by PLAL using laser of wavelength (i) 532 nm (ii) 1064 nm; (b) as well as their thin films fabricated by spin coating (I, II) SnS as-prepared (AP), (III, IV) annealed at 350 ℃, (V, VI) annealed at 450 ℃ (© from Elsevier 2022).

2.2.3 Characterization techniques utilized in the work

In Section 1.2.2, the characterization techniques are discussed in detail. The various techniques and equipment used for this thesis study are described below. Transmission electron microscopy (TEM) and high-resolution transmission electron microscopy (HRTEM) images recorded with the FEI Titan G2 80-300 were used to deduce the morphology, average size distribution and crystalline structure of the NPs. The patterns from HRTEM were indexed using Gatan Digital Micrograph software. To determine the crystalline structure and phase, X-ray diffraction (XRD) patterns were captured using a Panalytical Empyrean Diffractometer (X-ray source of Cu Kα1 radiation = 1.54056 Å). A dual-beam UV-Vis-NIR spectrophotometer was used

to analyze the optical characteristics of the nanocolloids and films (Jasco V770). Scanning electron microscopy (SEM, Hitachi Model SU 8020) was used to examine the morphology of the colloids and films, and cross-sectional SEM analysis and Stylus profilometer were used to measure the film thickness. Using monochromatic Al-Kα radiation with an energy of 1486.68 eV, X-ray photoelectron spectroscopy (XPS, Thermo Scientific K-Alpha) was used to gather information on the elemental composition and chemical states of the elements in the films. Using Keithley 6487 as the voltage source, the electrical properties of the films and response times were recorded.

2.3 Results and Discussion

2.3.1 Morphology and structure of SnS NPs by TEM

The TEM investigations revealed the morphology of SnS NPs. Additionally, SAED and HRTEM were used to analyze the crystal structure of the NPs. The colloidal suspensions of SnS NPs were deposited to a copper grid coated with carbon and the samples were then dried before analyzing in TEM. The TEM images of SnS NPs in isopropyl alcohol using 1064 (S1064) and 532 (S532) nm laser ablation are shown in Figs. 2.2 (a, b) and 2.3 (a, b), respectively. To enhance the image contrast for nm-scale resolution and viewing of the nanoparticles' surroundings, a bright field imaging mode was employed [136]. In both instances, spherical SnS nanoparticles that are linked together to create short chains could be seen in the TEM images. In comparison to S532 synthesized NPs, the average particle size for S1064 synthesized NPs was larger and more clearly defined. The computed particle size for S1064 was 12.27 ± 6.04 nm and for S532 it was 8.02 ± 1.33 nm. This difference in size results from how the laser wavelength affects the formation of NPs during the ablation of the SnS target. Grisel et al. [77] reported a comparison of SnS nanoparticles produced by laser ablation using 532 and 1064 nm wavelengths in various liquid environments and made a similar observation. They also discussed spherical SnS particles surrounded by some agglomerates with a similar morphology. When analyzing parametric investigations on the impact of laser wavelength and fluence in synthesizing NiTi NPs facilitated by PLAL, Patra et al. also made similar interpretations on varying particle sizes obtained for different wavelengths of laser [137]. Bremsstrahlung absorption may be the cause of the significant change in particle size for the nanocolloids produced at various wavelengths. In our experiments, a ns pulsed laser was employed, and plasma-induced ablation by the Nd:YAG laser at a wavelength of 1064 nm allowed us to observe a bottom-up mechanism. One of two photon absorption mechanisms can initiate nanosecond laser-induced plasma over the target surface. In one case, the

laser beam and collisions between atoms, ions and electrons provide free electrons with kinetic energy. The second mechanism—photoionization of excited species—causes multiphoton ionization of excited or ground state atoms at sufficiently high laser intensity. In the event of ablation by a 1064 nm laser, inverse Bremsstrahlung absorption is significant, the thermal impact dominates aggregation and this results in the generation of bigger nanoparticles [138]. In the case of 532 nm laser, because of their high photon energy, inverse bremsstrahlung absorption is a minor effect which can instead induce the top-down photo-ablation process to cause the reduction in particle size [139,140].

HRTEM images depicted in Fig. 2.2 (c) and Fig. 2.3 (c) reveal the orthorhombic crystal structure of SnS NPs synthesized using 1064 and 532 nm respectively. d-spacing values of 2.0, 2.7 Å were calculated for the lattice fringe separations of the crystallographic planes corresponding to the (141) and (040) in the case of S1064 NPs. For S532, the d-spacing values of 1.7, 3.2 and 2.3 Å matched to (151), (021) and (131) planes respectively. The projection image of the crystal lattice from the viewing direction determines the several planes that can be distinguished from the HRTEM images. The sample's orientation and placement at the time of analysis affect the crystal orientations that are indicated by the observed lattice fringes, which are perpendicular to the electron beam. The mostly exposed planes that appeared for both of the samples in our case (S1064 and S532) were therefore distinctive [141,142]. The scattering of the electron beam by the sample lattice produced selected region electron diffraction patterns. The SAED patterns of S1064 and S532 are shown in Figs. 2.2 (d) and 2.3 (d), respectively. The diffraction rings were used to distinguish several planes, proving the polycrystalline nature of the NPs. For S1064, the rings were indexed to (101), (111) and (040) and for S532 as (111) and (101). Together, the SAED and HRTEM results helped to corroborate the crystallinity of SnS and to identify its crystal planes in various directions.

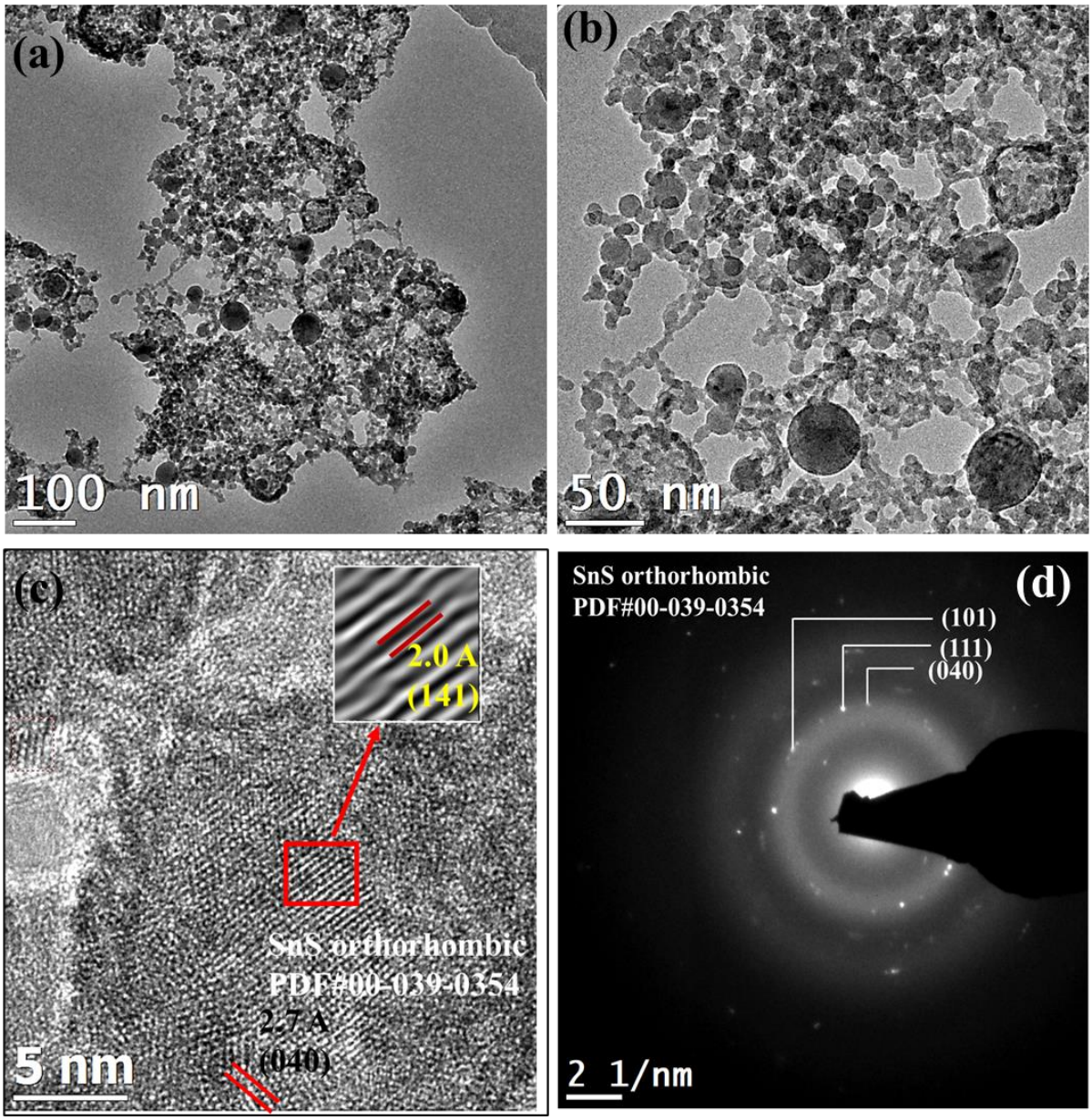


Fig. 2.2: (a, b) TEM, (c) HRTEM and (d) SAED patterns of SnS NPs produced with a laser output of 1064 nm wavelength in isopropyl alcohol (© from Elsevier 2022).

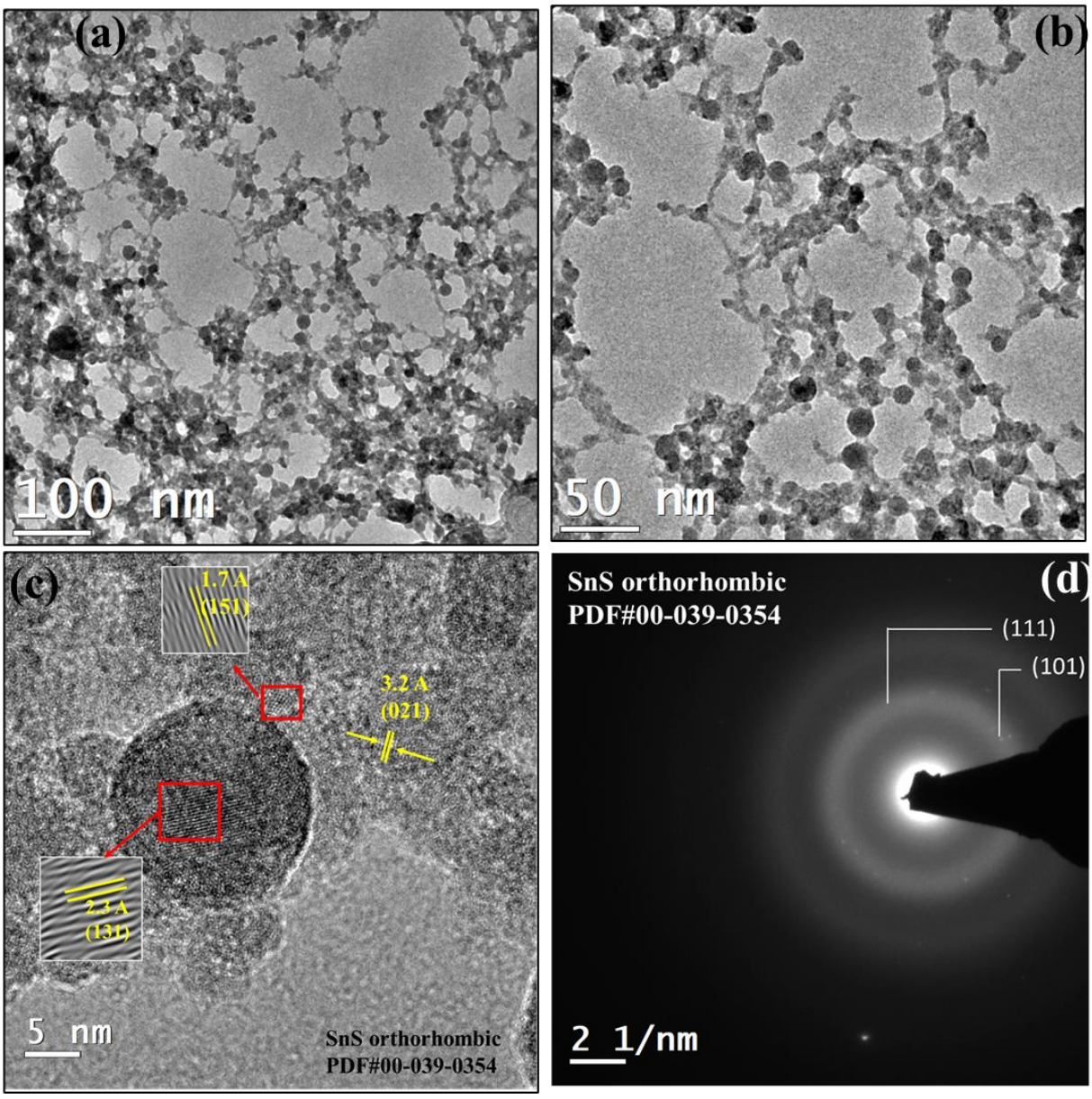


Fig. 2.3: (a, b) TEM, (c) HRTEM and (d) SAED patterns of SnS NPs produced with a laser output of 532 nm wavelength in isopropyl alcohol (© from Elsevier 2022).

2.3.2 Morphology by SEM

FESEM (Field emission scanning electron microscopy) was used to observe the surface morphology of the samples. For the SEM analysis of the nanoparticles, SnS nanocolloids were dropcasted onto ITO substrates to reduce charging effects. Fig. 2.4 shows the FESEM images of the SnS nanoparticles at scales of 1 and 5 µm. The images were captured in secondary electron imaging mode using a voltage of 3 kV and a current of 10 µA. Similar to the observations from

the TEM images, spherical connected grains of different sizes can be seen. In Fig. 2.5 (a–f), FESEM images of the SnS films are presented for both as-prepared and annealed states. The images at a scale of 3 μm and 1 μm (in the inset) scale are presented for all the films. A voltage of 1 kV and current of 10 μA was applied for collecting the images. In the subsequent figures, the films of SnS made using colloids prepared using wavelengths of 1064 and 532 nm (S1064, S532) and annealed at 350 and 450 °C, respectively, are denoted as A350 and A450. The films in their as-prepared state showed surfaces with less coverage. The morphology and compactness of the films were enhanced by annealing. The S532 film annealed at 450 °C has tiny, uniformly dispersed spherical particles over the film surface when compared to the S532 film annealed at 350 °C. Additionally, it is apparent that S1064 films have larger grains than S532 films. By promoting grain growth and so limiting the amount of grain boundaries that can catalyze recombination, Sinsermsuksakul et al. demonstrated that annealing aids in reducing recombination [143]. While several annealed films, particularly the S1064 films, exhibit pinholes in their SEM images, none of the annealed films exhibit cracks. Using cross-sectional SEM examination, the thickness of the samples was determined to be between 0.7-1.20 μm. Fig. 2.6 contains the cross-sectional images of the S1064 and S532 samples. We observed that the cross-sectional image of the as-prepared samples of S532 and S1064 (Fig. 2.6 (a, d)) was coarse and irregular, which is similar to the morphology of the surface. As a result, we got differences in thickness values for both samples.

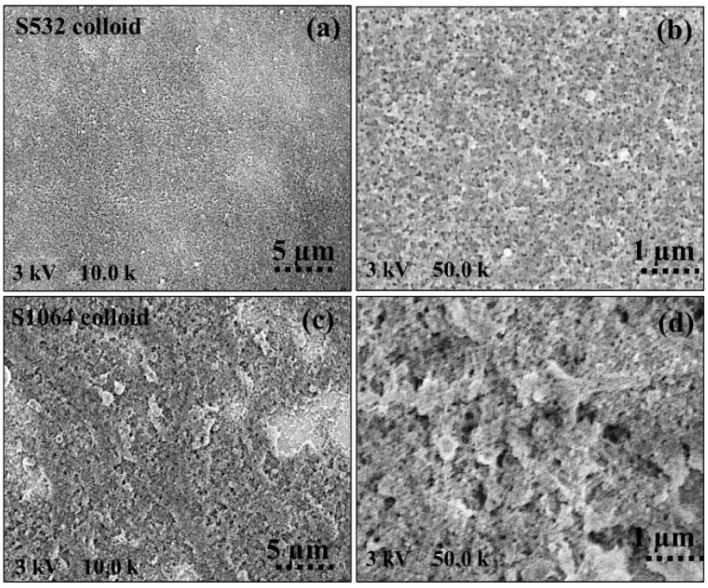


Fig. 2.4: Scanning electron micrographs of SnS colloid on ITO prepared using (a, b) 532 nm (c, d) 1064 nm colloid (© from Elsevier 2022).

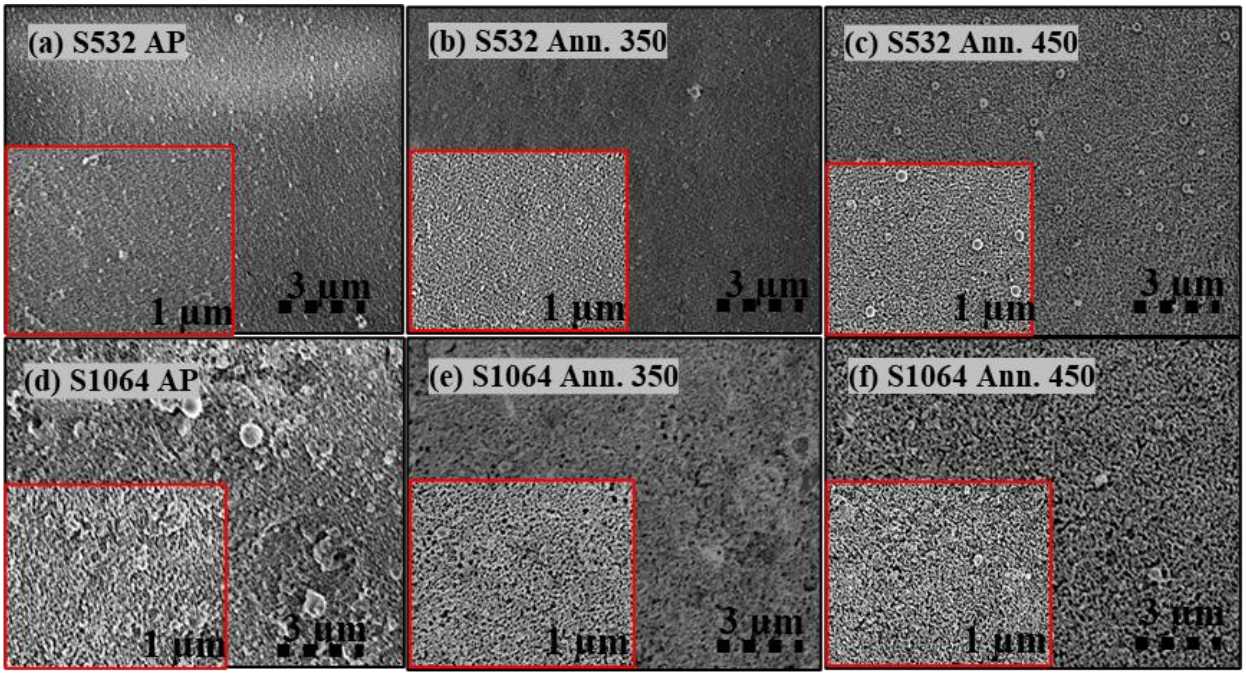


Fig. 2.5: Scanning electron micrographs of SnS films (a, d) as-prepared (b, e) annealed at 350 ℃ (c, f) annealed at 450 ℃ (inset: 1 µm scale images of the films) (© from Elsevier 2022).

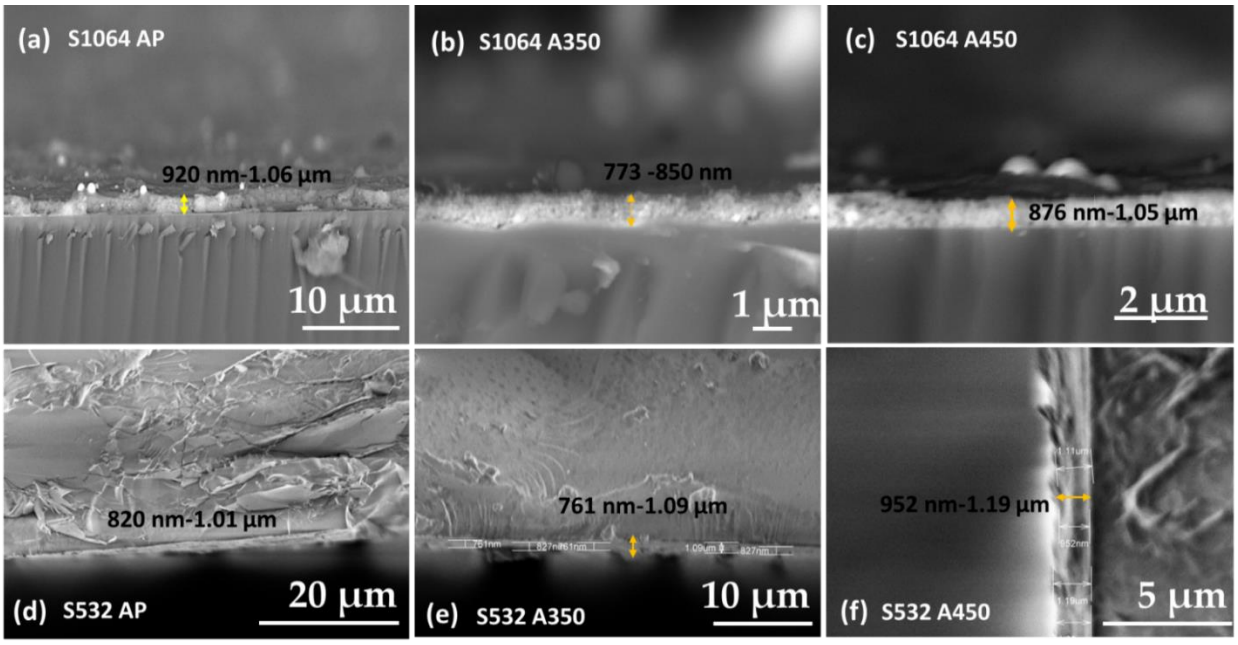


Fig. 2.6: Cross-sectional SEM images of S1064 and S532 films on glass substrate for thickness measurements.

2.3.3 Grazing Incidence X-ray Diffraction (GIXRD) of SnS films

The GIXRD patterns of the samples were acquired, and a 2θ scan was carried out with a grazing angle of incidence at 0.5° to remove strong signals from the glass substrate. Fig. 2.7 shows the GIXRD patterns of the annealed SnS thin films. For all the samples, a preferential orientation along the (040) plane was seen in the XRD patterns. No other crystalline phases were visible in the patterns demonstrating the purity of the nanocolloids produced by PLAL. The (120), (021), (101) and (040) planes are indexed to the 2θ values of 26.04°, 27.48°, 30.44° and 31.72°. At 2θ values of 39.08°, 45.4°, 48.5° and 51°, which correspond to the (131), (002), (211) and (151) planes, some weak reflections are also seen. All the patterns match with the orthorhombic structure of SnS and were indexed based on the PDF#00-039-0354. Compared to annealed S532 films, S1064 films have higher intensity peaks, which indicate better crystallinity.

The Debye-Scherrer equation [86] was used to determine the average crystallite sizes of the films.

$$D = \frac{0.9 \times \lambda}{\beta \times \cos\theta} \qquad (2.1)$$

where θ is the Bragg angle, β is the FWHM of the chosen peak ((040) in this analysis), and λ is the wavelength of the X-ray radiation utilized (1.540 Å). According to calculations, the crystallite sizes of S1064 and S532 films annealed at 450 and 350 °C were 29.9, 30.1, 25.5 and 21.6 nm, respectively. These outcomes supported the observation that the annealed SnS films made by spin coating the laser-ablated nanocolloids were nanocrystalline.

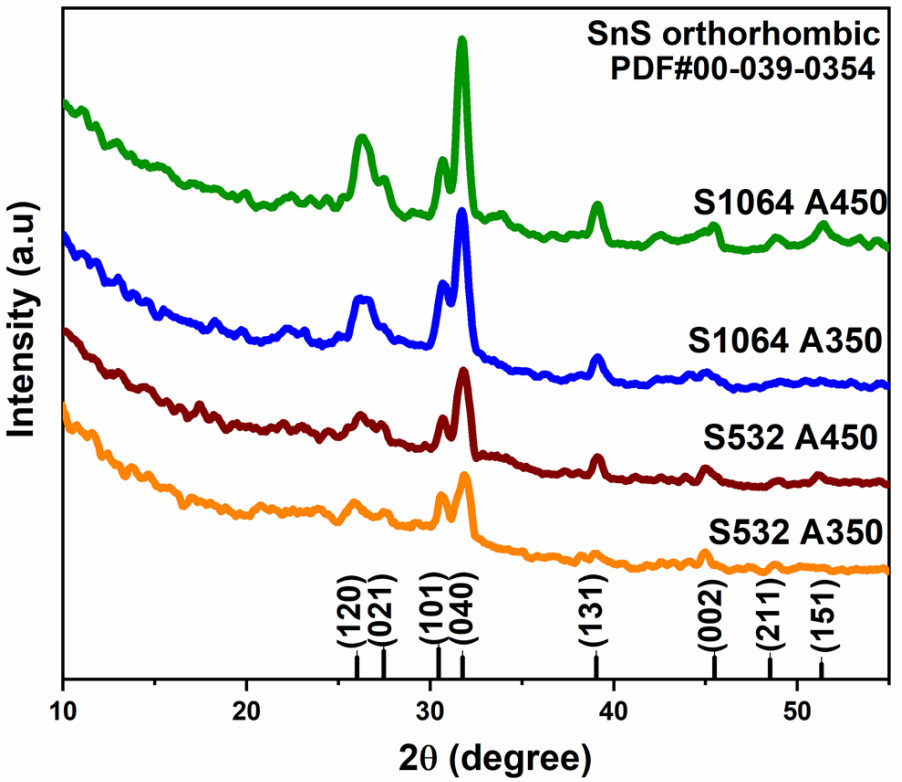


Fig. 2.7: A comparison of the GIXRD patterns of the SnS films annealed at 350 and 450 °C (© from Elsevier 2022).

2.3.4 Optical Studies of the SnS NPs

The absorption spectra measured for the nanocolloids generated under two conditions (532 and 1064 nm) are shown in Fig. 2.8 (a). The SnS target was ablated for 30 seconds, 2 minutes and 3 minutes prior to optimizing the laser ablation time as 5 minutes. The images of the colloids and absorbance plot for the same is provided in Fig. 2.8 (b-d). By comparing and choosing colloids with greater absorption and shorter ablation time, we were able to select the ablation time as 5 minutes because more nanoparticles are formed when the laser ablation time is longer which can be validated using the figure. But as we further increase the ablation time (> 5 minutes), NPs gets accumulated near the laser spot shielding the incident laser radiation reaching completely onto the target. As a result, the absorbance remains constant and thus further hinders an increase in the number of nanoparticles [144]. In addition, there are previous reports that if the ablation is continued for longer durations, there can be reduction in the size of the nanoparticles produced in the preceding steps as a result of fragmentation of the nanoparticles [145,146]. It is clear from the

fact that the absorption edge of the nanocolloid at 1064 nm is red-shifted relative to that at 532 nm, indicating that the 1064 nm nanoparticles have bigger particles.

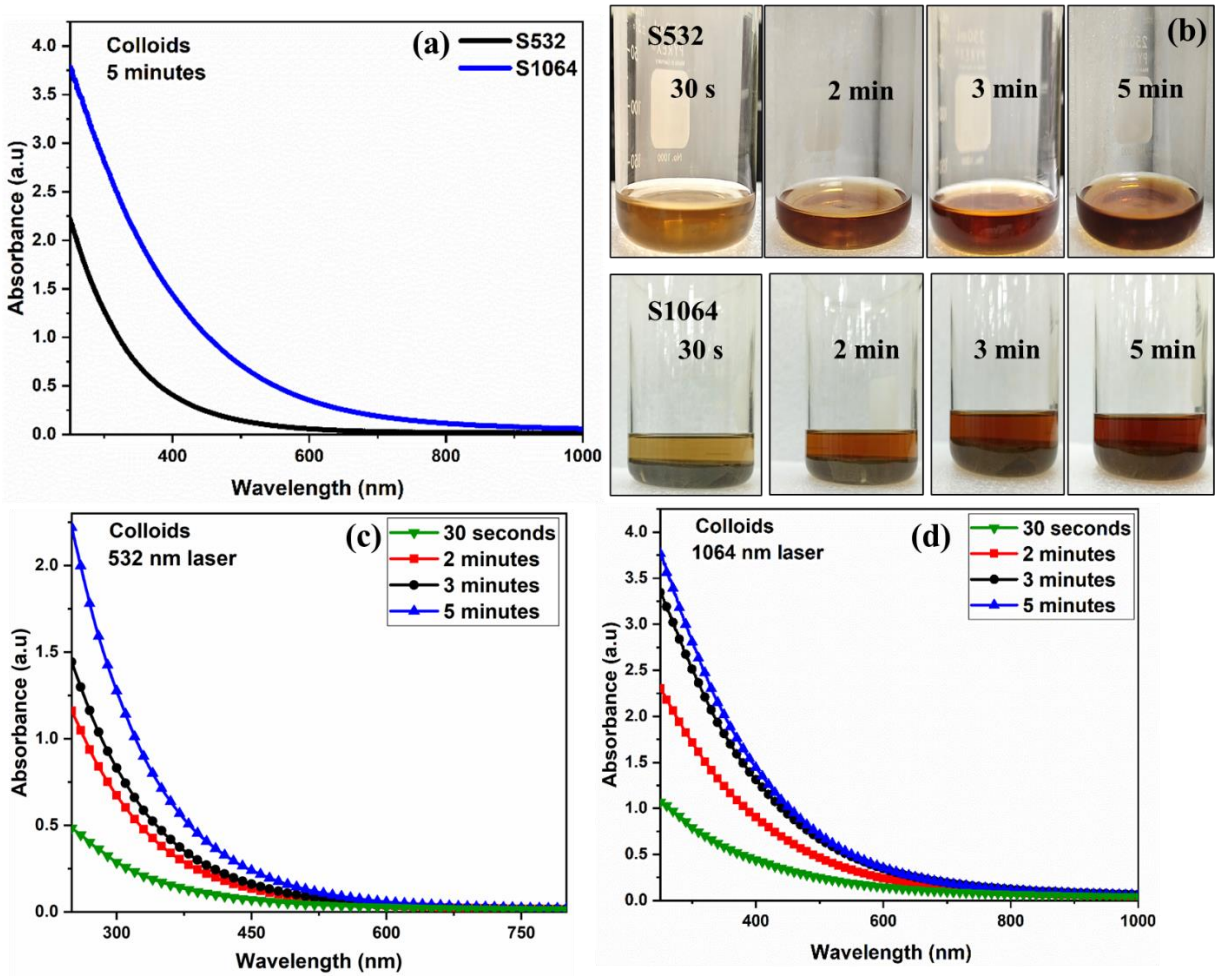


Fig. 2.8: (a) Absorption spectra of SnS NPs in IPA obtained by 5 min ablation using laser of wavelength 532 nm (S532) and 1064 nm (S1064) (© from Elsevier 2022) (b) Photos of the SnS nanocolloids prepared by PLAL using 532 and 1064 nm wavelength laser for different ablation times (c, d) Comparison of absorption spectra of SnS NPs in IPA obtained by laser ablation at different ablation times using 532 and 1064 nm wavelength.

In the case of SnS films, a red shift in the absorption values can be seen for the films fabricated using the colloids from 1064 nm compared to 532 nm (Fig. 2.9 (a)). The particle size difference that develops with increased laser wavelength and fluence is the primary cause of the absorption edge shifting. The sizes assessed using TEM analysis also demonstrate this. Lower absorbance was observed for the particles produced by a 532 nm laser as compared to the experimental condition of 1064 nm, which provided the maximum absorbance. In the case of films,

the absorption edges of the annealed samples also shifted to longer wavelengths than the as-prepared samples. The absorption spectra support the robust absorption properties of annealed SnS films for both visible and NIR photons [147]. Fig. 2.9 (b) provides the transmittance and reflectance spectra for the films. When compared to the films that had not been annealed, the transmittance of the annealed films was lower, showing that the energy bandgap (E_g) had changed and that the film thickness had increased as the transmittance decreased [124]. Nair et al. have noted a trend in the transmittance spectra of SnS that is comparable [148]. For all of the samples, the reflection loss was under 10%.

The optical energy bandgap (E_g) of the films was determined using the Tauc plot (Fig. 2.9 (c)) by plotting $(\alpha h\nu)^2$ vs. hν (energy) using the equation provided in Eq. (2.2).

$$(\alpha h\nu)^n = A\,(h\nu - E_g) \qquad (2.2)$$

where α denotes the absorption coefficient corresponding to photon energy $h\nu$, h denotes the Plank's constant, ν denotes the frequency of the input photon, A denotes a constant, and n = 2 denotes the material's direct bandgap [77]. The graph's straight-line segment was extrapolated and the intercept on the energy axis provides the bandgap value. For the S532 as-prepared and annealed films, the bandgap values were calculated to be 2.7, 2.1 and 1.9 eV, while for the S1064 as-prepared and annealed films, they were 1.63, 1.45 and 1.42 eV. Compared to the as-prepared films, the bandgap was smaller for the annealed films due to the increased crystalline structure of the films after annealing. SnS thin films have bandgap values in the range of 1.3-2 eV [149,150]. As a result of different ablation parameters and annealing conditions, the optical bandgap of SnS varies from the bulk SnS (1.1 eV). This difference is attributable to the change in morphologies and sizes of the nanoparticle [151].

The difference in size of the nanoparticles produced during the synthesis of nanocolloids by different ablation wavelengths is the primary cause of change in properties of the films. A bottom-up approach is used to create thin films out of the nanocolloids. On the substrate, the produced nanoparticles self-assemble. Sastry et al. [152] have thoroughly examined various methods for organizing nanoparticles into thin films and their interactions. The coalescence of the nanoparticles changes the shape and particle size when thin films are deposited utilizing nano colloids. The smoother morphology of the films produced by the smaller nanoparticles generated by 532 nm led to smaller crystallite sizes as determined by XRD. We noticed an adequate change

in the optical characteristics of the films because of annealing, which may also have an impact on their optoelectronic characteristics.

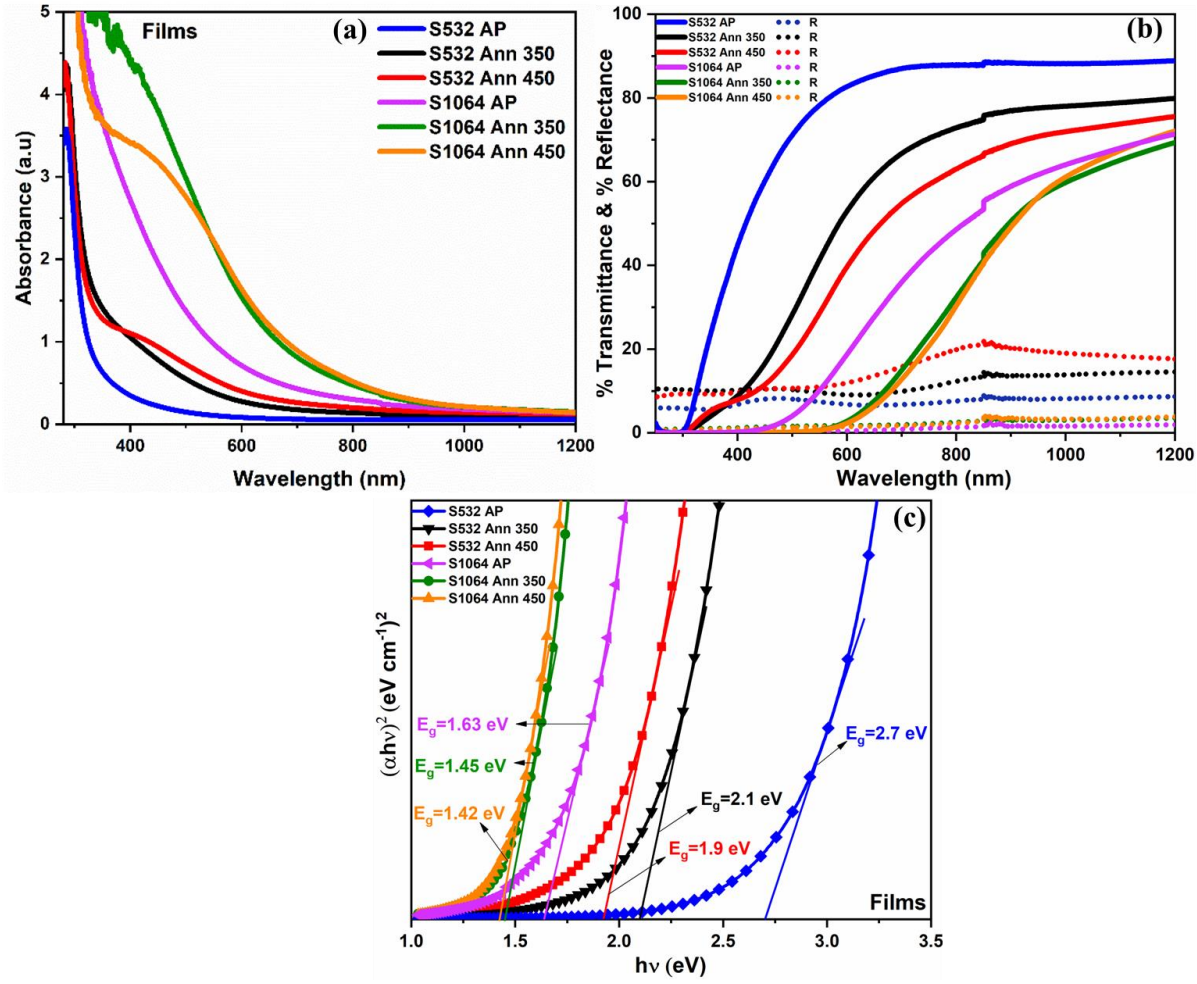


Fig. 2.9: (a) Absorption of SnS films under various conditions (as-prepared and annealed at 350/450 ℃) (© from Elsevier 2022) (b) % Transmittance and % Reflectance of SnS thin films, (c) Bandgap calculations using Tauc plot.

2.3.5 X-ray photoelectron spectroscopy

The elemental composition, oxidation states and binding energies of the Sn-S system are investigated using XPS. To collect signatures from every element present on the sample surface, a wide-range XPS survey spectrum scan was carried out. The survey spectra, which are shown in Fig. 2.10 (a) and (b), indicated the presence of the elements Sn, S, O, and C. The distinctive peak of adventitious carbon, C1s, is attributed to the peak with a binding energy value of 284.6 eV. All binding energies are calibrated using the C 1s peak binding energy to account for sample charging. A Shirley type background correction was done. It considers the fact that the amount of

inelastically scattered electrons increasing the background is directly proportional to the total flux of photoelectrons. The main concept of the background calculation is that the background intensity at the binding energy is inversely proportional to the total peak area within the specified energy range and the termination point on the peak's low binding energy side. Additionally, the outcome in this case is impacted by the arbitrary choice of the end points [153]. Utilizing the Gaussian-Lorentzian sum function, the peak positions, binding energy splitting, peak-area ratios between spin-split components and full width half maximum (FWHM) values were all considered. Fig. 2.11 depicts the high-resolution XPS scan of SnS nanocolloids prepared using 532 and 1064 nm laser. Fig. 2.12 and Fig. 2.13 represent the deconvoluted high resolution scan XPS spectra of SnS films made from S1064 and S532 colloids that were annealed at 450 and 350 °C after and before etching. To get rid of any carbon or oxygen impurities that might have come to the surface from exposure to the environment, the samples were etched.

The Sn $3d_{5/2}$ and Sn $3d_{3/2}$ core level peaks of the S1064 sample, which were formed by two distinct peaks, are shown in Fig. 2.12 after being annealed at 450 °C. The dominant peaks in Sn^{2+} in SnS occur at 485.82 and 494.23 eV, respectively. The elemental state of Sn (Sn (0)) is represented by the peaks that were seen at 484.54 and 492.95 eV. Fig. 2.12 (c, e) also shows the Sn 3d peaks from the S1064 sample annealed at 350 °C and the S532 sample annealed at 450 °C, respectively. Three distinct peaks of Sn are seen in the case of S532 film when it is annealed at 350 °C. The three Sn 3d peak energies in Fig. 2.12 (g) exhibit unique chemical shifts that point to the existence of an additional electronic state for tin. Peaks for Sn (0) are observed at 484.58 and 492.99 eV. The Sn^{2+} state in SnS is represented by the peaks at 485.84 and 494.26 eV, while the Sn^{4+} state in SnO_2 is represented by the peaks at 486.63 and 495.04 eV. In every instance, Sn^{2+} in SnS is the primary source of the XPS peaks. Peak area ratios of 3:2 and equal FWHM are used to fit the $3d_{5/2}$ and $3d_{3/2}$ doublets, which have peaks separated by 8.41 eV. The binding energies agree with the SnS literature that has been previously reported [77]. The reported data can also be compared to the variation in binding energies between elemental Sn and the various Sn oxidation states reported for SnS [122]. High resolution photoelectron spectra for the Sn $3d_{5/2}$ and Sn $3d_{3/2}$ core levels are shown in Fig. 2.13 for all film surfaces (before etching). Peak splitting energies and peak binding energies are consistent with the literature. The Sn^{4+} condition was also seen in all the films, as indicated in the figures. It was only present on the surface of the 350 °C annealed S532 film. After sample etching, the Sn^{4+} peaks were not present in the spectra for any other films. The

binding energy values of the deconvoluted peaks with an intensity ratio of 1:2 [154] correspond to S^{2-} in SnS, according to the high resolution spectra of the S $2p_{3/2}$ and S $2p_{1/2}$ core level peaks of S1064 annealed at 450 °C (Fig. 2.12 (b)), S1064 sample annealed at 350 °C (Fig. 2.12 (d)) and S532 annealed at 450 °C (Fig. 2.12 (f)). In these graphs, the peak splitting and binding energy values are shown. The doublet S 2p peaks seen at 161.37 and 162.55 eV for the S532 sample annealed at 350 °C (Fig. 2.13 (h)) are also widened. These binding energy values all accord well with the reported values for sulfur in SnS in the literature [88]. High resolution spectra of the S $2p_{3/2}$ and S $2p_{1/2}$ core level peaks of all the films before etching are shown in Fig. 2.13 (b, d, f, and h). Peak splitting in binding energies and the binding energies of the deconvoluted peaks are indicated in the corresponding figures.

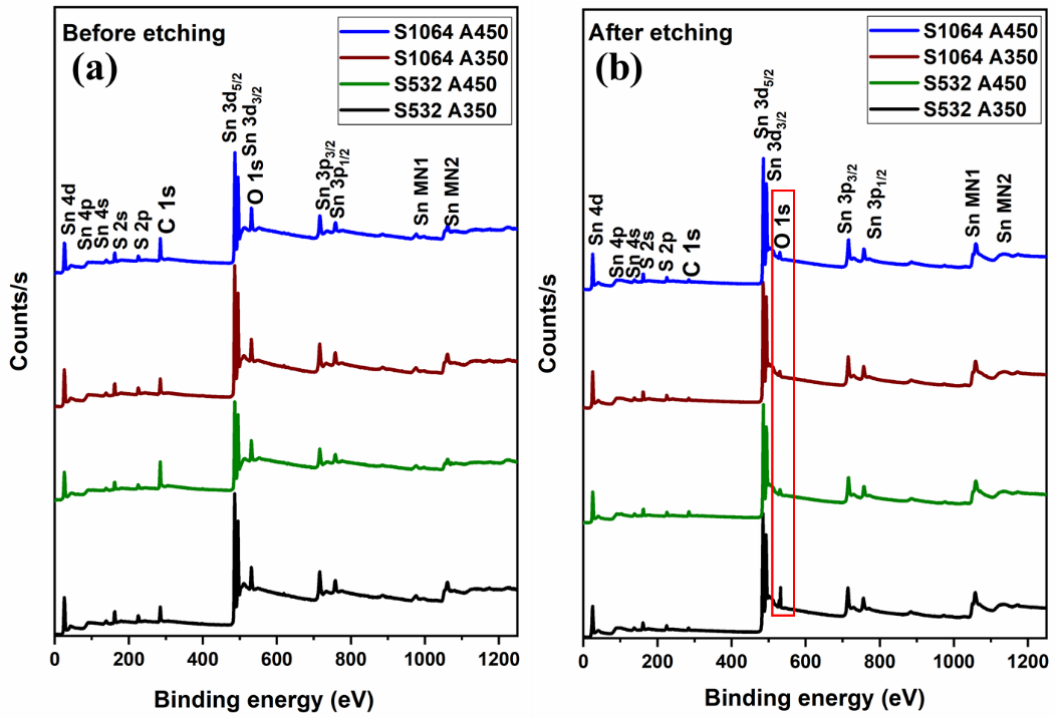


Fig. 2.10: XPS survey scan spectra of SnS films annealed at various conditions with Sn, S, O, and C line marked (a) before etching (b) after etching (© from Elsevier 2022).

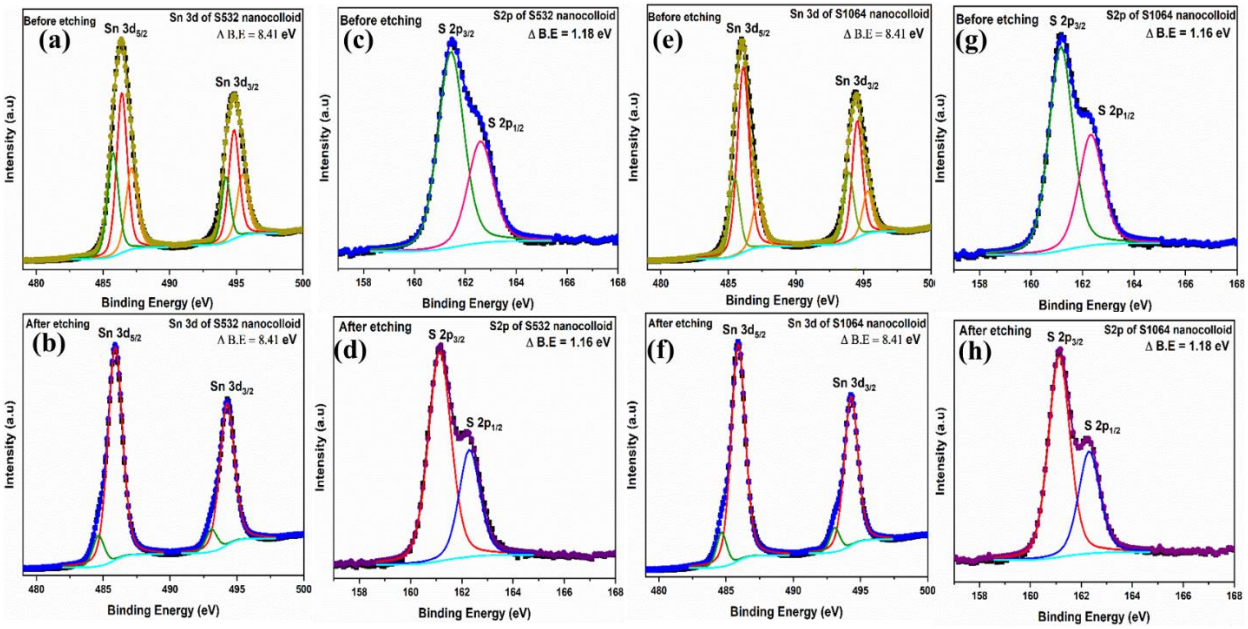


Fig. 2.11: High resolution XPS images of (a, b, e, f) Sn 3d, (c, d, g, h) S 2p of SnS nanocolloids (S532 and S1064) deposited on titanium (Ti) substrate (before and after etching) (© from Elsevier 2022).

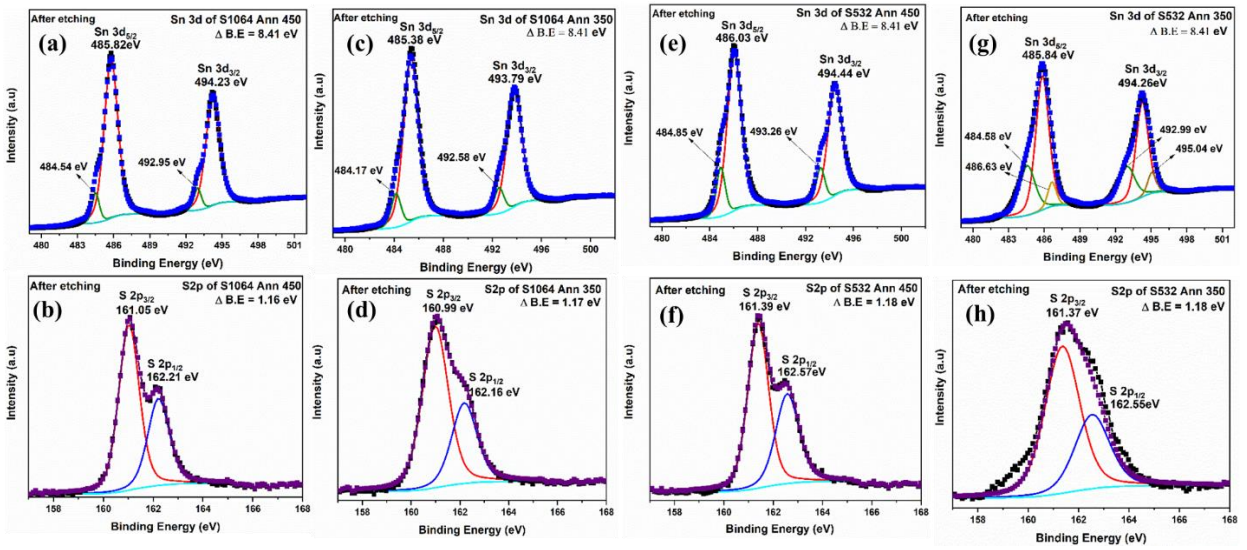


Fig. 2.12: High resolution XPS images of SnS films annealed at various conditions (a, c, e, g) Sn 3d, (b, d, f, h) S 2p s (after etching) (© from Elsevier 2022).

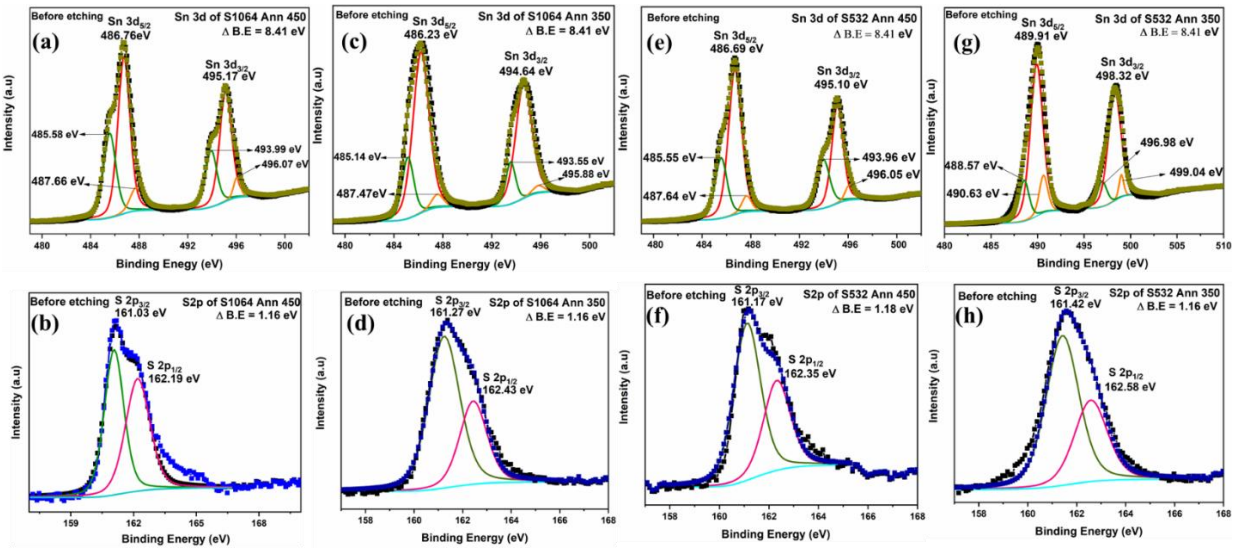


Fig. 2.13: High resolution XPS images of SnS films annealed under various conditions (a, c, e, g) Sn 3d, and (b, d, f, h) S 2p (before etching).

2.3.6 Current-voltage and photoresponse measurements

Fig. 2.14 (a) displays the current-voltage (I-V) characteristics of as-prepared and annealed SnS thin films for applied voltages ranging from − 5 to +5 V both in the dark and under light. Electrical contacts were made using silver (Ag) electrodes because the latter's work function (ϕm = 4.30 eV) is closer to that of SnS (ϕs = 4.20 eV) and has a higher electron affinity (χs = 3.14 eV) [124]. The Ag electrodes and nanostructured SnS thin films must have a good ohmic contact for the I-V curves to be straight and symmetric. Every film, with the exception of S532, that was annealed at 350 °C demonstrated improved conductivity compared to the corresponding as-prepared films. These samples calculated conductivity values were in the order of 10^{-3} $(\Omega\ cm)^{-1}$. Additionally, the creation of charge carriers by light absorption causes the current to increase dramatically when the device is illuminated. The I-V plots were used to determine the resistance of the films, which were determined to be 8.3×10^{10}, 1.29×10^{9}, 1.18×10^{9} and 1.09×10^{9} Ω for S532 film annealed at 350 and 450 °C and S1064 film annealed at 350 and 450 °C, respectively. These figures clearly show that the S532 film is relatively resistant when compared to other films when it is annealed at 350 °C, and this may be because SnO_2 was found on the film as determined by the XPS analysis. There have been reports on how the SnS film's physical characteristics are affected by the annealing temperature [155]. In that study, it was noted that annealing temperatures ranged from 100 to 250 °C and the rising annealing temperatures resulted in a deposit that was more crystalline. By annealing the film in air at 250 °C, the experiments showed that the film fully

deteriorated and oxidized. Another study on SnS showed the presence of additional phases including SnS_2 and Sn_2S_3 in films produced from a solution precursor and annealed at temperatures between 300 and 500 °C [133]. These binary phases are typically present in SnS-based films and invariably coexist as SnS_2 and SnO_2 even at high temperatures (500 °C), depending on the sample preparation and annealing temperatures [131]. The sample's poor conductivity brought on by SnO_2 in the film leaves no photoresponse. Three samples, S1064 annealed at 350, 450 °C and S532 sample annealed at 450 °C were used for further research based on the I-V plot. These three SnS film conditions are the only ones addressed in the subsequent discussion session.

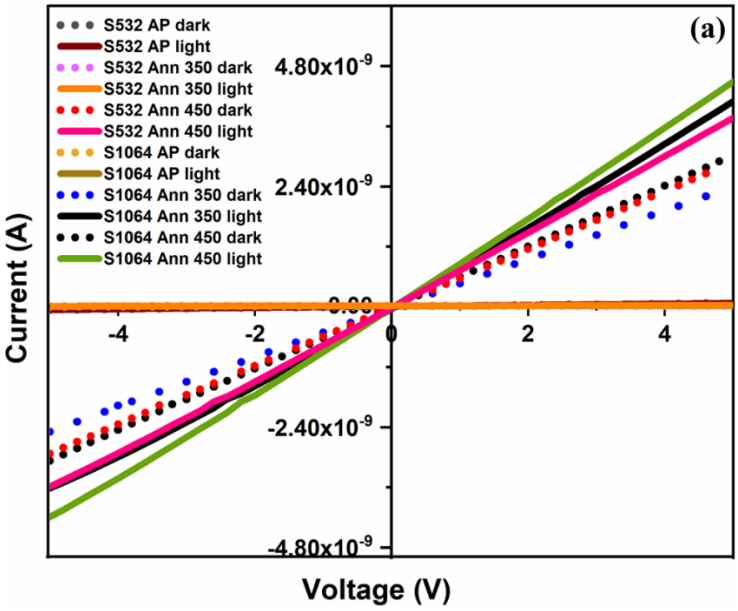


Fig. 2.14: (a) I-V graphs for SnS films measured from −5 to +5 V in the dark and under light (© from Elsevier 2022).

By applying a bias voltage of 5 V and testing them with LEDs of various wavelengths, observable responses under illumination were seen for these samples. Fig. 2.15 (a-c) shows the photocurrent responses of the analyzed films. Using LEDs with wavelengths of 465, 520, 590 and 620 nm, on-off response tests were performed at ambient temperature for 20 seconds in the dark, 20 seconds under light and 20 seconds more in the dark. The samples showed good responses to all these LEDs as in figure. Although the overall trend of response appears similar for various light wavelengths, which can be related to the samples' absorption spectra, it can be seen that the photocurrent response values vary for all of the samples. According to GIXRD and SEM results,

the sample's crystalline and morphological modifications post-annealing can be attributed for the response pattern. The SEM images show high-quality films that are uniformly distributed across the substrate surface, improving the surface to volume ratio, which subsequently aids in boosting light absorption [156]. By enhancing the creation of charge-carriers and resulting in a rise in the photocurrent, this aids in improving the performance of the photodetector [157].

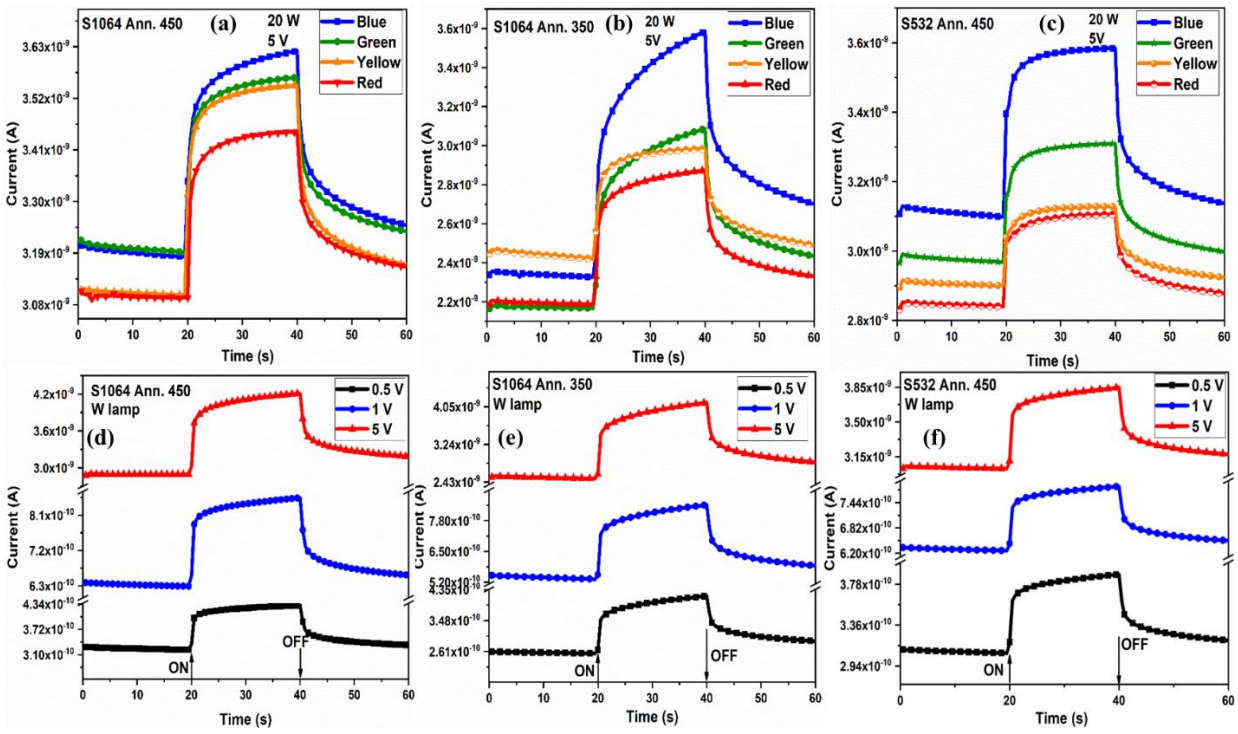


Fig. 2.15: Measurements of the photoresponse of the SnS films (S1064 A450, S1064 A350, and S532 A450) illuminated with (a-c) LEDs of wavelengths 465, 520, 590 and 620 nm at a bias voltage of 5 V, (d-f) tungsten lamp at a bias voltage of 0.5, 1, and 5 V (© from Elsevier 2022).

For each sample, the photocurrent's on/off character was discernible. The stability [158] and reproducibility of this material for photodetector applications are corroborated by the peak values, which increase to a constant photocurrent value before declining to the initial condition. Furthermore, the degradation of photocurrent is due to the two mechanisms, particularly the fast decay and the slow decay [124]. When the light source is turned off, the photocurrent initially rapidly decreases as a result of direct recombination between charge carriers. The device's response time is measured by the fast decay that is provided in this stage. The trapped electrons and holes are released from the trapping centers during the slow decay, which is mostly caused by the decay

of carriers in mid-gap states [157]. This release occurs via thermal excitation or tunneling effect. This explains why, even after a significant amount of time had passed after the light irradiation was stopped, the photoconduction of the SnS films could not return to the same initial dark value as in Fig. 2.15 (a-c). When the SnS films were activated by photon energy that surpassed their energy bandgap, there was a considerable rise in the photocurrent value that was higher than the value produced by energy below the band gap, showing that the sub-band gap states only marginally contribute to the creation of photocurrent. According to the reports by Mahdi et al. for the photoresponse behavior of the films, the photocurrent is dependent on the process of photoconductivity since electron-hole pairs are produced when a semiconductor is exposed with energy over its bandgap [147]. Fig. 2.15 (d-f) displays the current that was measured while illuminated by a tungsten lamp. An increase in current was seen with a bias voltage increase from 0.5 V to 5 V. The following equation illustrates how the current increases with applied bias voltage because of the rise in carrier drift velocity (v), which is exactly proportional to the applied bias voltage (V) [159].

$$v = \frac{\mu V}{l} \qquad (2.3)$$

where l is the distance between the electrodes and μ stands for the carrier mobility. The films are photoconductive, as shown by Fig. 2.15 (d-f), and the photocurrent increases quickly as the film thickness increases. When it comes to polycrystalline thin films, the film thickness increases along with the grain size, which enhances carrier mobility and effective carrier concentration [148]. As a result, it causes the carrier drift velocity to increase, decreasing the transit time [160,161], which is determined by:

$$T_t = \frac{l^2}{\mu v} \qquad (2.4)$$

Photoresponse studies were carried out using continuous laser irradiation at 532 and 785 nm as well. For the 532 and the 785 nm laser, the laser power was adjusted in increments of four milliwatts (4 to 24 mW) and ten milliwatts (10 to 60 mW) respectively at a bias voltage of 5 V and is depicted in Fig. 2.16 (a-f). The cyclic response to 10 mW power for a 532 nm laser and the response to 60 mW for a 785 nm laser are shown in Fig. 2.16 (g, h), and the plot validates the repeatability of the photodetector. All the samples exhibit a consistent rise in output current produced with increasing laser power. This is because the as-generated charge carriers quickly increase with light illumination and are proportional to the photon flux absorbed. With less light

intensity, it regains almost to the similar value, exhibiting the device's high repeatability, responsiveness, and recovery [156].

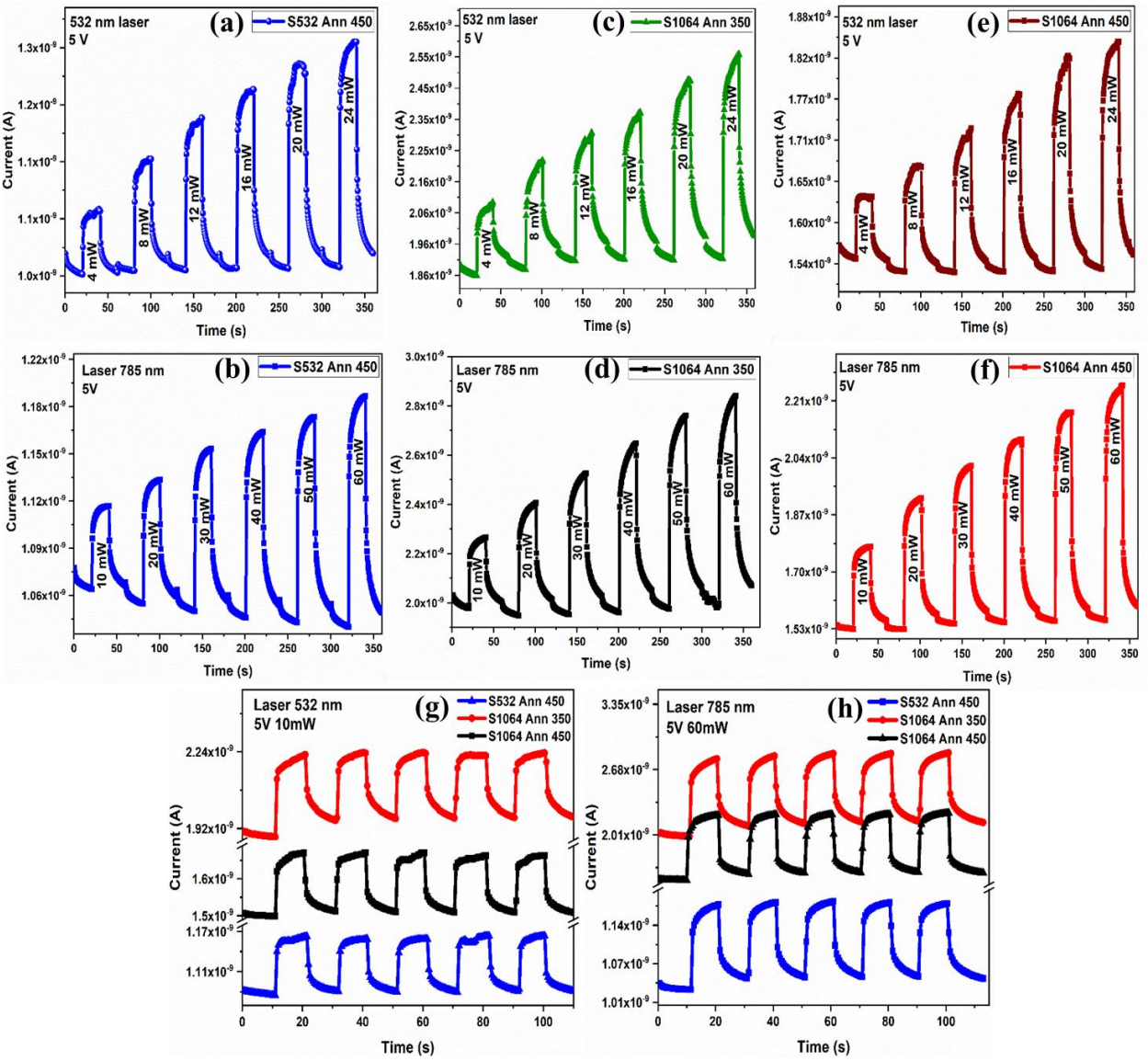


Fig. 2.16: Photoresponse of (a, b) S532 annealed at 450°C (c, d) S1064 sample annealed at 350°C and (e, f) S1064 annealed at 450°C to varying powers of 532 nm (4-24 mW) and 785 nm (10-60 mW) continuous laser, (g, h) cyclic photoresponse of SnS films for 10 mW and 60 mW continuous lasers operating at 532 nm and 785 nm, respectively, at an applied voltage of 5 V (© from Elsevier 2022).

In addition, measurements using laser diodes with wavelengths of 405, 840 and 980 nm were done (Fig. 2.17), and the overall result suggests that the constructed photodetector has a broad-spectrum wavelength range. The primary basis for detection up to 840 nm wavelength range is that it complements the photon energy corresponding to the energy band gap of SnS. Patel et al. [162] examined the photoresponse of the p-SnS/n-Si heterojunction device to 850 nm light at varied light intensities and bias voltages. When light intensities varied from 0.01 to 20 mW cm^{-2} at a bias voltage set to -1 V, the photoresponse value was reported as the ratio of photo-current to dark current density (J_h/J_d) and it ranged from 1.30 to 522.10. Photodetection of SnS thin films were also detected in the 850 nm region by Mahdi et al. [147] and Tian et al. [163] and at an applied voltage of 5 V, the current achieved was 6×10^{-10} A and 3×10^{-6} A, respectively. With photodetection up to this wavelength, no previous studies on SnS thin films have been reported. For all the films, we were able to extend the SnS photodetection up to 980 nm wavelength. The presence of vacancies (sulfur or tin) within the bandgap of SnS may be the cause of the extended response at 980 nm wavelength detection [164,165]. It is recognized that the poor lattice symmetry of the material is primarily responsible for the unusual behaviors of SnS, including anisotropic electronic properties [114] and optical absorption, which make them ideal candidates for sensitive light detection. The efficiency of electrical performance of 2D materials like SnS can be significantly impacted by defects other than vacancies, including interstitials, stacking faults and structural defects [166]. The extended wavelength detection in SnS is caused by the existence of such additional defect levels.

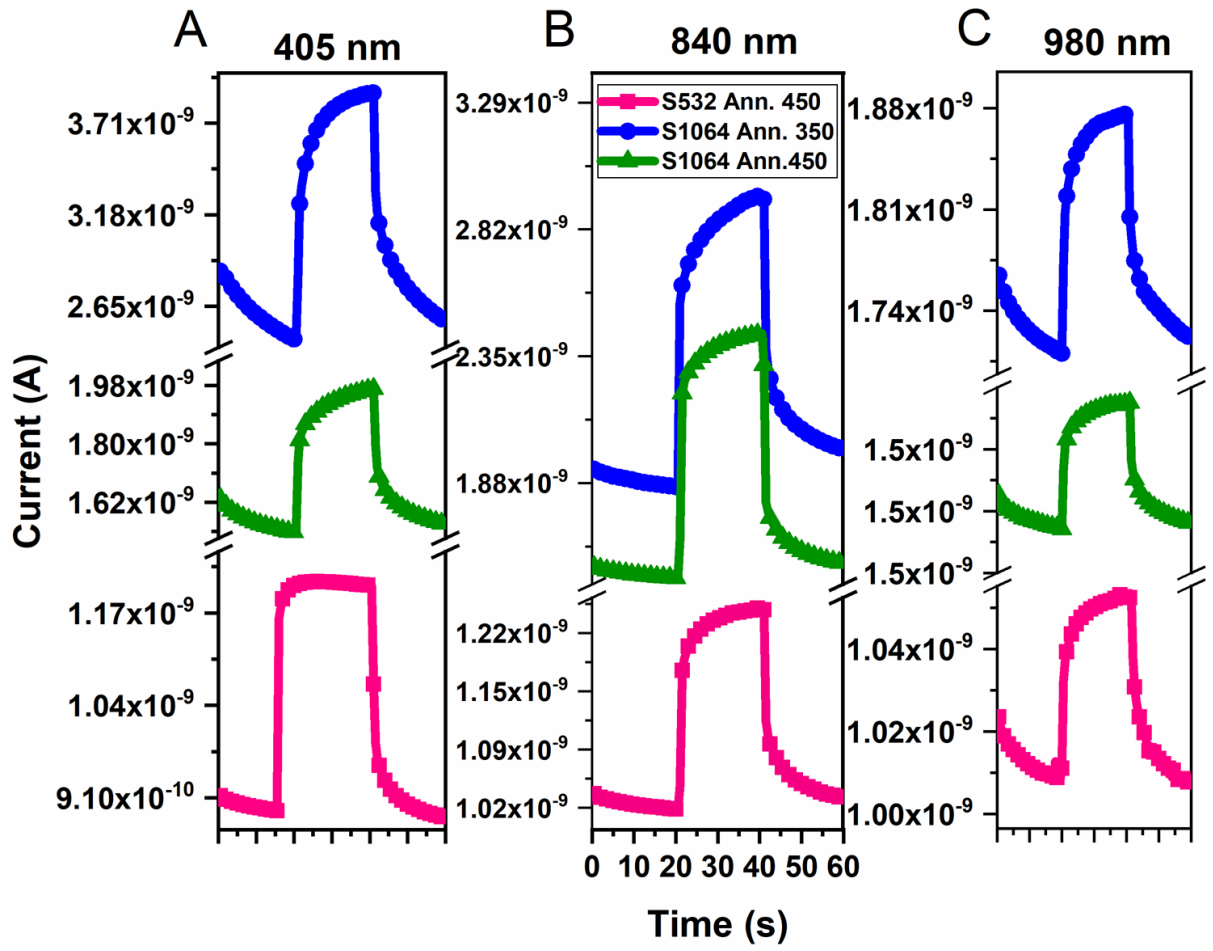


Fig. 2.17: Photocurrent of the samples in response to (A) 405, (B) 840 and (C) 980 nm diode lasers with an applied voltage of 5 V (© from Elsevier 2022).

For illumination from various sources, S1064 film annealed at 350 °C exhibits the highest photocurrents of all the samples. It has not only been noted that S1064 films (A450 and A350) have high crystallinity and composition uniformity, but also S1064 film annealed at 350 °C has a greater photoresponse to illumination using continuous laser and diode lasers in comparison to other samples. These films (S1064 A450 and A350) have similar values for the absorbance edge, bandgap, transmittance and reflectance. This behavior is supported by surface morphology as seen through FESEM analysis. The S1064 film annealed at 350 °C exhibited a denser surface coverage and more interconnected SnS nanoparticles than the film that was annealed at 450 °C, despite the surfaces of the samples appearing to be uniform. The dense surface and lack of non-uniformities like pin holes, which normally acts as trap centers (increasing charge recombination), led to a better photoresponse in S1064 film annealed at 350 °C [167,168].

2.3.7 Photodetector parameters

The sensitivity, responsivity and detectivity parameters were calculated for the films in order to evaluate the device's performance. The equations are already explained in 1.5.2 of Chapter 1 (Equation 1.2, 1.3 and 1.5). Based on how the device responded to continuous lasers of 532 and 785 nm wavelengths, the photosensitivity and responsivity values were calculated. Fig. 2.18 (a, c) shows the sensitivity and responsivity plotted against laser power density. The I_λ value increases with thickness of the film as shown in Fig. 2.16 (g, h), which is caused by an increase in the optical absorption coefficient of the films [124]. In most cases, I_λ, the light source intensity and the effective illumination area determine the photoresponsivity.

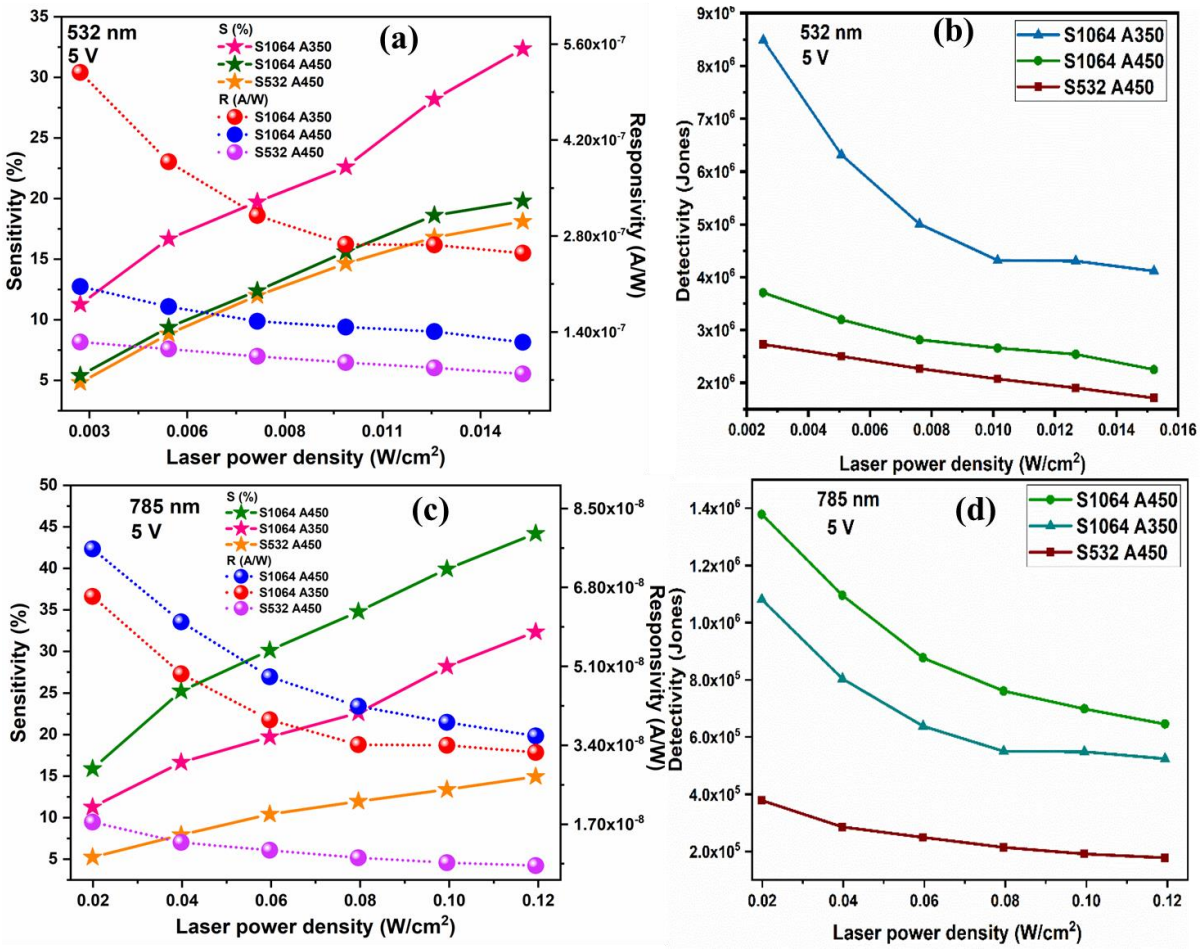


Fig. 2.18: Sensitivity, responsivity and detectivity plotted against laser power density for the films determined using the continuous lasers of wavelength (a, b) 532 nm and (c, d) 785 nm (© from Elsevier 2022).

Equation 1.4 is used to obtain the values of NEP for various laser powers and are listed in Table 2.1.

Table 2.1: NEP values for the SnS photodetectors for 532 and 785 nm.

	S1064 A450	**S1064 A350**	**S532 A450**
Power (mW) **532 nm**	**NEP ($WHz^{-1/2}$)**		
4	$1.07x10^{-7}$	$4.71x10^{-8}$	$1.46x10^{-7}$
8	$1.25x10^{-7}$	$6.33x10^{-8}$	$1.59x10^{-7}$
12	$1.42x10^{-7}$	$7.98x10^{-8}$	$1.76x10^{-7}$
16	$1.50x10^{-7}$	$9.25x10^{-8}$	$1.92x10^{-7}$
20	$1.57x10^{-7}$	$9.28x10^{-8}$	$2.09x10^{-7}$
24	$1.77x10^{-7}$	$9.72x10^{-8}$	$2.33x10^{-7}$
785 nm			
10	$2.9x10^{-7}$	$3.69x10^{-7}$	$1.05x10^{-6}$
20	$3.65x10^{-7}$	$4.97x10^{-7}$	$1.40x10^{-6}$
30	$4.56x10^{-7}$	$6.26x10^{-7}$	$1.60x10^{-6}$
40	$5.25x10^{-7}$	$7.26x10^{-7}$	$1.86x10^{-6}$
50	$5.72x10^{-7}$	$7.28x10^{-7}$	$2.08x10^{-6}$
60	$6.19x10^{-7}$	$7.63x10^{-7}$	$2.24x10^{-6}$

Moreover, we see that photoresponsivity also exhibits a high correlation with the device geometry. In light of the fact that the other measurement conditions are identical, we thus determined the specific detectivity (D*), that allows for a direct evaluation of the devices having varying

geometries (such as detector area) [169]. The detectivity plotted against the laser power density for illumination using continuous lasers (532 and 785 nm) is shown in Fig. 2.18 (b, d) respectively. For S1064 A350 film illuminated using 785 nm laser, at a NEP of 4.71×10^{-8} $WHz^{-1/2}$, a maximum detectivity of 8.48×10^{6} Jones is estimated; and for S1064 A450 film, the maximum detectivity of 1.37×10^{6} Jones at a NEP of 2.9×10^{-7} $WHz^{-1/2}$ is calculated. Table 2.2 lists the rise and decay time values related to lasers of 532 and 785 nm and tungsten (W) lamp. The basis for the delayed decay rates, however, is the phenomenon of persistent photocurrent, which is primarily caused by the confinement of the photogenerated electrons at crystal defects [170]. Table 2.3 includes a comparison of photodetection capabilities of SnS-based photodetectors.

Table 2.2: Rise and decay times of the SnS films under various illumination conditions. (© from Elsevier 2022).

Illumination Source		**S1064 A450**	**S1064 A350**	**S532 A450**
Rise time (s)	W lamp	3.31	5.5	4.7
	785 nm laser	3.15	5.7	5.4
	532 nm laser	3.63	1.8	1.1
Decay time (s)	W lamp	7.7	8.9	7.7
	785 nm laser	5.3	7.2	6.9
	532 nm laser	4.0	4.6	3.9

Table 2.3: Results of our SnS photodetector compared to those of SnS photodetectors reported in literatures.

Substrate	**Synthesis technique**	**Illumination source (nm)**	**Photocurrent (A)**	**Voltage (V)**	**Detectivity (Jones)**	**Responsivity (A/W)**	**Ref.**
Glass	Co-evaporation technique	Vis.	10^{-9}	5	10^{6}	10^{-3}	[124]
Si covered with Au catalyst	Physical vapor deposition	800	10^{-9}	1	10^{9}	10^{2}	[171]

Si/SiO_2	Hydrothermal	405-850	10^{-6}	5	10^{8}	10^{2}	[163]
n-Si	Solvothermal method	Vis.	10^{-4}	3	10^{11}	10^{-2}	[172]
PET	CBD	380-850	10^{-9}	5	-	10^{-5}	[173]
Glass	Quartz ampoule technique	532	10^{-6}	20	10^{9}	10^{-2}	[174]
Glass	Thermal evaporation	532	10^{-9}	5	10^{9}	10^{-2}	[175]
Mo coated/uncoated substrates	Powder preparation / thermal evaporation	UV-Vis	10^{-9}	0	10^{10}	10^{-2}	[176]
Glass	PLAL/spray-deposition	Halogen lamp	10^{-10}	10	-	-	[88]
Glass	PLAL/spin-coating	UV-Vis-NIR (up to 980)	10^{-9}	5	10^{6}	10^{-7}	**This work**

We used PLAL to create SnS nanocolloids, which is an environmentally friendly, economically viable method of producing pure nanocrystals [44]. It is a simple process that is free of hazardous chemicals. The spin-coated thin films exhibit an orthorhombic crystal structure and efficient photodetection with detectivity and responsivity in the order of 10^{6} Jones and 10^{-7} AW^{-1}, respectively. Reddy et al. reported photodetector of SnS with orthorhombic structure co-evaporated on glass substrate with responsivity of 10^{-3} AW^{-1} and detectivity of 10^{6} Jones [124]. Mahdi et al. [177] presented another study based on cubic SnS plated on glass by CBD for photodetector applications, exhibiting responsivity of 10^{-2} mAW^{-1}. The outcomes of this study are comparable to those of other published investigations into photodetection properties of SnS thin films.

2.4 Conclusions

- SnS NPs were synthesized by PLAL using two wavelengths.
- Spherical interconnected chain like morphologies were observed for the SnS NPs but average particle sizes varied as a result of varying laser ablation wavelengths. Larger particles measuring about 12.27 nm for ablation with a 1064 nm laser and 8.02 nm for those generated at 532 nm were obtained.
- SnS thin films were successfully fabricated by spin coating of the SnS nanocolloids produced by pulsed laser ablation in liquid (PLAL) at two different ablation wavelengths.

- Annealing the films helped in improving the crystalline nature of the films with higher crystallite size observed for thin film fabricated by nanocolloids of 1064 nm ablation (S1064)
- Optical absorption nature/range and band edges variation were observed.
- The band gap for films from nanocolloids of 1064 nm (S1064) was lower than that from nanocolloids of 532 nm (S532) as a result of the changes in morphologies and sizes of the nanoparticles due to different ablation wavelengths and annealing conditions.
- The annealed SnS thin films showed an extended wavelength up to 980 nm in photodetection.
- S1064 film annealed at 350 ℃ was the best sample with respect to the values obtained for photodetector parameters with a responsivity of 5.6 $\times 10^{-7}$ AW^{-1} and detectivity of 8.5×10^{6} Jones. This might be due to the larger grain size of S1064 films that might have reduced the recombination through grain boundaries.
- The results signify that for the synthesis of pure, surfactant free, crystalline SnS nanoparticles, an effective and effortless method, PLAL can be employed.

The findings from our work show that nanostructured SnS photodetectors with tunable optical properties for photodetection in the UV-Vis-NIR region having good photoresponse, high spectral selectivity and good stability can be fabricated combining PLAL and spin coating.

Chapter 3

SnS-Si hybrids by pulsed laser irradiation/ablation in liquid for photodetector and photocatalytic applications

3.1 Introduction

In this chapter, we describe the synthesis and photodetection properties of hybrid nanomaterials based on SnS and Silicon (Si). The optical transparency of silicon at photon energies lower than its band gap of 1.12 eV, one of its special features, makes the sub-band gap optoelectronic response extremely difficult [178]. Unfortunately, it is reported that the performance and application of Si-based photodetectors are severely constrained by their indirect bandgap and narrow absorption range. We used two types of silicon (i.e., monocrystalline and polycrystalline Si) to understand the variations in their properties. All silicon atoms in monocrystalline silicon have the same chemical structure and are continuous crystals without grain boundaries. Polycrystalline silicon is made up of tiny grains of silicon that have been joined by grain boundaries. Laser assisted techniques, (pulsed laser irradiation/pulsed laser ablation in liquid) were adopted for synthesizing nanocolloids of SnS and Si (monocrystalline Si/polycrystalline Si). The spin coating technique was used to fabricate the thin films using the laser processed nanocolloids. Characterization of the NPs in colloidal form and fabricated hybrid films attained by UV-Visible spectroscopy, XRD, Raman, XPS, SEM and TEM are presented in this chapter. Electrical studies like I-V characteristics, photoresponse measurements are also given. We also investigated the photocatalytic performances of the hybrid thin films.

3.2 Experimental Part

SnS NPs were synthesized by pulsed laser irradiation in liquid (PLIL) technique by irradiating SnS powder (99.9% purity, Heepani tools store, China) dispersed in isopropyl alcohol (IPA, Fermont; analytical grade, 99.9% purity). For optmizing the amount of SnS powder for the experiment, varying amounts of SnS (5, 20, 30, 100 and 200 mg) were dispersed in 20 mL IPA and ultrasonicated well for 10 minutes. This solution was exposed to irradiation from a second harmonic output of 532 nm from a pulsed Nd: YAG laser (Model LQ 929, Solar laser system) with a pulse width of 10 ns and a frequency of 10 Hz while being constantly stirred with a magnetic pellet. The laser irradiation set-up was arranged horizontally. During the initial trials of the

experiment, the laser irradiation was continued until there was a noticeable change in the color of the nanocolloids and no precipitation. After laser irradiation, the absorbance measured with a UV-Vis-NIR spectrometer for SnS powder dispersed in IPA ranging from 5 to 100 mg showed an increase in absorption edge to longer wavelength region. However, for 200 mg SnS nanocolloids, precipitation was occuring right away after laser irradiation and the majority of the educt remained unirradiated. With the time of laser irradiation varying from 5 to 15 minutes, beyond 10 minutes, the absorption edge started shifting to lower wavelength regions. Thus, the amount of SnS powder and duration of laser irradiation were optimized based on the absorption spectra of the nanocolloids. The images of different amounts of SnS dispersed in IPA and their respective nanocolloids after laser irradiation are given in Fig. 3.1 (a, b). A light golden brown colored nanocolloid was achieved for 5 mg SnS and with increase in the amount of SnS, dark brown colored colloids were obtained. The size, shape and distribution of nanoparticles generate changes in the color of the colloids [134,135]. The absorption spectra of these laser irradiated colloids is also shown in the same figure (Fig. 3.1 (c)). Fig. 3.1 (d) demonstrates different time of laser irradiation carried out for the 100 mg SnS dispersed in IPA. The laser fluence calculated was 0.89 J/cm^2 from the output energy measured (350 mJ) using an energy meter (Thorlabs PM100D with an ES245C pyroelectric energy sensor).

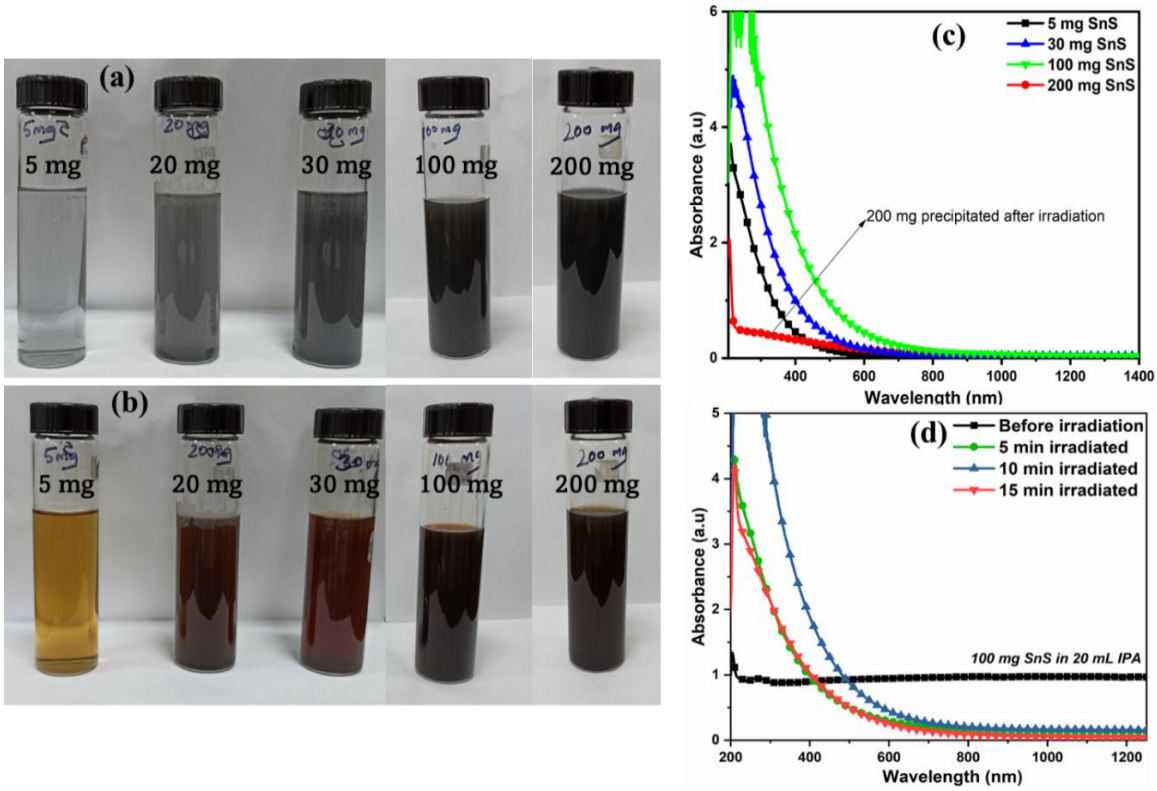


Fig. 3.1: Images of (a) different amounts of SnS powder dispersed in IPA (b) laser irradiated nanocolloids (c) Absorption spectra of the nanocolloids in image (b) (d) Absorption spectra of 100 mg SnS dispersed nanocolloids at different irradiation time.

PLAL technique was used for synthesizing Si nanocolloids. Monocrystalline and polycrystalline Si targets (99.9% purity, Beijing Goodwill Metals, China) were immersed in 35 mL of IPA for laser ablation. The targets were polished and washed in IPA each time to get rid of any surface impurities. A vertical arrangement of the experiment was used to ablate the Si targets using an output from an Nd:YAG laser of wavelength, 532 nm. A lens placed at a focal distance of 20 and 30 cm from the targets was used for the ablation setup of mono- and polycrystalline Si respectively. The output energy of the laser incident on the target was measured as 310 mJ (without considering the liquid medium) and the laser fluence was calculated as 0.79 J/cm^2. The laser ablation was carried out from 5 minutes to 30 minutes and it was observed that after 25 minutes of ablation, the absorption remained almost constant and therefore ablation wasn't continued further. The absorption spectra obtained for mono- and polycrystalline colloids for different ablation times are given in Fig. 3.2 (a, b) respectively. The images of the Si target used for the

ablation experiment and the colloids obtained after 25 minutes ablation in each case is provided in Fig. 3.4.

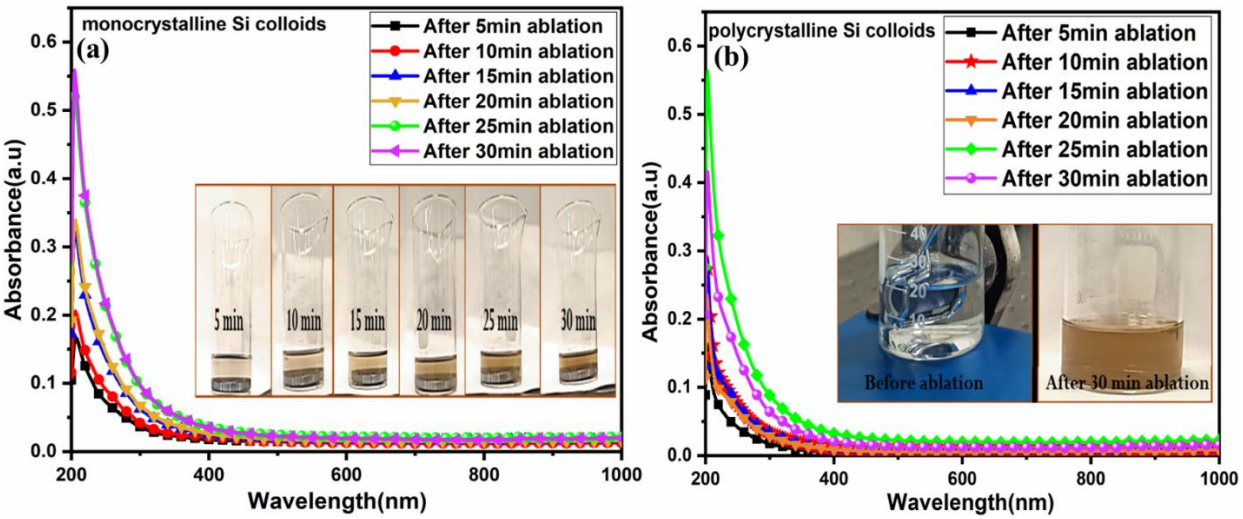


Fig. 3.2: Absorption spectra of (a) monocrystalline Si colloids (b) polycrystalline Si colloids obtained for different ablation times (Inset : Images of nanocolloids after ablation).

For SnS:Si film fabrication, spin-coating technique was employed. Using a compact spin coater (Model CY-SP4, CY Scientific Instruments, China), SnS nanocolloids were first spin-coated onto bare glass substrates over which a layer of monocrystalline Si colloids was spin-coated. This process was repeated to obtain much thicker films because the concentration of NPs obtained in PLAL is relatively low. A total of 110 mL nanocolloid (20 mL SnS+35 mL Si+20 mL SnS+35 mL Si) were spin-coated for fabricating a film of SnS:monocrystalline Si. A spin speed of 1000 rpm, acceleration speed of 100 rpm/s and a spin time of 30 s for each coating were used. SnS:polycrystalline Si films were also fabricated using the same experimental parameters and method. These films were vacuum annealed at 450 °C for 1 hour. The images of the as-prepared and annealed films are given in Fig. 3.3. The annealed films are visibly darker than the as-prepared films. In the figures and discussion, the colloids and films of monocrystalline silicon are referred to as ‘m-Si’ and those of polycrystalline silicon as ‘p-Si’. For comparison, thin films of SnS were also fabricated. The schematic diagram for the synthesis of Si and SnS nanoparticles and the construction of hybrid films using these nanocolloids is shown in Fig. 3.4.

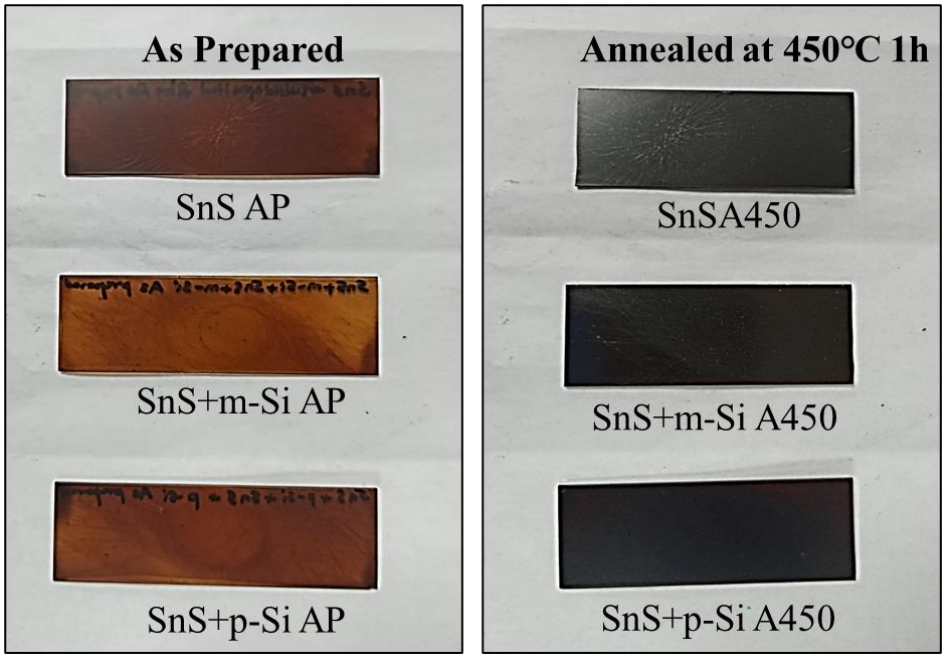


Fig. 3.3: Images of the SnS and SnS-Si films (AP refers to the as-prepared films and A450 refers to the films annealed at 450 ℃).

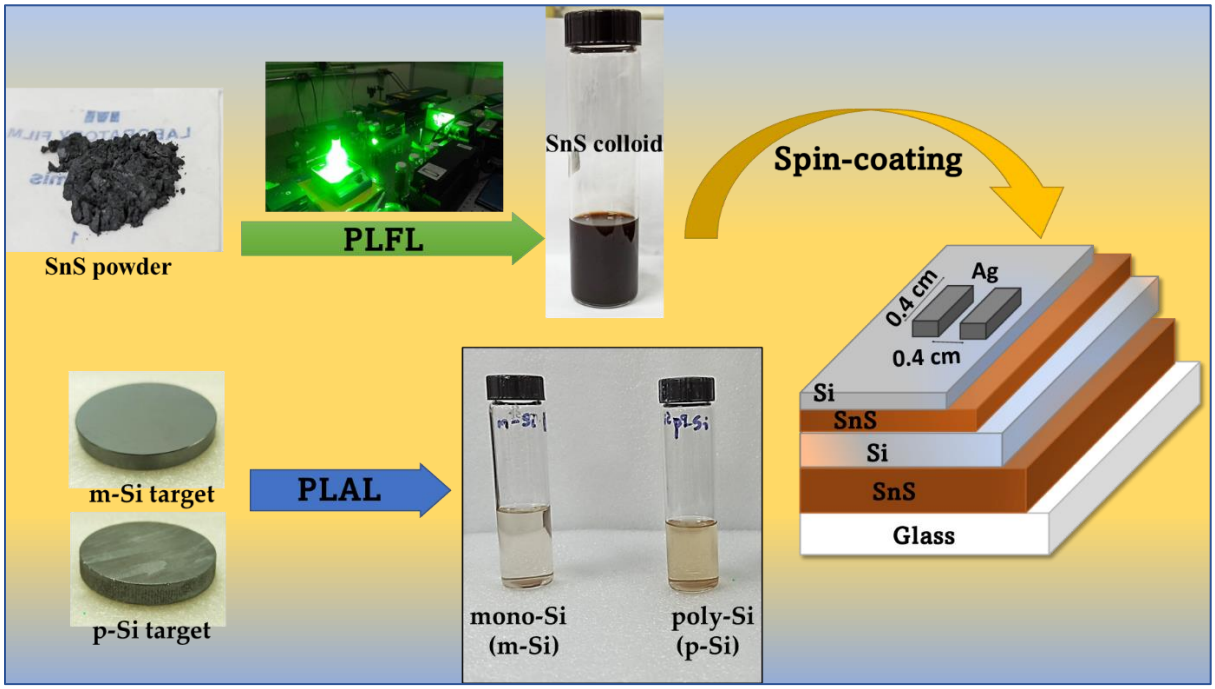


Fig. 3.4: Depiction of SnS and Si nanocolloid synthesis and device fabrication using these nanocolloids.

3.3 Results and Discussion

3.3.1 Transmission Electron Microscopy (TEM)

Transmission electron microscopy was employed to identify the colloidal nanoparticles' morphology and structural details. The TEM, HRTEM micrographs of SnS powder after laser irradiation are provided in Fig. 3.5. Spherical nanoparticles can be noticed in the TEM images shown at scales of 100 and 50 nm (Fig. 3.5 (a, b)). Short chains connecting these NPs are also observed along with them. These images were used to plot the size distribution curve, which is provided in Fig. 3.5. (c). There were particles with diameters between 5 and 67 nm. The SnS NPs had an average particle size of 22.26 ± 11.77 nm. By calculating the interplanar distance (d- spacing) between the lattice fringes of the HRTEM images, the crystallographic planes were identified. The (021), (120) and (101) planes are associated to interplanar distances of 3.23, 3.42 and 3.96 Å respectively. The patterns were correlated with the orthorhombic phase of SnS (ICDD card 039-0354). Fig. 3.5 (d) displays the indexed HRTEM pattern.

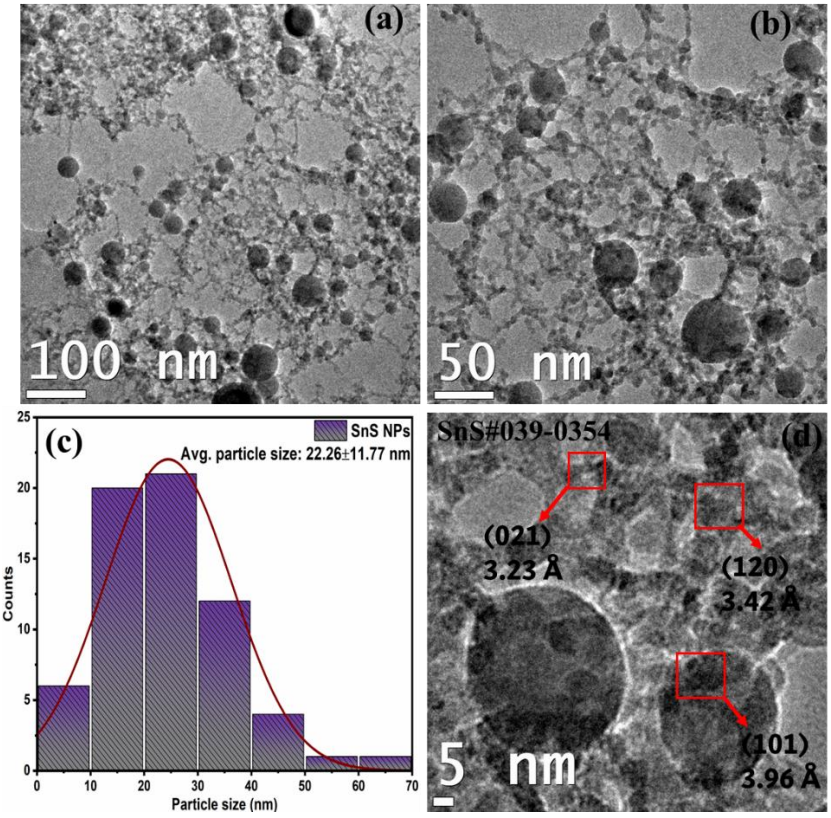


Fig. 3.5: (a, b) TEM images (c) size distribution chart and (d) HRTEM image of SnS NPs after laser irradiation.

Furthermore, the Si NPs synthesized by laser ablation were also analyzed using TEM. The TEM images of mono- and polycrystalline silicon are presented in Fig. 3.6 (a, b, d and e), respectively. In both conditions, ultrafine, tiny, spherical nanoparticles were identified. For monocrystalline Si, from the HRTEM image (Fig.3.6 (c)), (006) plane was identified related to the d-spacing value of 1.10 Å. For polycrystalline Si, the reflections from the planes of (222), (123) and (022) planes were identified corresponding to the interplanar spacing of 2.06, 1.76 and 2.34 Å respectively (Fig. 3.6 (f)). The HRTEM images are indexed with corresponding crystal planes according to the ICDD card 98-000-4592 for cubic Silicon. In the case of polycrystalline Si, in addition to the planes from Si, a reflection from (022) plane was observed at d-spacing of 2.52 Å and it matches to the cubic phase of SiO_2 (ICDD#98-001-6952). The sample's orientation and placement at the time of analysis affect the crystal orientations that are indicated by the observed lattice fringes [141,142]. This may be the reason why in monocrytsalline Si, only peaks of Si were observed.

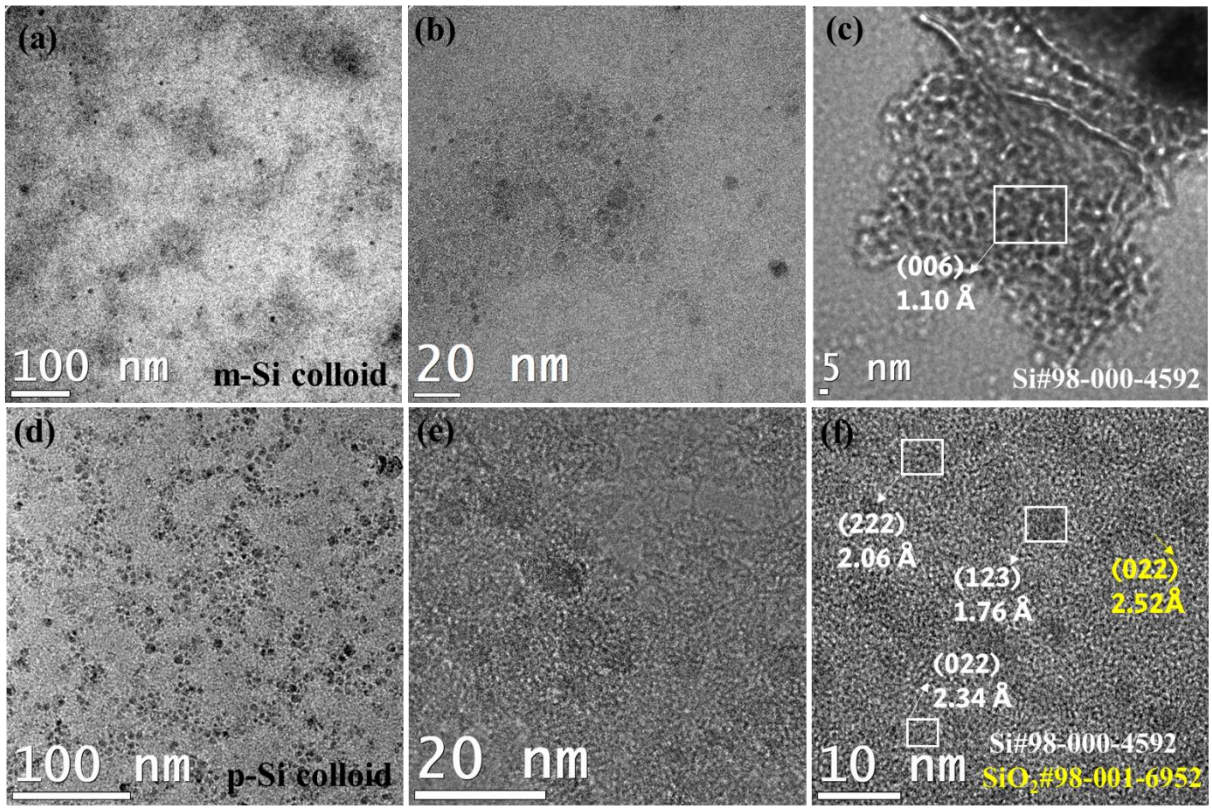


Fig. 3.6: TEM and HRTEM images of (a, b, c) monocrystalline Si NPs (d, e, f) polycrystalline Si NPs.

High-Angle Annular Dark Field Scanning TEM (HAADF-STEM) and Energy Dispersive X-Ray Spectroscopy (EDX-STEM) analyses were carried out for the confirmation of morphology as well as for their composition. The results of mono- and polycrystalline Si NPs are displayed respectively in Fig.3.7 and Fig.3.8. The STEM images at a scale of 100, 50 and 20 nm are provided. In the inset of the EDX image is the NP area chosen for the EDX analysis. Utilizing the software TIA (TEM Imaging and Analysis), silicon (Si) and oxygen (O) were particularly targeted for elemental analysis and the other peaks were removed. From the EDX analysis for both the samples, some additional peaks can be found which are identified as carbon and copper from the TEM grid. The STEM image and EDX results shown in Fig.3.7 correspond to monocrystalline Si. The average size distribution of m-Si calculated from the STEM image is also given in the figure. There were particles ranging from 2.7 to 9.5 nm. The average particle size was 4.84 ± 1.47 nm. For polycrystalline Si (Fig.3.8), the average particle size was 3.70 ± 1.17 nm with particles ranging from 1.6 to 6.2 nm. The particle size of p-Si was smaller than m-Si NPs. The synthesis of Si NPs in IPA by PLAL has not been investigated, although Yang et al. [179] reported the synthesis of Si NPs in ethanol by laser ablation, which showed similar spherical morphology for particle diameters ranging from 3.1-6.8 nm for laser fluences from 50-200 mJ/pulse. The elemental composition calculated from EDX is given in the inset of the figures. A weight% of 76.88% and 83.34% were identified for m-Si and p-Si respectively. The image includes a quantifiable indication of the corresponding atomic percentage. The EDX results showed that the colloid's major constituents are Si NPs, with very little oxygen present. The later part of the discussion goes into more detail about how the breakdown of the solvent during ablation may have caused the oxygen to diffuse into the colloidal solution and be the cause of the oxygen presence that was found.

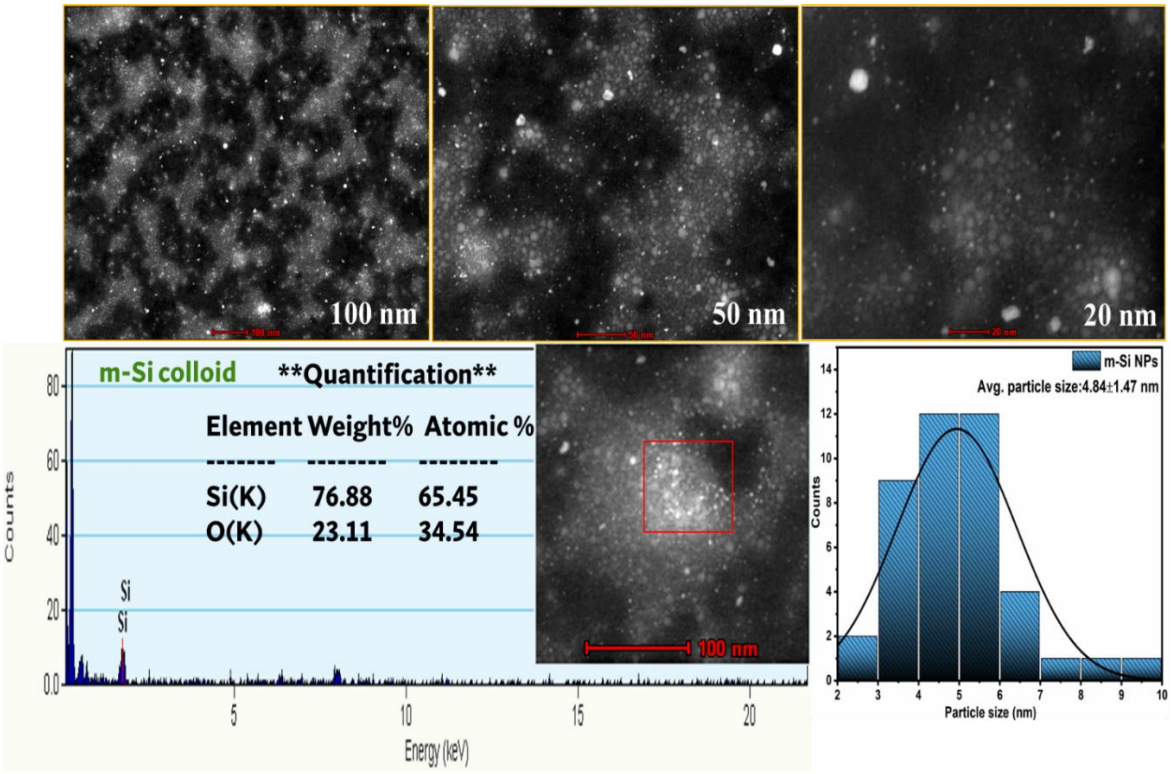


Fig. 3.7: STEM images, EDX quantification and average size distribution of monocrystalline Si.

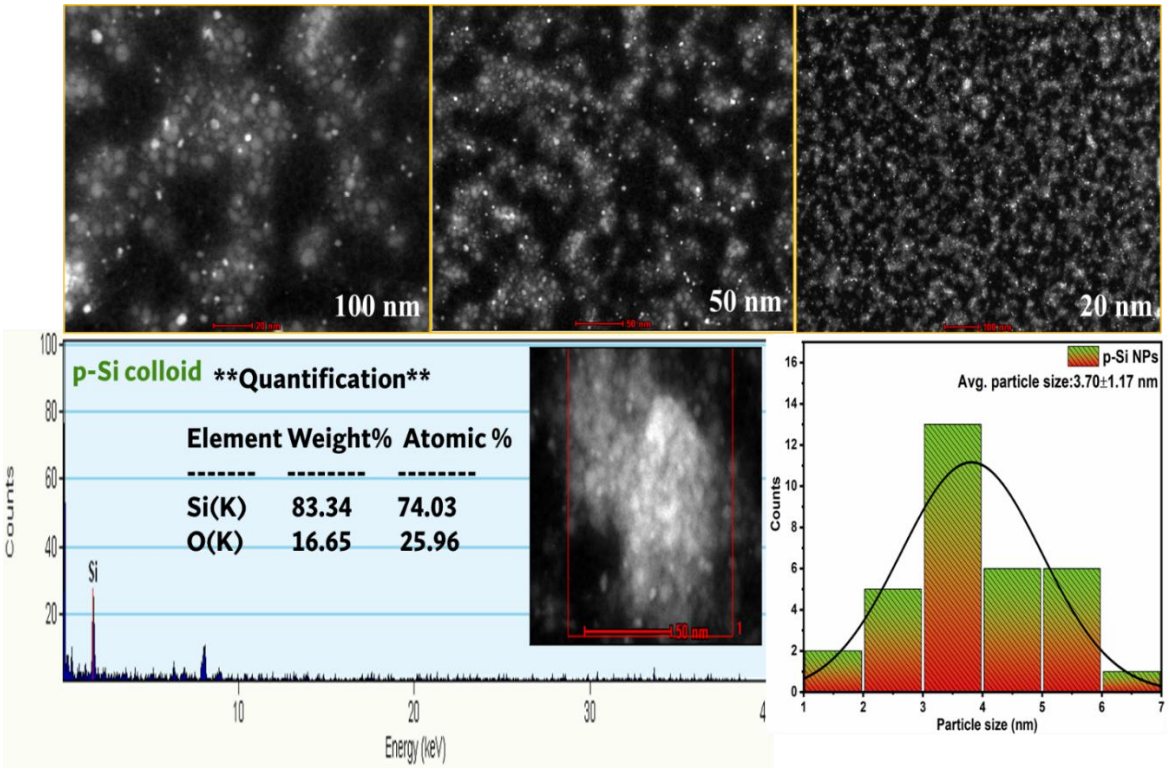


Fig. 3.8: STEM images, EDX quantification and average size distribution of polycrystalline Si.

Fig.3.9 shows the TEM and HRTEM images of hybrid SnS and m-Si colloidal NPs mixed. Images at a scale of 200, 100, 50 and 10 nm are shown. As was previously observed, both SnS and m-Si are spherical, making it difficult to distinguish between the NPs. Due to the lower proportion of Si NPs in the samples, the spherically interlinked feature of SnS was predominant.

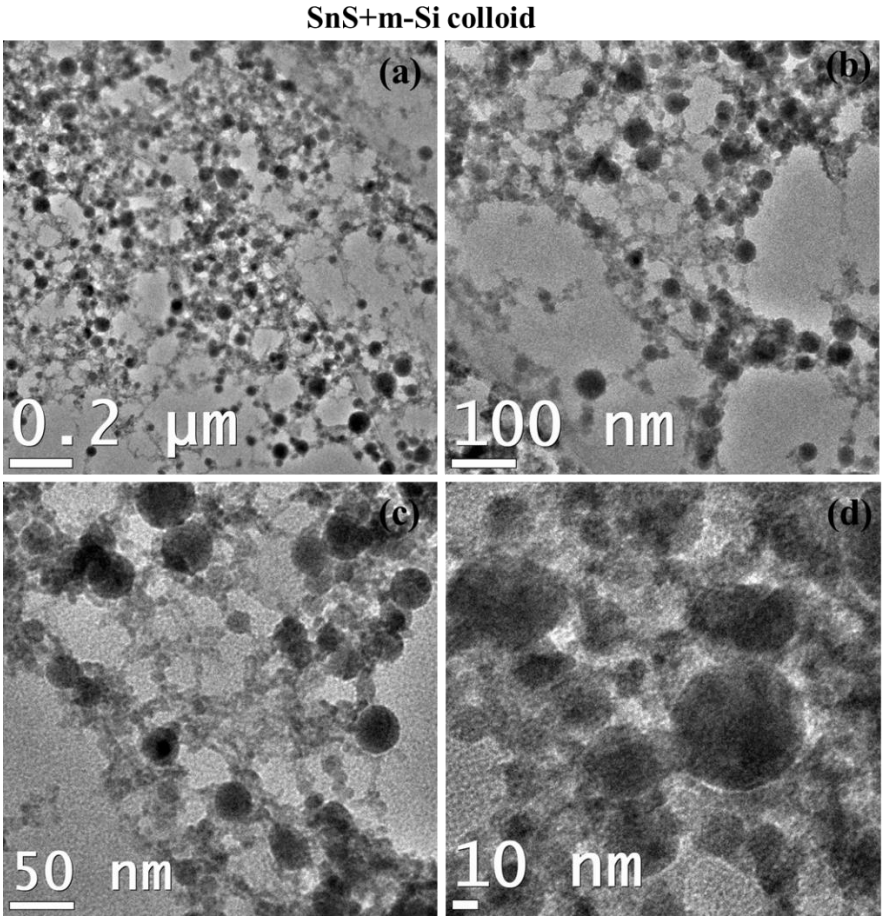


Fig. 3.9: (a-c) TEM and (d) HRTEM images of hybrid SnS NPs and monocrystalline Si NPs.

3.3.2 X-ray diffraction

The XRD pattern of the SnS and SnS:Si films is shown in Fig. 3.10 for both as-prepared and annealed films. Additionally shown in the figure is the XRD pattern of the SnS powder utilized in the experiment. All of the films can be seen to have a significant peak orientation toward the (040) plane at an angle of 2θ=31.99º. A (111) plane of SnS at 2θ=31.57º is seen as a shoulder peak along with the (040) plane. The shoulder peak is more noticeable in annealed films than in as-prepared films. The remaining planes for the films (120), (021), (101) and (131) at 2θ values of 26.08º, 27.48º, 30.55º and 39.08º respectively. The SnS orthorhombic phase is indicated by the XRD peaks (ICDD#039-0354). Tetragonal SnO_2 phases were also found in the XRD at 2θ= 32.14º

and 31.66º, which correspond to the (101) and (110) planes. The solvent effect or the laser settings used during the ablation tests are the causes of the secondary phases in SnS. SnO_2 was found to be present during PLAL of SnS, according to Grisel et al. [77]. In the case of SnS, the presence of other phases (SnO_2, SnS_2, Sn_2S_3) are frequently reported [180–182]. A low energy laser was also used to irradiate SnS in order to determine whether the oxide phase (SnO_2) was generated as a result of laser energy. The utilized low energy laser (LQ626) had an output of 532 nm, a pulse width of 10 ns and a frequency of 100 Hz. After the produced nanocolloids were spin-coated, the XRD pattern was captured and is shown in Fig. 3.11. In the XRD peaks, a similar trend was seen. In this instance as well, the SnO_2 peaks developed. As a result, we came to the conclusion that the presence of SnO_2 peaks alongside SnS may be caused by the solvent effect. Given the low quantity of silicon nanoparticles integrated into the films, it is possible that no peaks attributable to Si were seen in the hybrid films.

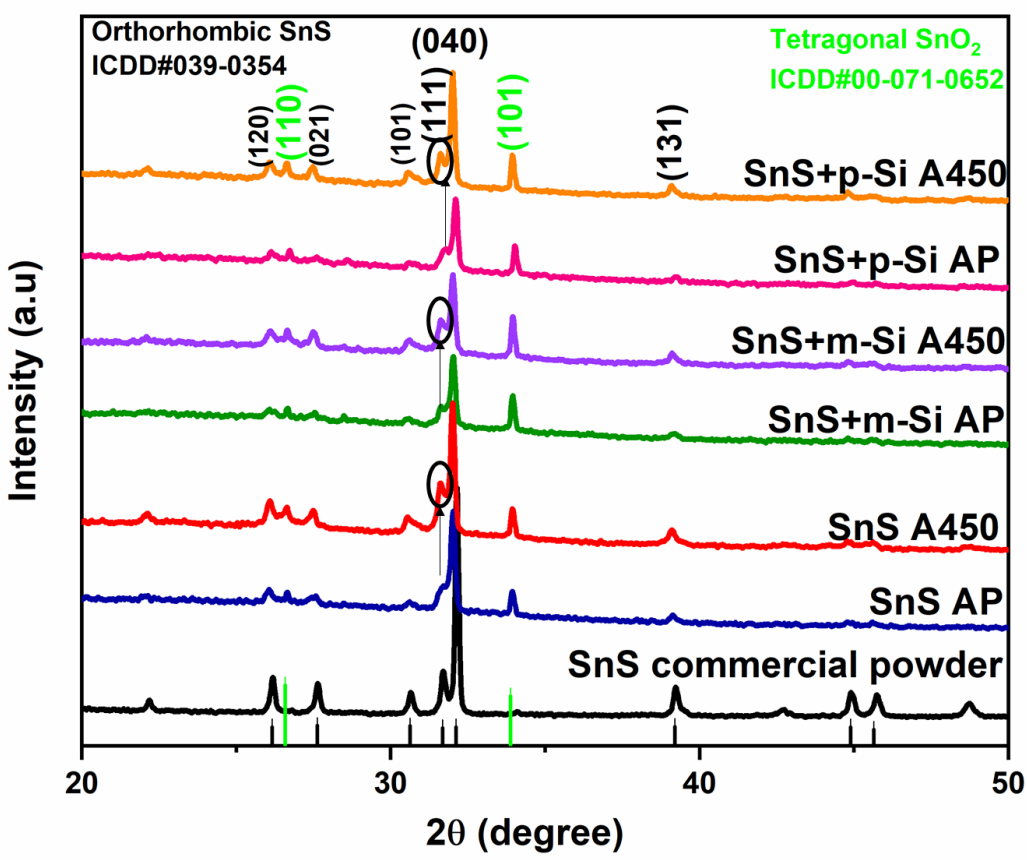


Fig. 3.10: XRD patterns of SnS and SnS-Si films at as-prepared and annealed condition.

The crystallite size of SnS and SnS:Si films was calculated using the Debye-Scherrer equation mentioned in Eq. 2.1 given in Chapter 2. The full width at half maximum (FWHM, β) of the average of the peaks at (040) and (111) were considered for the calculations. The values were 67.81, 68.08 and 60.11 nm for the as-prepared films of SnS, SnS:m-Si and SnS:p-Si, respectively, and 72.09, 72.42 and 70.57 nm for the annealed films. SnS and SnS:m-Si had better crystallinity than the SnS:p-Si films. Additionally, the size of the crystals increases with an increase in annealing temperature. This pattern has also been mentioned previously [183]. Additionally, this indicates a decline in the lowering of defects within the films [184].

Table 3.1: Crystalline size calculated from XRD for the as-prepared and annealed SnS and SnS:Si films.

	SnS AP	**SnS+m-Si AP**	**SnS+p-Si AP**	**SnS A450**	**SnS+m-Si A450**	**SnS+p-Si A450**
Crystalline size (nm)	67.81	68.08	60.11	72.09	72.42	70.57

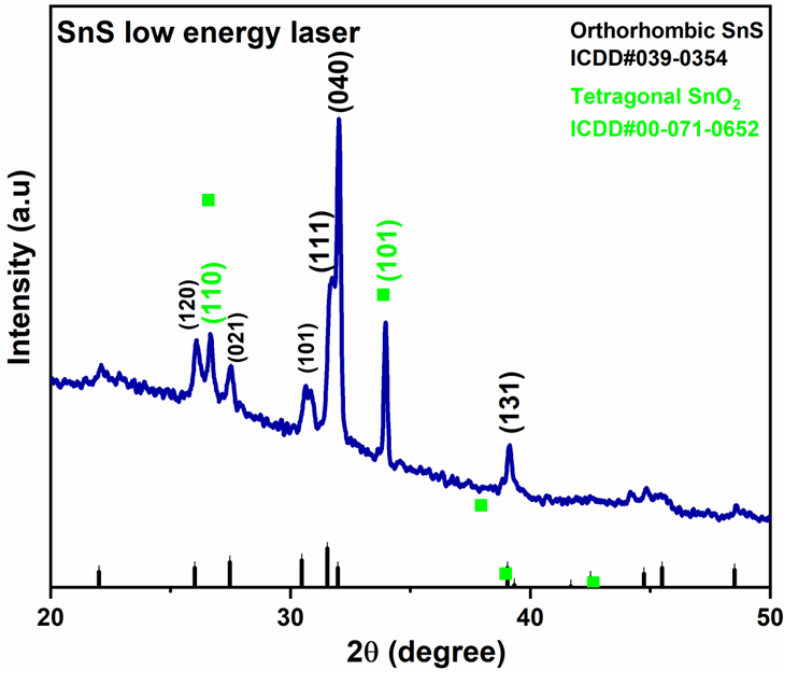


Fig. 3.11: XRD of SnS films synthesized using nanocolloids from a low energy laser output and spin-coated afterwards.

3.3.3 UV-Vis-NIR Spectroscopy

Fig. 3.12 (a) displays the UV-Vis spectra of the SnS NPs and in the inset is the absorption spectra of silicon nanoparticles. SnS NPs have an absorption below 600 nm and that of Si NPs is around 400 nm demonstrating the lower particle size of Si. The absorption of the films in their as-prepared and annealed states is shown in Fig. 3.12 (b). The smaller size and low concentration of Si NPs added to SnS may be the reason why little change in the absorption edge of the films is observed in their as-prepared state. Moreover, it should be noted that annealed samples exhibit a longer wavelength of absorption than as-prepared samples. The fact that could help to explain this disparity is that annealing improves the crystallinity of the samples. The bandgap was calculated using Tauc plot Eq. 2.2. Mono- and polycrystalline Si nanoparticles had band gap values of 2.72 and 2.83 eV, respectively. For luminous nanoparticles of silicon produced by nanosecond pulsed laser ablation, bandgaps of 1.59 and 1.64 eV were observed [185] and for Si nanoparticles prepared by stain etching of monocrystalline n-type wafers bandgaps between 2.0 and 3.2 eV were found [186]. Depending on the solvent used for laser ablation, the optical band energies varied, with Si NPs in water and hexane exhibiting optical band energies of 2.9 and 3.5 eV, respectively [187]. In contrast to direct bandgap materials, which experience direct carrier transfers from the valence band to the conduction band, indirect bandgap materials experience energy loss via phonon interactions. Indirect bandgap materials are well recognized to be inappropriate for optoelectronic applications since the production and recombination processes of electron-hole pairs demand momentum conservation via a phonon in addition to photon participation. As a result, there is a much smaller chance of photoelectric conversion [188]. Although Si is identified as an indirect bandgap material, it is asserted that when Si NPs' dimensions are comparable to or smaller than the exciton Bohr radius (~4 nm), which is pertinent in our case, they go through a transformation from an indirect to a direct band gap semiconductor and experience band gap widening [185]. In order to maximize light absorption, the quantity of charge carriers and the photodetection, Si and SnS were combined to form hybrids. The bandgap values for the as-prepared films were calculated as 2.02, 1.93 and 2.04 eV for SnS and mono-, polycrystalline Si incorporated films respectively. For annealed films (Fig. 3.12 (c)), the values are 1.64 eV for SnS, 1.51 eV and 1.68 eV, respectively, for monocrystalline and polycrystalline films. Upon annealing, a decrease in the bandgap values is seen. By vacuum annealing the films at 400 °C, Xu et al. noticed a drop in the bandgap of SnS from 1.54 eV to 1.38 eV [189]. Among the annealed films, the lowest bandgap

was observed for SnS:m-Si films and this may be due to the increase in crystalline size as observed from XRD [190]. We previously reported a bandgap of 2.5 and 2.03 eV for SnS films produced by combining PLFL with spin-coating [191], where the annealing time was shorter (20 min) than in this case (1 h). The transmittance and reflectance curves are also collected and provided in Fig.3.12 (d). The homogeneity of the films was demonstrated by the nearly identical %T and %R spectrum. All the films had reflectance of less than 10% and the transmittance curves of the annealed films were steeper than those of the as-prepared films. This is indicative that the bandgap (E_g) had changed and that the film thickness had increased with annealing [124]. The absence of contrasting fringes in the transmittance spectra of all the films, which is often attributed to a diffusion phenomenon, is suggestive of a rough film surface made up of tiny grains [192].

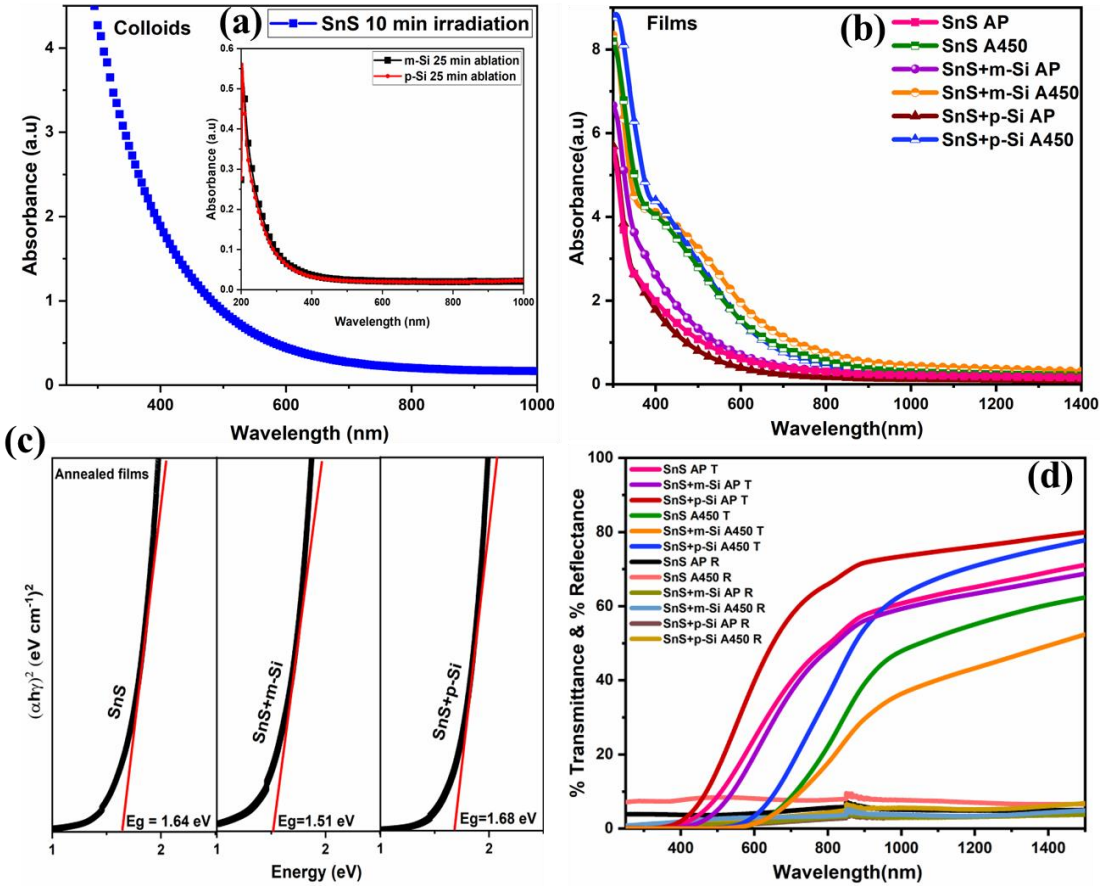


Fig. 3.12: Absorbance of (a) SnS NPs in the nanocolloid (Inset: Absorbance of Si NPs) (b) SnS and SnS:Si hybrid films, (c) Bandgap calculation of the films by Tauc plot (d) % Transmittance and reflectance of the films.

3.3.4 Raman Spectroscopy

To ascertain the crystallinity and phase of the films, Raman spectroscopy was performed. The Raman analyses were carried out using a 532 nm excitation laser of a DXR Raman microscope from Thermo Scientific. In Fig. 3.13 (a), the Raman spectra of the Si targets utilized for laser ablation are shown and the spectra denotes the crystalline nature of Si. The typical peak found in bulk Si is observed at 521 cm^{-1} and is attributed to longitudinal optical (LO) mode of Si-Si stretching vibrations [193]. The scattering of two transverse acoustic (2TA) and optical phonons (2TO) results in less strong, wider peaks that are seen about 302 cm^{-1} and between 945 and 984 cm^{-1}, respectively [194,195]. To make the spectra more obvious, a zoomed version is shown in the inset of the figure. The phonon modes of SnS are identified in the thin films at 92.8, 223.4 and 309.9 cm^{-1}. In Fig. 3.13 (b), the Raman peaks identified in the case of annealed SnS and SnS:Si are displayed. There are 12 active Raman modes for the orthorhombic crystal structure in SnS, out of the 21 phonon modes [196]. The peak associated with the A_g mode is 310 cm^{-1}, the longitudinal A_g (LO) optical mode peak is around 220 cm^{-1} and the transverse A_g (TO) optical mode peak is around 93 $cm^{-1}$and [171]. The peak position of Si in the Si incorporated films is seen at around 512 cm^{-1}, which is moved to a lower energy than the bulk Si peak at about 520 cm^{-1}. Each Si atom in bulk Si, which has a regular tetrahedron shape, is bonded to four other Si atoms. These covalent bonds have long-range order in their length and bond angle. The development of a translational symmetry aberration is theorized to be caused by changes in the length and angle of bonds in Si nanospheres (the Si NPs in our case is spherical as observed via TEM). The fact that the motion in the Si's spherical nanoparticles is constrained in the z-direction suggests that the two-dimensional well is where electron mobility is expected to exist. It is crucial to take into account surrounding phonon dispersion since phonon scattering will not simply take place at the Brillouin zone's center. Thus, the down-shift in Raman wave numbers in these films is due to the phonon confinement effect in 2D nanoscale Si crystals [197].

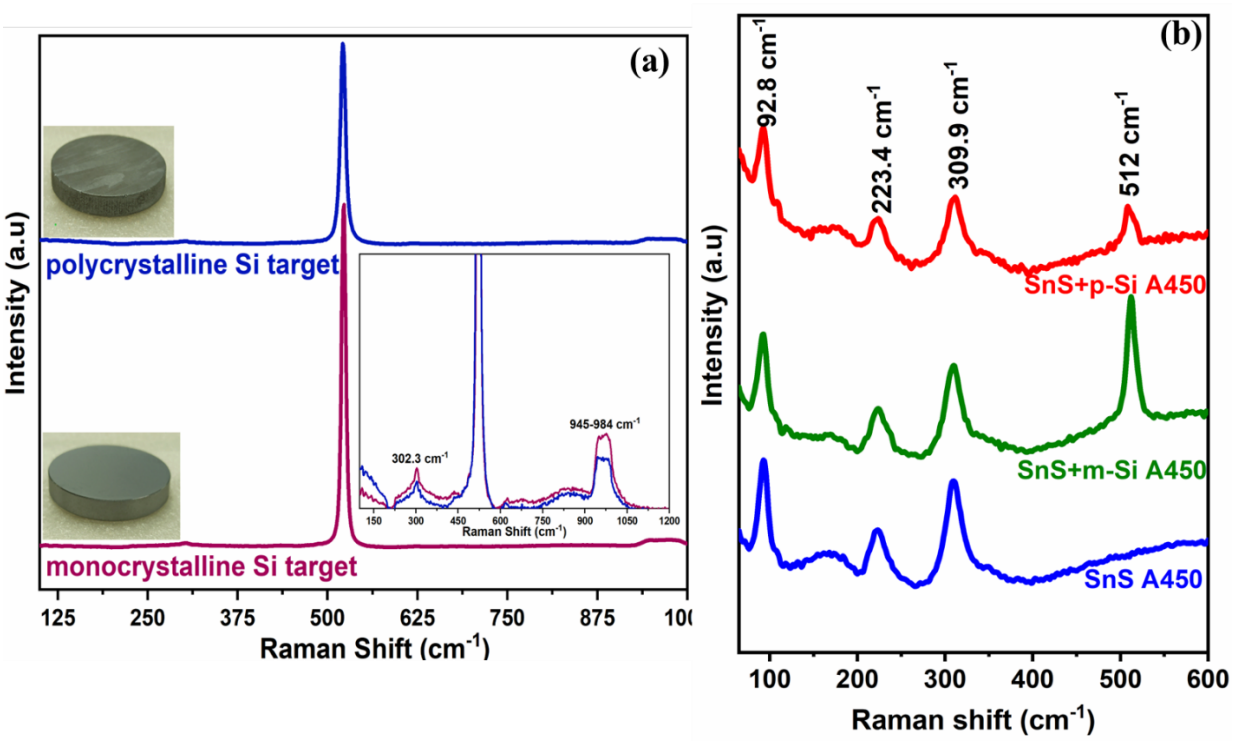


Fig. 3.13: Raman spectrum of (a) Si targets (Inset: Zoomed image of the Raman spectra of Si targets) (b) SnS and SnS:Si films annealed at 450 ℃.

3.3.5 Scanning Electron Microscopy

Fig. 3.14 depicts the SEM micrographs of SnS powder at 5 and 3 µm scales both before and after irradiation. An extremely erratic morphology with thick flakes and larger particles is seen before irradiation. Only little fragments are visible after irradiation, indicating laser fragmentation in liquid (LFL). The size reduction that takes place during LFL is believed to be caused by the mechanisms of photothermal evaporation and Coulomb explosion. Koda and colleagues [198] initially hypothesized the photothermal vaporization in the LFL process in 1999 while researching the size diminution of Au NPs obtained by nanosecond laser irradiation. It is believed that surface evaporation begins when particle temperature exceeds the bulk material's boiling point. Size reduction is influenced by a number of factors, including laser fluence, irradiation period and number of pulses. With more laser fluence and a longer irradiation period, the particles will often be smaller [199]. The second LFL technique, known as the Coulomb explosion, produces ionized NPs that rapidly break due to internal charge repulsion by ejecting electrons from the solid educt [43].

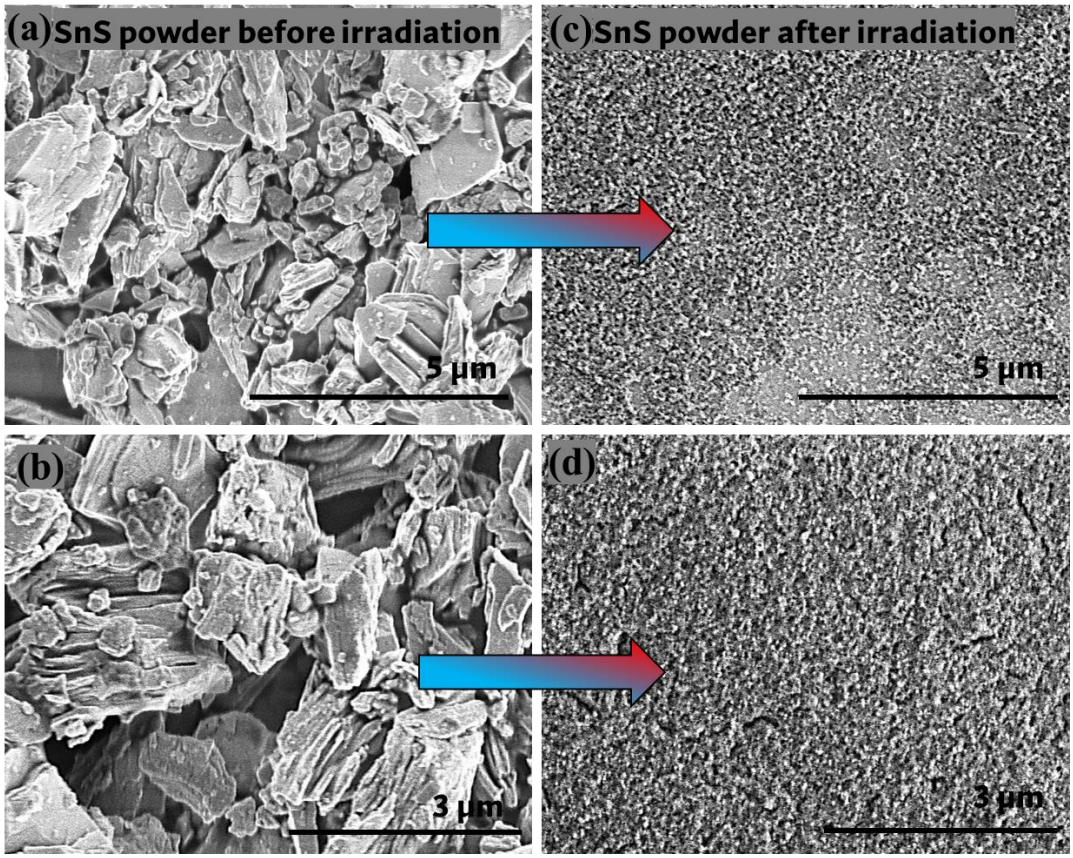


Fig. 3.14 SEM images of SnS powder (a, b) before laser irradiation (c, d) after laser irradiation.

The SEM micrographs for Si NPs are shown in Fig. 3.15. The PLAL-produced mono- and polycrystalline Si nanocolloids were dropcasted onto substrates of ITO and titanium (Ti) in order to obtain the SEM images. For samples in ITO, a voltage of 1 kV and for Ti, a voltage of 2 kV was applied. The current applied was 10 µA. Fig. 3.15 (a, b) shows monocrystalline Si NPs in ITO and Fig. 3.15 (c) shows the samples on titanium (Ti) substrate. For polycrystalline NPs, Fig. 3.15 (d, e) shows NPs on ITO and Fig. 3.15 (f) on Ti. Both the Si NPs showed spherical morphology which is well in line with TEM observations. The significantly larger spheres that are seen on ITO substrates are a result of the agglomeration that is brought about by the temperature that is applied to the substrate during the dropcasting of the nanocolloids.

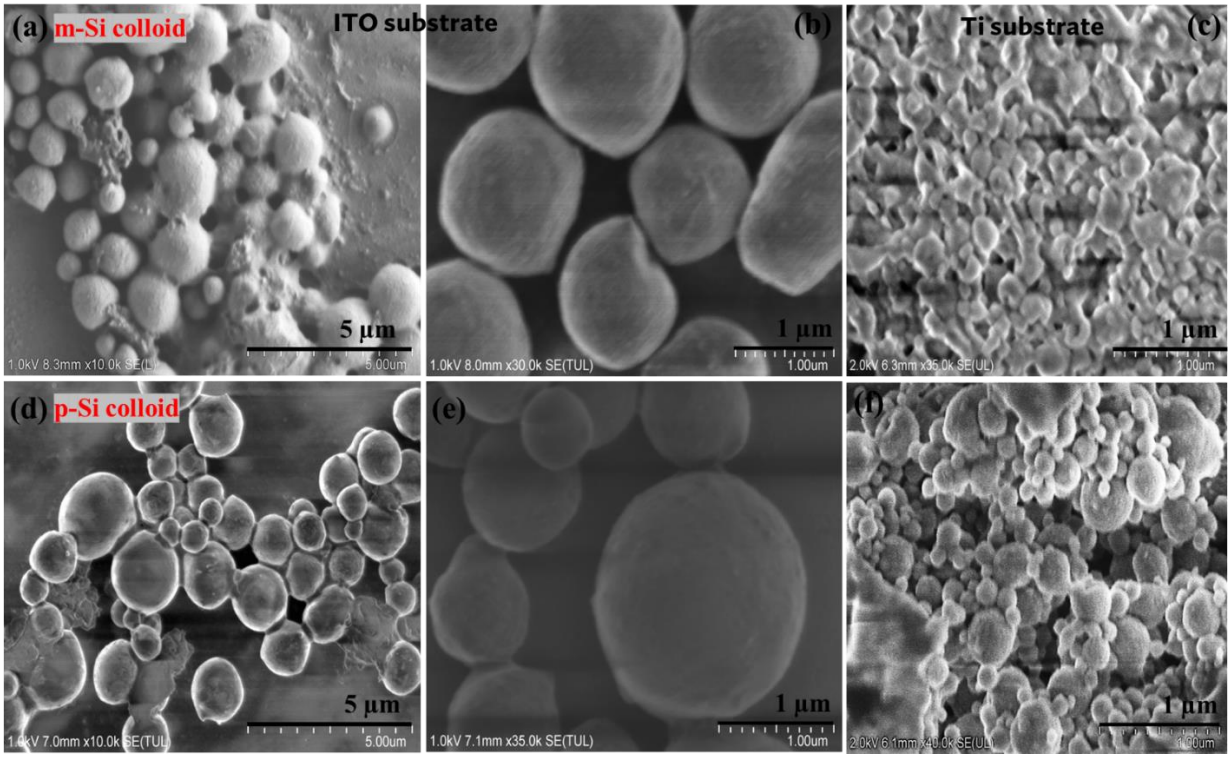


Fig. 3.15 SEM images of moncrystalline Si NPs deposited on (a, b) ITO and (c) Ti substrates; and SEM images of polycrystalline Si NPs on (d, e) ITO and (f) Ti substrate.

In the case of thin films, the SEM images of the as-prepared and annealed films are provided in Fig. 3.16. The annealed films had a more condensed and distinct morphology than the as-prepared films. The increase in temperature resulted in an improvement in the grain size and coverage. Spherical SnS NPs with connected chains could be seen in SnS and SnS:m-Si films, however they were less distinct in SnS:p-Si films. As-prepared films ranged in thickness from 870 to 980 nm, while annealed films had a thickness of 1.18 to 1.67 µm. In Fig. 3.17, cross-sectional SEM images are provided. We acquired varying thickness values for these samples as a result of the rough and uneven cross-sectional surface.

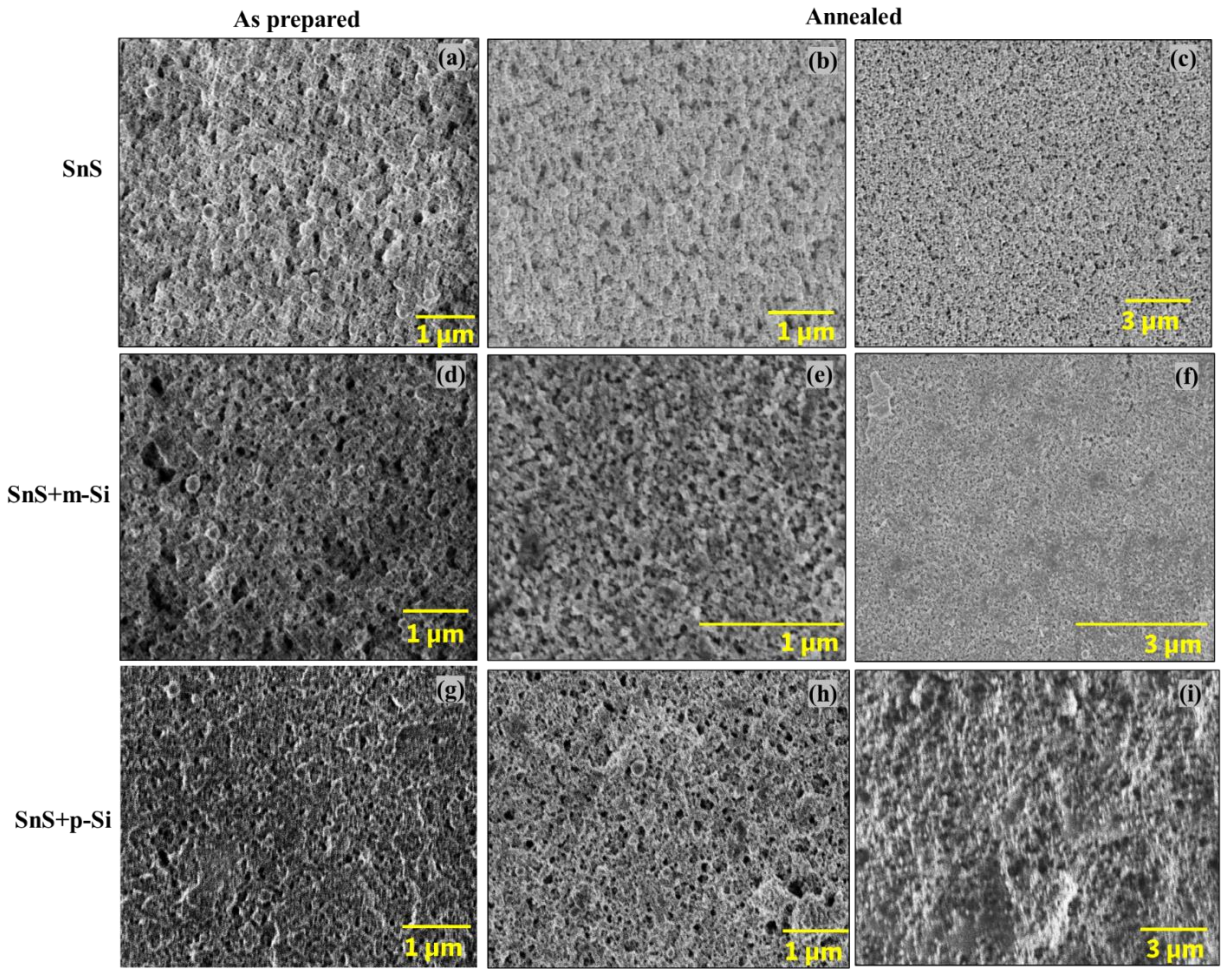


Fig. 3.16: SEM images of as-prepared and annealed (a, b, c) SnS (d, e, f) SnS:m-Si (g, h, i) SnS:p-Si films.

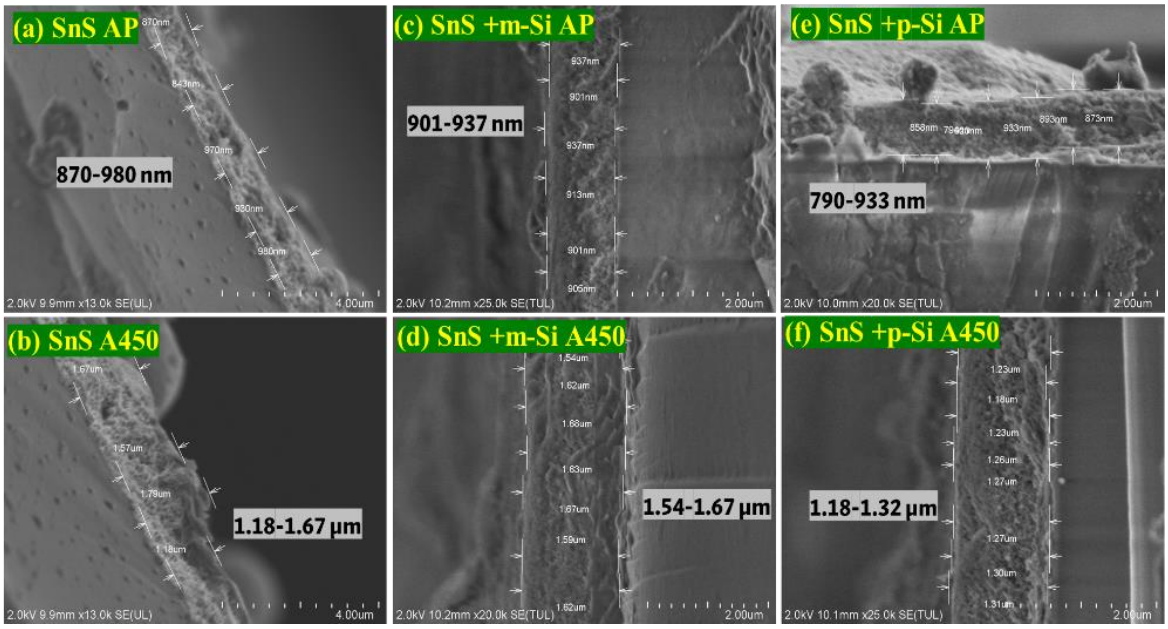


Fig. 3.17: Cross-section SEM for thickness measurements of (a, b) SnS (c, d) SnS:m-Si (e, f) SnS:p-Si films.

3.3.6 X-ray photoelectron Spectroscopy

Fig.3.18 (a-f) shows XPS survey spectrum recorded for the as-prepared and annealed thin films. The survey spectrum is used to detect the photoemission peaks of silicon (Si), sulfur (S) and tin (Sn). High-resolution scans for each element from the survey scan were also acquired in order to better understand chemical composition. A Shirley type background correction was applied to these spectra. For binding energy correction, the value of 284.6 eV assigned to the characteristic peak of adventitious carbon, C1s was chosen. When fitting peaks using the Gaussian-Lorentzian sum function, the peak positions, binding energy splitting, peak-area ratios and full width at half maximum (FWHM) values were taken into account. Table 3.2 lists the binding energy values for each of the core levels.

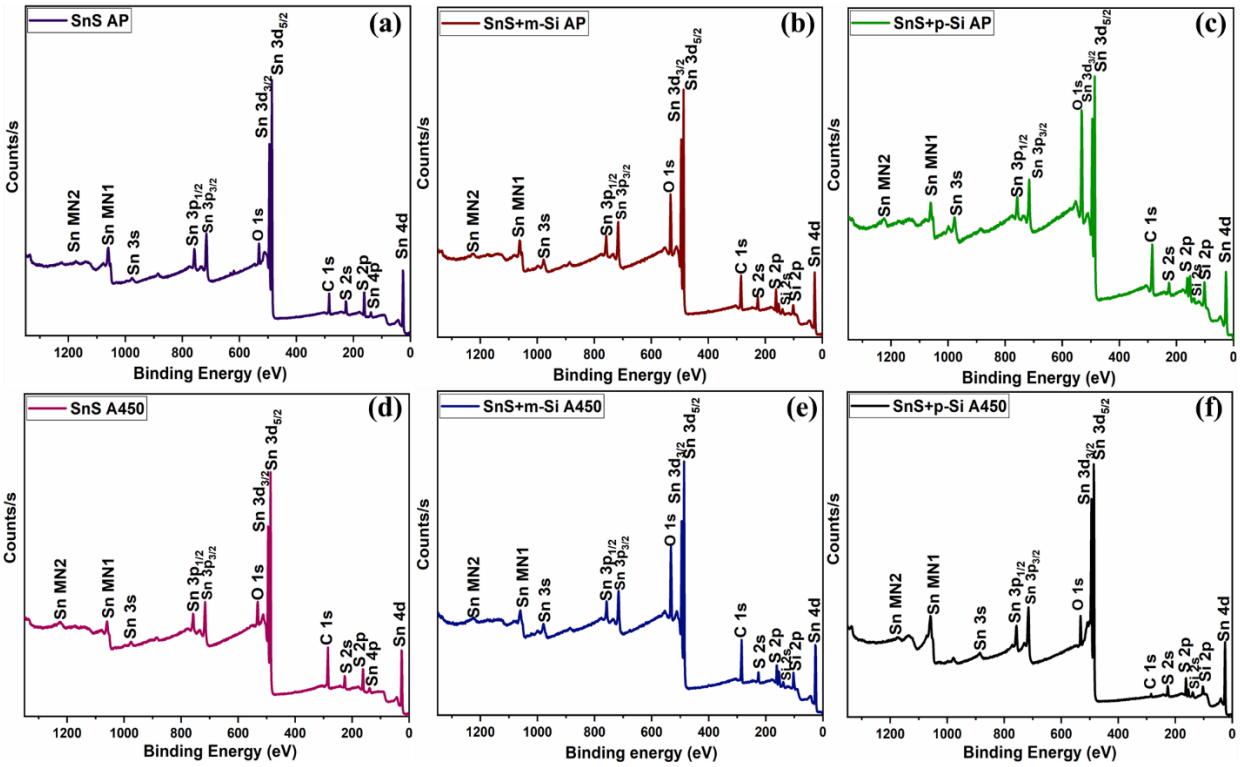


Fig. 3.18: (a-f) XPS survey scan spectra of the as-prepared and annealed SnS and SnS-Si films.

In Fig. 3.19 and Fig. 3.20, respectively, are shown the high resolution spectra of Sn 3d, S2p and Si 2p of the as-prepared and annealed films. Fig. 3.19 (a, b, c) and Fig. 3.20 (a, b, c), respectively, exhibit the core level peaks of Sn $3d_{5/2}$ and Sn $3d_{3/2}$. The peaks at 485 eV and 494 eV are the dominant peaks associated to Sn^{2+} in SnS [200]. Minor peaks corresponding to Sn^{4+} state as in SnO_2 is also observed around 486 and 495 eV [201]. Peak fitting was done while maintaining a peak separation value of 8.41 eV, a peak area ratio of 3:2 and FWHM [202]. The discussion section of XRD already provides an explanation for the existence of SnO_2. The high-resolution spectrum of S 2p is depicted in Fig. 3.19 (d, e, and f) and Fig. 3.20 (d, e, and f), and it has two core level peaks at S $2p_{3/2}$ and S $2p_{1/2}$. Comparing the annealed films to the as-prepared films, the annealed films exhibit a symmetric and well-resolved doublet. The peaks are roughly at binding energy values of 161 and 162 eV, respectively, for S $2p_{3/2}$ and S $2p_{1/2}$. Peak separation values ranged from 1.16 to 1.18 eV and the two peaks from the doublet in S 2p were constrained to a 2:1 intensity ratio. The binding energies are in close accord with the S^{2-} state in SnS [88]. For Si integrated SnS films, the deconvoluted peaks of Si 2p are shown in Fig. 3.19 (d, e, and f) and Fig. 3.20. (d, e, f). The figures show a low oxidation on the surfaces of Si integrated films, which is

supported by the Si 2p binding energies. In mono- and polycrystalline Si films formed under as-prepared and annealed conditions, the peak of elemental Si (Si (0)) is present at 99.41, 99.31, 99.67 and 99.39 eV. The deconvoluted peaks of Si-C, Si-O/Si-O-C, and SiO_2 are the other deconvoluted peaks. SiO_2 was found to have a greater % atomic concentration in films with p-Si NPs. SnS:m-Si films had a SiO_2 content of just 4.44%, but SnS:p-Si films had a SiO_2 content of 14.42%. Since their binding energies are often within 104 eV (i.e., of pure SiO_2), silicon oxides are regarded as oxygen-doped oxides [197]. For m-Si films, these values were 103.21 and 103.92; for p-Si films, they were 104.71 and 103.47 eV. The peaks between 100 and 104 eV, according to data from the literature, can be attributable to Si bound to Si, C or O. Therefore, it is impossible to distinguish between silicon bonded to carbon or oxygen based on our results [203]. It has been reported that silicon NPs can undergo chemical alterations such as oxidation, sulfurization and carbonization when they are reassembled with solvent molecules through plasma-activated chemical interactions [204]. Therefore, the presence of SiO_2 may have resulted from oxygen diffusing into the colloidal solution during the ablation process. Charee et al. found that oxygen and carbon diffused into silicon during ns laser ablation of the material in free air [205]. Although oxygen and carbon could not be entirely eliminated, they observed a decrease in their amount while doing ablation in water [141,142]. In their research on the laser ablation of silicon in ethanol, Kuzmin et al. noted the partial breakdown of ethanol into elementary carbon during the ablation process, identifying SiC. We assume SiC or SiO_2 is only present on the surface of the films since their proportions were too low to be detected by Raman spectroscopy [206]. The high resolution XPS spectra of Sn 3d and S 2p recorded for these films matched with the reported values for Sn^{2+} and S^{2-} in SnS as mentioned previously [207].

Table 3. 2: Binding energy values from high resolution spectra of Sn 3d, S 2p and Si 2p of the as-prepared and annealed SnS and SnS:Si films.

Oxidation state	**Core levels**	**Binding Energy (eV)**					
		SnS AP	**SnS+m-Si AP**	**SnS+p-Si AP**	**SnS A450**	**SnS+m-Si A450**	**SnS+p-Si A450**
Sn^{2+}	**Sn $3d_{5/2}$**	485.93	485.99	486.25	485.47	485.47	485.44
	Sn $3d_{3/2}$	494.34	494.40	494.66	493.88	493.88	493.85
Sn^{4+}	**Sn $3d_{5/2}$**	486.71	486.84	487.52	486.62	486.68	486.65

	Sn $3d_{3/2}$	495.12	495.25	495.93	495.03	495.09	495.06
S^{2-}	**S $2p_{3/2}$**	161.16	161.28	161.17	160.90	160.95	161.51
	S $2p_{1/2}$	162.34	162.46	162.35	162.08	162.13	162.67
Si (0)	**Si 2p**	-	99.41	99.31	-	99.67	99.39

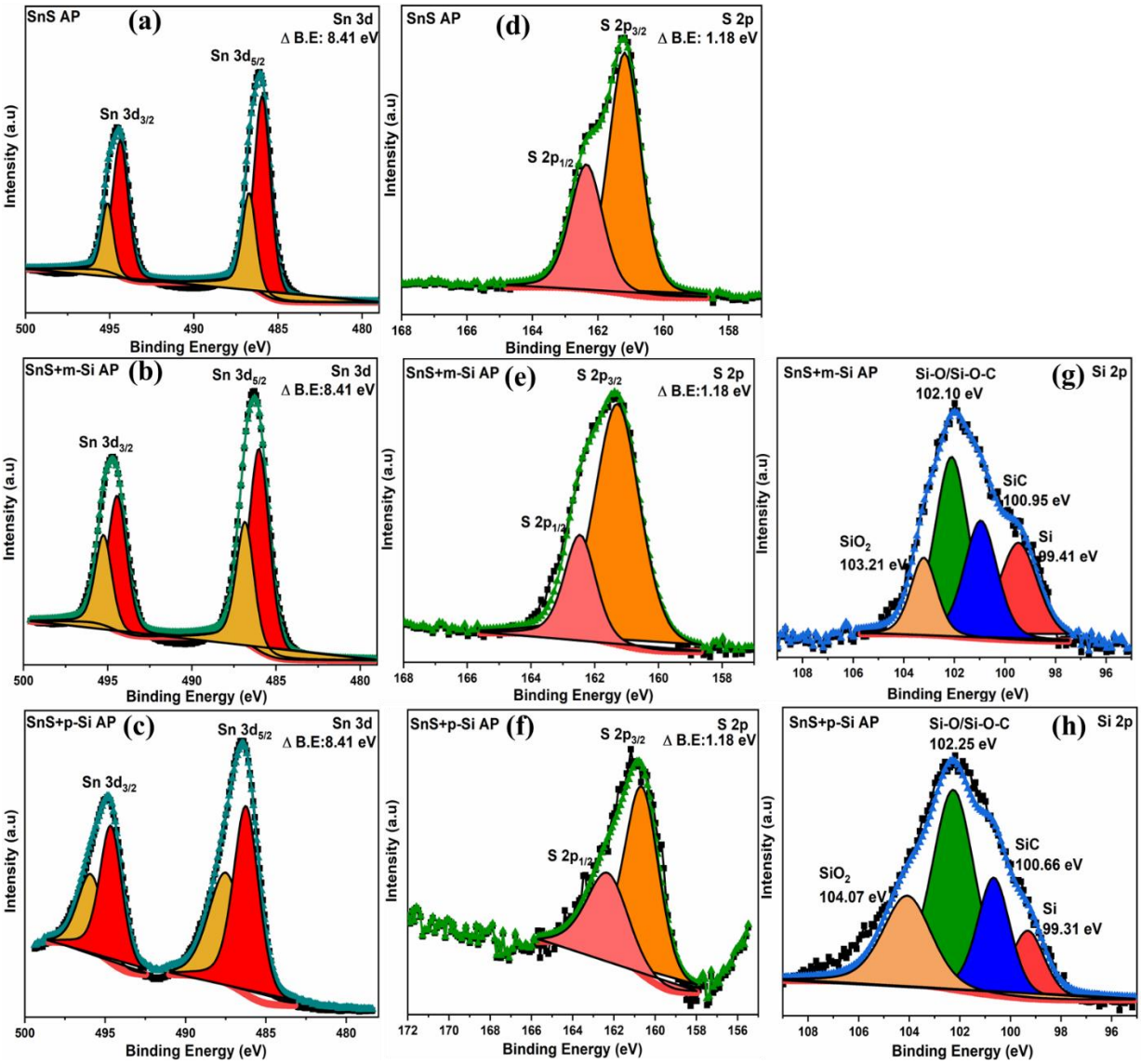


Fig. 3.19: High resolution XPS spectra of (a, b, c) Sn 3d, (d, e, f) S 2p and (g, h) Si 2p of SnS and SnS-Si as-prepared films.

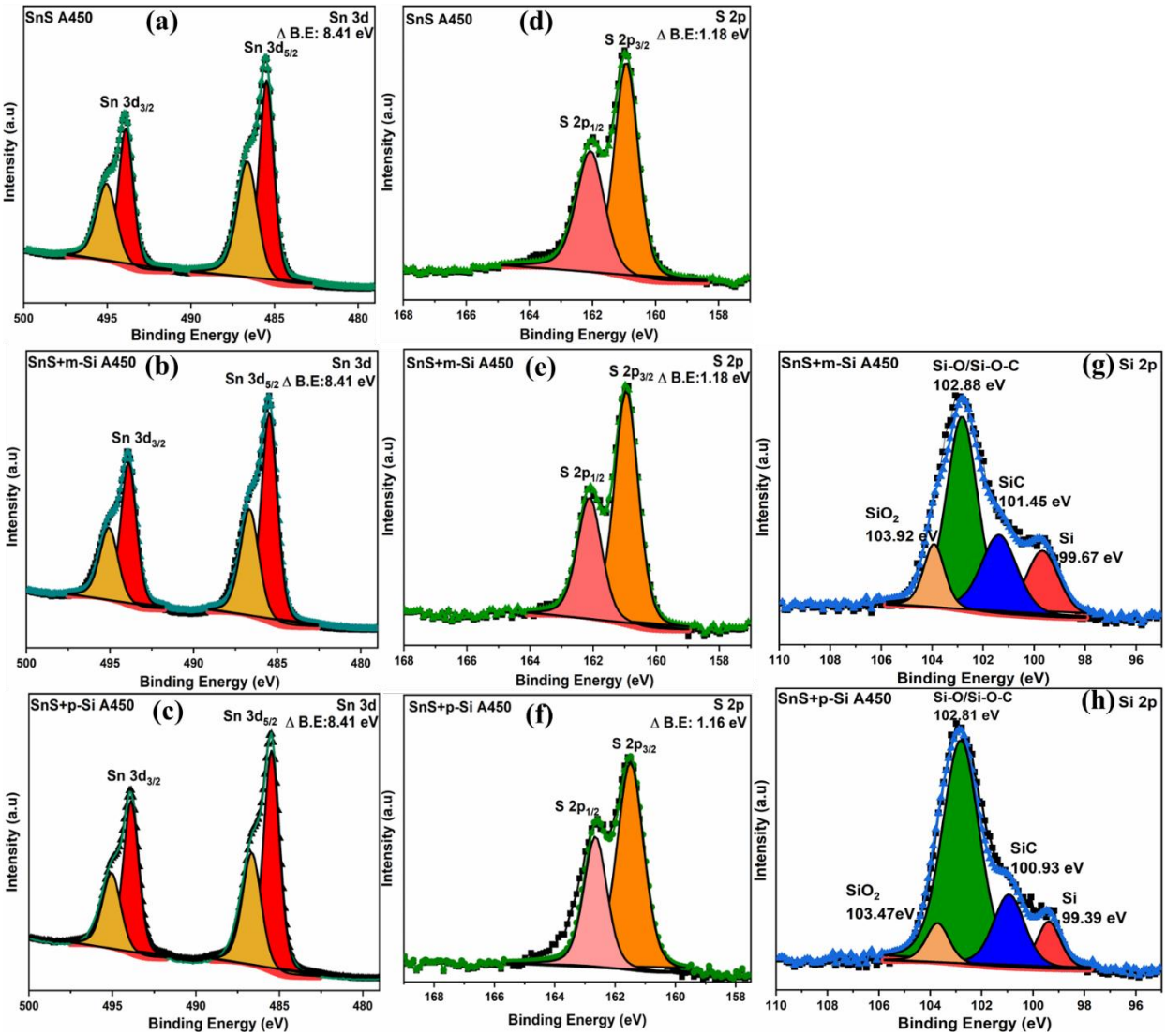


Fig. 3.20: High resolution XPS spectra of (a, b, c) Sn 3d, (d, e, f) S 2p and (g, h) Si 2p of SnS and SnS-Si annealed films.

3.3.7 I-V characteristics and Photoresponse measurements

The current-voltage characteristics of annealed hybrid films of SnS and SnS:Si are demonstrated in Fig. 3.21 (a) at applied voltages between -5 and +5 V both in the dark and under light. The linear and symmetrical characteristics of the I-V figure suggest a good ohmic contact between the Ag electrodes and nanostructured thin films. The I-V plot of the SnS film with p-Si incorporation is provided separately since the current value of the SnS:p-Si film was lower than that of SnS and SnS:m-Si films. In comparison to SnS and SnS:m-Si films, which had estimated conductivity values of 10^{-3} $(\Omega\ cm)^{-1}$, SnS:p-Si films had estimated conductivity values of

10^{-5} $(\Omega\ cm)^{-1}$. The SnS:p-Si A450 film is demonstrated by these figures to be relatively resistant when compared to other films. The increased atomic percentage of SiO_2 or the surface oxidation in SnS:p-Si that was detected by XPS may be the cause of this. The enhanced electrical resistance of the SnS:p-Si film is a result of its smaller grain size. As the grain size increases, the grain boundary scattering decreases, increasing the film's electrical conductivity [192].

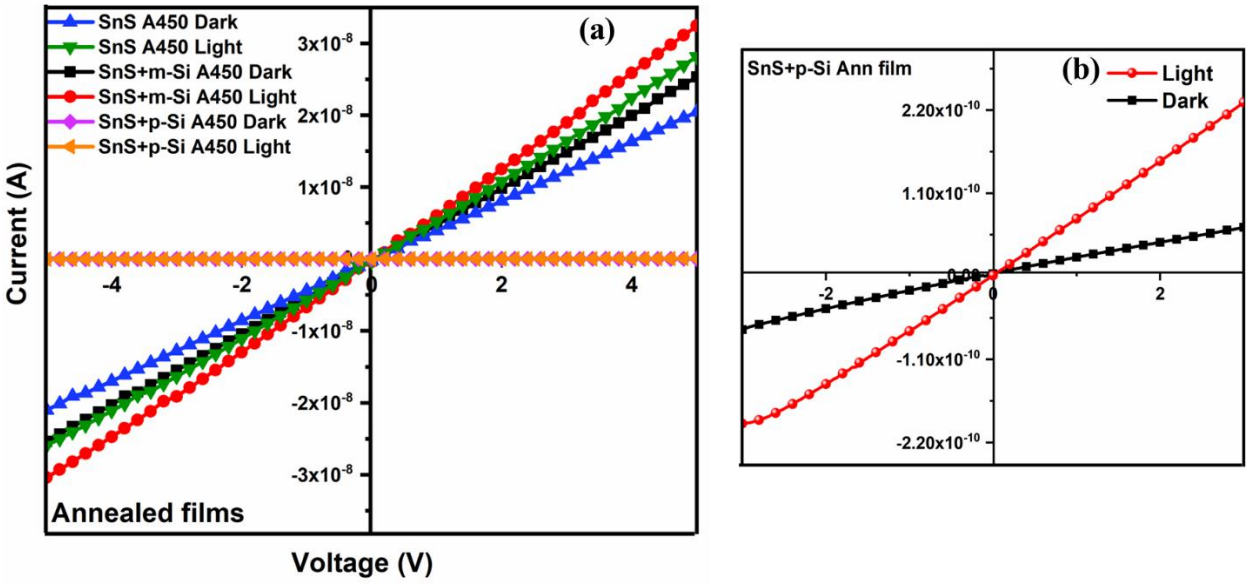


Fig. 3.21: I-V plot of (a) SnS and SnS:Si hybrid annealed films (b) SnS:p-Si annealed film.

The photoresponse of the samples was tested using a variety of illumination sources including tungsten (W) lamp, full spectrum, IR, Red and UV LEDs by applying a voltage of 5V. Notable responses for these samples were seen under various illuminations. The full spectrum LED covers the complete UV-Vis spectrum, whereas the IR LED used has a wavelength of 740 nm, the red LED was 620 nm and the UV LED is between 395 and 400 nm. The photoresponse of the annealed samples to these illumination sources is shown in Fig. 3.22 (a-c).

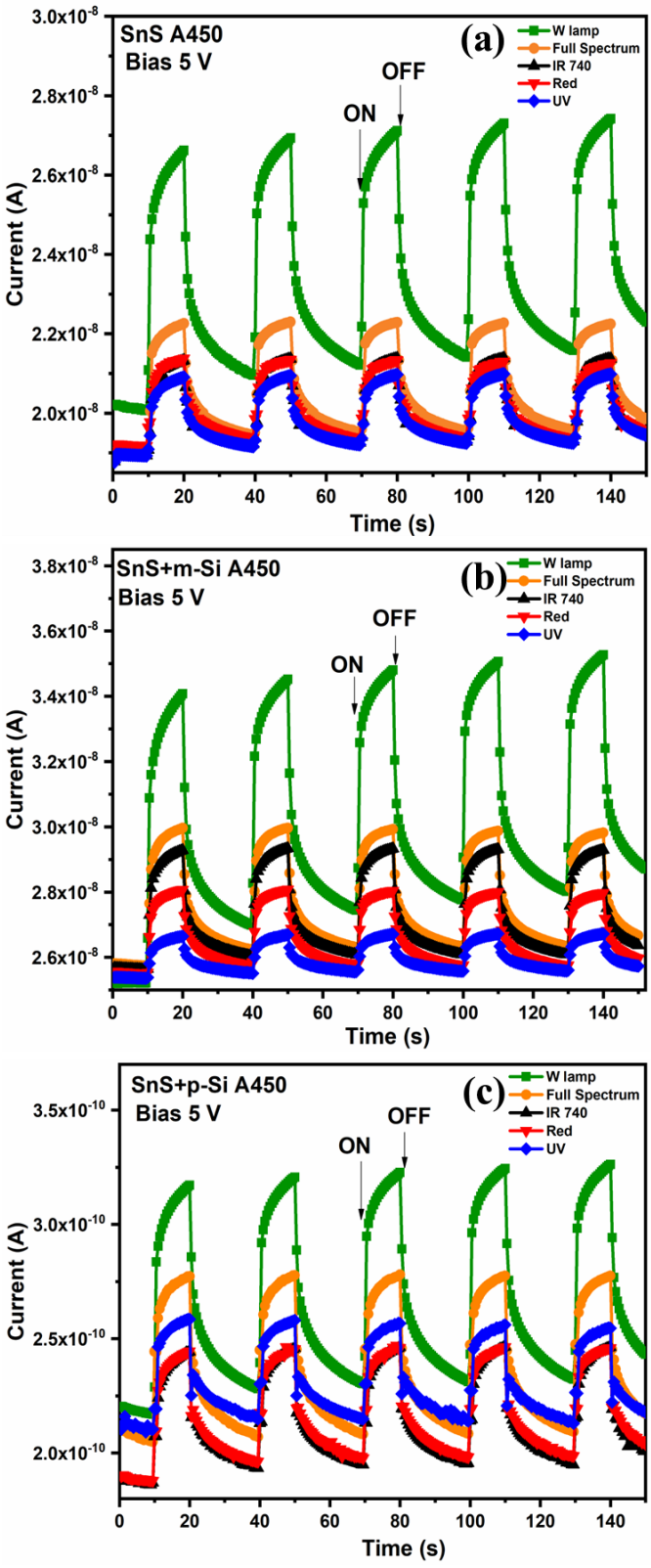


Fig. 3.22: Photoresponse behavior of the annealed (a) SnS (b) SnS:m-Si (c) SnS:p-Si films to illumination using W lamp and different wavelength of LEDs.

It was also noted how the sample responded to continuous-wave lasers of 532 and 785 nm wavelengths. For every measurement, a laser power with a 10 mW step size was employed. Fig. 3.23 (a, c) displays the photoresponse measurements using 532 and 785 nm lasers with different powers varying from 10 to 60 mW. It is believed that the repeatability and stability of photoresponse are key factors in determining if a photodetector is appropriate for a particular application. For cyclic illumination in the UV-Vis-NIR region at a 5 V bias voltage for the SnS based photodetectors, the photocurrent dynamic (current vs. time) curves are shown in Figs. 3.22 (a-c) and 3.23 (b, d). The current increases and decreases for all illuminating wavelengths over repeated cycles of ON/OFF illumination indicating strong repeatability [173]. Fig. 3.23 (b, d) displays cyclic photoresponse measurements taken at 60 mW laser power for 532 nm and at 50 mW for 785 nm laser. Although the overall trend of response for various light wavelengths appears comparable, it can be seen that the photocurrent response values for each sample varied. This can be attributable to the absorption spectra of the films. Better photocurrent values than SnS films can be seen in SnS:m-Si films. Despite having lower values than the other two films, SnS:p-Si responds to various illuminations quite effectively. Also, the response to IR LEDs and 785 nm continuous laser is lower than to UV LEDs or 532 nm laser. According to XRD, the response pattern may be connected to the sample's post-annealing crystalline modifications. A polycrystalline substance is made up of tiny crystallites joined by grain boundaries. An area in between the various orientations of nearby crystallites is represented by the atoms at the grain boundary. The atoms at the grain boundary are disorganized and have a large number of defects as a result of insufficient atomic bonding. As a result, trapping states are produced which can trap carriers and render them immobile. There are consequently fewer accessible free carriers for electrical conduction. When mobile carriers are trapped, electrically charged traps produce a potential energy 10 that limits the mobility of the charge carriers. A polycrystalline semiconductor would, in accordance with this theory, have lower mobility and carrier concentration than a monocrystalline material [208]. These observations are supported by our findings.

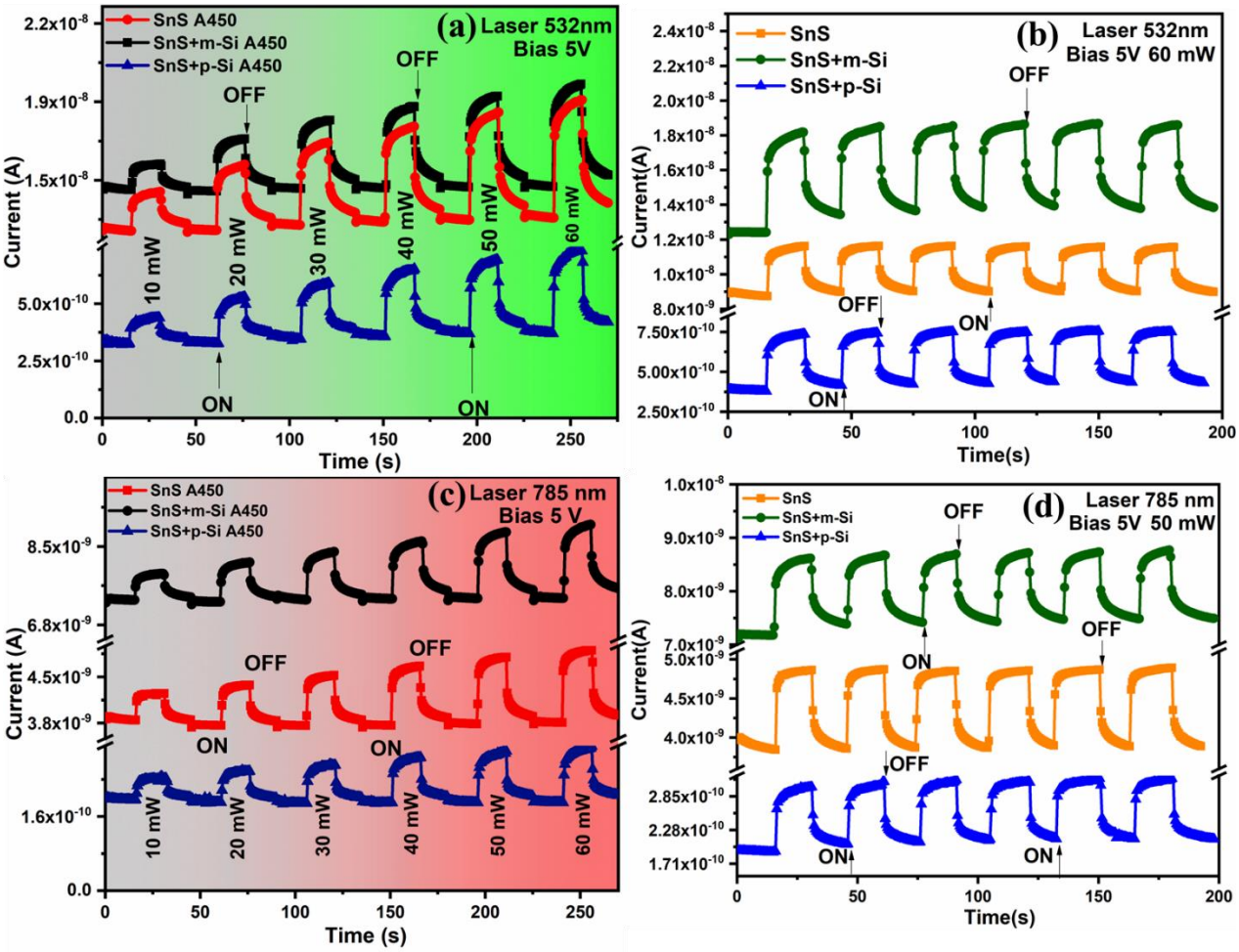


Fig. 3.23: Photoresponse of the annealed SnS and SnS:Si hybrid films to (a, c) varying powers of 532 nm and 785 nm (10-60 mW) continuous laser (b, d) 532 nm and 785 nm continuous laser operated at 60 mW and 50 mW respectively at an applied voltage of 5 V.

The photodetector parameters such as sensitivity, responsivity and detectivity were determined for each SnS film-based photodetector based on its response to 532 and 785 nm laser wavelengths in order to assess the performance of the device. Fig. 3.24 displays the sensitivity and responsivity characteristics plotted versus laser power density.

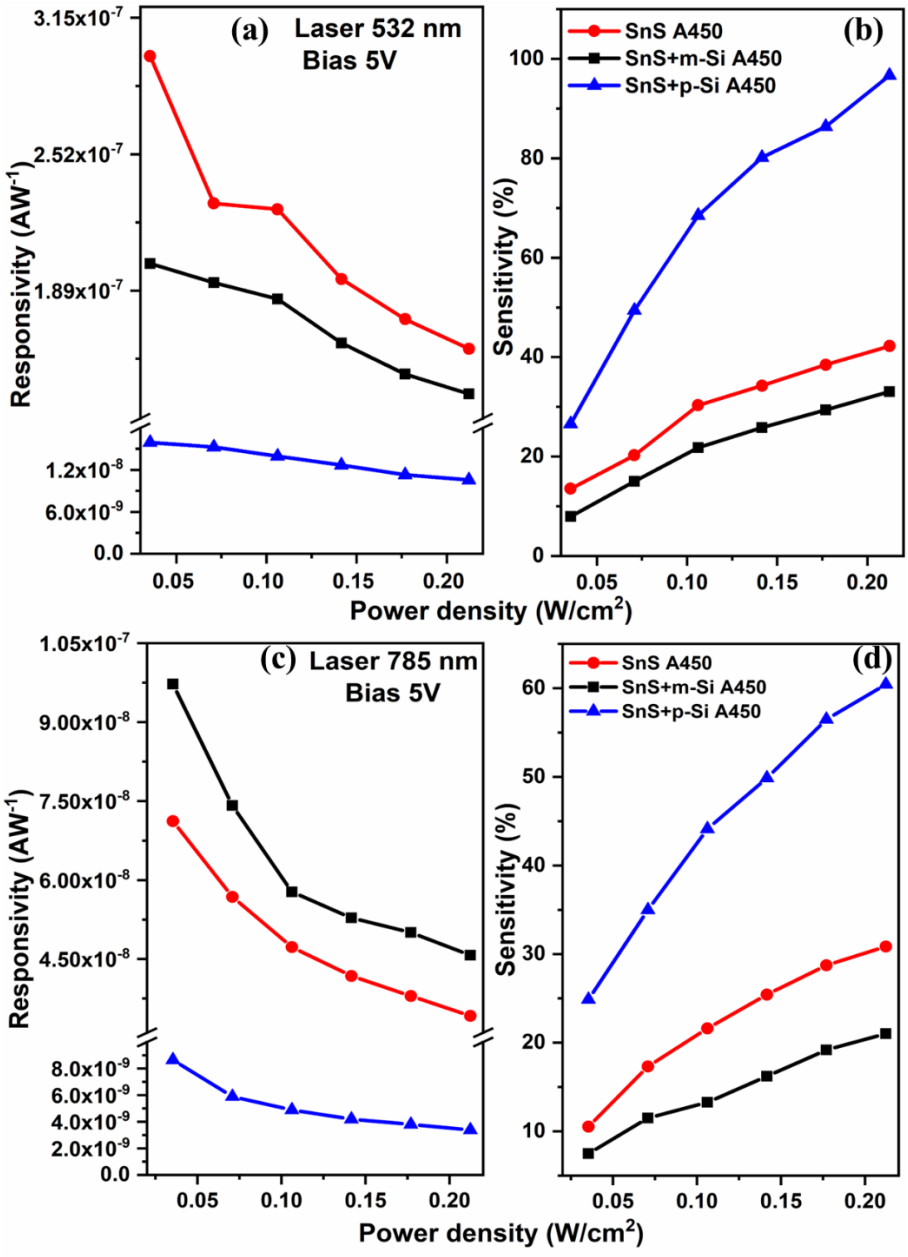


Fig. 3.24: Plot of sensitivity and responsivity vs laser power density for the films estimated using (a, b) 532 nm and (c, d) 785 nm continuous laser.

For SnS films annealed at 450 °C, with a power density of 0.03 W/cm^2, the peak detectivity is measured to be 8.14×10^5 cm Hz$^{1/2}$W^{-1} (Jones) for wavelengths around 785 nm and 1.88×10^6 Jones for 532 nm. Fig. 3.25 shows the detectivity plot for the films measured using continuous lasers with wavelengths of 785 and 532 nm. The detectivities of films range from 10^5 to 10^6 Jones. Similar to responsivity, detectivity values tend to decrease with increasing laser

power intensity. The observed trend in the R and D* parameter fluctuation with incident light power intensity may be caused by two causes. The first is that as illumination power increases, the density of hot carriers increases as well, which lowers the device's performance by accelerating scattering or recombination. The other is the Coulomb-repulsion effect, which functions similarly to a capacitor and inhibits carriers from being injected into SnS as a result of the material's rising excess charge density [163].

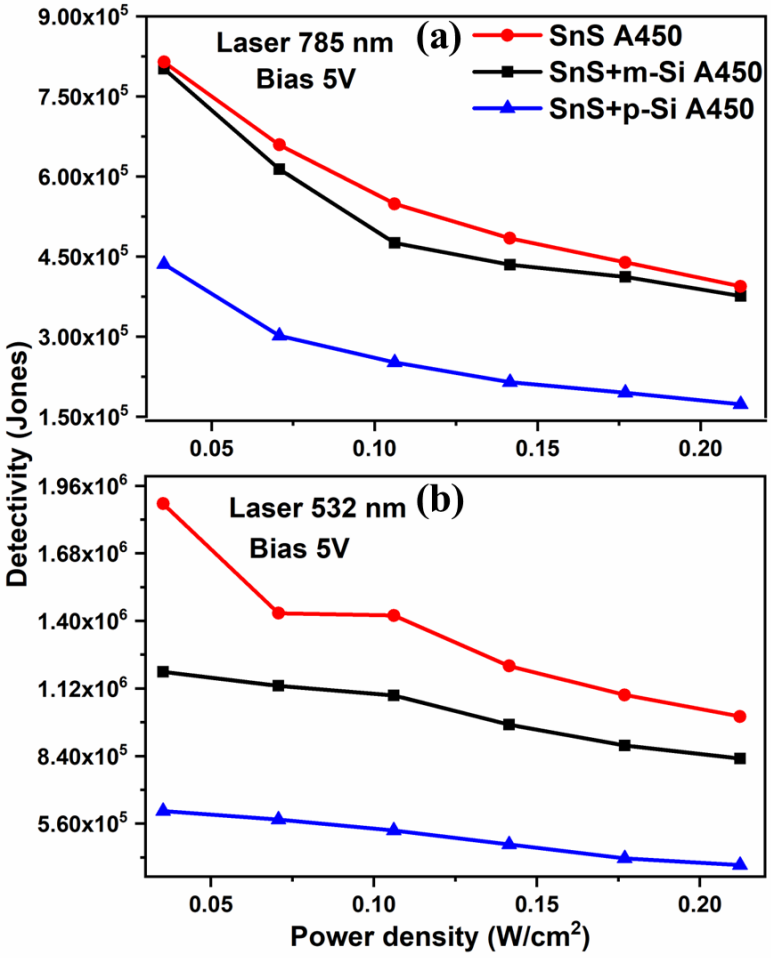


Fig. 3.25: Plot of detectivity vs laser power density for the films estimated using (a) 785 nm and (b) 532 nm continuous laser.

The rise time and decay time values corresponding to the samples' response to tungsten (W) lamp are shown in Table 3.3. The persistent photocurrent phenomenon, mostly caused by photogenerated electrons captured at crystal imperfections is what accounts for the delayed decay values in the films [170].

Table 3.3: The rise time and decay time calculated for the annealed SnS and SnS:Si hybrid films.

Sample	**Rise time (ms)**	**Decay Time (ms)**
W lamp		
SnS A450	430	806
SnS:m-Si A450	461	829
SnS:p-Si A450	452	818

The response of the films to laser diodes of 840, 980 and 1064 nm is shown in Fig. 3.26 which justifies the extended wavelength range of absorption in the near IR region. For the 1064 nm laser diode, an output power of 200 mW was used, compared to 100 mW for 840 and 980 nm. The fact that it matches the photon energy of the SnS bandgap [162,163,209] is the primary reason for detection up to the 840 nm wavelength range. We've already discussed how defects affect the absorption till 980 nm in the previous chapter. In this instance, the same holds true for detection up to 1064 nm. The prolonged wavelength detection of SnS may be due to the existence of sulfur or tin vacancies within the bandgap [164,165]. It is understood that SnS exhibits distinctive behaviors (anisotropic electrical characteristics and optical properties). These peculiar behaviors are principally caused by the poor lattice symmetry. Defects present within the material can also have a large impact on the electrical performance SnS [166]. These increased defect levels inside SnS are what lead to the extended wavelength detection in this material.

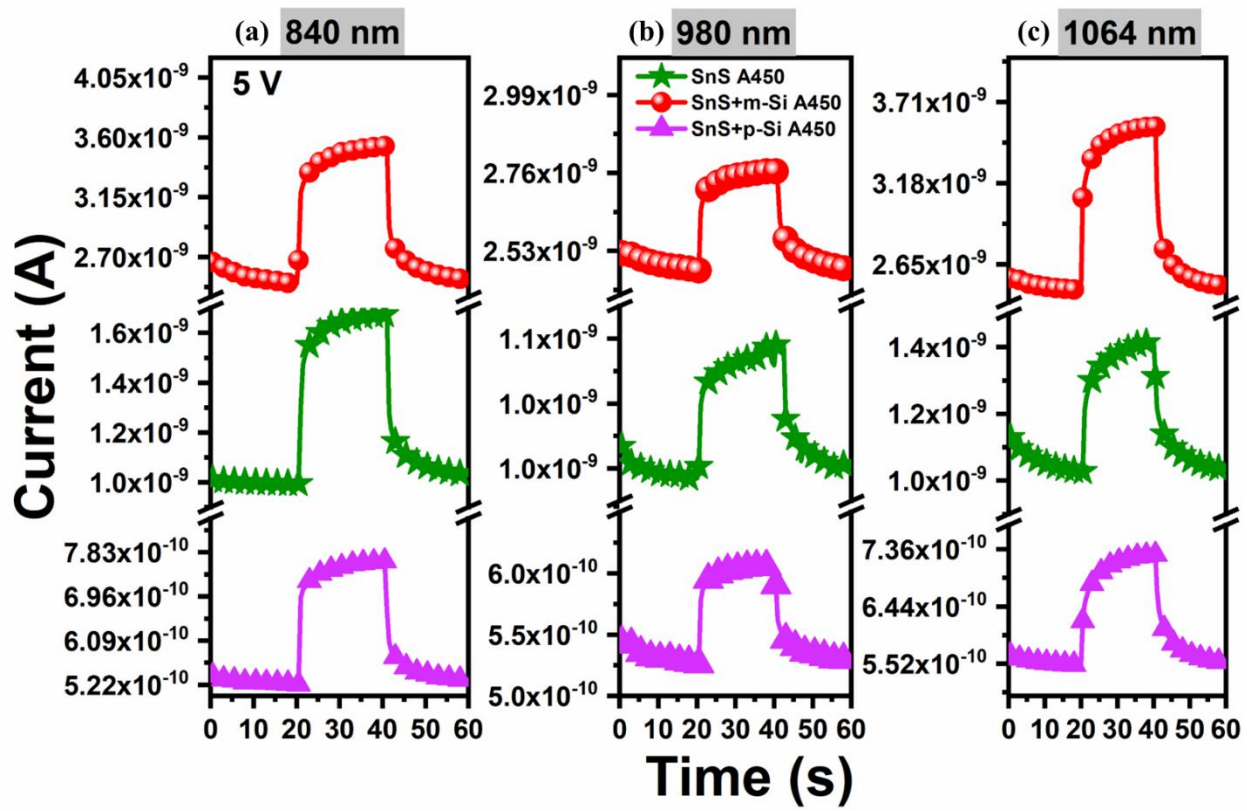


Fig. 3.26: Photoresponse of the annealed SnS and SnS:Si hybrid films to laser diodes of wavelength (a) 840 nm (f) 980 nm and (c) 1064 nm at an applied voltage of 5 V.

Without failing to mention, experiments to enhance the performance of SnS:Si hybrids were conducted by experimenting with various annealing conditions. The films were vacuum annealed at various temperatures, including 380 °C for 1 h. The films were also heated by rapid thermal processing (RTP) at 450 °C for 5, 6 and 7 minutes; at 500 °C for 1, 3 and 5 minutes and at 550 °C for 3 minutes. Fig. 3.27 (a, b) compares the absorbance curve for the SnS:m-Si films under each of the aforementioned conditions. In the same figure, separate plots for absorbance, % transmittance and % reflectance of SnS:m-Si and SnS:p-Si films are also provided. The impact of annealing or RTP treatments in these films was not readily apparent in the optical or photoresponse characteristics therefore further research on them was omitted. In the figure 'MD' refers to the multideposition. These samples were also prepared by the same methodology explained for the other films discussed in the chapter.

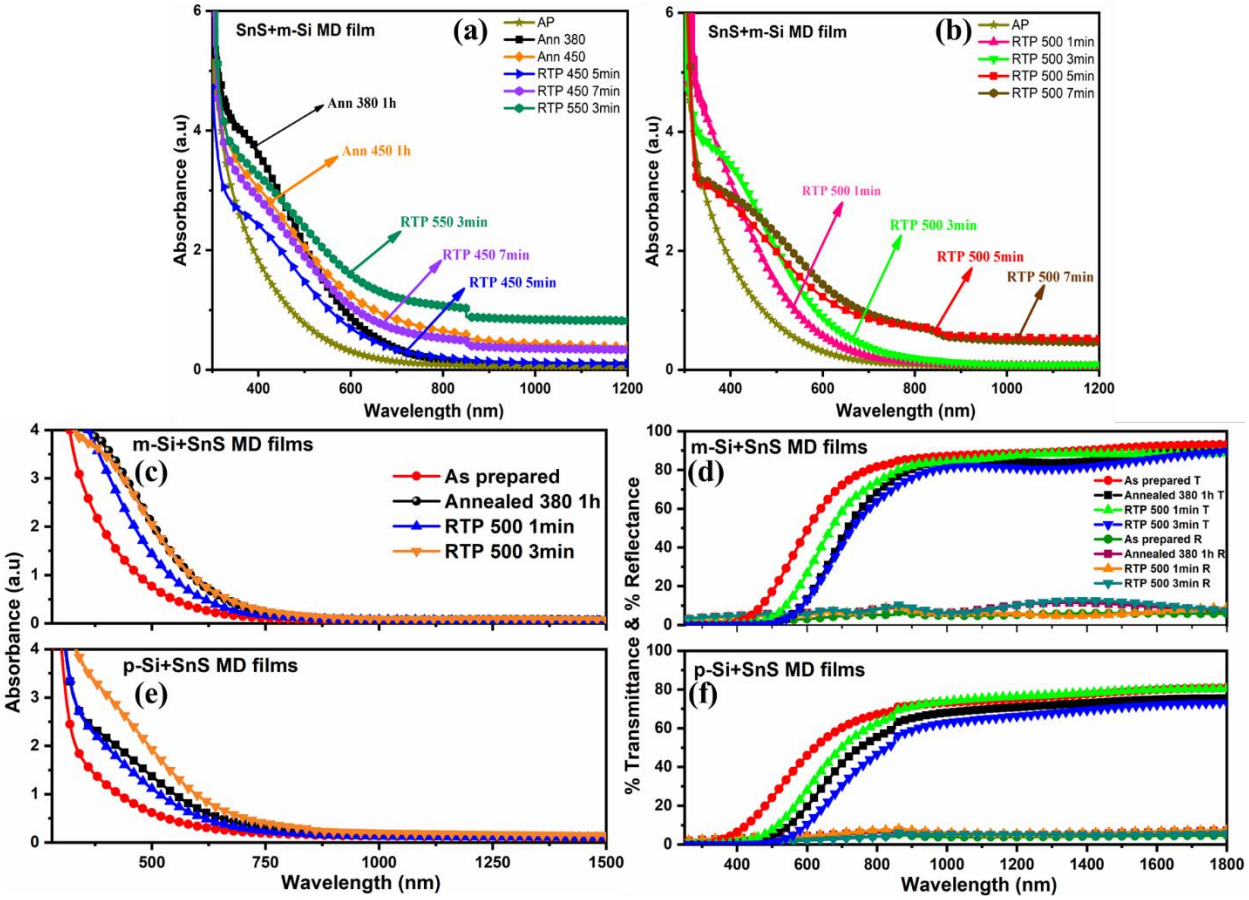


Fig. 3.27: (a, b) Absorbance plot of SnS:m-Si films at different annealing and RTP conditions; Absorption, % Transmittance and % Reflectance of (c, d) SnS:m-Si and (e, f) SnS:p-Si films.

In comparison to the results of previous work on SnS synthesized using 532 nm laser (provided in the preceding chapter), a completely different synthesis route was adopted for the nanocolloid synthesis. These findings can be used to support a part of the thesis work's hypothesis, which states that the optical, electrical and electronic properties of the same material vary depending on the fabrication methods. Previously, PLAL was employed, and in this work, PLFL. In this instance, the average particle size obtained was 22 nm, compared to 8 nm in the earlier study. The bandgap and crystallinity values of the films in their as-prepared and annealed states clearly changed. In the films created by combining spin-coating with PLFL, the bandgap values were lower (2.02 eV for as-prepared and 1.64 eV for annealing at 450 °C) than those prepared by PLAL (2.7 eV for as-prepared and 1.9 eV for annealing at 450 °C). The responsivity, sensitivity and detectivity values of the photodetector characteristics also demonstrated a change. Due to the low concentration of silicon NPs incorporated, we were unable to significantly alter the

photodetector properties in the case of the SnS:Si hybrids we synthesized. Further investigations with more concentration of silicon can be tried out as future work to enhance the optical and electrical properties of the hybrid film and improve the photocurrent value.

3.3.8 Photocatalysis

From literature, SnS nanostructures show good photocatalytic capabilities but are hardly explored and this motivated us to study the photocatalytic activity of the fabricated films. The photodegradation of methylene blue (MB) under visible light irradiation was used to investigate the photocatalytic properties. The most well-known and often used photocatalyst is TiO_2 due to its strong photocatalytic activity, chemical and photochemical stability and affordability [210]. TiO_2, on the other hand, has a large bandgap of 3.2 eV which allows it to absorb and use ultraviolet (UV) light, which makes up only a small portion (4%) of solar radiation. Traditional methods like doping or combining with another semiconductor with a narrow bandgap are used to adjust the bandgap of TiO_2 [211,212]. However, activity is still at a modest level, and these solutions have issues with stability or applicability. Therefore, the goal of contemporary photocatalysis research is to create affordable photocatalysts that are visible-light active and capable of absorbing the majority (about 43%) of the solar radiation spectrum. Utilizing the free and inexhaustible solar radiation that is naturally available is of interest.

In this study, the photocatalytic effects of the samples, dye decays of thin films of SnS and SnS:Si hybrids were compared. The spin-coated thin films were attached to the side of a beaker containing methylene blue solution (20 mg/L). In order to give the SnS film time to interact with the entire solution and reach the adsorption/desorption equilibrium, the solution was kept under the dark for 30 minutes while the blue dye solution was stirred in ambient conditions. The visible light source for the photocatalysis was a 200W solar simulator. The overall irradiation time was 120 minutes. For all the fabricated thin films, photocatalytic investigations were carried out in the same way. In Fig. 3.28 and Fig. 3.29, dye decay absorption studies for cyclic activity for the as-prepared and annealed films are given. StellarNet's UV-Vis spectrometer was used to measure the absorbance for photocatalytic investigations. The SpectraWiz® Software Suite was used to record the absorbance.

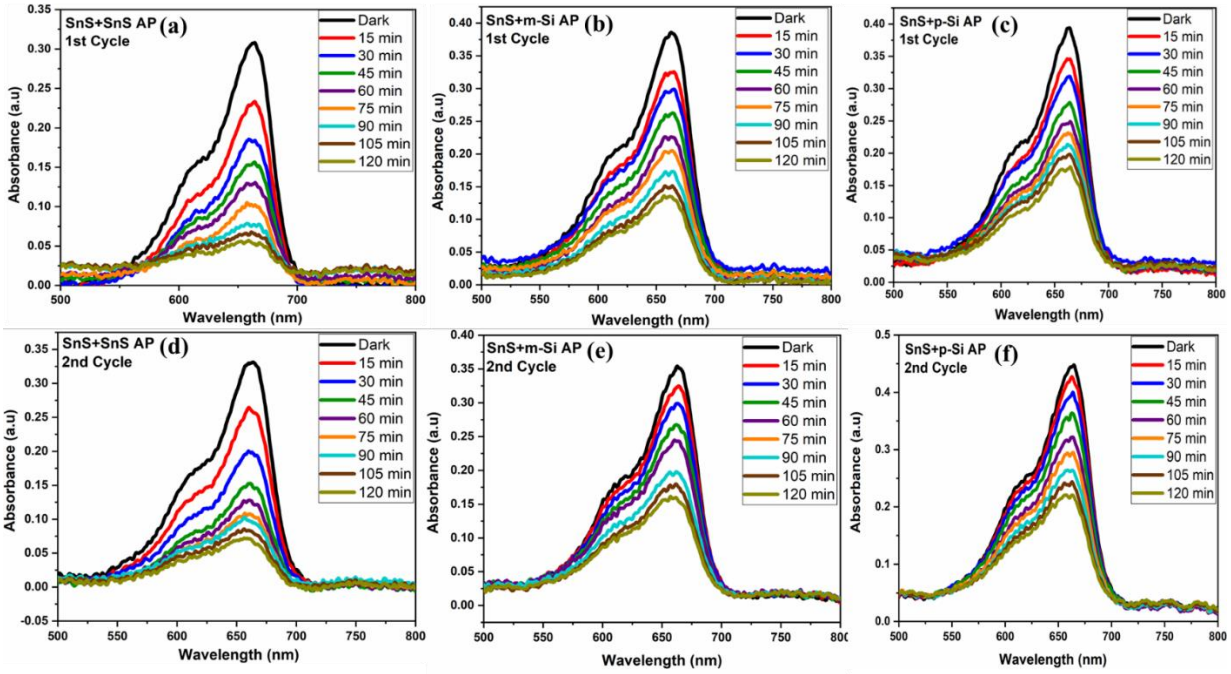


Fig. 3.28: Dye decay absorption studies of the as-prepared SnS and SnS:Si hybrid films (two cycles).

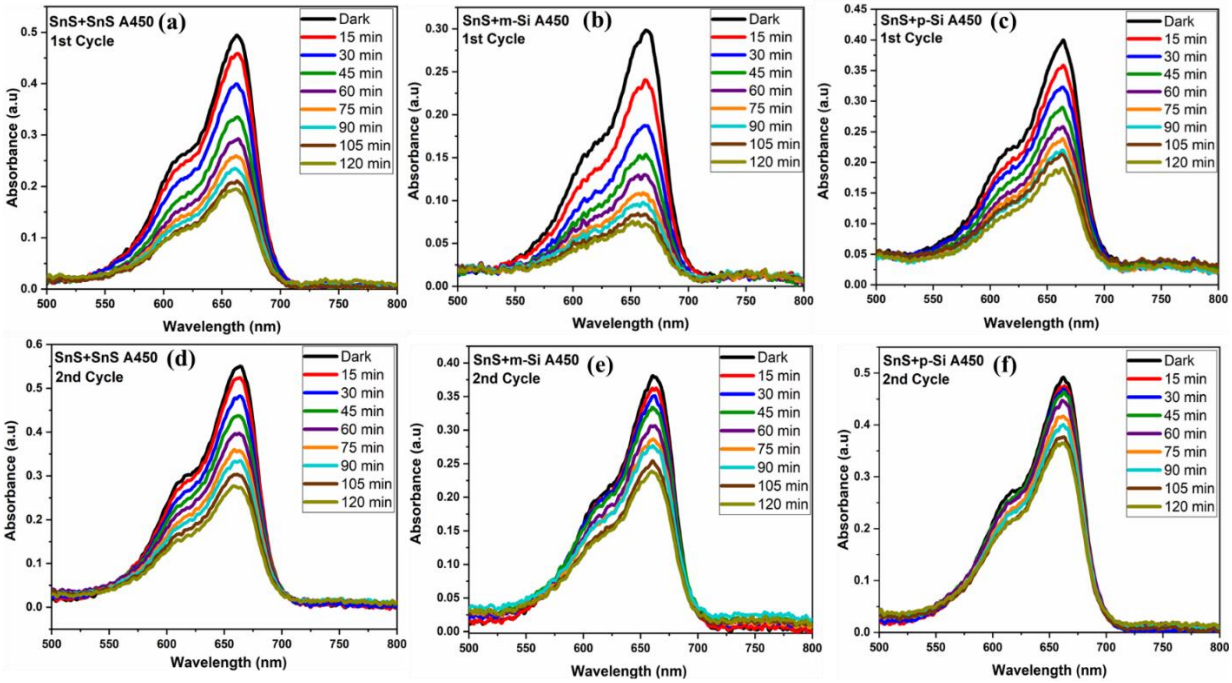


Fig. 3.29: Dye decay absorption studies of the annealed SnS and SnS:Si hybrid films (two cycles).

The measurement of absorption can be used to determine the dye's maximum peak. For methylene blue, it is approximately 664 nm. The peak at 664 nm loses intensity as the photocatalytic reaction continues.

The decay percentage was calculated using the equation below [213]:

$$Decay\ percentage = \frac{C_0 - C_t}{C_0} \times 100 \qquad (3.1)$$

In the equation above, C_0 stands for the beginning at the start of the experiment (in terms of intensity values, the value on the y-axis corresponds to 664 nm) and C_t stands for the concentration at the given time, t. This equation results in the plot given in Fig. 3.30 (a, b). From the graph we could understand that the photocatalytic activity is in the order SnS AP>SnS:m-Si A450>SnS:m-Si AP> SnS A450>SnS:p-Si AP>SnS:p-Si A450 when the decay studies were done for the first cycle. For the second cycle, the order was SnS AP>SnS:m-Si AP>SnS:p-Si AP> SnS A450>SnS:m-Si A450>SnS:p-Si A450. In both the cycles the best performance was observed for SnS AP films and the lowest for SnS:p-Si A450 sample.

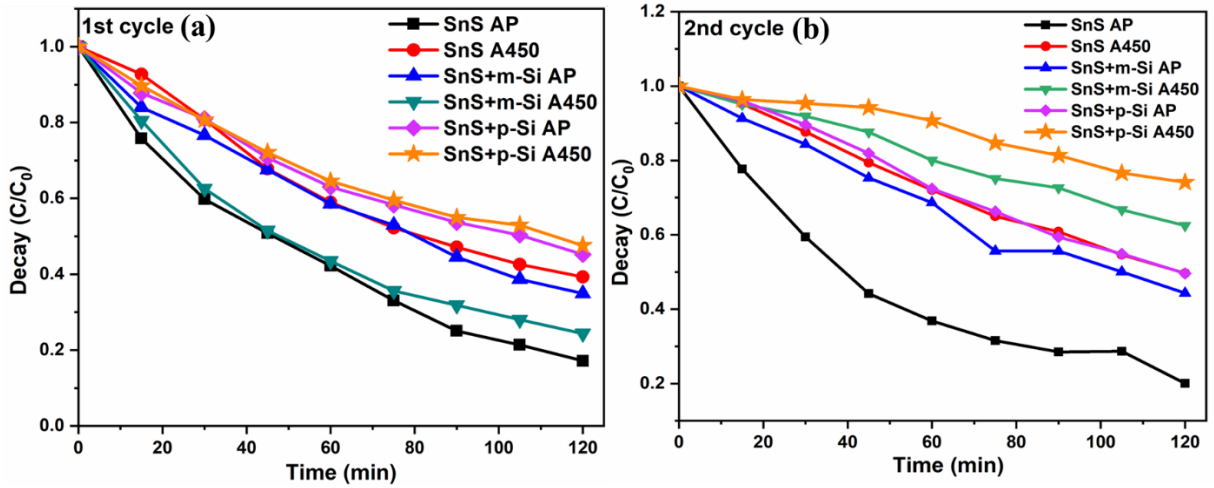


Fig. 3.30: Photocatalytic results of SnS and SnS:Si hybrid films (as-prepared and annealed).

The schematic representation of the mechanism of dye-degradation is given in Fig. 3.31 (a). For SnS films, an electron-hole pair is produced when SnS absorbs a photon during the photocatalytic event, moving it from the valence band to the vacant conduction band. The unbound electrons in SnS's CB interact with O_2 to form superoxide radicals ($^{\bullet}O_2^-$). The hydroxyl radicals ($^{\bullet}OH$) are created when the holes (h^+) react with OH and H_2O. These released active radicals

interact with the ionized dye molecules to transform them into less dangerous substances like a new class of smaller hydrocarbons, water, carbon dioxide, and mineral acids (NO_3^-, SO_4^{2-}, etc.). In this phase, the MB dye molecules can also be actively broken down by strong oxidizing holes (h+) [214,215]. The mechanism is described in the following equations.

$$SnS/Si + h\gamma = e^- + h^+ \quad (3.2)$$

$$h^+ + H_2O \rightarrow H^+ + OH^\bullet \quad (3.3)$$

$$h^+ + OH^- \rightarrow OH^\bullet \quad (3.4)$$

$$e^- + O_2 \rightarrow {O_2}^{-\bullet} \quad (3.5)$$

$$2e^- + O_2 + 2H^+ \rightarrow H_2O_2 \quad (3.6)$$

$$e^- + H_2O_2 \rightarrow OH^\bullet + OH^- \quad (3.7)$$

$$Organic\ pollutants + OH^\bullet + O_2 = CO_2 + H_2O + other\ degradation\ forms \quad (3.8)$$

Both SnS and Si function as light-absorbing materials in the case of films containing Si, producing charge carriers. The CB electrons in SnS have a tendency to shift to the CB of Si due to band alignment. The VB of SnS receives holes from the VB of Si in a manner similar to this. Photoreduction and photooxidation take place in respect to electrons and holes, as per the mechanism described above for SnS [216]. However, the repulsion from the electrons already existing in Si will impede the continuing transfer of electrons from SnS. The electrons in SnS are also prevented from migrating to Si by the electrostatic interaction between the holes and electrons in SnS. Due to the difficulty in achieving the projected charge transfer, prolonged light absorption, delayed charge recombination and other factors, photocatalytic activity in Si integrated films has degraded [217,218].

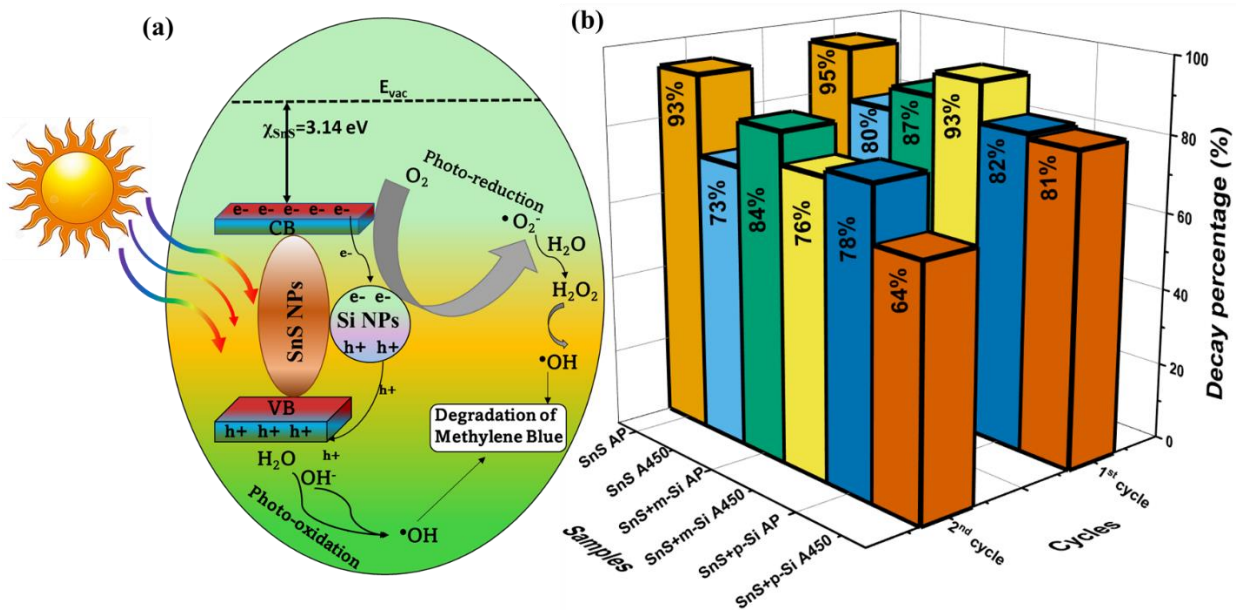


Fig. 3.31: (a) Schematic representation of the mechanism of photocatalysis (b) Dye decay vs time plot for cyclic photocatalysis of SnS and SnS:Si hybrid films.

A comparison of the decay percentage for cyclic photocatalytic experiments of various samples is shown in Fig. 3.31 (b). The photodegradation efficiencies of the as-prepared SnS films over MB dye were found to be 95% and 93% for cyclic studies with an irradiation period of 120 minutes. The figure shows that the as-prepared samples practically maintain the same decay percentage even after the second cycle, but the decay rate for the annealed samples rapidly decreases. This might be as a result of the sample surfaces compensating for oxygen vacancies brought on by exposure to the dye solution. The presence of SnO_2 in the films was discussed previously as observed from XPS and XRD and upon annealing this might have reduced, which might be the reason for the decreased activity of SnS annealed films compared to the as-prepared films. m-Si films outperform polycrystalline Si when it comes to films with Si incorporation. This could be attributed to the greater crystalline size and the smaller bandgap seen in m-Si films. By minimizing the recombination of photogenerated charge carriers, larger crystallites contain fewer defects and lesser grain borders, which improves the quantum efficiency of the nanoparticles [219]. Other more prevalent semiconductors, including gallium arsenide or silicon, are frequently unsuitable for robust photocatalytic systems due to their severe photoelectrochemical breakdown [220]. For this reason, pure SnS films exhibit better photocatalytic activity than films with silicon.

Fig. 3.32 and Fig. 3.33 show the SEM images of the films in their as-prepared and annealed states both before and after catalysis. No discernible morphological alterations were visible in the SEM images. The surface of the thin films includes more active oxygen, according to the structural and chemical analyses done with XRD and XPS. The porous surface morphology of the as-prepared films may have been influenced by the spherical morphologies of SnS nanoparticles, which were revealed through TEM and SEM analyses. The improvement in the visible light photocatalytic activity in this work may be attributed to the increased surface oxygen concentration and the surface morphology for nanostructured SnS thin films. The enhanced photocatalytic activity of the films as-prepared may be due to their higher surface roughness in morphology. In other words, the drop in the photocatalytic activity may be due to the roughness reduction brought on by heat treatment [221]. The results support the potential application of SnS and its hybrids in the photocatalytic oxidation of industrial colors under natural light and the accompanying cost-effective treatment of textile industry waste water [219].

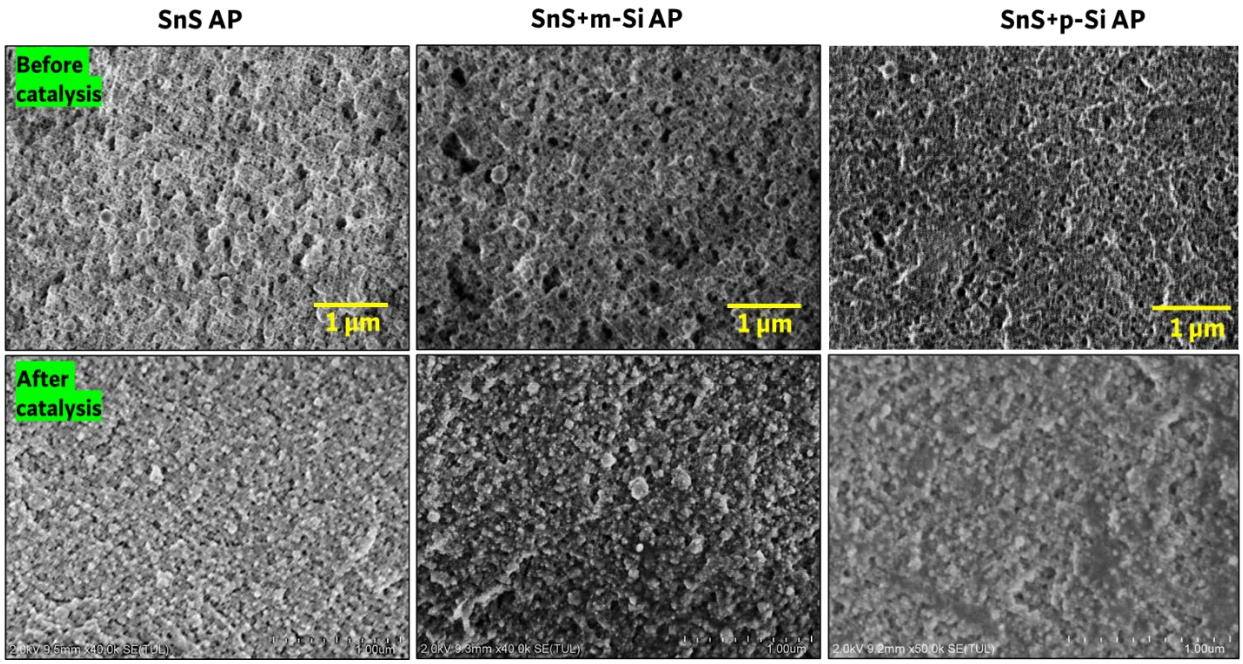


Fig. 3.32: SEM images of the as-prepared SnS and SnS:Si hybrid films before and after catalysis.

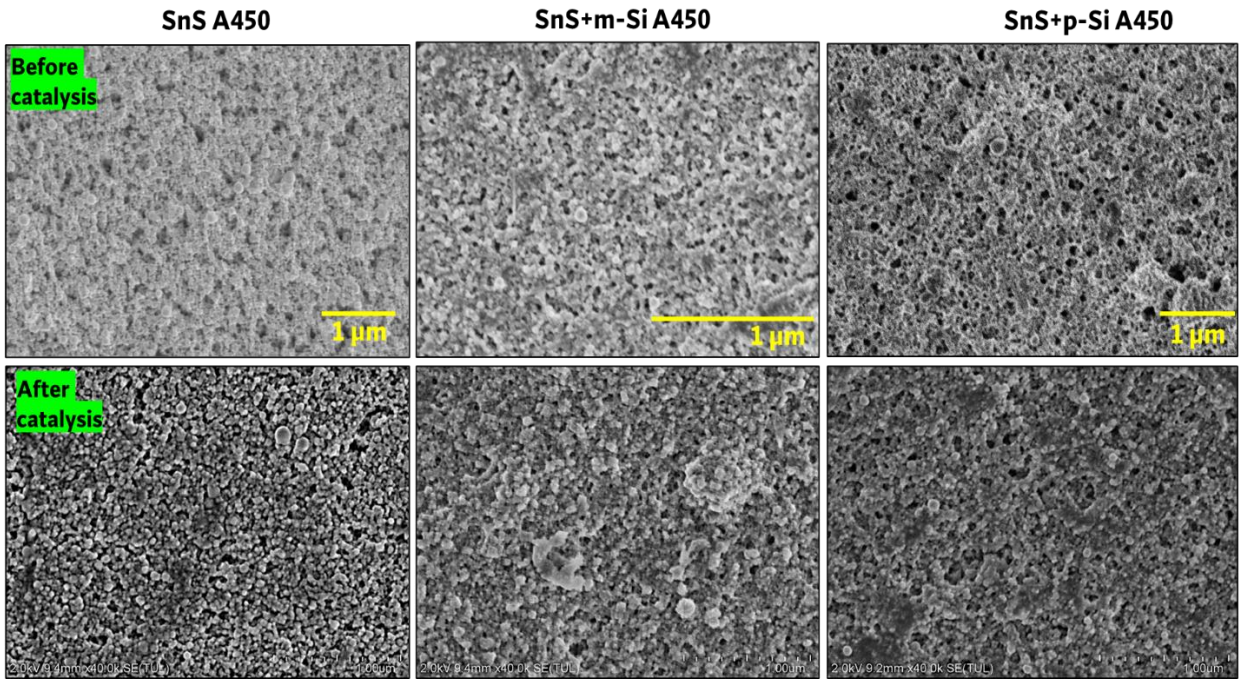


Fig. 3.33: SEM images of the annealed SnS and SnS:Si hybrid films before and after catalysis.

3.4 Conclusions

- First report on Si nanoparticle incorporated hybrid for photodetection.
- The hybrid thin films of SnS:Si were fabricated by spin-coating method completely using the colloidal NPs of SnS and Si.
- Two completely different laser synthesis and processing in liquid techniques were employed: pulsed laser fragmentation in liquid (PLFL) and pulsed laser ablation in liquid (PLAL) for the synthesis of NPs.
- The NPs exhibited spherical morphologies and Si NPs were too small in size (~4-5 nm) in comparison to SnS NPs (~22 nm).
- Post-deposition annealing improved the material properties of the hybrid films.
- The bandgap of monocrystalline incorporated Si was less than SnS and polycrystalline Si incorporated films. This might be due to the improvement in crystallinity upon annealing as observed from XRD.
- Responsivity, sensitivity and detectivity values were also calculated.

Photodetector with ultra-short response/recovery times in the range of 400-800 milliseconds.

- The annealed films exhibited detection of up to 1064 nm.
- All the samples (SnS and hybrids) exhibited good photocatalytic activity and the as-prepared SnS thin film sample showed the greatest photocatalytic performance for up to two consecutive cycles.
- The photocatalytic performance was mainly promoted due to the existence of SnO_2 on the films and the superficial roughness of the as-prepared films.
- The results suggest that SnS and SnS:Si hybrids can be used for photodetection as well as photocatalytic applications.

Chapter 4

Color insensitive UV-Vis-NIR photodetection using SnS:Graphene hybrid thin films

4.1 Introduction

As two dimensional (2D) nanomaterials comprise nanostructures with exposed surfaces, graphene, one of the first materials with a fully 2D nature, has garnered attention for extensive research. Particularly, 2D layered semiconductors have attracted interest because of their distinctive electrical and optoelectronic properties, which are the result of their noticeable bandgaps. A honeycomb lattice containing single layers of carbon atoms makes up graphene [222]. Since it is a gapless/zero bandgap 2D material, it can absorb light from ultraviolet to terahertz and has great carrier mobility and strong electrical conductivity [223]. However, the major challenge is the limited responsivity of graphene photodetectors, which only absorbs 2.3% of the incident light in each layer [224]. Semiconductor nanoparticles can be used to reduce this complexity since they are more effective at absorbing incident light than graphene [225]. Graphene has other benefits that make it suited for advanced applications, including its atomic thinness, specific surface area, transparency, thermal conductivity, charge density, strength, flexibility and durability [226]. To produce photoconductive-based devices that are fundamentally different from those of conventional arrangements, we used the notion of coupling 2D materials like graphene with highly absorbent materials like SnS [227]. This chapter describes in detail how to create hybrid nanostructures effectively coupling graphene and tin sulfide NPs that can benefit from both the capabilities of graphene and SnS to enhance device features.

The experimental path used to synthesize the SnS nanocolloids in this work makes it unique. This is the first report on SnS NPs synthesized by pulsed laser irradiation in liquid (PLIL). For fragmenting SnS powder to produce nanoparticles, pulsed laser irradiation—more specifically, pulsed laser fragmentation in liquid (PLFL) technique—was employed. Photodetection with SnS NPs-graphene has not been studied extensively and the development of this hybrid is still in its early stages. We explore hybrid thin films of graphene-incorporated SnS as wavelength-independent photodetectors operating in the broadband (till 980 nm) range of wavelengths in this chapter. Comparative research on the impact of adding graphene to SnS versus SnS NPs alone on

the optoelectronic properties is also presented. Results of this chapter of the thesis has been published [191].

4.2 Nanocolloid synthesis and SnS:Graphene photodetector fabrication

SnS nanocolloids were synthesized using the PLIL method. 100 mg of SnS powder (99.9% purity, Heepani tools store, China) was dispersed in 20 mL of isopropyl alcohol (IPA; Fermont; analytical grade, 99.9% purity) in a 60 mL glass container. The laser irradiation setup was in a horizontal configuration. Using a pulsed Nd: YAG laser (Model LQ 929, Solar laser system) with a pulse width of 10 ns and a frequency of 10 Hz, this solution was constantly exposed to radiation for 10 minutes while being stirred with a magnetic pellet. No lenses were used in the experiment. An energy meter was used to measure the output energy, which was 350 mJ. (Thorlabs PM100D with an ES245C pyroelectric energy sensor) and the laser fluence was calculated as 0.89 J/cm^2 considering the Gaussian beam profile.

To determine the ideal condition for SnS:graphene films, three sets of experimental routes were tried. In the first set of experiments, 10 mg of graphene powder (> 95% purity, CAS: 1034343-98-0, Graphene composite, Hungary) was dispersed in 20 mL of IPA followed by 10 minutes of ultrasonication. This solution was laser irradiated for different times varying from 3 minutes to 45 minutes. The laser pulse energy used was 342 mJ and the fluence was calculated as 0.87 J/cm^2. In Fig.4.1(a), the images of graphene colloid for various ablation times are provided. After 25 minutes of irradiation, the absorbance values were saturated, and this condition was chosen to continue with the experiment based on the absorbance curves (which are also shown in Fig. 4.1 (b)). The graphene nanocolloid prepared by 25 min irradiation is marked as G25 throughout the figures and discussion. SnS nanocolloids which was synthesized by PLIL using the aforementioned condition were mixed into this graphene colloid followed by ultrasonication. The colloid is marked as S+G25 (SnS nanocolloid+graphene nanocolloid). Using a compact spin coater, this colloid was spin-coated onto glass substrates at 1000 rpm spin rate, 100 rpm/s acceleration speed and 30 s spin time (CY Scientific Instruments China, Model CY-SP4). Under the same conditions, SnS nanocolloids were spin-coated on glass substrates as a reference sample as well. The films were annealed at 350 and 450 ℃ for 20 minutes. The scheme is shown as Set I in Fig. 4.2. The same experiment was attempted in dimethyl formamide (DMF) as well, however due to the solvent's low viscosity and high boiling point, the solution flung off during spin-coating

and required a lengthy evaporation period, squandering a lot of colloid and producing films with a very low thickness. As a result, the experiments were all carried out in IPA.

In the subsequent series of trials, to the graphene colloid (G25), 100 mg of SnS powder was added and ultrasonicated. This nanocolloid of graphene with SnS powder (marked as SG25) was laser irradiated for 10 minutes while being constantly stirred using a magnetic pellet. For the fabrication of the films, the nanocolloids were spin-coated and then annealed at 400 ℃ for 20 minutes. The methodology is presented as Set II in Fig. 4.2.

The final set of experiments involved dispersing 10 mg of graphene powder directly into a stable SnS colloid that had been laser-irradiated to produce a dark brown color nanocolloid. The solution was then thoroughly ultrasonicated for 15 minutes. Spin-coating of this SnS:graphene colloid onto glass substrates (same parameters as mentioned above) was done. Additionally, SnS films without graphene were also fabricated. This made it easier to understand how the characteristics of films with graphene integrated SnS improved. All the films underwent vacuum annealing (20 minutes) at 350 and 450 °C. The schematic is shown in Fig. 4.2 (Set III). For each set of studies, multiple depositions (amount to 40 mL nanocolloid) were performed in order to produce thicker films. Silver (Ag) paint was used to make contact electrodes on the films that were 5 mm long and 5 mm apart for photoresponse measurements. As the ideal circumstance for synthesis, the schematic representation of the experimental approach described in Set III (Fig. 4.2) was chosen. The graphs and discussion of this chapter refer to the films prepared utilizing graphene distributed in SnS nanocolloids as GPS films.

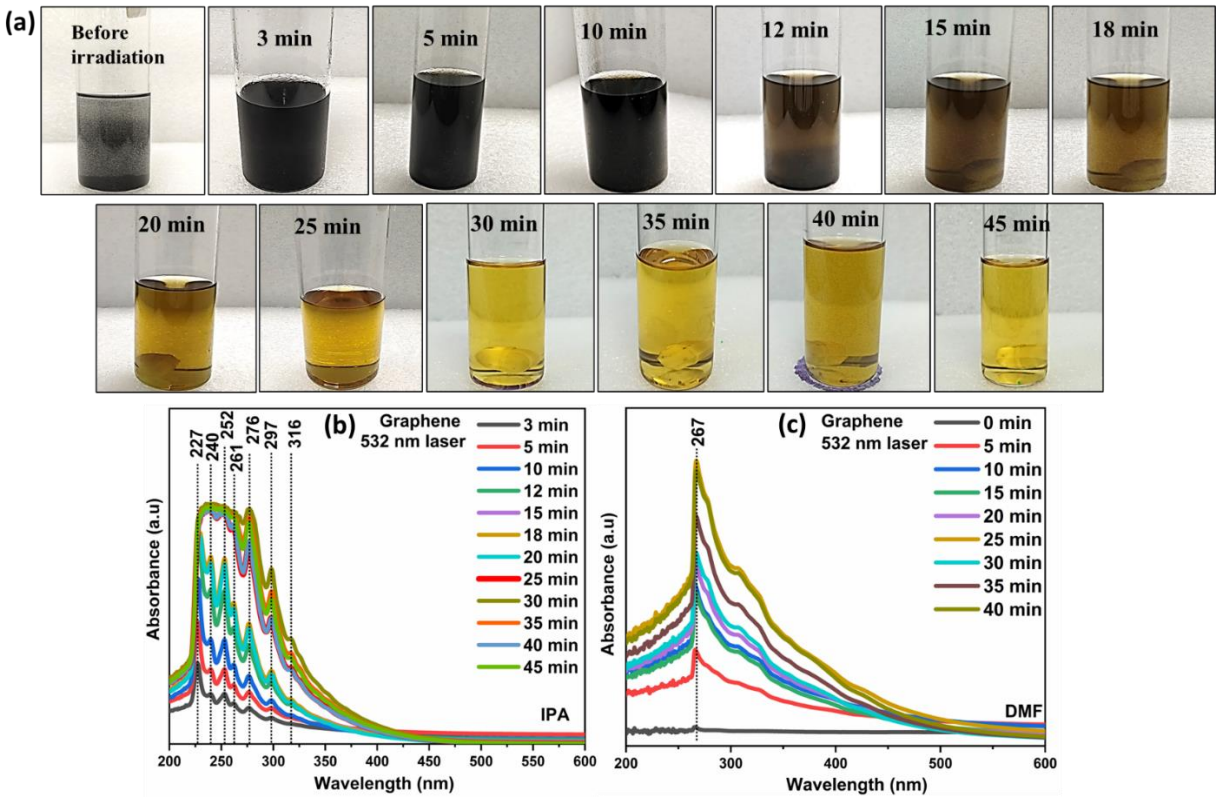
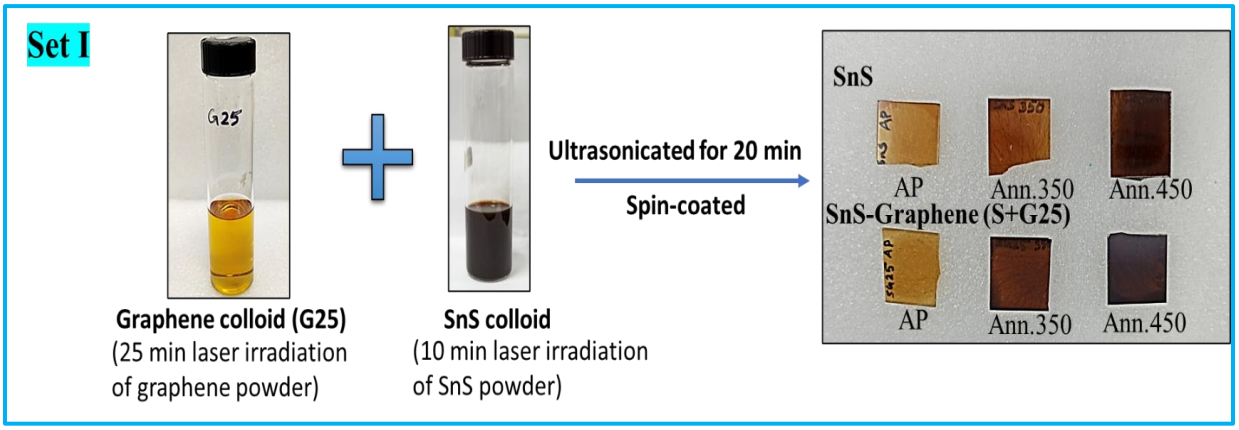


Fig. 4.1: (a) Nanocolloids of graphene synthesized by laser irradiating graphene powder at different ablation times. Absorbance plot of graphene nanocolloids in (b) IPA and (c) DMF.



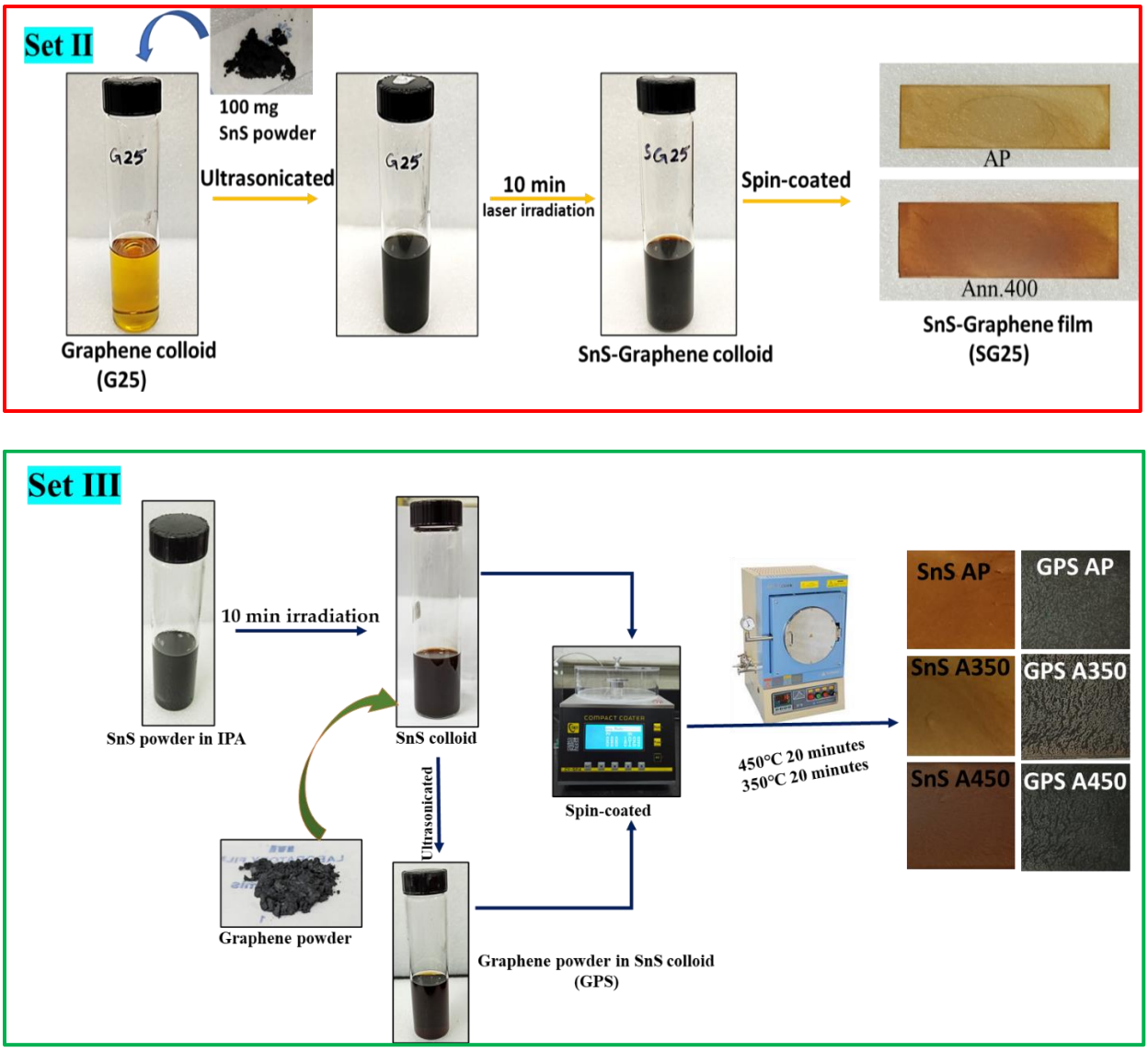


Fig. 4.2: Different experimental paths for the synthesis of SnS:graphene hybrid films.

4.3 Results and Discussion

4.3.1 Optical Studies

The absorption spectra of the graphene nanocolloids in IPA and DMF obtained after laser irradiation are presented in Fig. 4.1 (b, c). Since the detected bands closely resemble those of polyynes, the bands seen in the UV-Vis spectra of graphene in IPA (Fig. 4.1 (b)) irradiated at various times can be attributed to a combination of different hydrogen-capped polyynes. According to published research, the electronic absorption spectrum of a polyyne, C_nH_2, with an even number of n, has a substantial absorption band as well as well-separated vibrational bands at shorter wavelengths [228,229]. We conclude that the graphene colloid synthesized by laser

irradiation in IPA contains polyynes with n=8, 10, 12, 14 and 16, relying on a close comparison of the wavelengths of the bands with those of polyynes described in literature [230]. This is due to the interaction of C-based material (graphene) with the solvent (especially alcohols). In the case of DMF (Fig. 4.1 (b)), the peak around 267 cm^{-1} can be assigned to the π-π^* transition of C=C [231]. The modifications in graphene by laser irradiation in this case did not have any visible effect in improving the morphology, electrical or optoelectronic properties of the SnS films and hence further investigations were based on Set III of the experimental routes. However, this chapter also covers the morphological and electrical properties of the graphene colloids and their films.

Fig. 4.3 (a) displays the absorbance of the SnS colloid and the SnS colloid that has been combined with graphene (GPS) [Set III]. The absorption spectra of the as-prepared and annealed SnS and GPS films are displayed in Fig. 4.3 (b). The absorbance across the full UV-Vis-NIR range in the examined spectral range is improved by the incorporation of graphene into SnS films. GPS films had a lower % transmittance than SnS films. Additionally, as the annealing temperature increases, the transmittance decreases. This is supported by the absorption spectra, which also show an increase in the absorption [182]. Also included in Fig. 4.3 (d) are the percentage transmittance (%T) and reflectance (%R) values of the films. With the help of the Tauc plot (Fig. 4.3 (c)), the optical bandgap of the films was assessed (Eq. 2.2). With the inclusion of graphene, the bandgap of as-prepared SnS films was fine-tuned, changing from 2.5 to 2.19 eV and from 2.13, 2.03 eV to 1.89 and 1.54 eV for films annealed at 350 and 450 °C, respectively. The Tauc plot shows a transition of a direct type (n=1/2). The reported bandgap for bulk SnS is between 1.0 and 1.3 eV, higher values for these films may be the result of size confinement effects in the nano realm. This may have been influenced by the small size of the particles and their morphologies during their synthesis [232]. Previous studies have shown that SnS nanocolloids made in IPA by PLAL have an optical bandgap of about 1.7 eV and SnS films have an optical bandgap of 1.9–2.1 eV [88,233]. There are many studies that report bandgap of SnS in the 1.3–2.0 eV range [149]. There may be remnants of SnO_2 (E_g = 2.4 eV) in SnS films, which would also explain their greater bandgap value [182], which will be explained in the subsequent discussion on XPS and XRD results. The bandgap engineering seen in the SnS films with the addition of graphene results in the basic absorption edge moving to a longer wavelength (red-shift) due to the synergistic electronic interactions between graphene and SnS. For graphene-TiO_2 nanocomposites, this kind of interaction has been seen, resulting in a bandgap reduction from 3.06 eV to 2.2 eV [234]. The

optical properties (absorption shift) of the films are also influenced by the annealing temperature. As a result of the recrystallization process, it has been observed that bandgap values decreased at higher annealing temperatures [235]. The bandgaps obtained for these nanocomposites enable high absorption coefficients, making them advantageous for optoelectronic applications and appropriate for charge carrier generation [236].

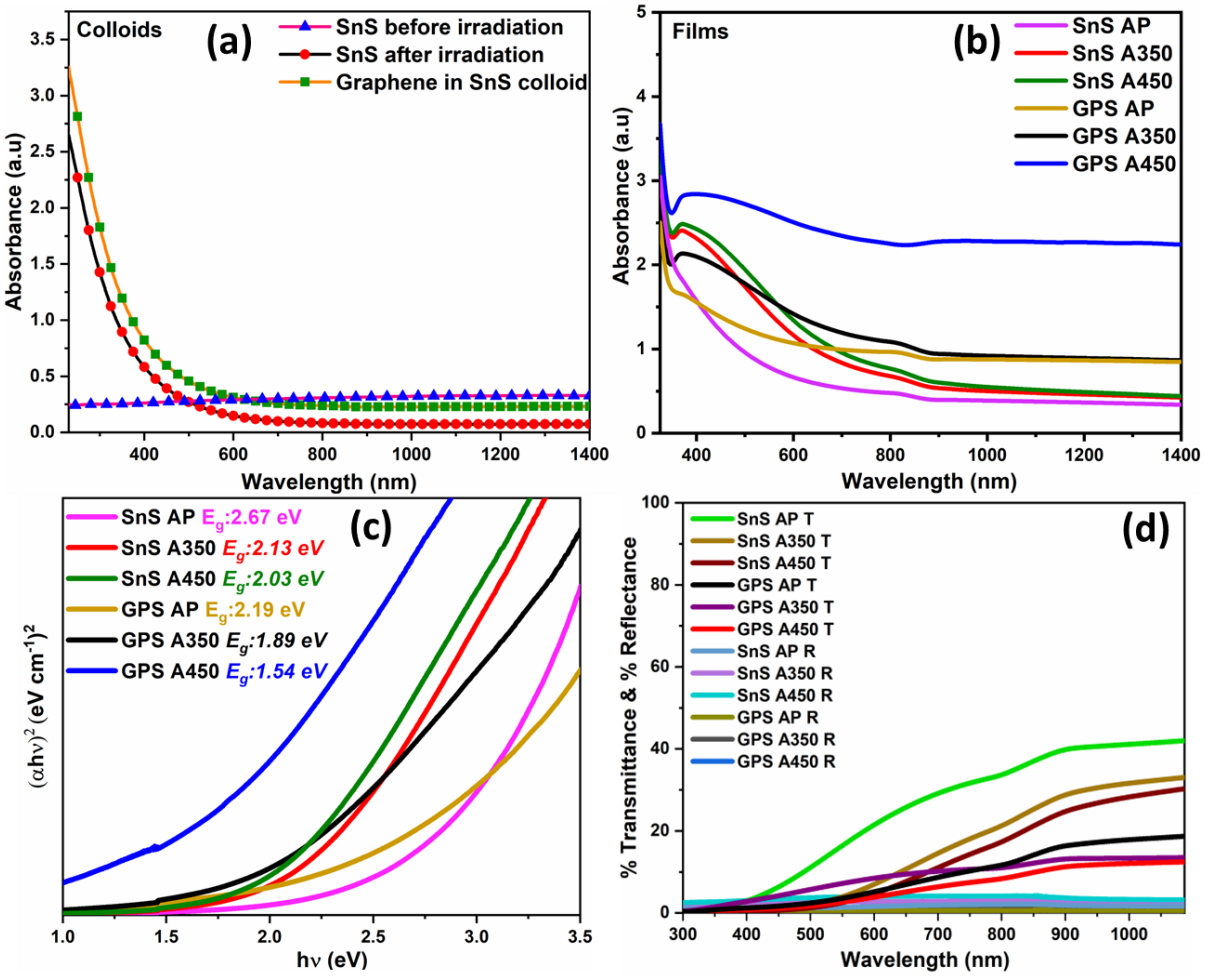


Fig. 4.3: (a) Absorption of the SnS nanocolloids before and after laser irradiation in liquid; and graphene incorporated SnS nanocolloid (b) UV-Vis spectra of the as-prepared and annealed SnS and GPS films (c) Tauc graph for calculating the bandgap in SnS and GPS films (d) %Transmittance and %Reflectance of the films (© from Elsevier 2022).

4.3.2 Morphological Analyses

Using TEM and SEM investigations, the morphology of the SnS NPs, graphene and graphene NPs were determined. The samples were prepared for TEM by drop casting SnS nanocolloids, graphene nanocolloids and graphene dispersion in isopropyl alcohol (IPA) onto carbon-coated

copper grids, followed by drying. Fig. 4.4 (a, d, g, h, i) displays TEM images of SnS NPs, graphene, and SnS:graphene hybrids that were taken in bright field imaging mode. Spherical particles that are linked together to create short chains are observed in the case of SnS NPs. The calculated average particle size was 17.3 ± 7.4 nm. Fig. 4.4 (b) shows particles with a size range of 5 to 45 nm. The PLAL of SnS in various liquid media has formerly been studied by our group, and previous studies have shown comparable spherical nanoparticle shape of SnS surrounded by some agglomerates with particle size of 28 ± 10.3 nm [233]. Fig. 4.4 (d) shows the multi-layered sheet-like structure of graphene, which is similar to the research in [22,23]. Fig. 4.4 (c, f) also displays the HRTEM images. The crystallographic planes corresponding to each value were then indexed using the associated ICDD cards after the d-spacing values were calculated using the lattice fringes. While the HRTEM fringes of SnS with interplanar spacing of 1.62, 2.11 and 1.29 Å are assigned to (042), (210) and (162) planes of the orthorhombic SnS phase, those of graphene with interplanar spacing of 1.96, 1.46, and 2.03 Å are assigned to (110), (221) and (010) planes of the rhombohedral graphite structure (ICDD #00-075-2078). The SnS:graphene hybrid is depicted in TEM images (at various magnifications) in Fig. 4.4 (g-i). The micrographs clearly show spherical SnS nanoparticles scattered in layers of graphene. Fig. 4.5 (a) shows the TEM image of graphene NPs. Small spherical particles are observed and from the HRTEM images (Fig. 4.5 (b, c), the planes are indexed as (112) and (010) corresponding to an interplanar distance of 1.61 and 2.02 Å respectively. In SG25 NPs synthesized by dispersing SnS powder in graphene colloid (G25) and irradiating afterwards, the TEM images (Fig. 4.5 (d)) show similar morphology as that observed for SnS NPs. Spherical interchained particles can be seen and the HRTEM images are also provided in Fig. 4.5 (e, f) and only planes corresponding to orthorhombic SnS could be indexed.

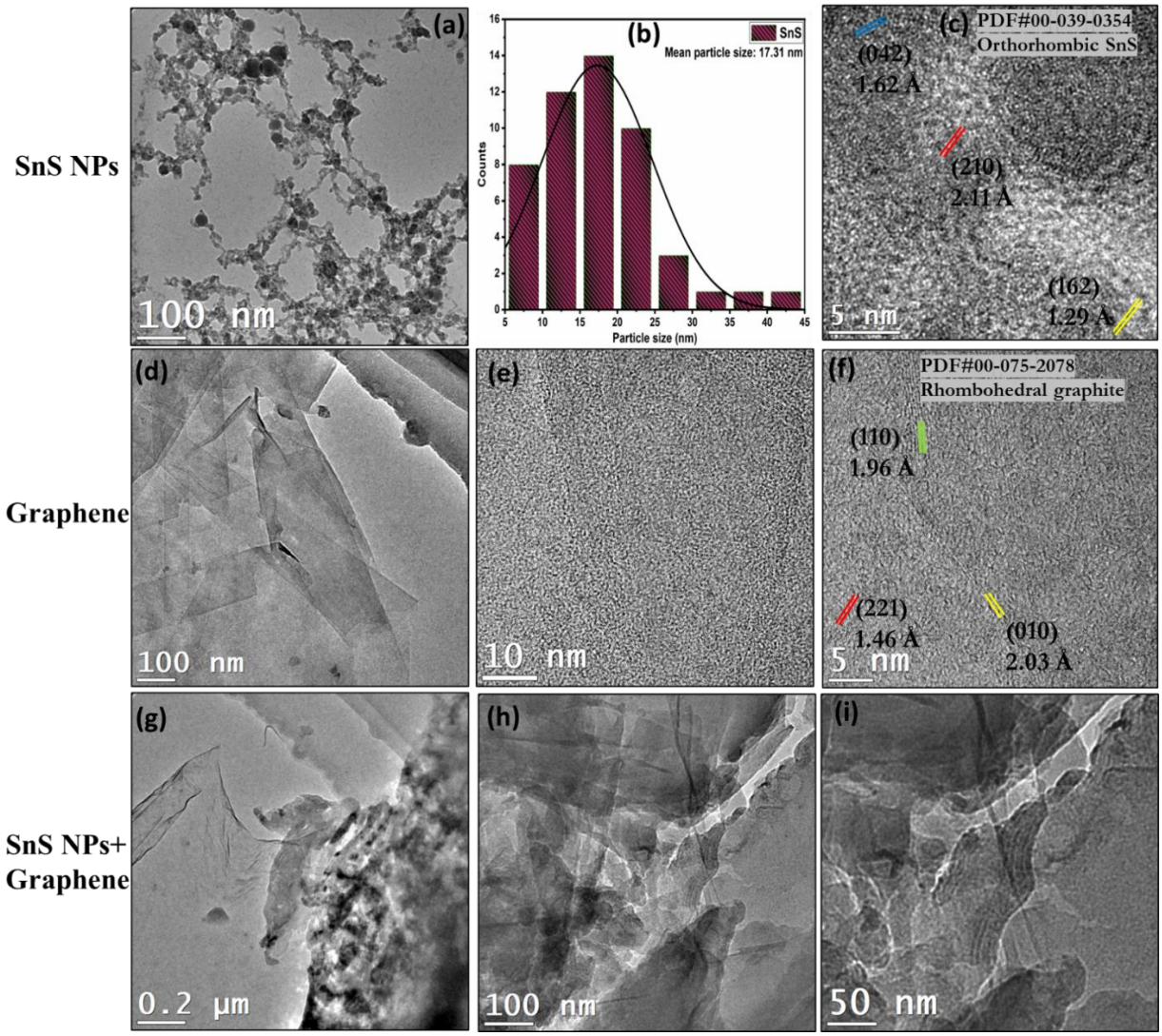


Fig. 4.4: TEM, particle size distribution and high resolution-TEM (a-c) SnS NPs (Set I and III) (d-f) TEM and HRTEM images of Graphene (Set III), (g-i) TEM images of the hybrid nanocolloid of SnS-graphene recorded for various magnifications (Set III) (© from Elsevier 2022).

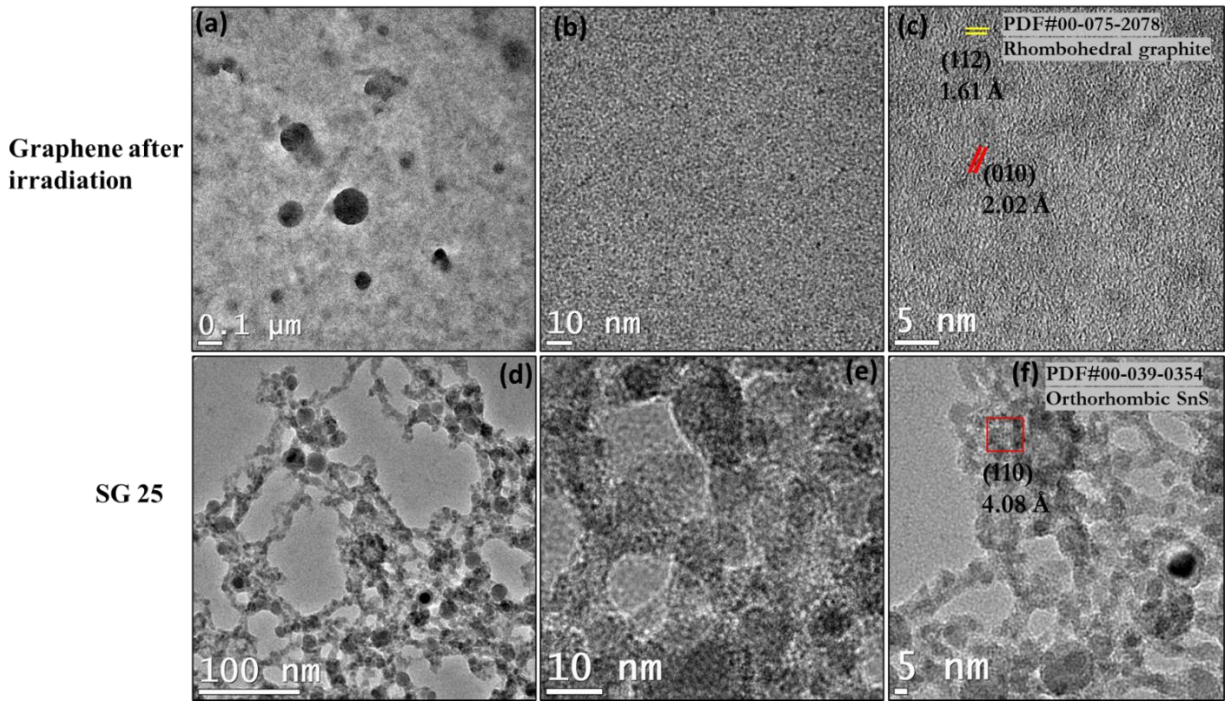


Fig. 4.5: TEM and HRTEM images of (a-c) graphene after irradiation (Set I and II) (d-f) Graphene:SnS NPs i.e.; nanoparticles synthesized by SnS powder in graphene colloid (25 minutes) and irradiating afterwards (Set II).

SEM micrographs of graphene and SnS powder in secondary electron imaging mode taken before and after irradiation are displayed in Fig. 4.6. In Fig. 4.6 (a, b), the morphology of the graphene powder used in the experiment is depicted. Small, randomly distributed platelets or flake-like particles make up the flat, layered structure of graphene [237]. These edges of the layers often roll and fold in on themselves. The SEM micrographs for scales of 10, 5, 3 and 1 μm are provided. Prior to irradiation, the SnS powder educt has a highly irregular, heterogeneous morphology that comprises larger particles as well as stacked, thick flakes-like structures (Fig. 4.6 (c, d)). It is obvious that laser irradiation caused the SnS particles to fragment, resulting in the formation of interlinked chains of spherical nanoparticles. Laser fragmentation is confirmed by the small, crumbled particles that were found when the samples were exposed to radiation. The photons from the nanosecond laser are absorbed, which results in electron-electron coupling, lattice energy transfer and an abrupt thermalization of the electrons. The process as a whole will lead to an increase in SnS lattice energy, which will cause fragmentation [65].

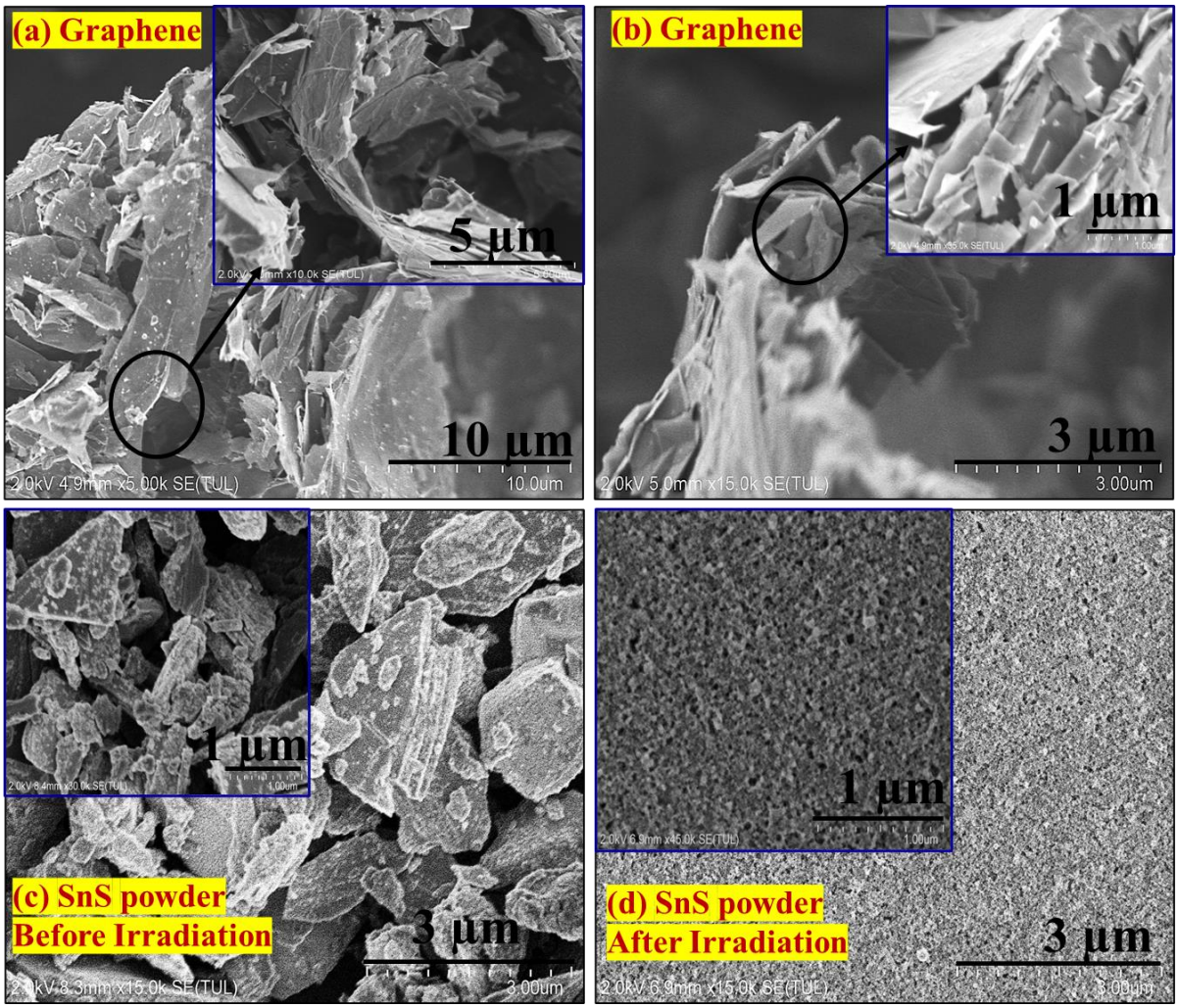


Fig. 4.6: SEM images of (a, b) Graphene (c) SnS powder prior to laser irradiation (d) SnS powder after laser irradiation (A voltage of 2 kV and a current of 10 µA were used to capture the images) (© from Elsevier 2022).

Fig. 4.7 (a, b) displays the SEM images of graphene powder before and after irradiation (Set I and Set II). The images are displayed at a scale of 5 µm. It is observed that after irradiation, graphene totally loses its layer-like nature and tiny, spherical particles are produced instead. When SnS powder was introduced to this colloid (for Set II experiments), only the large SnS flakes could be seen (Fig. 4.7(c)). However, after laser irradiation, this colloid formed small, chained particles Fig. 4.7 (d). It was similar to the morphology of SnS powder before and after irradiation (Fig. 4.6 (c, d)). No morphological modifications due to graphene NPs were observed. SEM findings for all these samples are in good agreement with morphological findings from TEM.

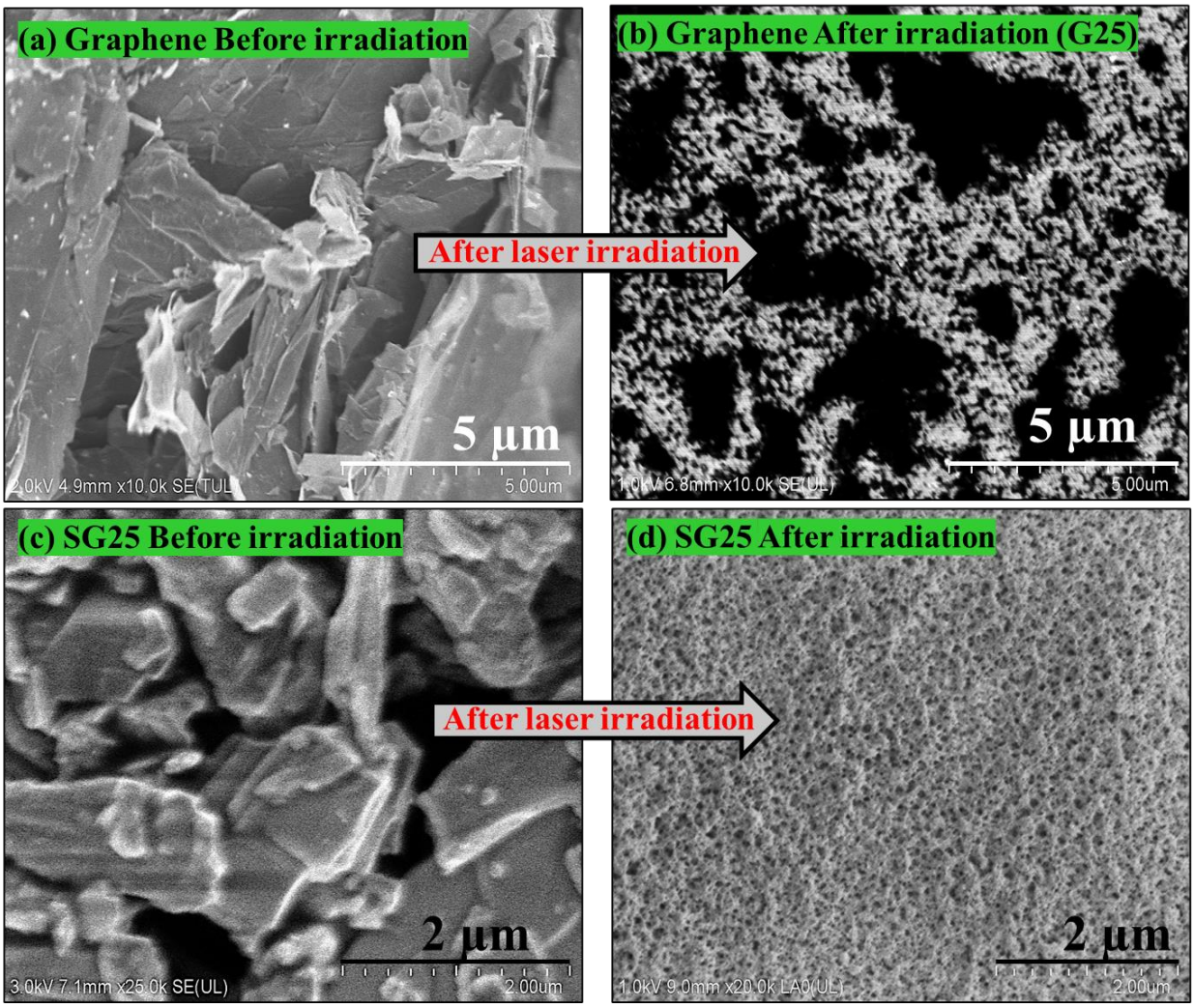


Fig. 4.7: SEM images of Graphene (a) before irradiation (b) after 25 min irradiation (G25); (c) SnS powder dispersed in graphene colloid (G25) prior to laser irradiation (d) laser irradiated colloid of SnS dispersed in G25.

The SnS and graphene-incorporated SnS (GPS) films of the as-prepared and annealed samples made by spin-coating are depicted in SEM images given in Fig. 4.8 (a-f). The films are labeled "AP" for as-prepared and as "A450" and "A350" for the annealed films indicating the annealing temperatures utilized. Both the spherical nature of SnS particles and the flake-like layers of graphene could be seen. For GPS films, graphene layers completely cover the film surface, substantiating homogeneous surface coverage by spin coating. The images at higher magnification provided in the inset of the figures clearly show the spherical interconnected SnS nanoparticles as well as the layered graphene. The outer and interior layers of graphene are completely decorated

with spherical SnS NPs. In general, graphene has a high surface-to-volume ratio, and the morphology we saw in the hybrid films increases the effective surface area for actively absorbing incident photons, which also enhances the efficacy of photocurrent and photodetection [238]. The average thickness of the SnS films was found to be 1.4 ± 0.4 µm and that of the GPS films to be 1.7 ± 0.5 µm, respectively, based on the cross-sectional SEM analysis of the films (as-prepared and annealed), which is shown in Fig. 4.9 (a, b). With the help of profilometric analysis, these values were also confirmed.

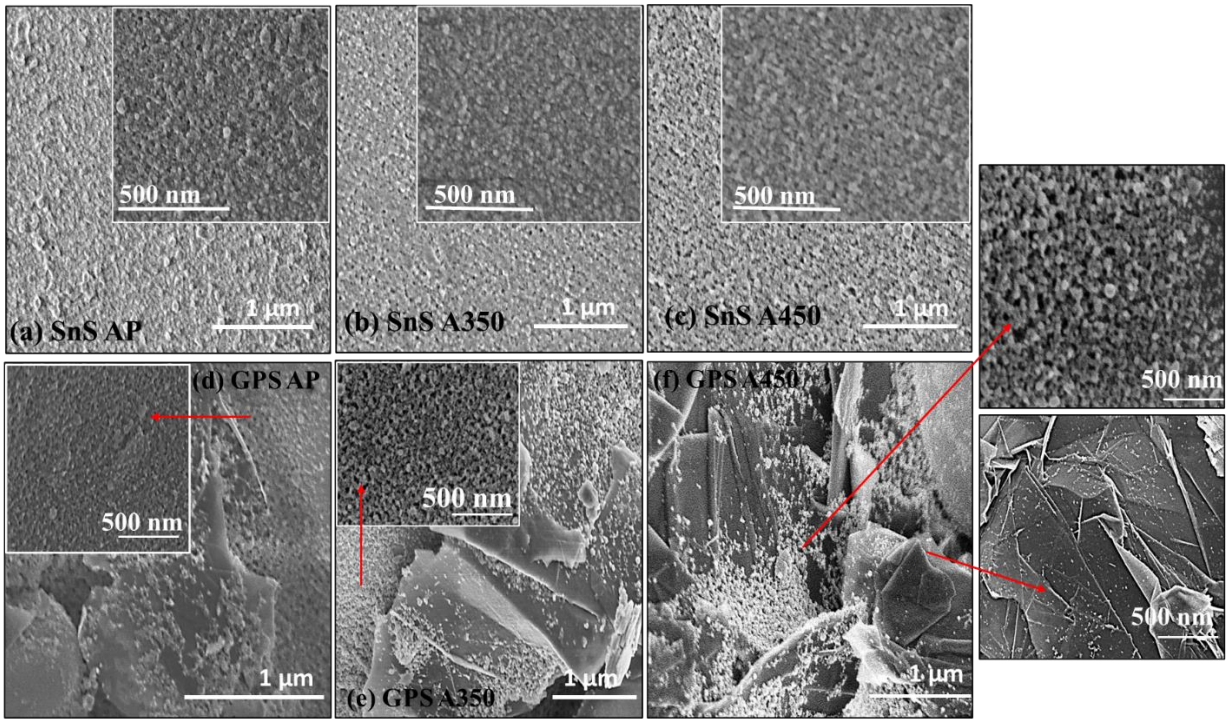


Fig. 4.8: SEM micrographs of (a, d) as-prepared (b, e) annealed at 350 ℃ (c, f) annealed at 450 ℃ films of GPS and SnS (© from Elsevier 2022).

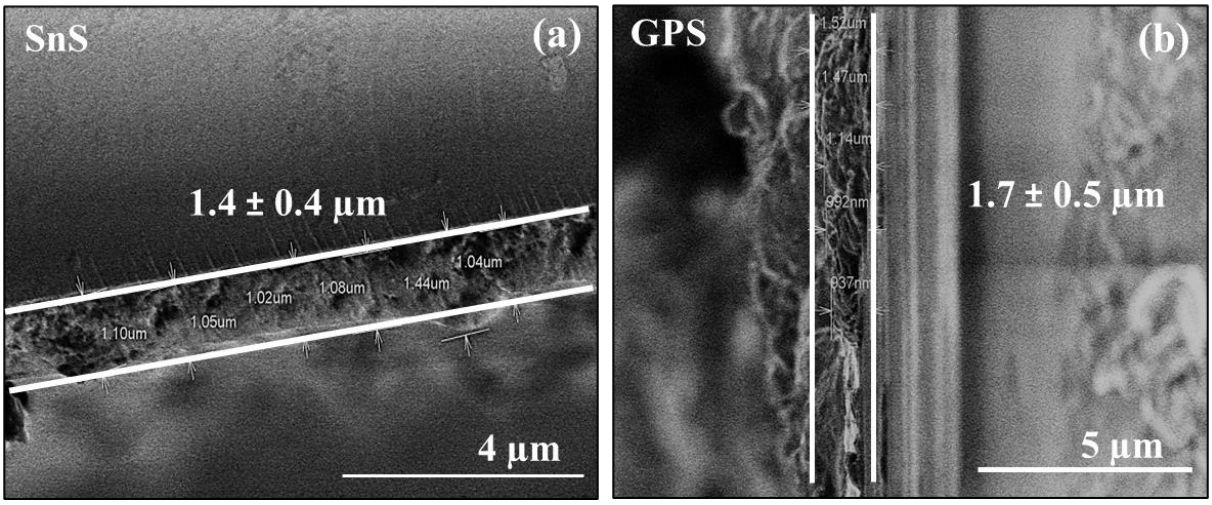


Fig. 4.9: Cross-sectional SEM images of (a) SnS (b) GPS films (© from Elsevier 2022).

SEM images of SnS and graphene:SnS annealed films prepared by Set I and II experimental routes are also given below in Fig. 4.10 (a-f). For Set I (S+G25), the SnS and graphene films showed similar morphology i.e., spherical connected particles. As already explained from the SEM and TEM images of graphene NPs, small particles are formed after irradiation of graphene. The SnS NPs have a dominant nature when combined with graphene NPs since only a small amount of graphene (10 mg) is employed in comparison to SnS (100 mg). This could be the cause of the lack of obvious variations in the morphology of SnS and SnS:graphene hybrids. For SnS films from Set II, small spherical grains were distributed on the surface of SnS films. With graphene (SG25), these spherical particles got converted to elongated particles on the surface. For the both the sets of samples, images at a scale of 1 µm is shown and in the inset, images at 500 nm are also presented.

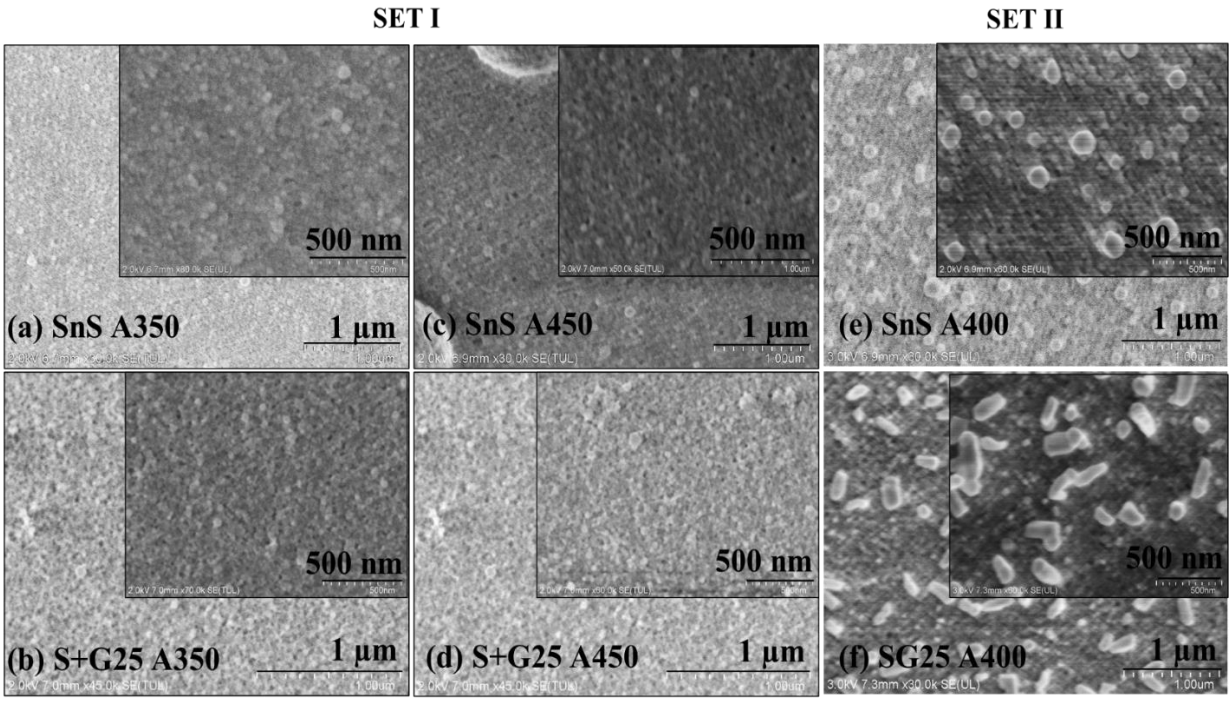


Fig. 4.10: SEM of SnS and graphene:SnS films fabricated by Set I and II experimental routes.

4.3.3 Structural, Phase and Compositional Analyses

In Fig. 4.11, the results of X-ray diffraction (XRD) of graphene powder, SnS and GPS films are presented. A very intense peak with an orientation towards the (111) plane can be seen in the XRD pattern of graphene (Fig. 4.11 (a)) at $2\theta=26.58^{\circ}$, whereas the peak at 54.72° corresponds to the (222) plane. The graphene peaks were compared to the rhombohedral structure (ICDD #075-2078) while the SnS peaks were compared to the orthorhombic crystal structure (ICDD #039-0354). Fig. 4.11 (b) shows the comparison of the XRD patterns of GPS and SnS films. The significant orientation of the diffraction peak at $2\theta=32.01^{\circ}$ in the GPS films is related to the (040) plane, as opposed to the 100% intensity peak that corresponds to the standard SnS pattern. At 21.99°, 26.00°, 27.48°, 30.49°, 31.59°, 39.06°, 44.80° and 45.57°, additional peaks have been noted. These are indexed to the SnS crystallographic planes (110), (120), (021), (101), (111), (131), (141), and (002) [239]. In GPS films, the peaks are significantly oriented towards the (040) plane and the (111) plane observed in SnS films is relatively suppressed. The variation in the peak intensities might be due to the morphological changes in GPS films i.e., the distribution of SnS NPs on the surfaces of the graphene layers. Similar trend has been reported by Tao et al. also [240]. The XRD pattern of SnS showed a major peak orientation along (130) followed by (111) plane and for

SnS/graphene nanocomposite, it was just the reverse. Tetragonal SnO_2 (ICDD #071-0652) was found to have weaker intensity peaks around 33.92° and 26.9° for SnS films, which are relatively unimportant for GPS films. According to Debataraja et al., graphene can restrict the growth of SnO_2 because it weakens the peaks of SnO_2 when it is present [241]. The XRD results did not reveal the graphene peaks. This could be due to the fact that graphene's 2θ value overlaps with that of SnO_2 (2θ=26.5°), or it could be that the concentration of graphene is too low to be identified in XRD [242]. According to the Debye-Scherrer equation, the crystallite sizes of SnS and graphene-incorporated SnS films are 32.1, 33 and 32.7 nm for the as-prepared and annealed SnS films, respectively. The values for the AP, A350 and A450 GPS films were 53.8, 55.5 and 57 nm, respectively. It has been previously reported that increasing the annealing temperature causes the crystallite size to grow [183]. The decrease in bandgap value observed for the SnS and GPS films can also be attributed to the increase in crystalline size.

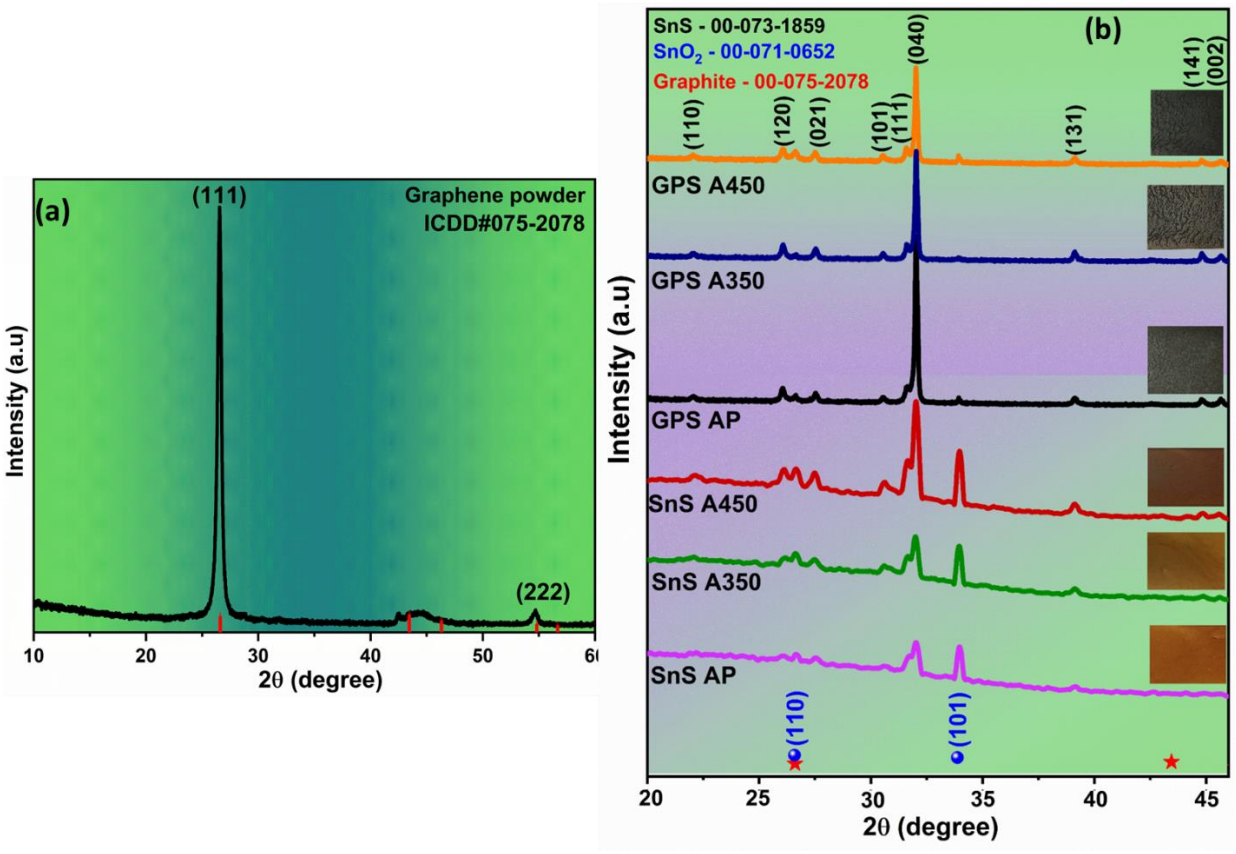


Fig. 4.11: XRD of (a) Graphene powder (b) SnS and GPS films at various annealing conditions.

Raman spectroscopy further supported in phase identification. Raman spectra of the GPS and SnS samples are given in Fig. 4.12. Additionally, the Raman peaks corresponding to the graphene used for the experiments are also included. The G-band and 2D-band are identified in GPS films as two clear and distinct peaks at 1576 and 2707 cm^{-1}, respectively. The G-band is the E_{2g} mode, which manifests as a result of the stretching modes of the carbon-carbon bonds in common graphite [243]. Around 1350 cm^{-1}, a D-band with substantially lower intensity is seen, signifying the high quality of the graphene layer. Additionally, the intensity of G-band is double that of the 2D-band, indicating that graphene films are multilayers [244]. The sample also contains the SnS phonon modes at 93, 221 and 310 cm^{-1}. Fig. 4.12 (b) shows the Raman spectrum of the SnS films with the identified peaks. There are only 12 Raman active modes for the orthorhombic crystal structure of SnS out of the 21 phonon modes in SnS [196]. Around 93 cm^{-1} is the transverse A_g (TO) optical mode peak, 220 cm^{-1} is the longitudinal A_g (LO) optical mode peak, and 310 cm^{-1} is the peak associated with the A_g mode [171].

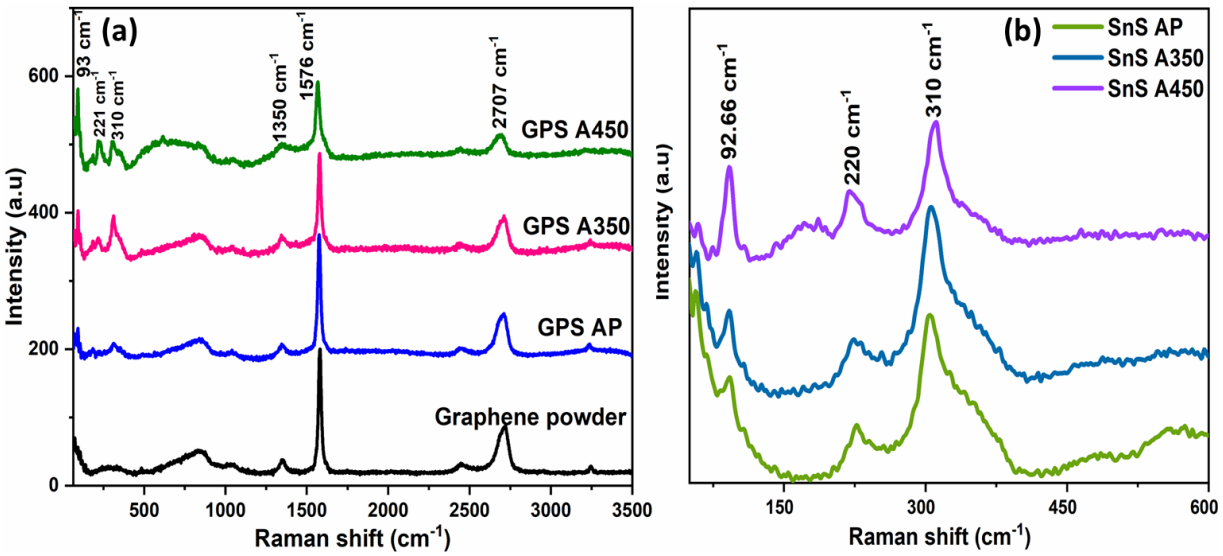


Fig. 4.12: Raman spectrum of GPS and SnS films (© from Elsevier 2022).

The elemental composition and oxidation states of the samples are investigated using X-ray photoelectron spectroscopy (XPS). For a fast identification of the components present on the sample's surface, a wide-range XPS survey scan was carried out. The XPS spectra obtained for SnS, GPS films are provided in Fig. 4.13 (a, b) respectively, and that of graphene powder is given in Fig. 4.14 (a). Sn, S and C were detected from these spectra. For binding energy correction, an

energy value of 284.6 eV was chosen. The Gaussian-Lorentzian sum function was employed for peak fitting and a Shirley-type background correction was used. Fig. 4.14 (b) displays the high resolution spectra of C 1s in graphene powder. The sharp intense peak around 284.56 eV corresponds to the sp^2 hybridized C=C peak and the sp^3 hybridized C-C peak is identified at binding energy position of 285.19 eV indicating the presence of amorphous carbon. The peaks present at 285.71 and 286.58 eV corresponds to the C-OH and O-C-O bonds respectively. These groups are present as a result of oxidized carbon contamination or adsorption contamination during preparation processes of graphene such as chemical or thermal reduction, electrochemical exfoliation or chemical vapor deposition approach [245].

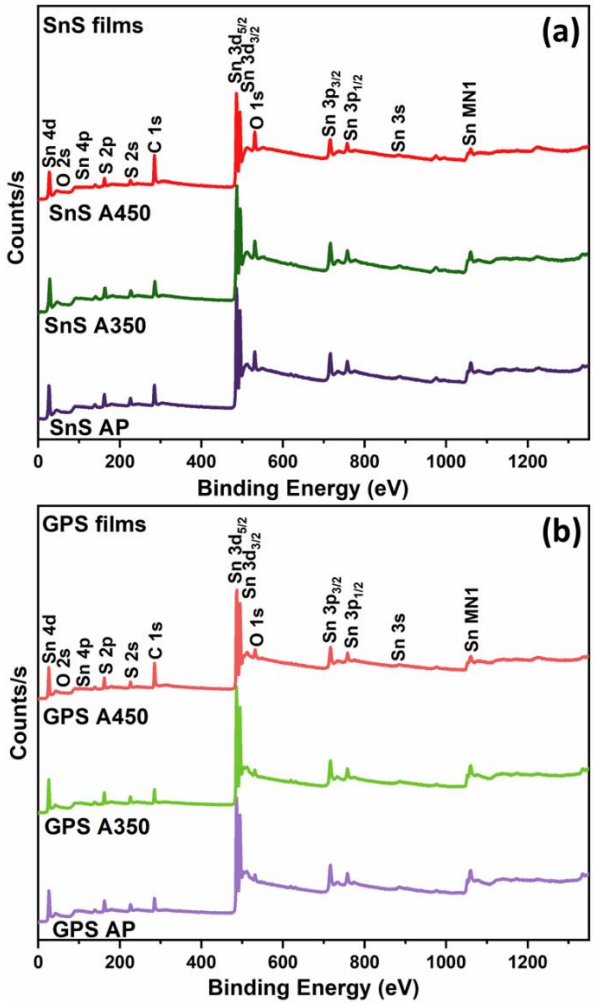


Fig. 4.13: XPS survey spectra of SnS and GPS films.

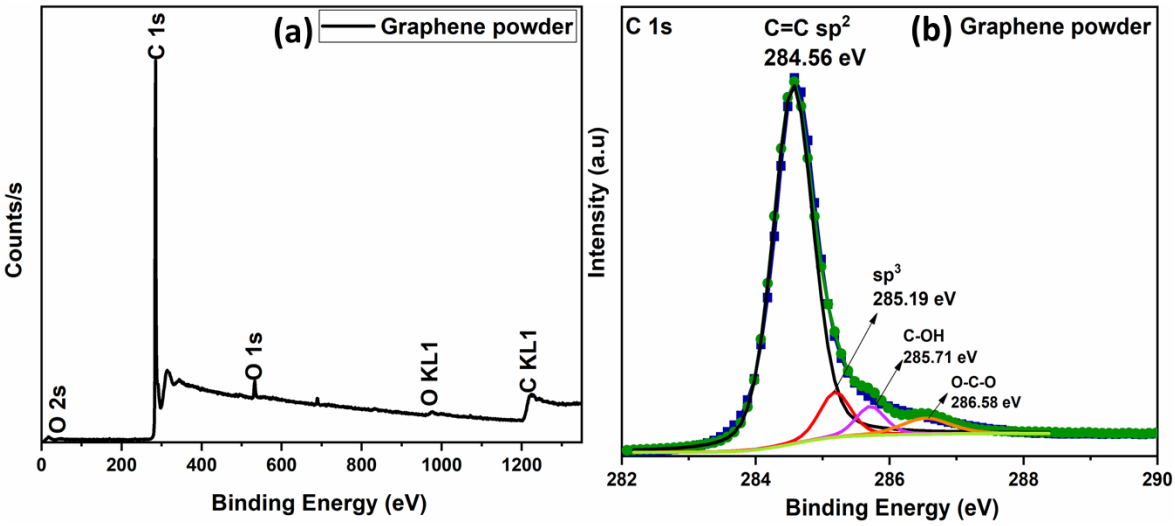


Fig. 4.14: (a) XPS survey spectra of graphene (b) High resolution C 1s spectra of graphene.

Fig. 4.15 displays the high-resolution XPS spectra of Sn 3d, S 2p and C 1s in GPS films in as-prepared and annealed condition. The GPS sample's Sn $3d_{5/2}$ and Sn $3d_{3/2}$ core level peaks are shown in Fig. 4.15 (a, d, and g) under 350 and 450 °C annealing conditions. For all three samples, the dominant peaks are located around 485 and 494 eV and are well congruent with those of Sn^{2+} in SnS [200]. The Sn^{2+} state in SnS contributes the most to the XPS peaks, whereas the minor peaks at 486 and 495 eV after deconvolution are due to the Sn^{4+} state as in SnO_2 [201]. The binding energy difference we determined is in good agreement with the known differences for elemental Sn and the various Sn oxidation states reported for SnS. As the Raman measurements indicate phase pure GPS films, it is assumed that the Sn^{4+} state observed in XPS exists only on the sample surface. All of the XPS data were collected from the surface alone (without any etching), suggesting that the sample's contact to air may have caused the formation of SnO_2. Peak area ratio (3:2), FWHM and peak separation parameters were taken into account for the $3d_{5/2}$ and $3d_{3/2}$ doublet peak fits (8.41 eV) [202].

The high-resolution spectra of S 2p, which has two core level peaks at S $2p_{3/2}$ and S $2p_{1/2}$, is shown in Fig. 4.15 (b, e and h). The S 2p peaks for the A350 and A450 films show symmetric, well-resolved doublets; however, as-prepared samples exhibit a small broadening. For S $2p_{3/2}$ and S $2p_{1/2}$, the values are approximately estimated as 161 and 162 eV respectively. The intensity ratio between the two peaks from the doublet was kept at a maximum of 2:1 in all of the deconvolutions. The binding energies of S^{2-} in SnS are in good accord with those of the literatures [88]. In the relevant figures, the spin orbit splitting values are also indicated (1.16 - 1.18 eV). Two peaks about

284.6 and 285.3 eV, corresponding to the sp^2 C=C and sp^3 hybridized C [246], were visible in the deconvoluted C 1s spectra (Fig. 4.15 (c, f and i)). Similar to the high-resolution spectra of S 2p, the C 1s peaks likewise become distinct with rising annealing temperature. The high resolution XPS spectra of Sn 3d and S 2p were acquired for the as-prepared and annealed SnS films. These spectra matched the reported values for Sn^{2+} and S^{2-} in SnS [207].

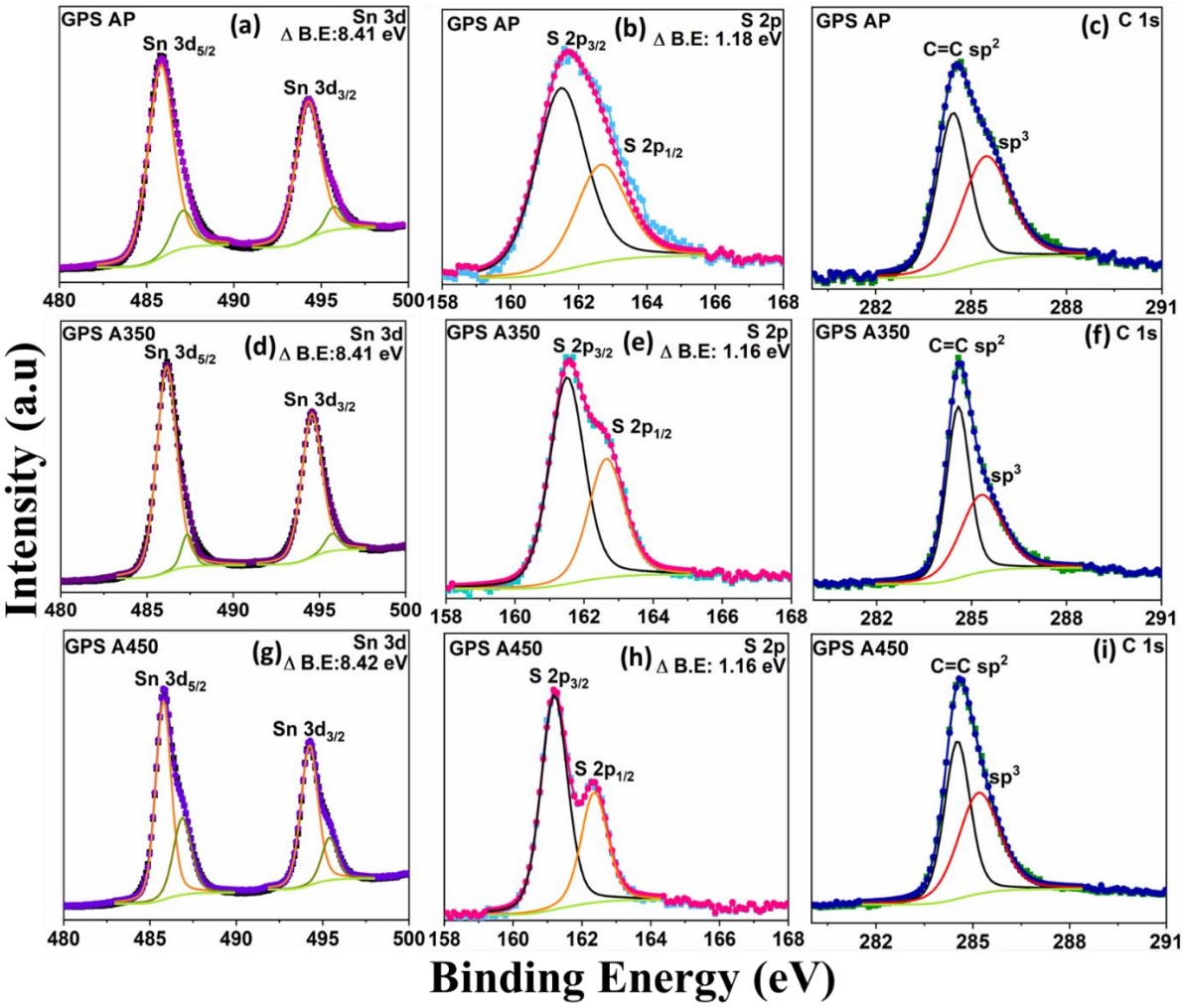


Fig. 4.15: High resolution XPS spectra of (a, d, g) Sn 3d, (b, e, h) S 2p and (c, f, i) C 1s of GPS films at different conditions (© from Elsevier 2022).

The XPS mapping of SnS and GPS films under as-prepared and annealed condition of 450 °C is shown in Fig. 4.16 (a-d). For mapping, a 1 x 1 mm^2 area scan of the sample's surface was carried out. Sn 3d and S 2p are depicted in blue and pink, respectively, for the SnS sample. Sn 3d is depicted in blue, C 1s in light green and S 2p in red in GPS films. The results demonstrate

uniform distribution of the elements Sn and S in SnS surfaces as well as Sn, S and C in GPS films, maintaining chemical states that are identical to those found in high resolution XPS analysis. An explanation is given for the color blending in Fig. 4.16 (c, d). The color yellow is produced by blending the colors red and green, cyan blue by combining the colors blue and green, and magenta by the mixing of the colors blue and red.

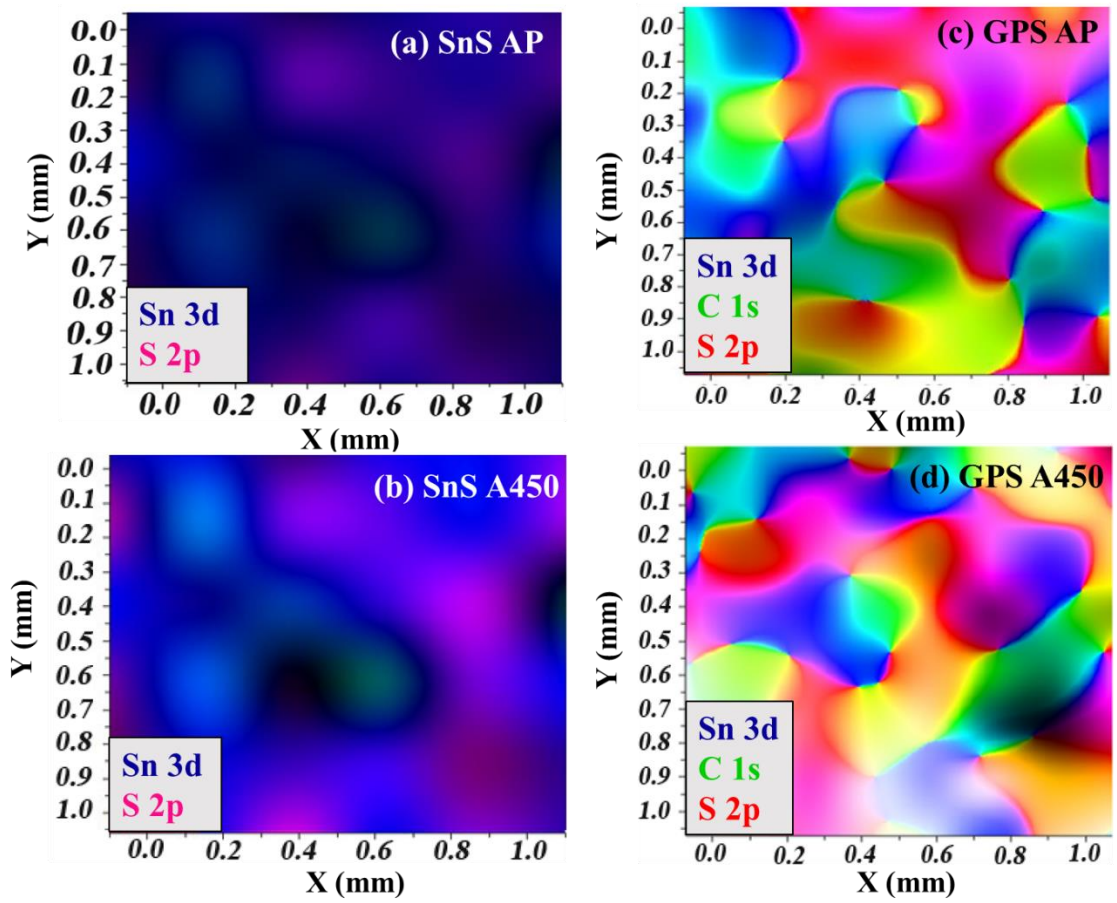


Fig. 4.16: XPS mapping of SnS and GPS films (a, c) as-prepared (b, d) annealed at 450 ℃ (© from Elsevier 2022).

4.3.4 Electrical Studies

The electrical characteristics of the films were identified using current-voltage (I-V) and current-time characteristics. Applying voltages from 0 to +5 V, the I-V plot was measured both in the dark and in the presence of light (Fig. 4.17 (a, b)). The symmetry and straightness of the I-V curves confirmed that the Ag electrodes and films had good ohmic contact. Graphene-incorporated SnS films (GPS) from Set III demonstrated a three-order increase in conductivity values when

compared to SnS. SnS films had conductivity in the range of 10^{-5} cm^{-1}, while GPS films had conductivity values in the range of 10^{-2} cm^{-1}. Even though we observed an increase in the current values upon illumination for the annealed samples of Sets I and II (S+G25 and SG25 films) as seen from Fig. 4.17 (a), the increase in current values when compared to those of bare SnS films were too low. As the impact of graphene was not readily apparent in the cases of films fabricated using laser-irradiated graphene colloid (Set I and II), we focused on films fabricated using Set III route. We concentrate on the performance analysis of the annealed samples; therefore, the rest of the discussion will only be based on those samples. This is based on the film quality as determined by the analysis findings of SEM, XRD, XPS, Raman and optical investigations.

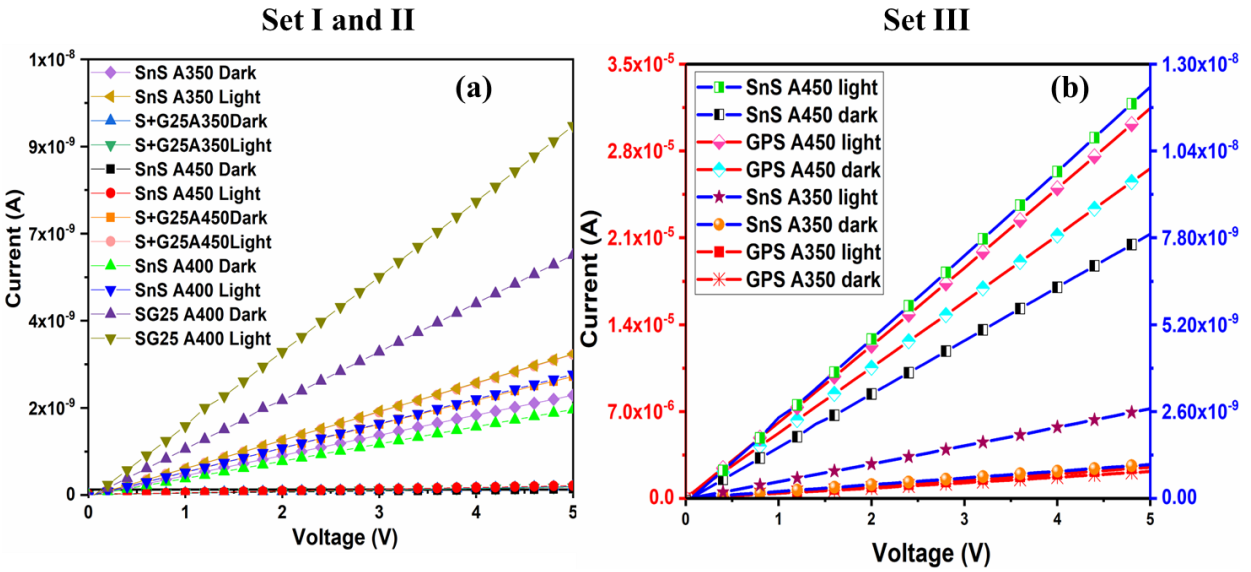


Fig. 4.17: I-V plot of (a) SnS and SnS:graphene hybrids prepared by Set I and II routes (b) annealed films of GPS (The axis in red (left y-axis) represents the current values for GPS films) and SnS (The axis in blue (right y-axis) represents those for SnS films) (© from Elsevier 2022).

The response of the films to W lamp were measured by periodically turning on and off the illumination for 20 s each. The photocurrent values were recorded by applying voltages of 1, 5 and 10 V and a rise in photocurrent was seen as the applied voltage increased. At a bias voltage of 1 V, the photoresponse of the films recorded is depicted in Fig. 4.18 (a). Graphene incorporated SnS films (GPS) showed an increase in the photocurrent magnitude (which was in the order of 10^{-6} A) than the SnS films (10^{-9} A). We tested the photoresponse of the films to various LEDs to examine their sensitivity to specific wavelengths (Fig. 4.18 (b-e)). At a bias voltage of 5 V, the sample's response to continuous-wave lasers with wavelengths of 532 and 785 nm was also

recorded. For each measurement, a laser power of step 4 mW (4-26 mW) for 532 nm and 5 mW (5-30 mW) for 785 nm was used. Fig. 4.19 (a, b) shows the photoresponse measurements with varying powers of 532 and 785 nm laser. Fig. 4.19 (c, d) also displays cyclic photoresponse measurements taken at 532 nm (at 26 mW) and 785 nm (30 mW). With laser diodes of 840 and 980 nm wavelength and 100 mW output, the wide range of wavelengths this detector is capable of operating was demonstrated. The cyclic responses of all the films are shown in Fig. 4.20 (a). Even in this NIR range of light, the responses of the photodetectors of SnS and GPS remain noise-free and consistent. Regardless of the irradiation wavelength, we were able to achieve the same order of photocurrent for illumination utilizing W lamp, LEDs, 532 and 785 nm sources. Fig. 4.21 (a-d) shows a plot of I_{light} against wavelength for the films to illustrate this. For wavelengths ranging from UV-Vis to NIR, the order of photocurrent remains constant and the minor difference that is seen is mostly brought on by variations in light intensity among the many illumination sources that have been employed. Otherwise, the photocurrent fluctuation can only be seen when the laser power density and applied voltage are both increased.

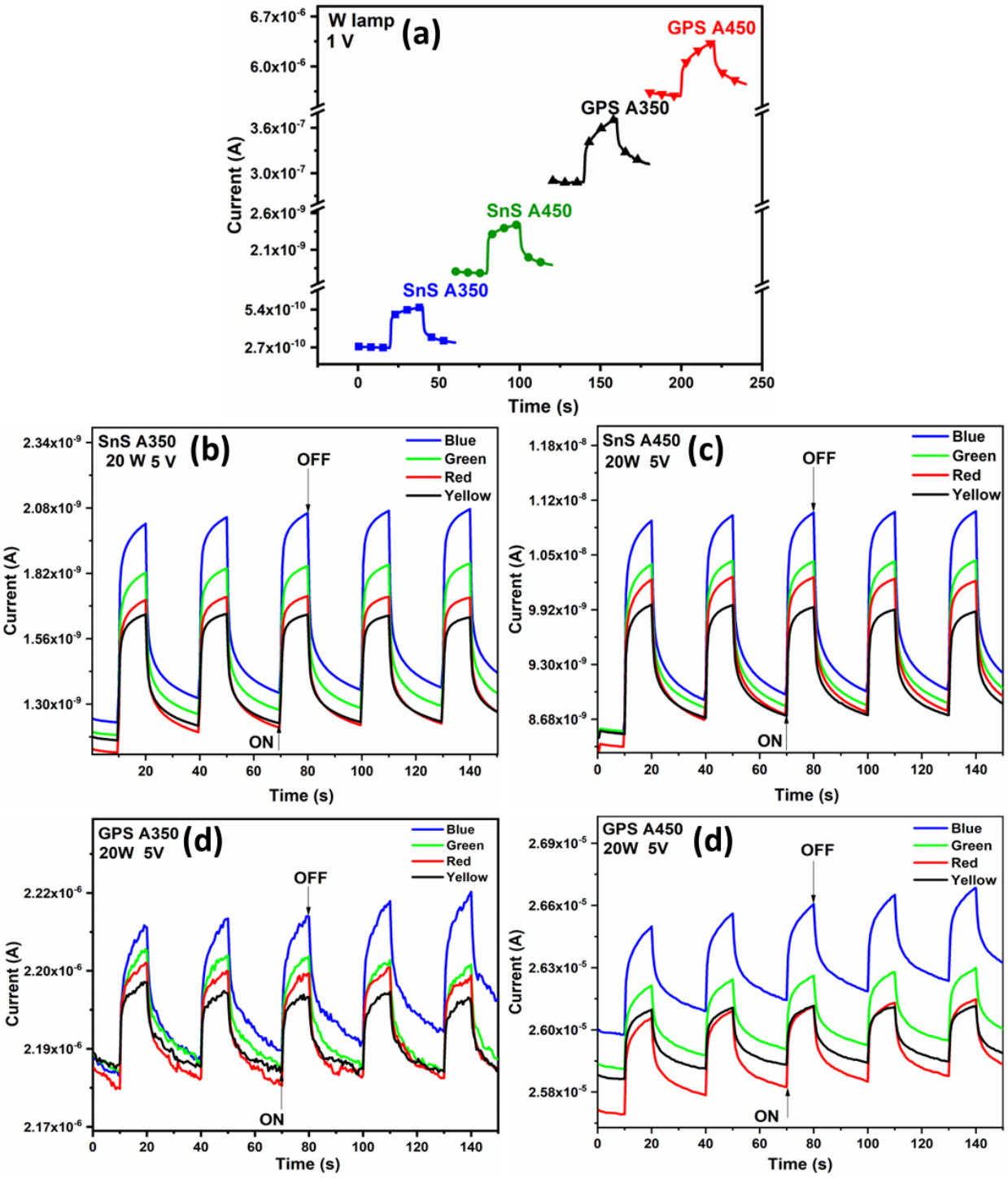


Fig. 4.18: Photoresponse behavior of the films under illumination using (a) W lamp (b-e) different wavelength of LEDs (© from Elsevier 2022).

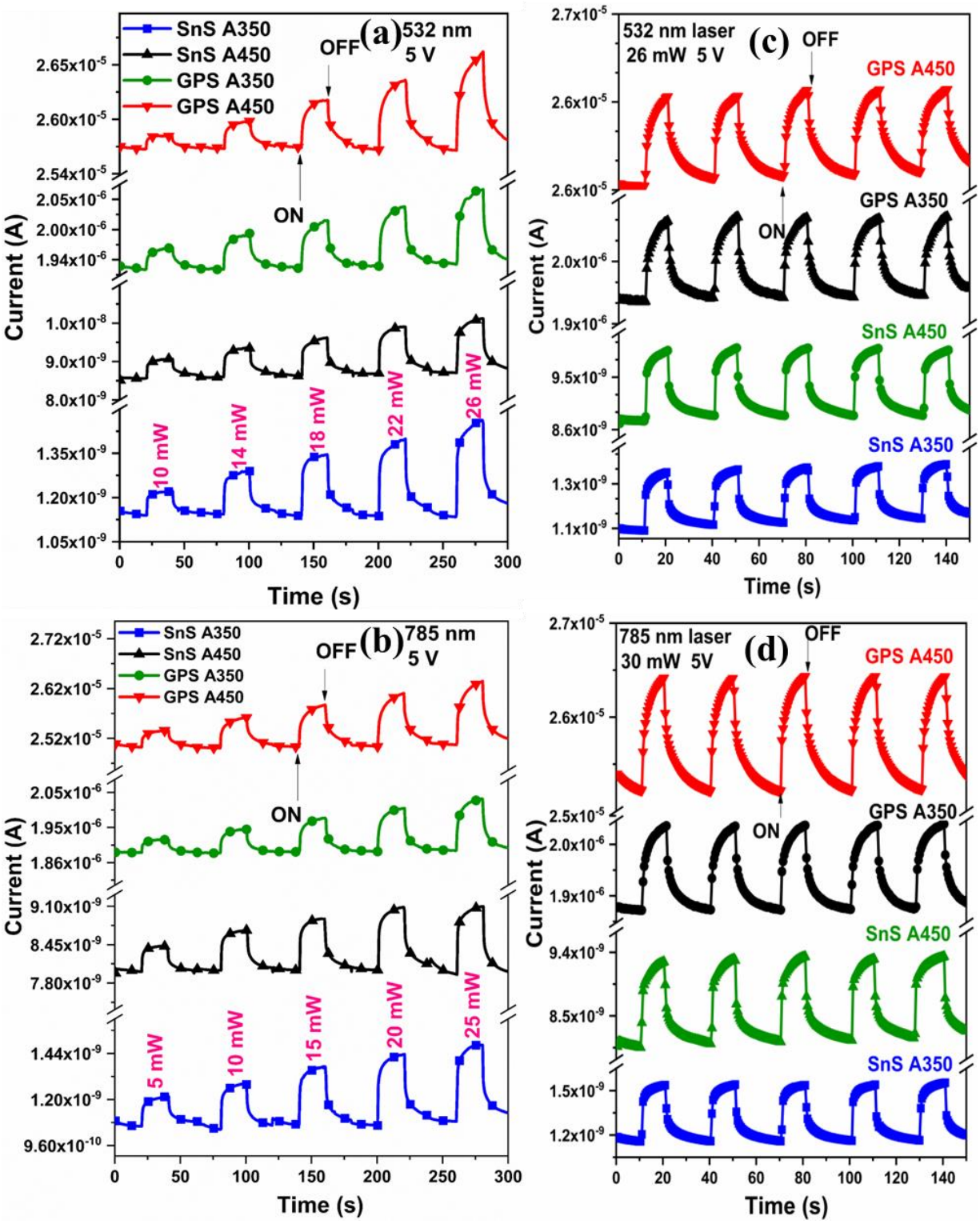


Fig. 4.19: Photoresponse behavior of SnS and GPS films to illumination using continuous-wave laser of wavelengths (a) 532 (b) 785 nm at different laser powers (c, d) Cyclic photoresponse behavior at constant laser powers (© from Elsevier 2022).

Based on techniques for different hybrid nanostructured materials that have been put out by other groups, it is possible to explain why GPS films have better photocurrent values than SnS films [247,248]. The electron affinity of SnS is 3.14 eV [174] while the work-function of graphene is 4.6 eV [247]. Both sides of the graphene layers are decorated with spherical SnS NPs, as was already seen from the morphology. When illuminated, SnS serves as the light harvesting medium and significantly contributes to the phenomenon of light absorption. SnS can transport the produced carriers from its conduction band to graphene with minimal energy loss. On the other hand, graphene serves as an electron transport pathway [249]. The energy band diagram for the SnS:graphene structure given in Fig. 4.20 (b) can be used to understand the mechanism proposed. Due to its high carrier mobility, graphene exhibits less electron buildup, which enhances carrier transport efficiency and increases the photocurrent. The carriers produced by illumination recombines again when it is turned off. The enhancement of the hybrid films' crystallinity favors the synergistic mechanism of charge transfer in SnS:graphene. An earlier investigation on a graphene composite enhanced the electrical and ionic conductivity and reduced the polarization of the charge/discharge processes in the material (5 nm) decorated with SnO_2 [250]. Similarly, spherical CdSe NPs and CdS NPs dispersed onto graphene sheets and reduced graphene oxide (rGO), respectively, showed exceptional interfacial interactions. The tight anchoring of NPs onto graphene not only improved its non-linear features but also led to higher crystallinity, a higher surface-to-volume ratio and a lower carrier recombination rate [251,252]. These findings support our conclusion that the photocurrent values with graphene incorporated SnS films are improved (10^3 times) as a result of noticeable morphological features. The photocurrent curve switches between the on/off states in each of the cyclic measurements. This confirms the photodetector's stability as well [233].

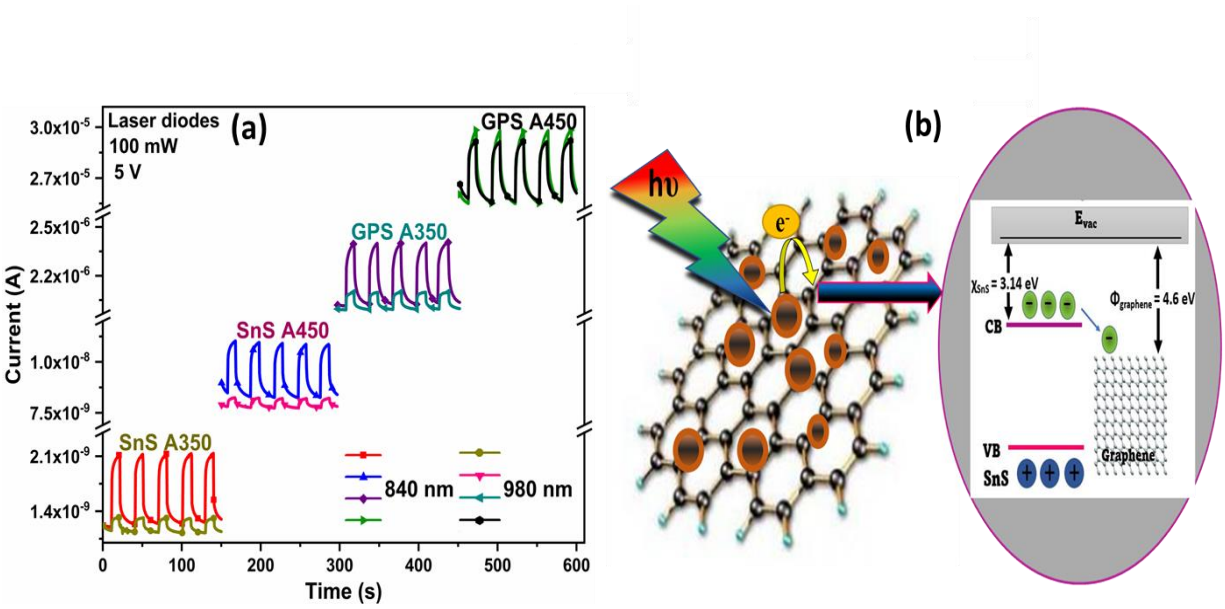


Fig. 4.20: (a) Photoresponse behavior of GPS and SnS films to illumination using laser diodes of wavelength 840 and 980 nm (b) Energy band alignment and charge carrier transport mechanism in SnS:graphene films (© from Elsevier 2022).

Graphene-semiconductor hybrid nanomaterials are where interfacial and chemical interactions are most frequently seen [253]. Two layers of Sn-S atoms that are firmly bonded to one another make up the orthorhombic crystal structure of SnS. This bonding may also play a major role in how SnS NPs interact with the graphene layer [254]. After incorporating graphene into the colloid and producing the film, the surface charges of the SnS nanocolloid may potentially cause interactions with the graphene layers. As suggested in those graphene nanocomposites/hybrids, the possibility of a chemical interaction between SnS and graphene increasing the light absorption range cannot be disregarded. Sn-S-C bonds can also form as a result of a bond between the tin atoms in SnS and the carbonate structure of graphene, which has unpaired π electrons [255,256]. Beginning with photon absorption, which includes bandgaps or sub bandgaps brought about by PLIL [65,257,258] defects in semiconductor NPs (in this case SnS), charge carrier generation occurs. To prevent recombination, the carriers are subsequently delivered to the electrodes through the extremely conductive graphene channels. The high surface area and significant electrical conductivity of graphene facilitate charge separation and migration to the electrodes. SnS nanoparticles of various sizes, spherical morphologies, surface defects brought on by laser irradiation in liquid, nanoparticles with large contact areas and strong interface

interactions with graphene layers could all contribute to the improved linkage and consequently, the better device performance. The interfacial interactions of graphene with coupled SnS nanoparticles, as well as the significant improvement in crystallinity of the SnS nanoparticles and GPS films after annealing, are what give rise to the wavelength independent photodetector properties. The mechanism shown in Fig. 4.20 (b) for the generation and transfer of charge carriers in the SnS:graphene system may be facilitated by these likely interactions, allowing wavelength-independent detection.

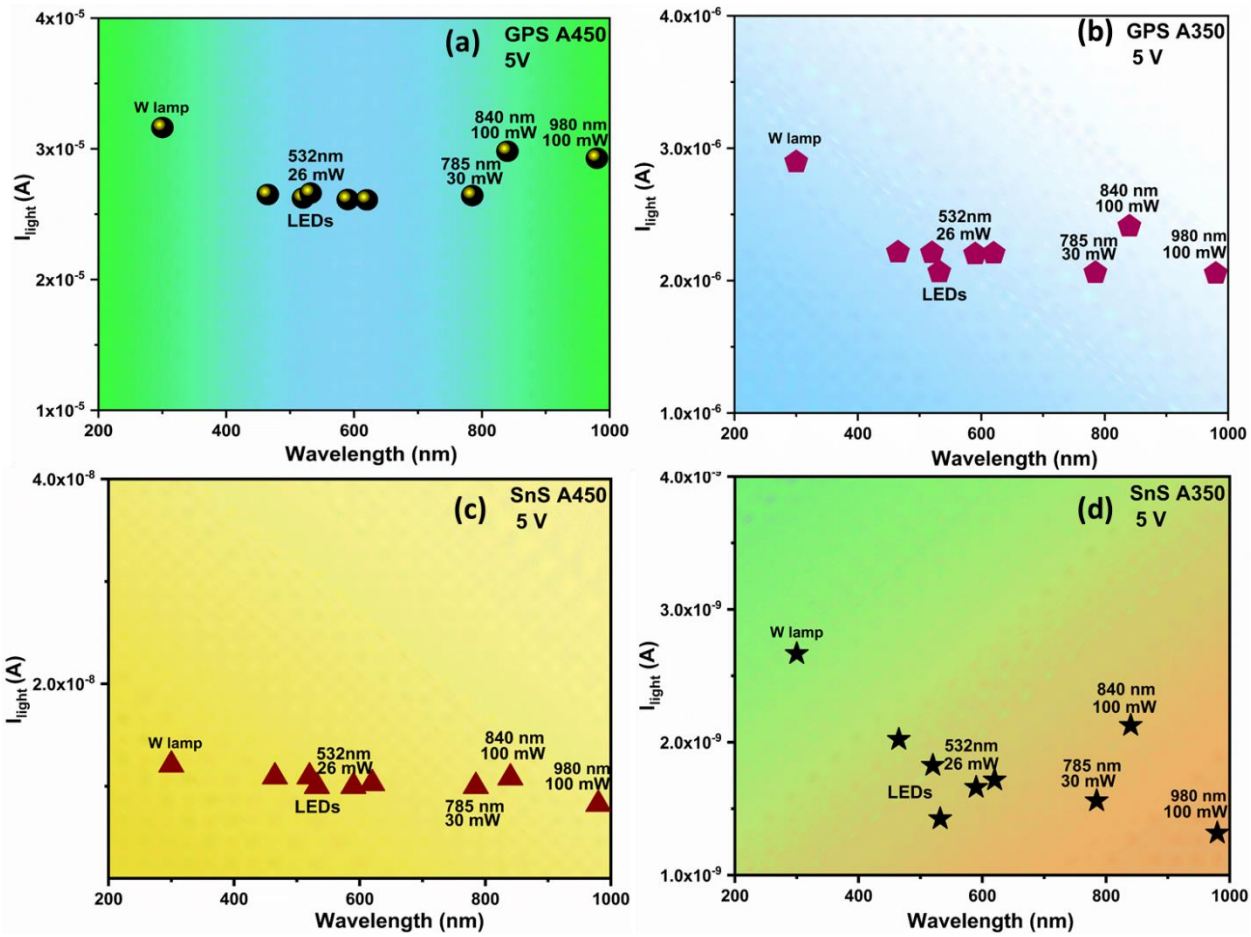


Fig. 4.21: I_{light} vs wavelength plot of GPS and SnS films annealed at 350 and 450 °C (© from Elsevier 2022).

Based on the time-dependent curves, various photodetector parameters, such as specific detectivity, sensitivity and spectral responsivity were evaluated. The calculations are based on photocurrent measurements obtained while being subjected to laser sources with a wavelength of 532 and 785 nm. In Fig. 4.22 (a-d), the calculated parameters are graphically displayed in relation

to laser power density. With increasing laser power, the responsivity for the samples in Fig. 4.22 (a, b) tends to rise in one case and fall in the other. As seen in Fig. 4.22 (b), more injected electrons may be captured in the trap states as laser power increases, reducing the amount of electron-hole recombination for a 532 nm laser with photon energy sufficient for direct band to band excitation. According to the effects of carrier recombination and photon energy (532 or 785 nm), however, responsivity may decrease when laser power density rises, as shown in Fig. 4.22. (a). Lower photon energies in 785 nm lasers cause trap state recombination to play a larger role, which reduces responsivity. For hybrid photodetectors based on graphene, similar behavior were reported [259,260].

We could extend the wavelength detection ranges of SnS and GPS films. SnS nanoparticles are principally responsible for detection over a wider range of wavelengths, even if graphene helps to improve the photocurrent value of detection [82]. SnS has distinctive optical absorption and anisotropic electronic features [114] that help with sensitive light sensing. The direct bandgap of SnS, which would enable a broad range of spectral detection from UV to NIR due to its high absorption coefficient and efficient electron-hole pair formation under illumination, was reported by Mahdi et al. with a bandgap of 1.65 eV and a detection range of up to 850 nm. Additionally, they mentioned that detection in the 850 nm band is caused by defects in SnS [147]. Studies from the literature reveal the existence of substantial density of states (DOS), which tend to fall within the SnS bandgap and can be connected to vacancies [261]. These defects are described as those from Sn vacancies, Sn^{2+}, Sn^{4+} ionized states of Sn, as well as from S vacancies. Similar reports on the presence of sulfur or tin vacancies within the bandgap of SnS may be found in [164,165]. Deep trap states are produced by these crystal imperfections. The band gap of the material may broaden due to these structural defects thus affecting the electronic states [262].

Two other important parameters that were looked at were the rise time and decay time. The calculated rise times for GPS A450, GPS A350, SnS A450 and SnS A350 are 1.1, 2.8, 4.8 and 4.9 s respectively, and the corresponding decay times are 1.7, 4.4, 5.3 and 6.8 s. The GPS A450 film had the quickest rise decay time, indicating that the sample had stronger photosensing capabilities. GPS films have quicker rise and decay times than SnS films because of the two-dimensional network of graphene that helps them properly route the charge carrier transport system.

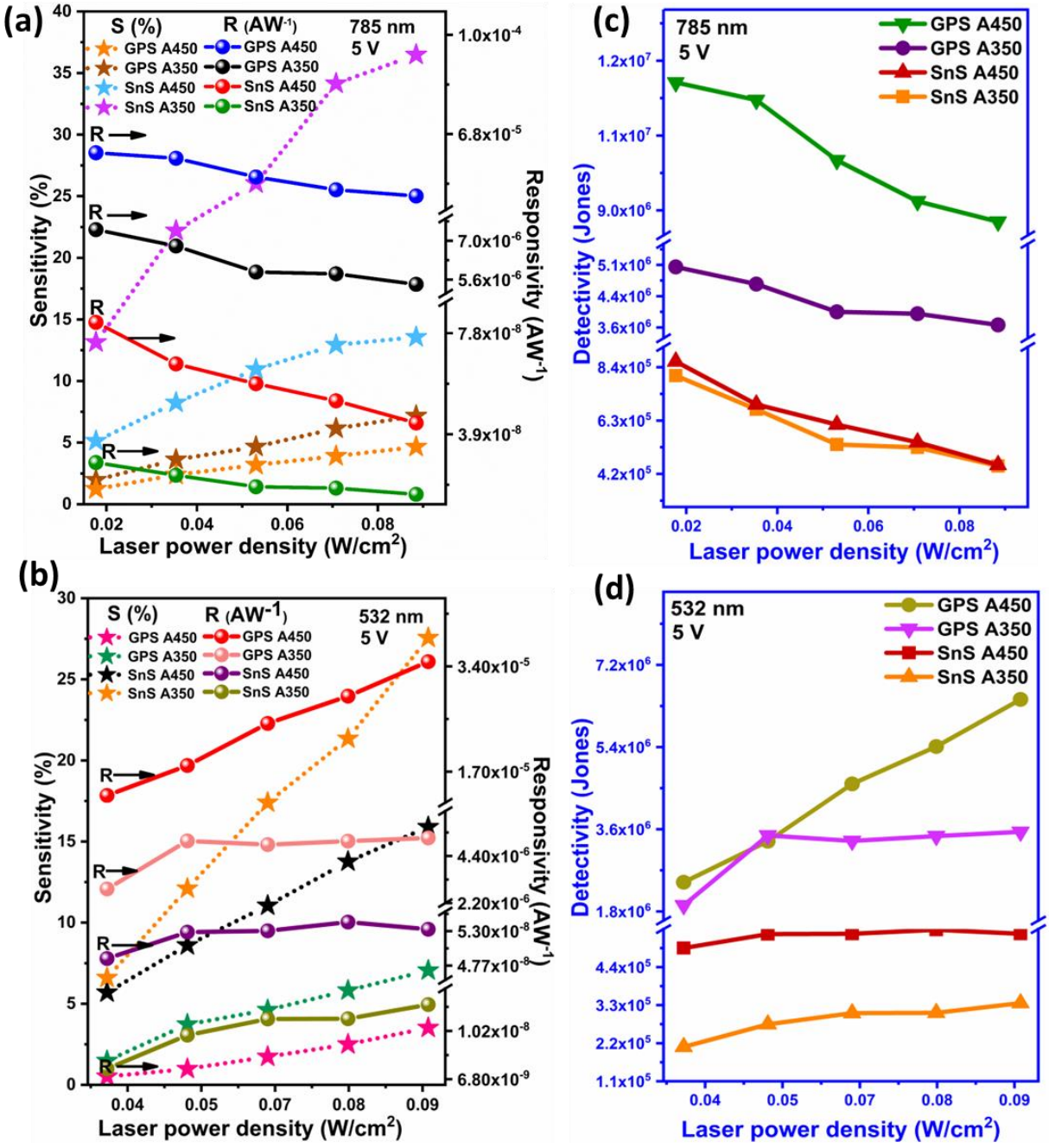


Fig. 4.22: Sensitivity(S) (represented using ★), responsivity(R) (represented using ●) and detectivity plots for annealed GPS and SnS films calculated from photoresponse curves obtained from illumination using (a, c) 785 nm and (b, d) 532 nm laser source.

Table 4.1 is a summary of important findings about the photodetection capabilities of several materials based on graphene-semiconductor NPs.

Table 4.1: Key device performance metrics of photodetection devices based on graphene-semiconductor nanoparticles.

	NP incorporated	**Wavelength of operation**	**Mode of operation**	**Photocurrent (A)**	**Bias voltage (V)**	**Responsivity (A/W)**	**Ref.**
Graphene	Ti_2O_3	Mid infrared (4.5-10 µm)	Phototransistor	6×10^{-11}	V_{sd}- 0.002 V_g- 80	150	[263]
Graphene	TiO_2	250-500 nm	Photodiode	10^{-6}	3	4.82×10^{-1}	[264]
Graphene QDs	TiO_2/plasmonic hybrid	UV 275 nm	Photoconductive	1.58×10^{-5}	10	5.4×10^{-2}	[259]
Graphene	GaN	UV 266 nm	Photoconductive	1.04×10^{-1}	5	2×10^{2}	[265]
Graphene	UCNPs	405-1064 nm	Phototransistor	$0.5\text{-}2.8\times10^{-6}$	1	10^{4}	[266]
Graphene	GaAs/UCNPs	980 nm	Photodiode	3.3×10^{-6}	0	5.97×10^{-3}	[267]
Graphene	ZnO NPs	UV 365 nm	Phototransistor	10^{-3}	V_{sd}- 0.001	3×10^{5}	[268]
Graphene	ZnO NPs	UV 375 nm	Photoconductive	5×10^{-3}	20	6.4×10^{2}	[247]
Graphene	ZnO NPs	UV < 400 nm	Phototransistor	10^{-3}	V_{sd} = 1 V_g = 0	4×10^{4}	[269]
Graphene	Perovskite $CH_3NH_3PbI_3$	400-800 nm	Phototransistor	6×10^{-3}	0	180	[270]
Graphene	Germanium	350 nm to 1650 nm	Photoconductive	9×10^{-6}	1	66.2	[260]
Graphene	SnS	UV-Vis-NIR (200-980 nm)	Photoconductive	10^{-5}	5	10^{-5}	**This work**

In general, the photovoltaic effect, photoconductive effect, photogating effect, photo-thermoelectric effect and pyro-phototronic effect are the operating mechanisms of photodetection technology, according to an analysis of various results on graphene-based photodetectors [271]. Our broadband photodetectors perform at extremely low voltages, producing high steady photocurrent and detectivity values when compared to the cutting-edge photodetectors mentioned above. Most graphene-semiconductor devices, according to recent research, are based on field-effect phototransistors or Schottky junction photodiodes. Our research may offer an alternative for

creating hybrid devices made of graphene that operate in photoconductive mode and in Ohmic contact.

Combining the observations, it was found that the hybrid's morphology, which included SnS NPs scattered over graphene layers in the film, enhanced the optical properties and the surface-to-volume ratio, all of which contributed to increasing the device's overall performance. The characteristics of the films were clearly impacted by annealing the samples as well. For demonstrating that the films are made of graphene and the pure phase of SnS, Raman analysis is crucial. The elemental distribution was identified evenly and unambiguously by XPS mapping. The idea that 2D materials like graphene can be combined with highly absorbent materials like SnS to create hybrid integrated properties with fast transport, tunable absorption and simple integration was used [227]. This helped to provide a platform for ultrasensitive and broadband photodetection. The hybrid here can be developed to different materials for sensitive and spectrally distinct light detection as well as extended wavelength detection. This study also opens the door for the material's use in batteries and other electrochemical energy storage systems, including lithium-ion batteries (LIBs) and sodium-ion batteries.

In terms of synthesis and fabrication, PLFL approach is a very simple top-down procedure in which at room temperature and pressure, a variety of nanostructured materials can be produced with straightforward experimental parameters that primarily includes physical changes. In comparison to the often-reported methods of synthesizing nanocolloid, the time required for this approach is less and does not entail adding surfactants or chemical stabilizers to help keep colloids stable. The final product we obtain can also be put to immediate use without further purification. The SnS:graphene wavelength-independent functional photodetector created by pulsed laser fragmentation of SnS powder in liquid, followed by spin-coating for film fabrication, is what makes this work unique. When compared to other chemical methods, using nanocolloids to create devices has the advantage of producing the least amount of chemical waste possible. The produced devices work consistently and reliably. One of the few examples of wavelength-insensitive detectors for the UV-Vis-NIR range is the SnS:graphene mentioned here. This opens up a new route for research into the technique for making semiconductor nanocolloids and the subsequent design of thin film devices.

4.4 Conclusions

- ∞ SnS NPs synthesized by PLFL exhibited spherical morphology with an average particle size of 17.3 ± 7.4 nm.
- ∞ Graphene NPs obtained by irradiating graphene lost its multi-layer like nature and exhibited spherical morphology and the absorbance spectra showed presence of polyyne bands.
- ∞ In the cases of films made with laser-irradiated graphene NPs, the effect of graphene was not visible.
- ∞ SnS nanocolloids with dispersed graphene achieved optimum results.
- ∞ Thin films of SnS and SnS:graphene was fabricated using these nanocolloids.
- ∞ A UV-Vis-NIR SnS:graphene hybrid operating as wavelength-independent photodetector was created .
- ∞ The inclusion of graphene enhanced the crystallinity of the films (XRD and Raman) and aided in their ability to absorb light throughout the whole UV-Vis-NIR spectrum (E_g reduced to 1.8 eV and 1.5 eV from 2.13 eV and 2.03 eV after graphene incorporation).
- ∞ The addition of graphene to SnS nanocolloids produced a morphology that encourages quick charge carrier transfer between the graphene layers and chalcogenide semiconductor nanoparticles.
- ∞ For GPS films, a value of detectivity in the order of 10^7 Jones was obtained.
- ∞ A straightforward two-terminal device that can be used at low voltage in ambient circumstances was created as an alternative to the usually described graphene-based detectors that operate in three-terminal phototransistor mode.

Chapter 5

Hybrids of SnS with metal/bimetallic nanoparticles for visible photodetection

5.1 Introduction

The primary significance of noble metal Ag/Au/Ag:Au nanoparticles is their ability of plasmon absorption, in the solar/visible spectrum. Due to their exceptional capacity to focus, regulate and route light at the nanoscale, plasmonic nanostructures offer a potential method for creating high-performance photodetectors [272]. Researchers used a novel technique that involved dispersing noble metal nanoparticles in the semiconducting layer in order to improve the ability of inorganic semiconductor NPs to capture light. Due to their potential use in plasmonic solar cells, photonic devices and surface plasmon enhanced sensors, noble metal NPs like Ag and Au implanted in a semiconducting medium have attracted a lot of attention. The hybrid thin films in this case were made by ultrasonic spray deposition technique using the nanocolloids of SnS and metals/bimetals (Ag/Au/Ag:Au) synthesized by pulsed laser ablation in liquid. Different techniques were employed to characterize these materials and photodetector investigations were conducted using thin films.

5.2 Experimental

5.2.1 Metallic/Bimetallic and SnS nanocolloidal synthesis

For the metallic and bimetallic nanoparticle syntheses, each of the targets of Ag, Au and Ag:Au (50:50) (from Beijing Goodwill Metals, China (99.99% purity)) were placed in a 100 mL beaker with 30 mL IPA (Fermont; analytical grade, 99.9% purity). The laser beam was focused onto the targets using a lens at a focal distance of 30 cm from the target. A nanosecond pulsed laser with a wavelength of 532 nm; pulse width of 10 ns and a frequency of 10 Hz was used. Ag, Au and Ag:Au targets were respectively ablated for 5, 20 and 10 minutes, changing the ablation spots manually at constant intervals. The time of ablation was optimized based on the measurements of absorption spectra of the colloids. Each target was initially subjected to 30 seconds of ablation, which continued until a saturation in the absorption was noticed. The absorption spectra measured in all three cases are given in Fig. 5.7 of the results and discussion section. Using an energy meter (Thorlabs PM100D with ES245C pyroelectric energy sensor), the output energy was calculated as 280 mJ and the laser fluence was 0.71 J/cm^2.

For the synthesis of SnS nanoparticles, the target of SnS was laser ablated for 10 minutes using two different wavelengths i.e., 532 and 1064 nm from the output of a Nd:YAG pulsed laser (same specifications as mentioned above). For 532 nm laser, the target was immersed in 30 mL IPA; and for 1064 nm laser a volume of 60 mL IPA was used. Larger sized particles are formed while ablating SnS in IPA using 1064 nm [82]. For the synthesis of SnS, no focusing lens was used. The laser fluence calculated was 0.84 and 0.71 J/cm^2 for 1064 and 532 nm ablation respectively.

In another set of experiments, the same approach as described above was used to synthesize Ag, Au, Ag:Au, and SnS NPs using an output from a low energy Nd:YAG laser with a 532 nm wavelength, 10 ns pulse width and a frequency of 100 Hz. The laser fluence in this case was calculated as 0.23 J/cm^2 corresponding to an output energy of 90 mJ. A laser ablation time of 10 minutes was used for ablating all the targets in 30 mL IPA. For hybrid colloidal synthesis, the nanocolloids of SnS and Ag, Au, Ag:Au were mixed separately and ultrasonicated well for 15 minutes.

5.2.2 SnS-metallic/bimetallic hybrid thin film fabrication

The thin films were fabricated on glass substrates by an ultrasonic spray deposition system (Zhengzhou Tainuo Film Materials Co., Ltd.) using a 40 kHz, 130 W ultrasonic nozzle, while the spray rate, droplet size and speed were carefully controlled by a computer program. The ultrasonic source current was set to 0.09 A, and compressed gas at 0.1 MPa was employed to form and transport the aerosol to the heated surfaces. The optimum conditions decided through multiple trials were that good quality films were obtained when a total volume of 240 mL nanocolloid was sprayed on the substrate kept at 125 ℃ and the spray rate was 3 mL/min at 22.3 rpm. For a total of 240 mL solution, equal volumes of SnS and the metallic/bimetallic nanocolloids were taken (120 mL SnS+120 mL Ag/Au/Ag:Au). The hotplate temperature of 125 ℃ was preferred based on the boiling point of the solvent used (IPA~82.5 ℃). At lower temperatures (100 ℃), the spray droplets took more time to evaporate leaving spots/drying marks on the surface of the films. For higher temperature (150 ℃), coatings were not uniform which also peeled off from the substrate. After deposition, the films were taken off the hotplate when the temperature was lowered below 70 ℃ and as soon as they were dried. The schematic representation of the methodology (nanocolloid synthesis and ultrasonic spray deposition for film fabrication) is given in Fig. 5.1.

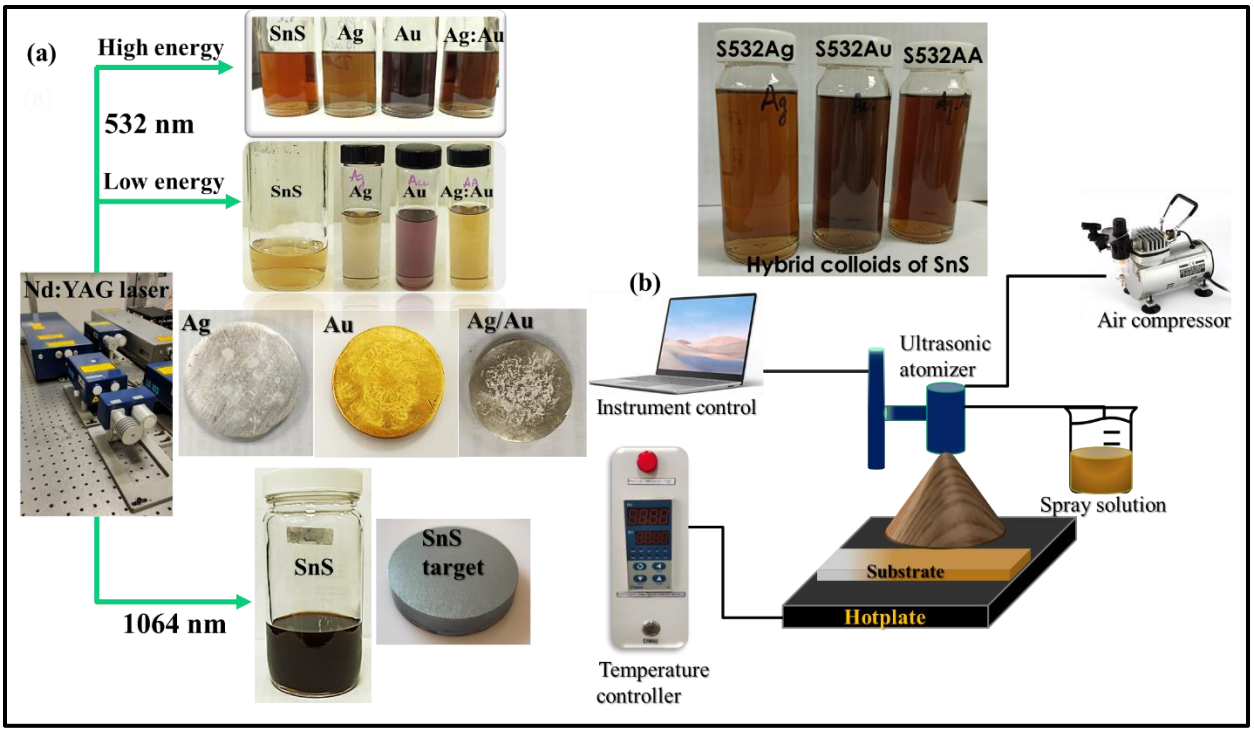


Fig. 5.1: Schematic representation of the (a) experimental methodology for the synthesis of SnS, Ag, Au and Ag:Au nanocolloids and (b) film fabrication from these nanocolloids using ultrasonic spray deposition technique.

The hybrid films of S532 and S1064 are given in Fig. 5.2 (a). The images of the SnS:Ag hybrid films synthesized by varying substrate temperature is given in Fig. 5.2 (b). For the trials, only half the amount of nanocolloids was sprayed (i.e., 120 mL), so the films appear much lighter. The nanocolloids and films of SnS synthesized using 532 and 1064 nm laser are labelled as S532 and S1064 respectively; the Ag:Au bimetallic is labelled as 'AA'(eg: S532 AA represents the colloids/films of SnS synthesized by 532 nm laser with Ag:Au nanoparticles incorporated).

For the second set of films, a total of 120 mL nanocolloid (60 mL SnS+ 60 mL Ag/Au/Ag:Au) and an additional 30 mL of metallic/bimetallic colloid were sprayed as the top layer for film formation using the nanocolloids from the low energy laser (LQ629) at a substrate temperature of 125 °C and a spray rate of 7 mL/min. In Fig. 5.2 (c), photos of the SnS hybrid films that were created using these nanocolloids are provided. 'LE' in the figure notations denotes the colloids and films synthesized using low energy laser. The films formed using high energy laser

were annealed in an MTI corporation low vacuum furnace (VBF-1200X, ~ 10^{-2} Torr) at 350, 375 and 400 °C for 1 h; and the films using low energy laser at 400 °C for 1 h.

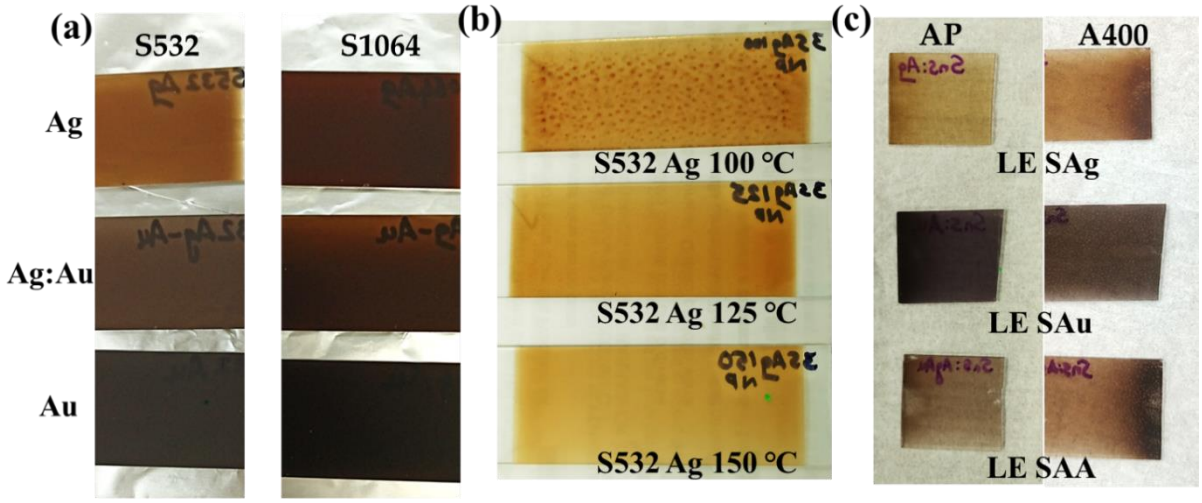


Fig. 5.2: Hybrid films of (a) SnS (532 and 1064 nm) with metallic/bimetallic NPs synthesized using nanocolloids from high energy laser (b) SnS:Ag fabricated in glass substrates placed at different substrate temperatures (c) SnS (under as prepared and annealed condition) with metallic/bimetallic NPs synthesized using nanocolloids from low energy laser.

5.3 Results and Discussion

5.3.1 Transmission Electron Microscopy

The morphology and crystal structure of the SnS NPs obtained in the two sets of PLAL using 1064 and 532 nm analyzed by bright field-TEM, STEM and HRTEM are given in Fig. 5.3. Spherical interchained particles were observed and the average particle size of SnS NPs synthesized by 1064 nm laser (S1064) were higher than that by 532 nm (S532). This is mainly due to the effect of laser wavelength on the generation of NPs. The discussion for the same has already been made in Chapter 2. For SnS, the planes were indexed based on the ICDD card 039-0354, belonging to the orthorhombic crystal structure. No other phases of SnS were identified from the HRTEM analyses.

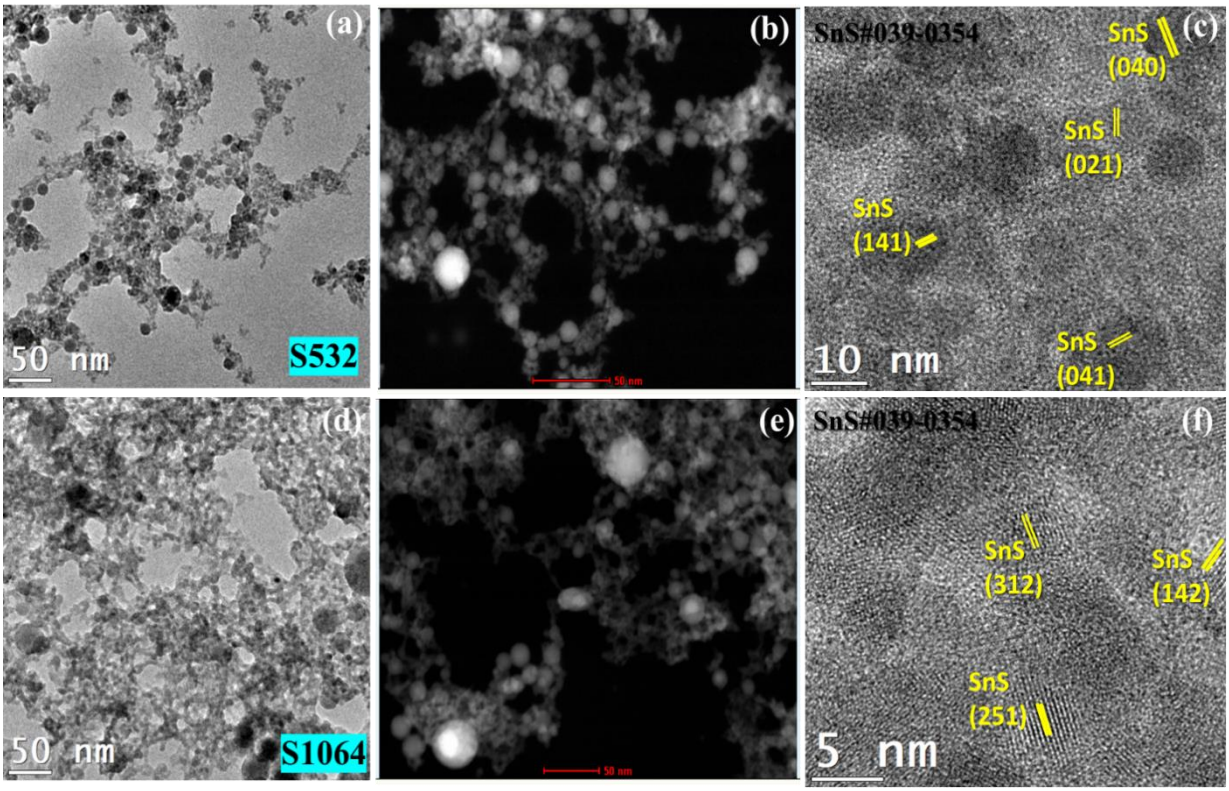


Fig. 5.3: (a, d) TEM images (b, e) STEM images and (c, f) HRTEM images of S532 and S1064 NPs.

Fig. 5.4 shows the TEM, STEM and the average particle size distribution of the metallic and bimetallic NPs synthesized by PLAL. Ag, Au and Ag:Au (AA) NPs exhibit spherical morphology but the average particle sizes differ. Average particle size for Ag NPs is 13.98 ± 6.7 nm; for Ag:Au, it is 12.15 ± 5.09 nm; and for Au, as 5.04 ± 1.59 nm, the lowest particle size observed.

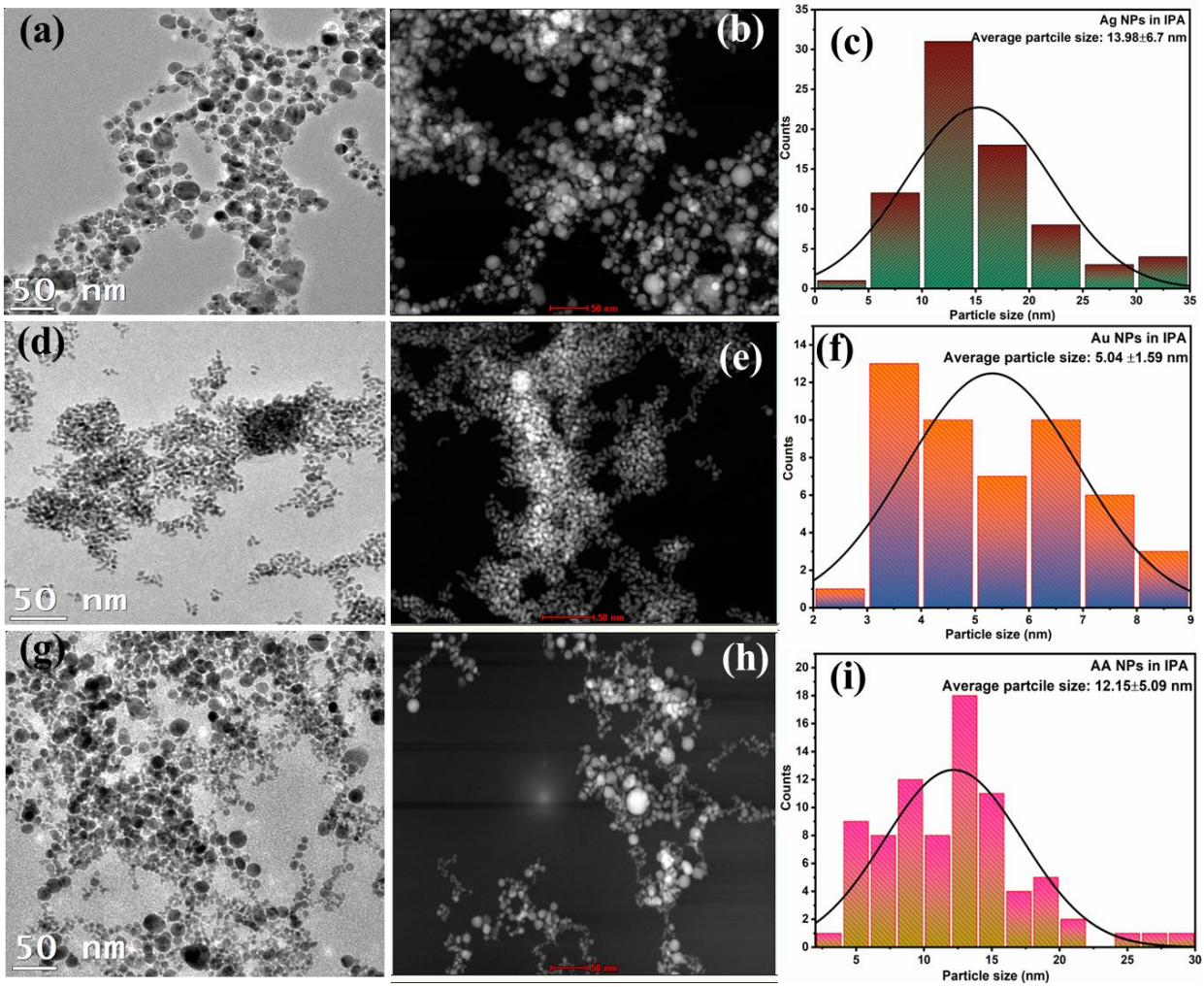


Fig. 5.4: (a, d, g) TEM images (b, e, h) STEM images and (c, f, i) average size distribution chart of Ag, Au and Ag:Au NPs.

The TEM, STEM, HRTEM and EDX analyses of SnS hybrid NPs i.e., SnS NPs synthesized by 532 and 1064 nm mixed with Ag, Au and Ag:Au NPs are shown below. The planes of Ag and Au were indexed to ICDD cards 004-0783 and 004-0784 respectively and both had cubic structure. The value achieved for Ag:Au is actually extremely near to those of pure Ag and Au. This may be explained by the fact that Ag and Au have nearly equal lattice constants, making them indifferentiable in HRTEM analysis. For S532 and S1064 hybrids, the planes of SnS identified were matching with the ICDD database of SnS mentioned earlier. From EDX analysis, the respective elements were also identified. The hybrids of S532 are shown in Fig. 5.5, while those of S1064 are shown in Fig. 5.6.

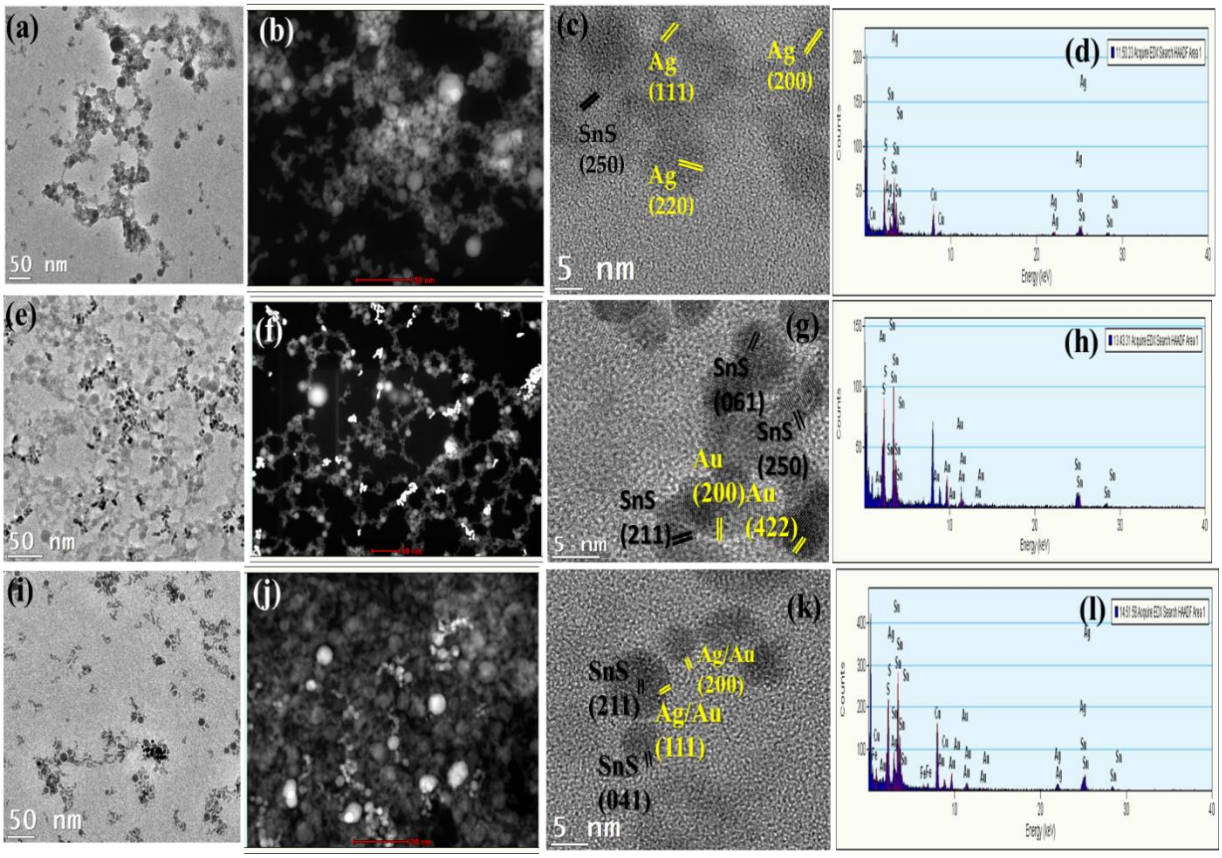


Fig. 5.5: (a, e, i) TEM images (b, f, j) STEM images (c, g, k) HRTEM images and (d, h, l) EDX of S532 NPs with Ag, Au and Ag:Au NPs.

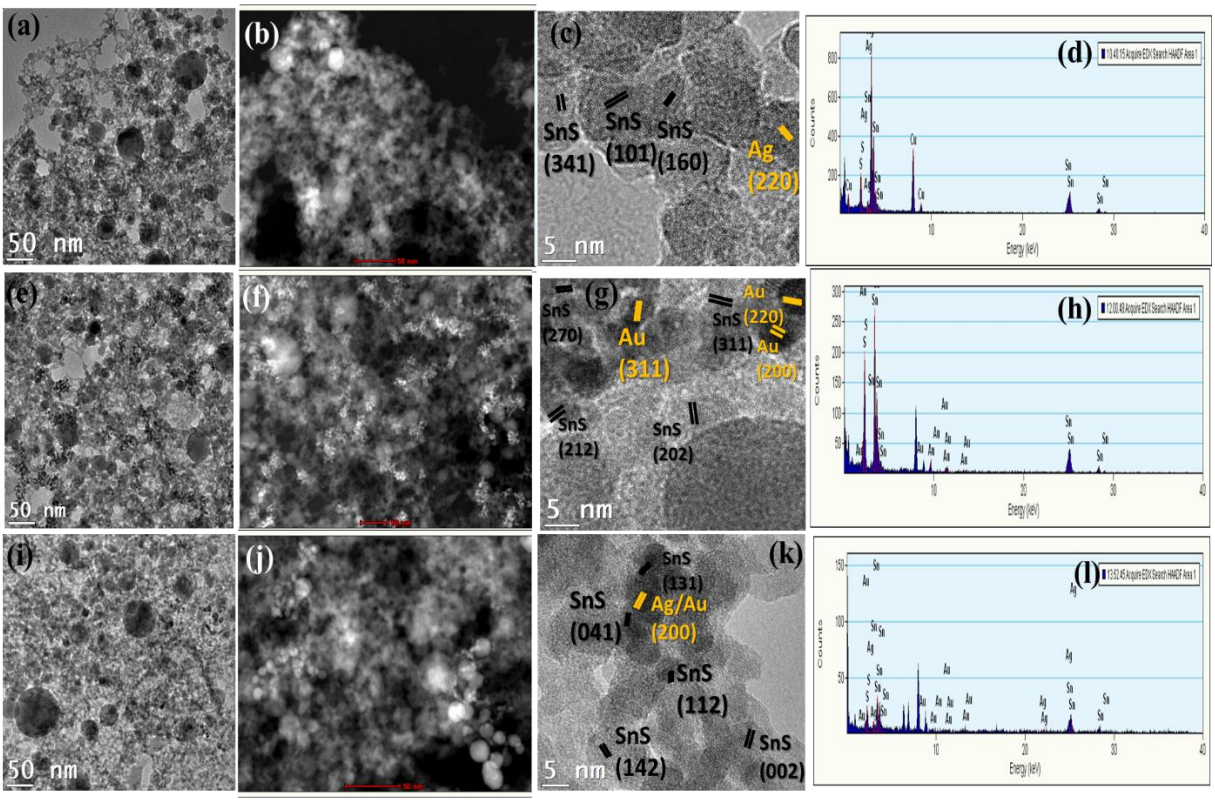


Fig. 5.6: (a, e, i) TEM images (b, f, j) STEM images (c, g, k) HRTEM images and (d, h, l) EDX of S1064 NPs with Ag, Au and Ag:Au NPs.

5.3.2 UV-Vis Spectroscopic studies

An absorption saturation with increase in ablation duration (Fig. 5.7) has been mentioned in the experimental section of this chapter. The reason is explained as follows. Higher ablation times result in a fall in the ablation rate because more nanoparticles are created with increasing ablation rate and they gather near to the laser spot. The generated nanoparticles screen the incident laser light once their number is sufficiently large. As a result, the incident laser intensity at the metallic and bimetallic bulk target is reduced, which prevents the number of nanoparticles from further increasing and causes the absorbance to become constant [273].

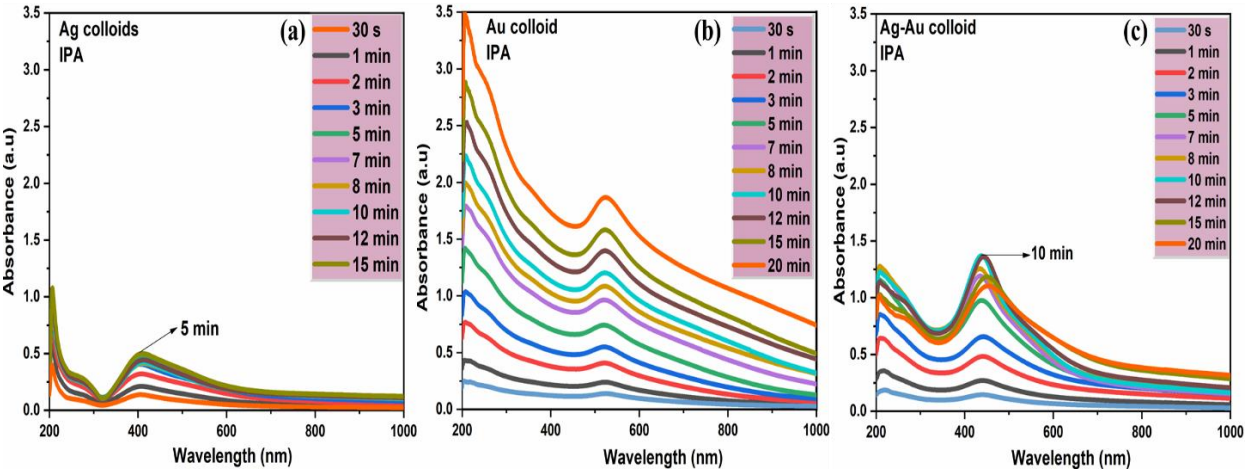


Fig. 5.7: The absorption plots of (a) Ag, (b) Au and (c) Ag:Au NPs in IPA for different ablation times varying from 30 s to 20 min.

The absorption spectra of Ag, Au and Ag:Au NPs obtained by PLAL are given below in Fig. 5.8 (a, c). The plasmonic peaks were observed around 405, ~525 and ~440 nm for Ag, Au and Ag:Au respectively in both the cases (NPs produced from high and low energy lasers). Due to excitations from surface plasmons, metallic NPs display distinctive, sharp and well-defined peaks in the visible region (i.e. SPR or surface plasmon resonance) [274]. The position and shape of the SPR bands provide information about the size distribution and polydispersity (alteration in size and shape) of metal nanoparticles. While the SPR location for the most frequently used chemical technique of preparing Ag nanoparticles is centered in the vicinity of 415-425 nm, the absorption spectra of plasmonic Ag NPs show that the resonance is shifting towards a short-wavelength range (405 nm) due to the influence of small-sized nanoparticles [275]. It is notable that the plasmon absorptions of the Ag:Au bimetallic NPs are red-shifted from those of a monometallic Ag peak owing to the presence of Au content in them. The absorption peaks observed matches with the values reported in literatures [276]. Fig. 5.8 (b, d) shows the hybrid colloids of SnS with metallic and bimetallic NPs. The absorption edge is seen for S532 nanocolloids from Set I (high energy laser) and Set II (low energy laser) around 600 nm, while for S1064 nanocolloids from Set I, the absorption begins around 800 nm. On incorporation of each of the monometallic and bimetallic NPs, the absorptions were blue shifted for nanocolloids from Set I. The main reason for this shift is due to the size of the noble metallic/bimetallic NPs. The plasmonic peaks were not noticeable and this may be due to the higher concentration of SnS NPs in comparison to the Ag, Au and

Ag:Au NPs. In contrast, the hybrid nanocolloids in Set II showed plasmonic peaks, particularly in the case of colloids with Ag and Au NP, and their absorption edges were nearly identical to those of SnS nanocolloids. This is mostly because the concentration of nanocolloids of SnS in this case was far lower than that of the SnS colloids created with a high energy laser, making the plasmonic peaks more obvious.

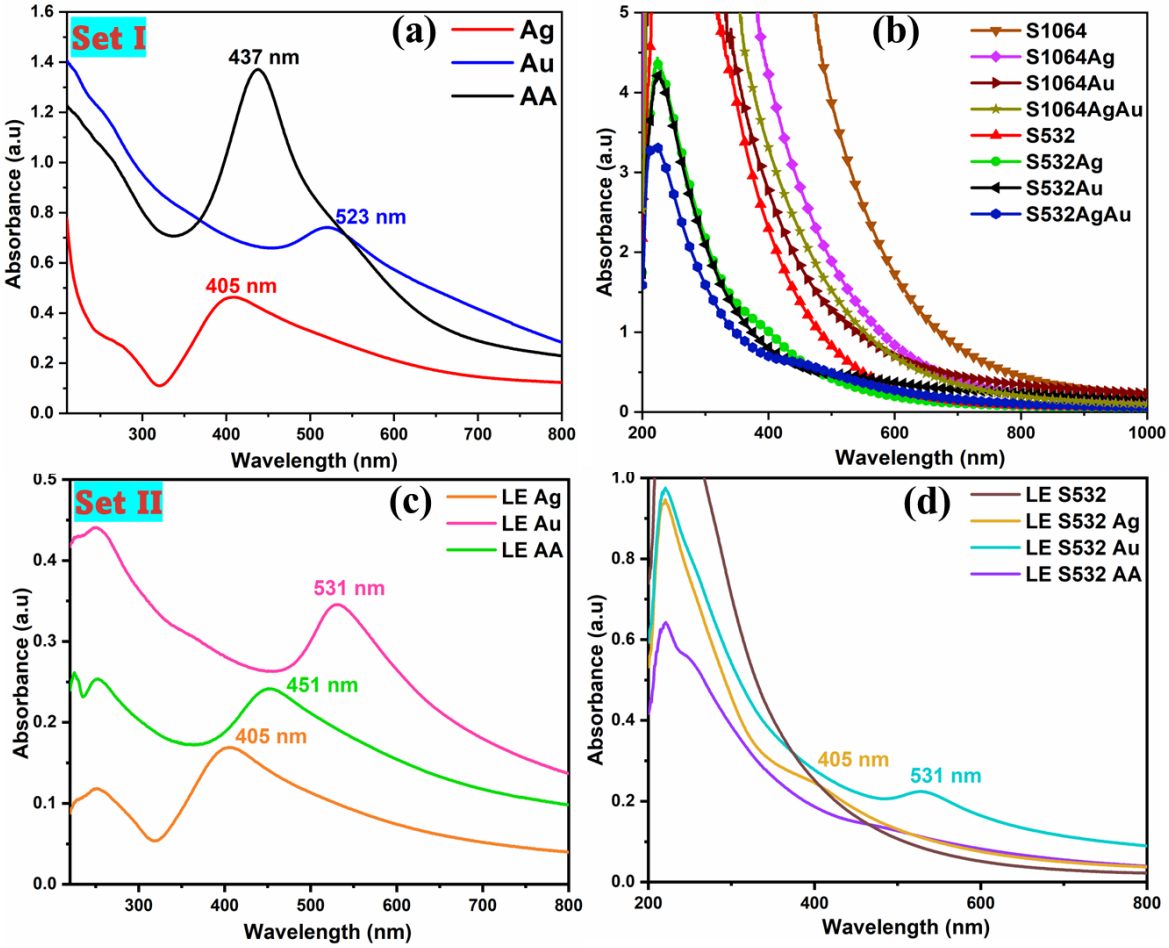


Fig. 5.8: Absorption spectra of (a, c) monometallic and bimetallic NPs (b, d) Hybrid colloid of SnS: Ag, Au and Ag:Au NPs synthesized using high energy and low energy lasers.

Fig. 5.9 (a) and (b) depicts the absorption spectra of the hybrid films of S532 and S1064 fabricated by ultrasonic spray deposition and their respective bandgaps were also calculated by Tauc plot [277], and is given in Fig. 5.9 (c) and (d). The bandgap values are between 1.20 to 1.43 eV for S532 hybrid films and between 1.27 to 1.48 eV for S1064 hybrid films. The optical absorption spectra of the films especially that for S532:AA and S1064:Au show resonances in the

visible and near-UV spectral area that come from both the metal's (plasmon resonance peak) and the semiconductor's contributions (exciton band edge absorption peak). An absorption tail is seen in the NIR band, and it diminishes as it moves into the IR. The constant increase in the hybrids' absorbance toward higher photon energy is caused by the excitation of bound electrons into higher bands in both the metal and semiconductor portions [31]. The % transmittance and reflectance of the S532 and S1064 hybrid films are given in Fig. 5.9 (e-h).

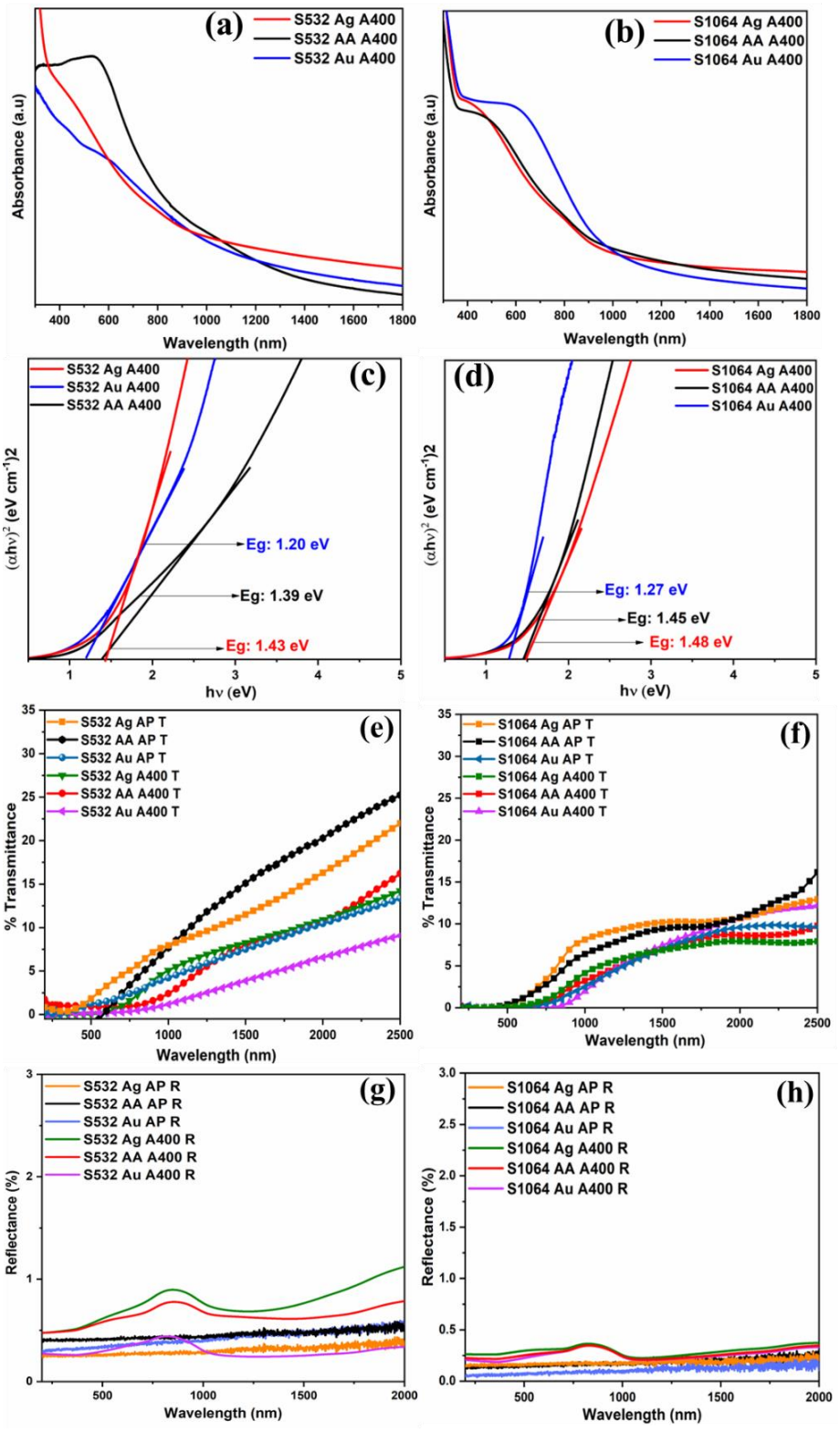


Fig. 5.9: (a, b) Absorption spectra (c, d) Tauc plot (e, f) % Transmittance and (g, h) % Reflectance of S532 and S1064 as-prepared and annealed hybrid films.

The absorbance spectra of the hybrid films of S532 that were deposited utilizing low energy laser colloids together with their transmittance and reflectance are shown in Fig. 5.10 (a, b). Also, the absorption, transmittance and reflectance spectra of S1064:Ag films under as-prepared and different annealing conditions are given in Fig. 5.10 (c, d). The % reflectance of all the films were below 1% so it could be neglected. The film that underwent annealing at 400 °C had the lowest transmittance of all the films, indicating that other films are transparent in comparison to this one. Additionally, it suggests that these films have a higher absorbance, which is one of the reasons the investigations were focused on 400 °C annealed films.

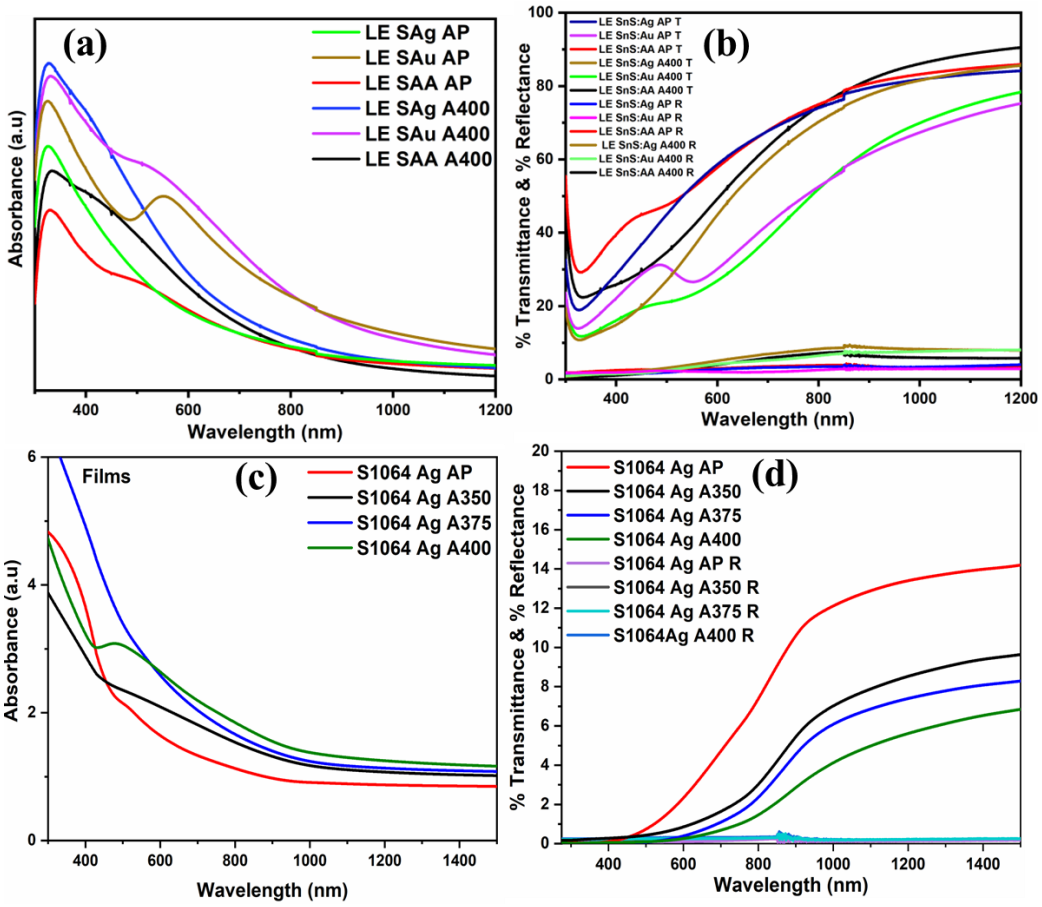


Fig. 5.10: (a) Absorption spectra of SnS hybrid films prepared using colloids from low energy laser and their (b) % Transmittance and % Reflectance (c, d) Absorption spectra, % Transmittance and % Reflectance of the SnS:Ag hybrid films annealed at different temperatures.

5.3.3 X-ray diffraction studies

The X-ray diffraction (XRD) analysis of the Ag-incorporated SnS films (S1064) annealed at 350, 375, and 400 °C is shown in Fig. 5.11. The peaks were matched to the orthorhombic crystal structure of SnS (ICDD#039-0354). No peaks corresponding to Ag could be detected in XRD and this may either be due to the successful incorporation of Ag into SnS without any change in crystal structure or due to the low concentration of the noble metallic NPs incorporated. The peak intensities were increasing as the annealing temperatures increased. This suggested an increase in crystallite size and, hence, using the Debye-Scherrer equation [184], the crystallite sizes of the films were calculated. The values were 41.9, 39.4 and 38.7 nm respectively, for the films annealed at 400, 375 and 350 ℃. No other impurity peaks were noted. The highest intensity peak was observed at 2θ=31.7º corresponding to the (040) plane. Other peaks are observed at 2θ = 30.67, 39.07 and 45.34º matching to the (101), (131) and (002) planes. Planes related to (120) and (021) are more visible in 400 °C annealed SnS:Ag hybrid films. The replacement of Sn^{2+} by Ag^{+} ions may account for the minor shift in the peaks observed in the films in comparison to the standard data [278]. Based on the XRD analysis and optical studies, further research was focused on the samples annealed at 400 ℃ alone.

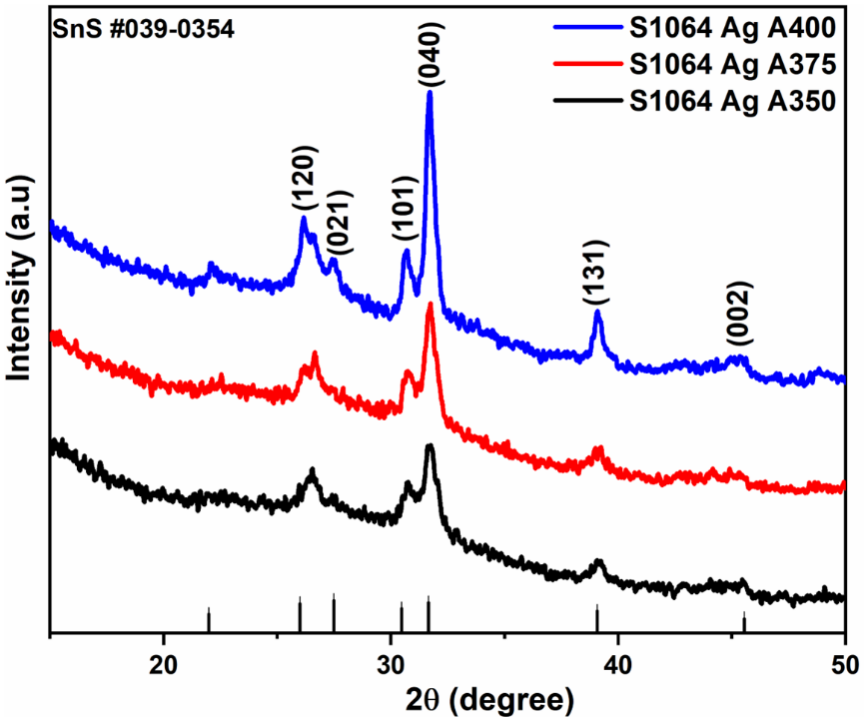


Fig. 5.11: XRD patterns of the SnS:Ag hybrid films annealed at 350, 375 and 400 ℃ for 1 h.

5.3.4 Scanning Electron Microscopy

In secondary electron imaging mode, the SEM micrographs of the annealed films were recorded. The images of S532 and S1064 films were captured at scales of 100 µm, 3 µm, 1 µm and 500 nm and is given in Fig. 5.12 and Fig. 5.13 respectively. A 3 kV voltage and 10 µA current was applied to collect the images. The surface of the samples shows a porous layered type. The high magnification image shows the porous surface of the films, while the low magnification image clearly shows the layered morphology. Similar morphology has been reported in the fabrication of SnS films by spray deposition using the nanocolloids of SnS synthesized by PLAL [88]. The spraying conditions, the substrate temperature and the evaporation rate of the solvents influence the morphology. It has been reported that porous morphology is beneficial for optoelectronic applications [279].

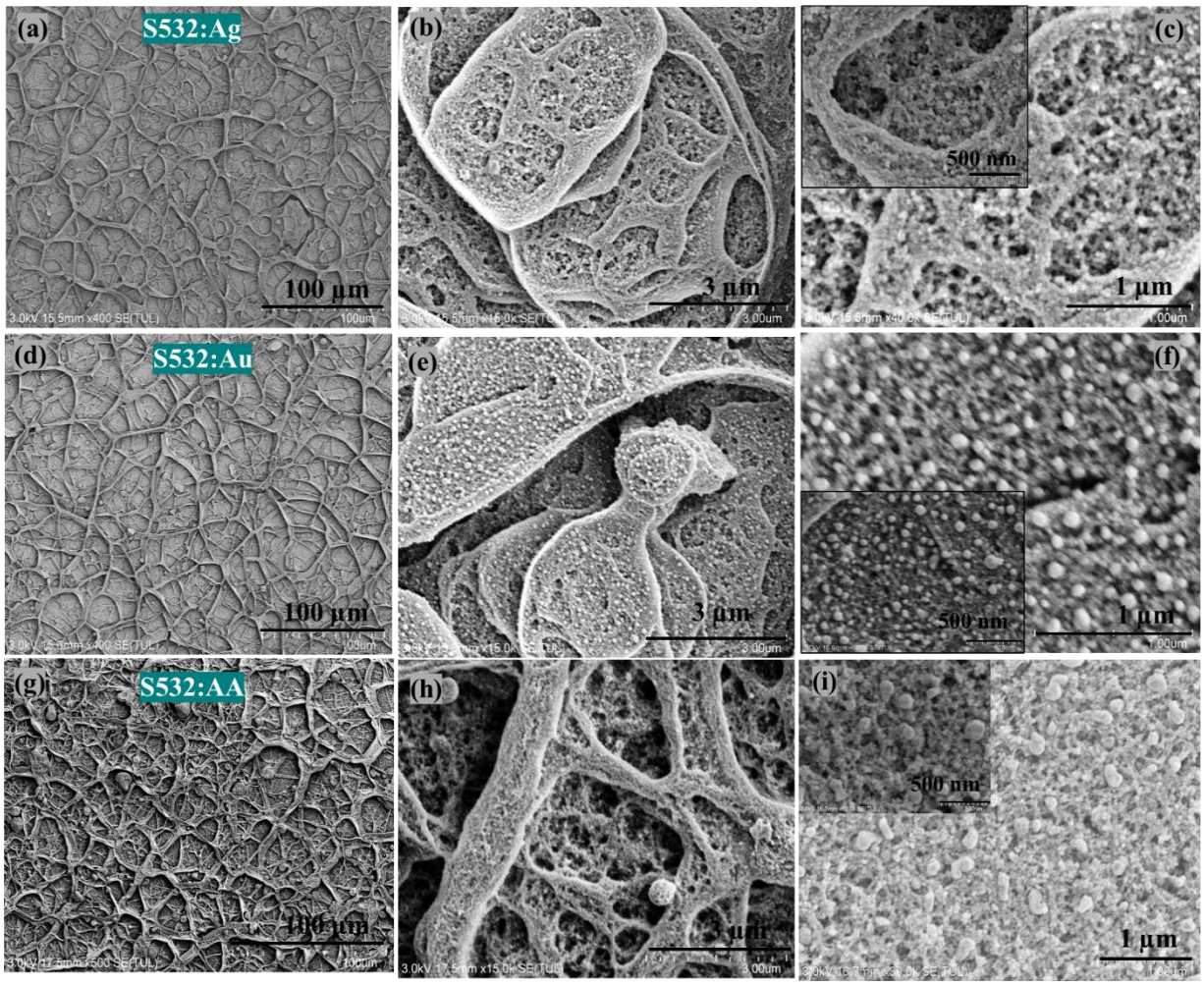


Fig. 5.12: SEM images of S532 hybrid films with Ag, Au and Ag:Au annealed at 400 °C.

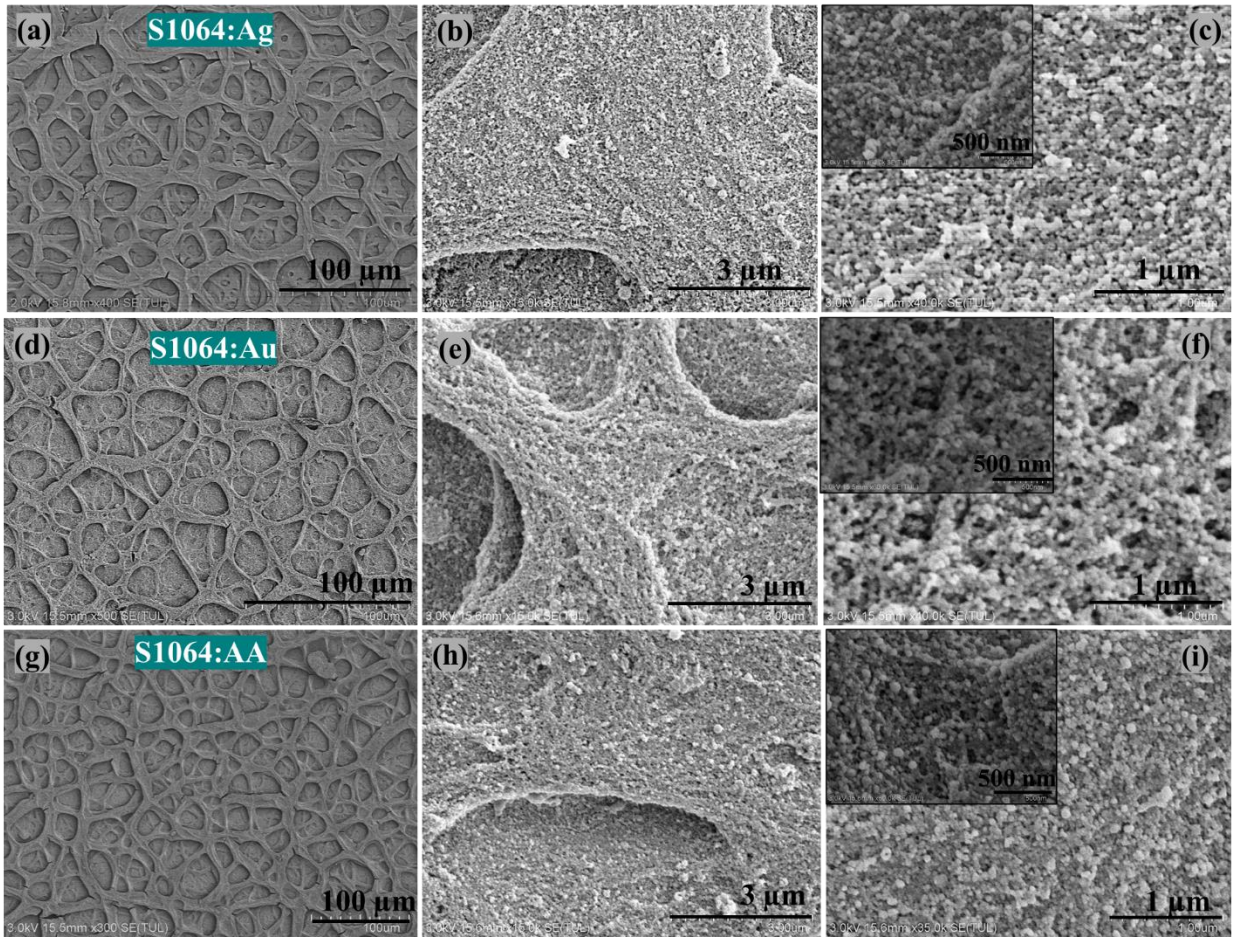


Fig. 5.13: SEM images of S1064 hybrid films with Ag, Au and Ag:Au annealed at 400 ℃.

5.3.5 X-ray photoelectron spectroscopy

The XPS analysis of the annealed hybrid S532 films fabricated using a low energy laser is presented below. The high-resolution spectra, both before and after etching of Sn 3d, S 2p, Ag 3d, Au 4f are provided. The binding energy for the C 1s peak was set to 284.6 eV for calibration. Fig. 5.14 and Fig. 5.15 depict the elemental spectra before and after etching, respectively. For hybrid films with monometallic Ag, the peak values observed around ~368 eV and ~374 eV corresponds to the typical Ag $3d_{5/2}$ and Ag $3d_{3/2}$ in pure Ag [280]. For Au 4f, the peaks seen at ~ 84 eV and ~ 87 eV matches the Au $4f_{7/2}$ and Au $4f_{5/2}$ peaks [281]. It can be concluded that pure Ag and Au NPs were generated by PLAL. The peaks of Ag and Au were marginally moved to the higher binding energy but around the same region for the films containing Ag/Au NPs indicating its bimetallic nature [282] and that no other oxidation states of Ag and Au were formed [283]. The splitting energy between the doublets of Ag 3d was maintained at 6 eV and that of Au 4f at 3.7 eV. For high resolution peaks of Sn 3d (Fig. 5.14 (a-c)), the peaks of Sn

$3d_{5/2}$ and Sn $3d_{3/2}$ were observed around 485 eV and 494 eV [191]. For S 2p peaks, the peaks of S 2p was seen at ~162 eV [191]. The binding energy values after etching corresponding to all the elements are tabulated in Table 5.1.

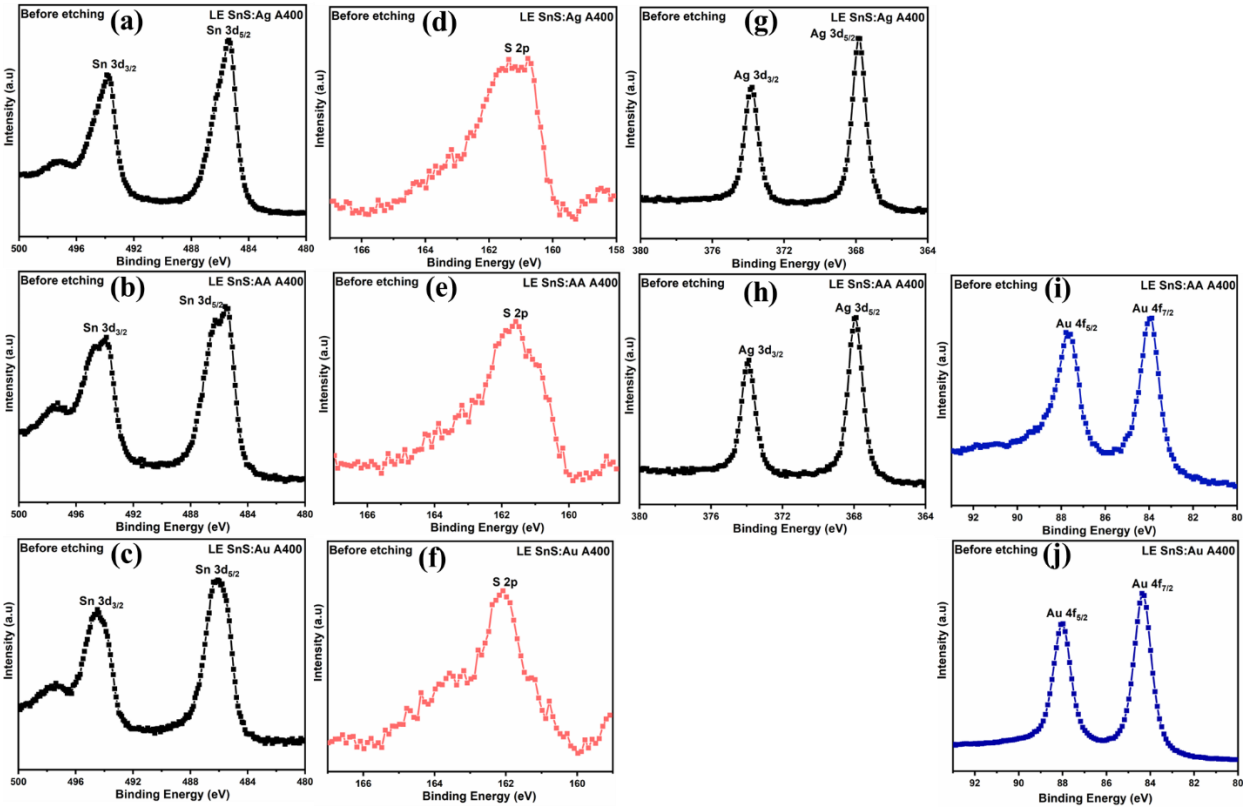


Fig. 5.14 : XPS spectra of (a-c) Sn 3d (d-f) S 2p (g, h) Ag 3d and (i, j) Au 4f in the hybrid SnS films (before etching).

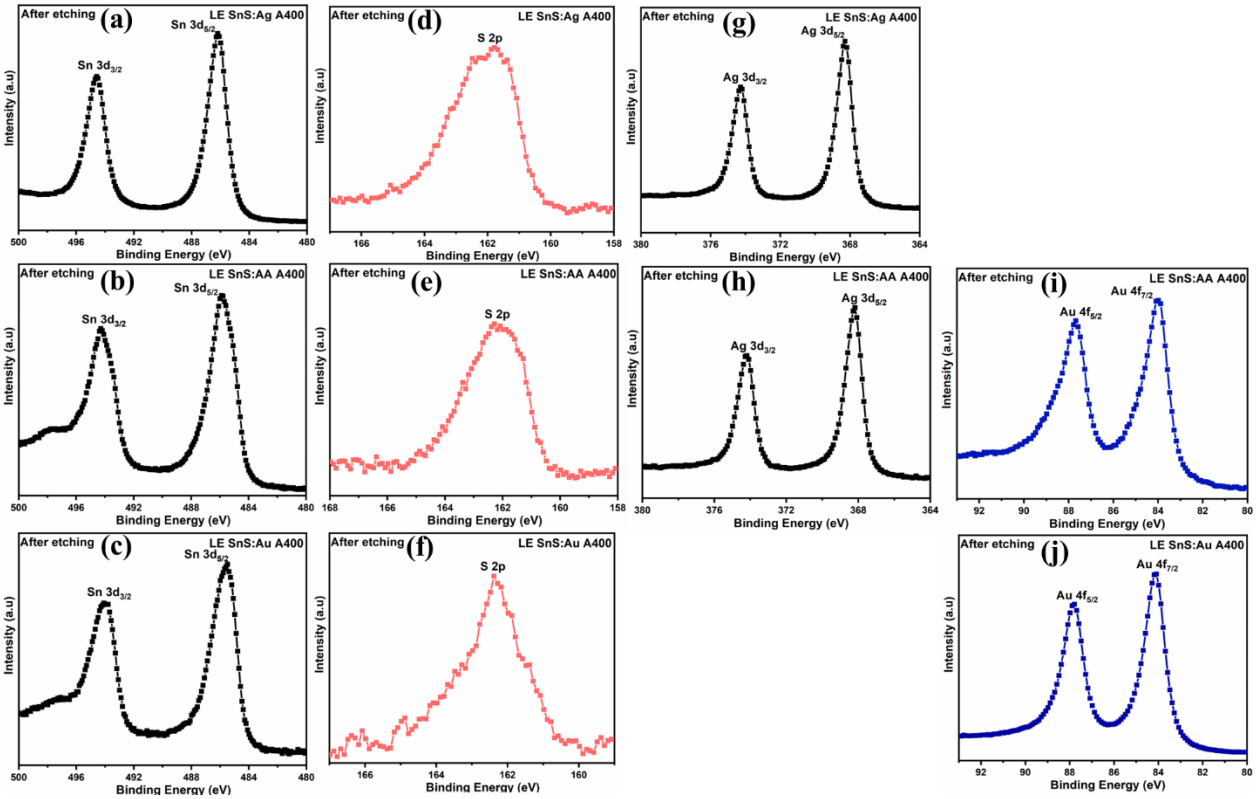


Fig. 5.15: XPS spectra of (a-c) Sn 3d (d-f) S 2p (g, h) Ag 3d and (i, j) Au 4f in the hybrid SnS films (after etching).

Table 5. 1: Binding energies of Sn, S, Ag and Au in the hybrid SnS films after etching.

Films	**Binding Energy (eV)**						
	Ag 3d		**Au 4f**		**Sn 3d**		**S 2p**
	Ag $3d_{5/2}$	**Ag $3d_{3/2}$**	**Au $4f_{7/2}$**	**Au $4f_{5/2}$**	**Sn $3d_{5/2}$**	**Sn $3d_{3/2}$**	**S $2p_{3/2}$**
LE SAg A400	368.25	374.25	-	-	486.15	494.56	162.00
LE SAA A400	368.29	374.29	84.11	87.81	485.82	494.23	162.32
LE SAu A400	-	-	84.00	87.71	485.61	494.02	162.15

5.3.6 I-V and Photoresponse studies

Since the films from low energy lasers were rather thin and did not produce any significant results due to the low concentration of the nanocolloids, the electrical properties of the films presented are exclusively based on the nanocolloids created from high energy lasers. The I-V graphs of the annealed hybrid films of S532 and S1064 are given in Fig. 5.16 (a, b). The linear I-V plot demonstrates the Ohmic contact between the silver electrodes and the film.

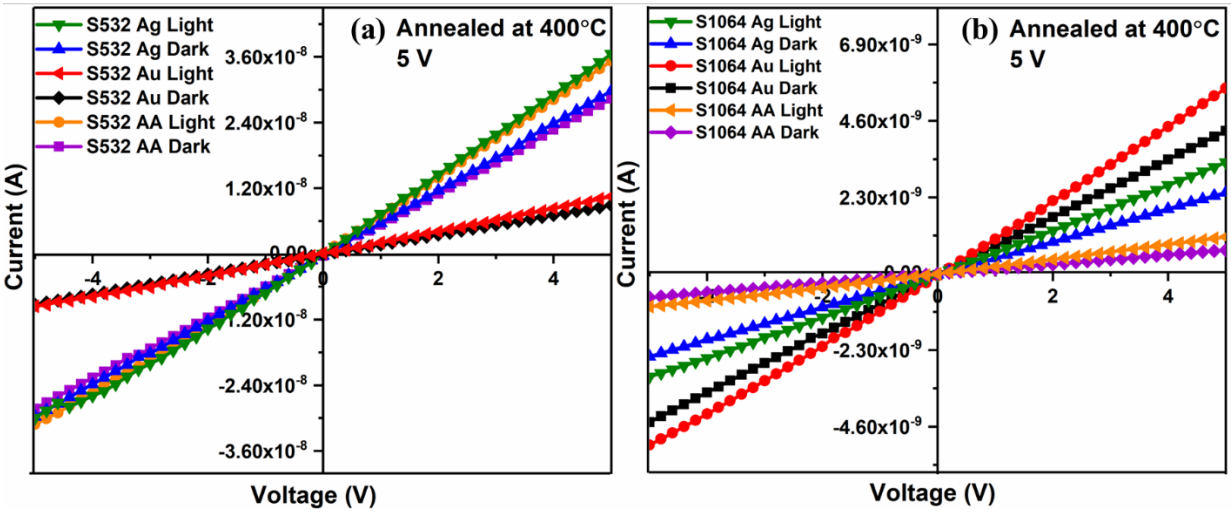


Fig. 5.16: I-V plots of (a) S532 hybrid films (b) S1064 hybrid films under dark and under illumination using W lamp.

The photocurrent measurements of the S1064 hybrid films with silver NPs (S1064 Ag) at different annealed conditions (350, 375, 400 and 450 ℃) recorded at a bias voltage of 10 V is given in Fig. 5.17. It clearly shows that as the annealing temperature raised from 350 °C to 400 °C, the photocurrent values increased as well, but beyond 400 °C, the values started to decrease, suggesting the change in stoichiometry or formation of other phases such as SnS_2, Sn_2S_3 or SnO_2, which often occurs at high temperatures [284]. Therefore, further research was conducted using hybrid films annealed at 400 °C.

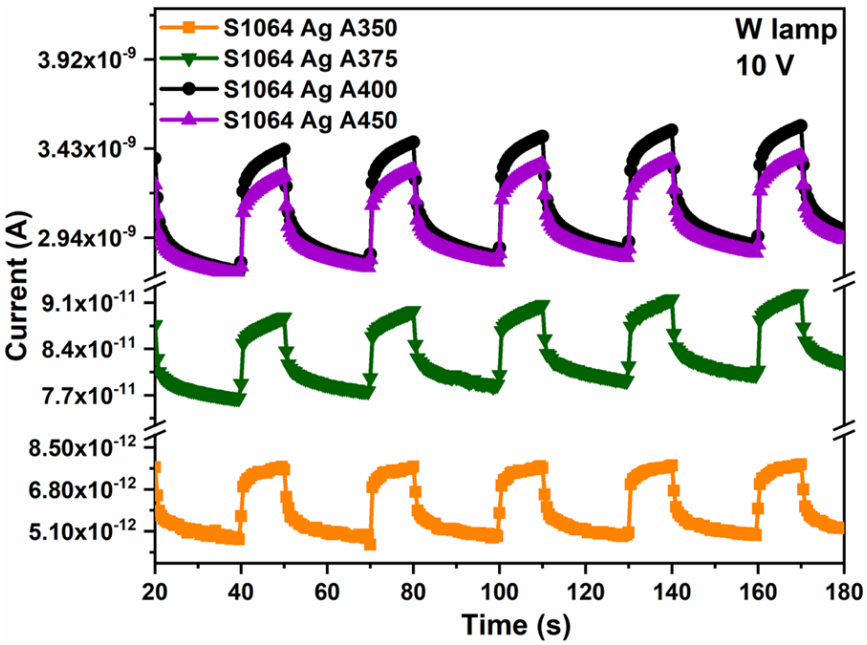


Fig. 5.17: Cyclic photoresponse of the SnS:Ag hybrid films annealed at different temperatures.

Fig. 5.18 and Fig. 5.19 shows the photoresponse recorded for increasing voltages applied from 0.5 to 10 V. It is evident that the photocurrent rises with applied bias voltage because of the rise in carrier drift velocity, which is directly proportional to applied bias voltage. Therefore, an increase in carrier drift velocity results in a decrease in the transit time [147].

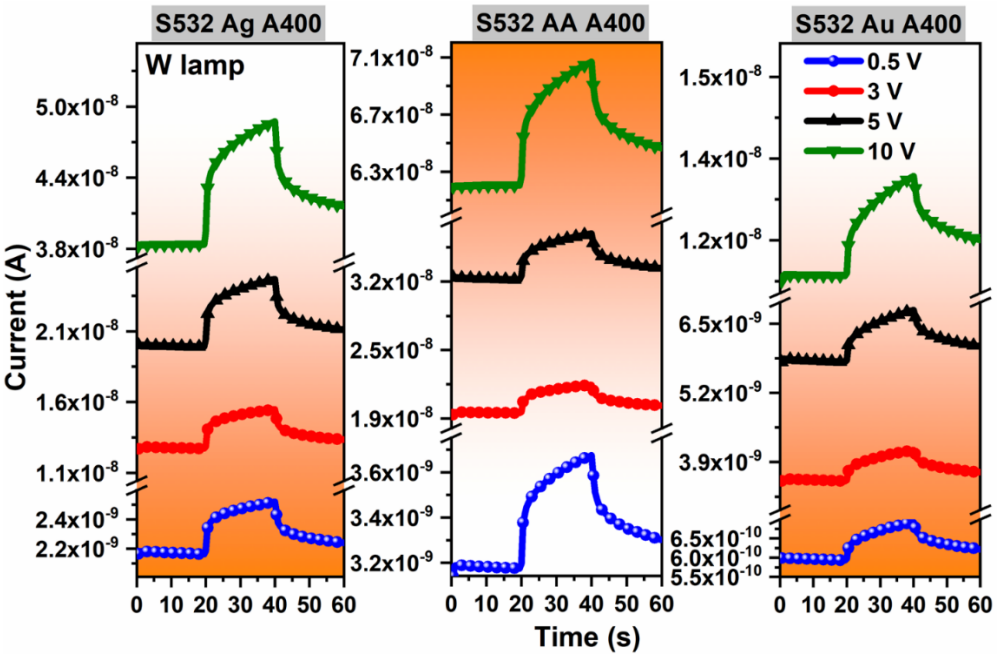


Fig. 5.18: Photoresponse measurement of S532:metallic/bimetallic hybrid films to W lamp at increasing applied voltages.

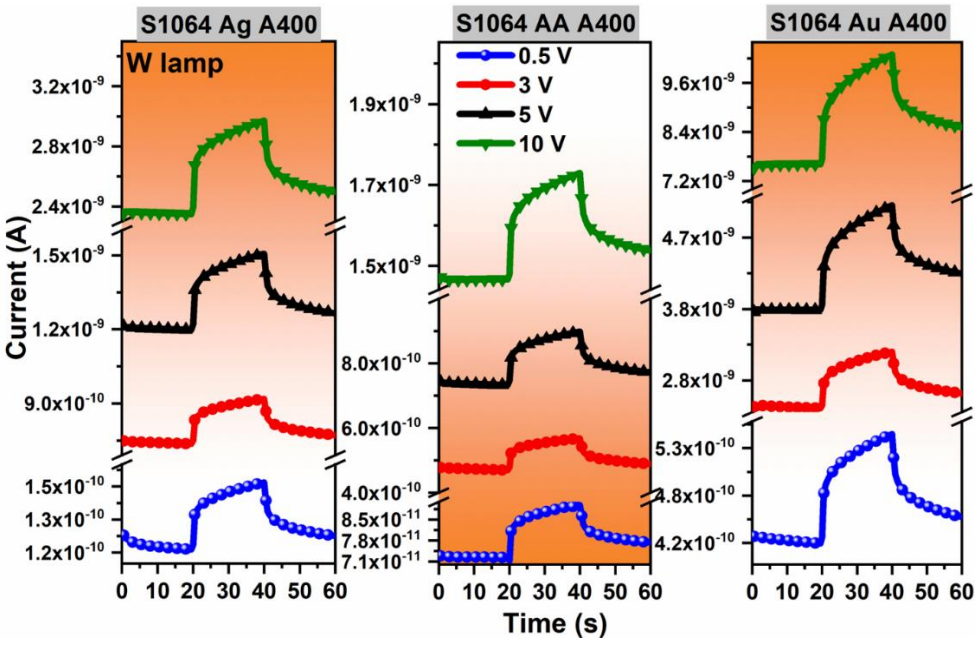


Fig. 5.19: Photoresponse measurement of S1064:metallic/bimetallic hybrid films to W lamp at increasing applied voltages.

Current vs time measurements were made under various illumination sources at different wavelengths to examine the range of detection and stability of the device. The external bias voltage was set to 5 V and the ON/OFF switching duration is 20 s for single cycle measurements and 10 s for cyclic measurements. The results of measurements using various LEDs (395-400 nm; 465 nm; 520 and 590 nm) are displayed in Fig. 5.20. In the respective figures, the value of the photocurrent, I_λ (I_{light}-I_{dark}) is also noted. Incorporation of metallic/bimetallic NPs into SnS was done in an attempt to produce photodetectors that were wavelength-specific comparable to the plasmonic peaks of Ag, Au, and Ag:Au. The hybrid films made of S532:Ag only showed a wavelength-selective response showing the highest values of I_λ for illumination using UV and Blue LEDs. In S1064, films with Ag:Au incorporation performed better than films with Ag or Au incorporation. This might be because of the high concentration of SnS nanocolloids (prepared using 1064 nm laser) that the impact of the metallic/bimetallic NPs is too low. Ag, Au and Ag:Au have less of an impact in S1064 than they showed in S532. The low concentration of the metallic/bimetallic NPs in the films would have resulted in such a response.

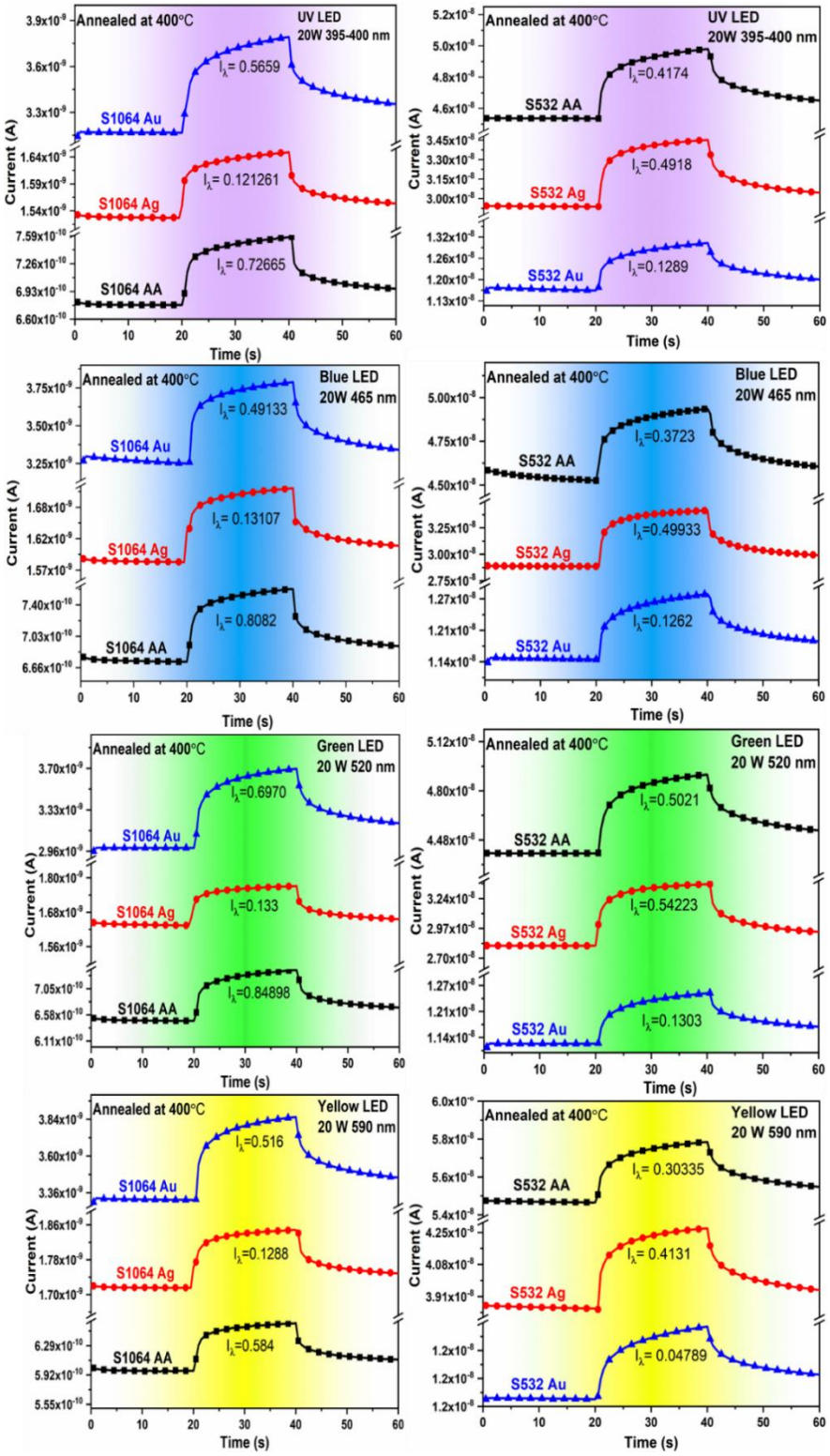


Fig. 5.20: Photoresponse measurements of different SnS hybrid films (S1064 and S532 with Ag, Au and Ag:Au) illuminated using UV, Blue, Green and Yellow LEDs of wavelengths 395, 465, 520 and 590 nm respectively.

Continuous-wave lasers with wavelengths of 532 and 785 nm, and power intensities ranging from 6 mW to 50 mW, were used as another illumination source. The photoresponse recorded for the S532 hybrid films are given in Fig. 5.21 (a, c) and for S1064 are given in Fig. 5.21 (b, d) respectively. This graph shows how the current rises noticeably as illumination power density rises. As expected, illumination at increasing power densities increases the photon flux density, which increases the production of electron-hole pairs [285]. Therefore, when the photodetector is illuminated by higher power density, higher photocurrent is generated.

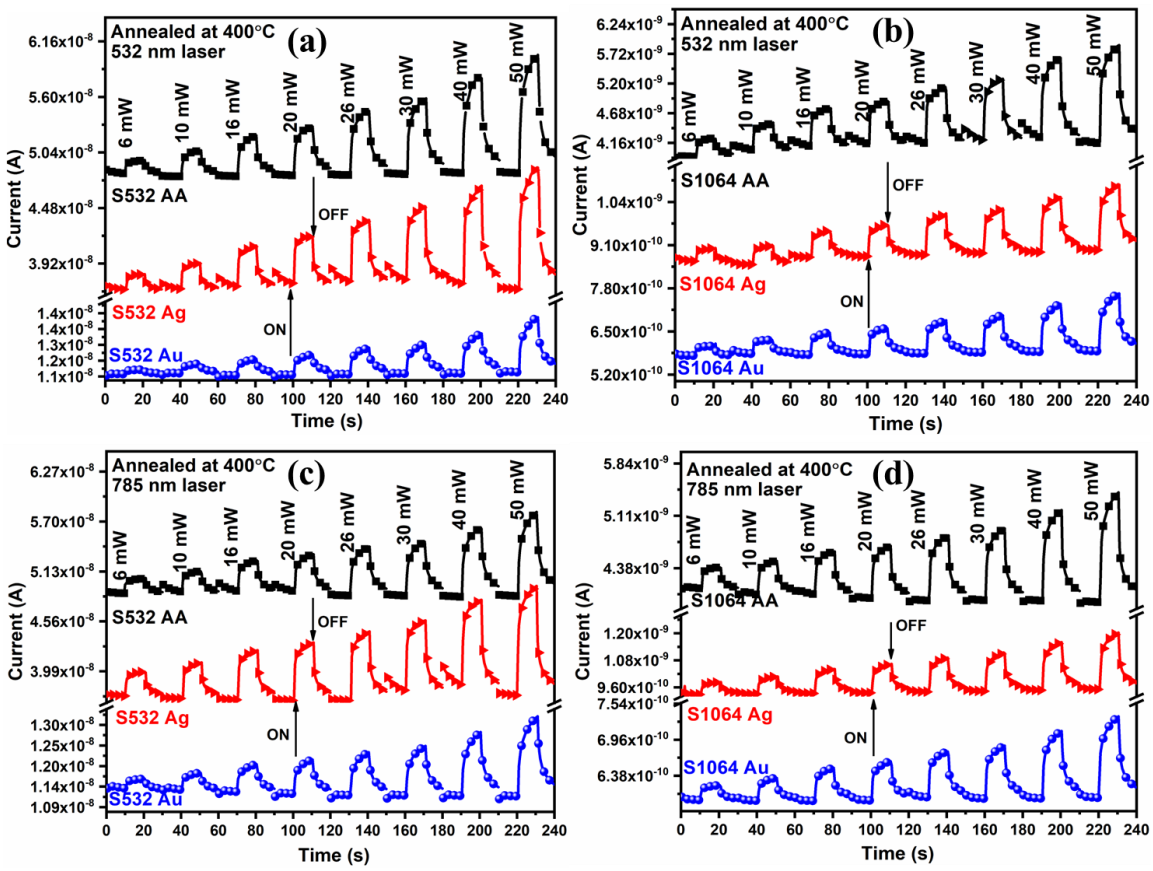


Fig. 5.21: Photoresponse behavior of S532 and S1064 hybrid films to illumination using continuous-wave laser of wavelengths (a, b) 532 (c, d) 785 nm at different laser powers.

Laser diodes of wavelengths 405, 840 and 980 nm were also used to measure the current vs time curves. This was to justify the extended range of detection of the photodetectors of SnS:metallic/bimetallic hybrids. Fig. 5.22 represents the same. From the graphs, it can be seen that for S532 hybrid films, the highest response is observed for S532:AA films and for S1064 it is the

Au incorporated (S1064:Au) films. This can be explained based on the bandgap of the material. The lowest bandgaps or the highest absorption was observed for AA and Au in S532 and S1064 films respectively.

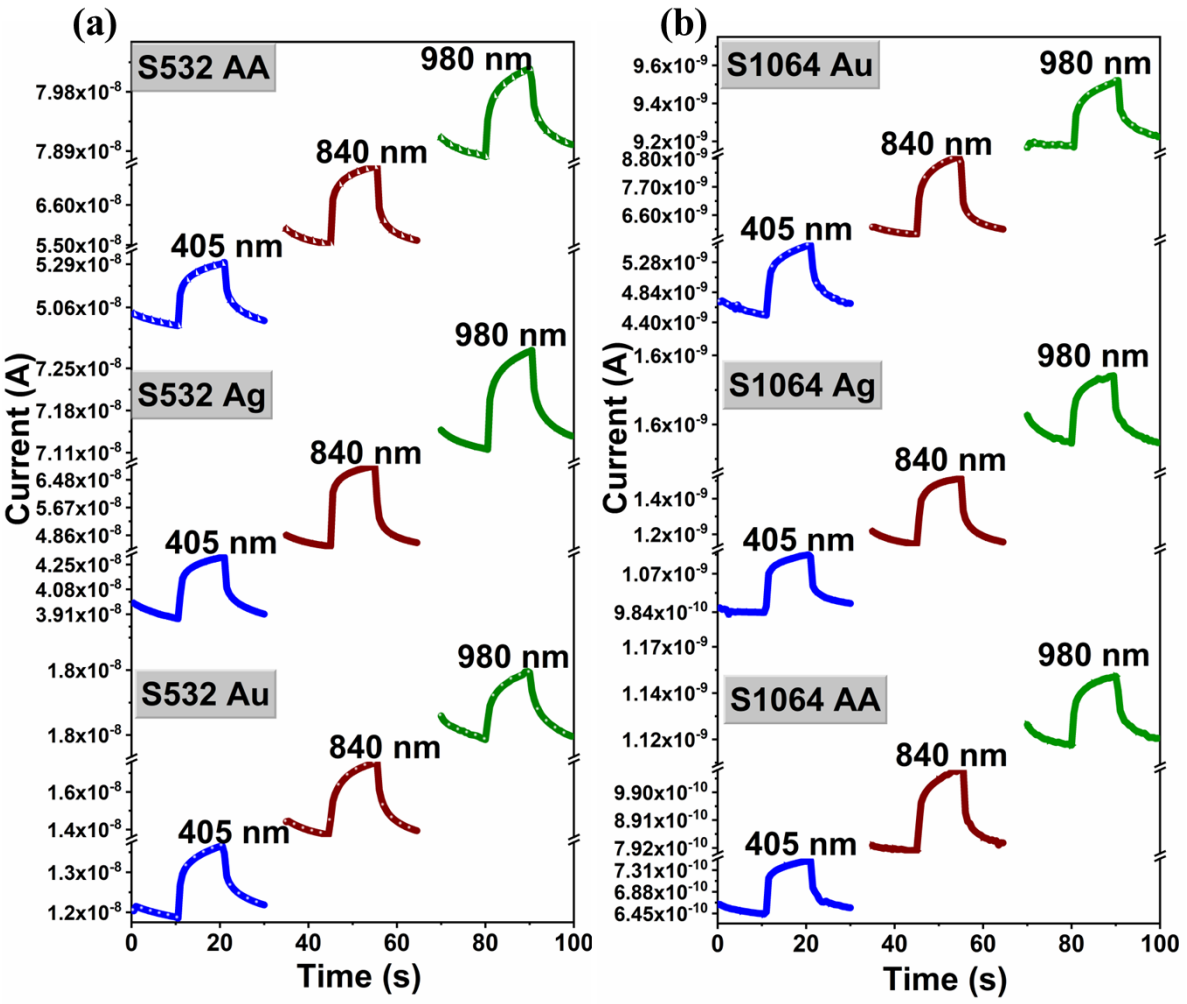


Fig. 5.22: (a, b) Photoresponse behavior of S532 and S1064 films to illumination using laser diodes of wavelengths 405, 840 and 980 nm.

The photosensitivity, detectivity and responsivity values were calculated. The equations used for the calculations are already explained in Chapter 1. The plots are given in Fig. 5.23 and Fig. 5.24. All the photodetectors fabricated had detectivity greater than 1.3×10^{6} Jones and responsivity between 10^{-6} and 10^{-8} AW^{-1}. A power law (Eq 5.1) was used to fit the relationship between the photocurrent and the intensity of the illumination (P_{inc}).

$$I_{ph} = CP_{inc}^{\gamma} \qquad (5.1)$$

where C is the proportionality constant. The value of γ is ~ 0.7 in all the cases except S532 Au which has γ ~ 0.9. It is evident from Fig. 5.23 (c-h) that the fitting results in exponent non-unity, which is caused by the variation in photocurrent with incident light intensity. The complicated processes of electron-hole generation, trapping, and recombination within the semiconductor lead to the non-unity exponent [120,286].

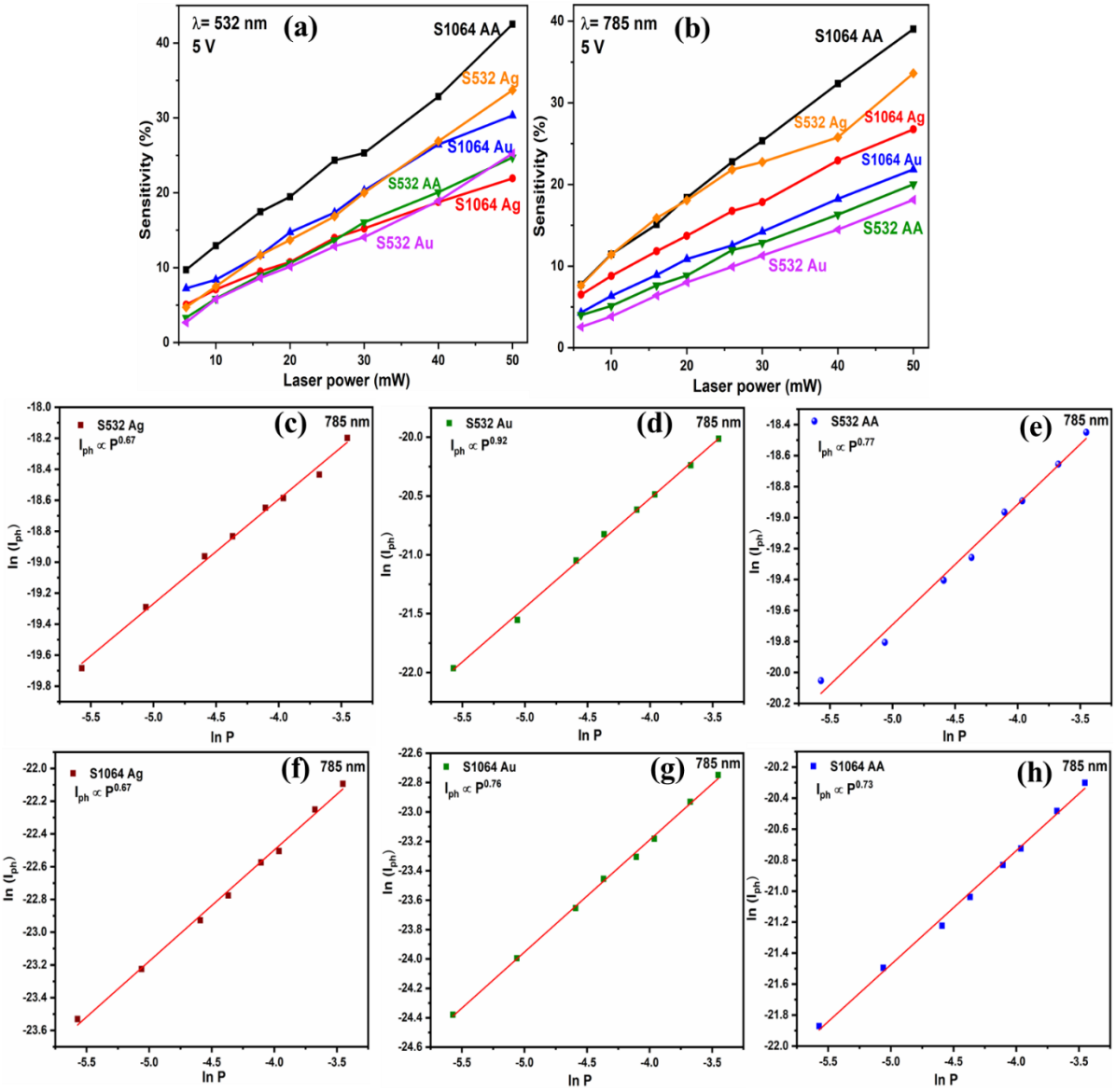


Fig. 5.23: Sensitivity (S) calculated from photoresponse curves obtained from illumination using (a) 532 nm and (b) 785 nm laser source (c-h) The dependence of photocurrent on illumination using 785 nm laser.

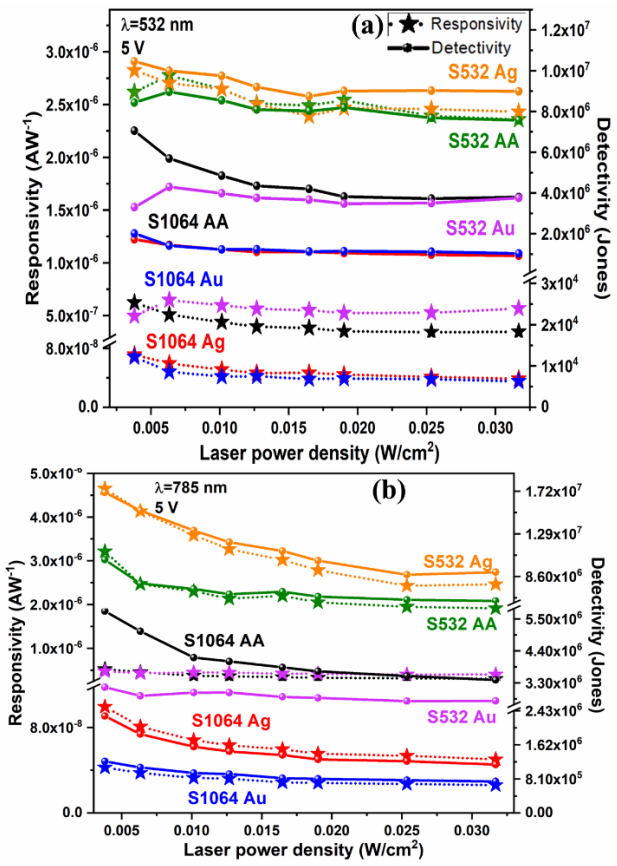


Fig. 5.24: Responsivity (represented using ★) and detectivity (represented using ●) plots calculated from photoresponse curves obtained from illumination using (a) 532 nm and (b) 785 nm laser source.

5.4 Conclusions

- The metallic/bimetallic and SnS NPs were synthesized by Pulsed laser ablation in liquid (PLAL) technique.
- The hybrid films of SnS:Ag/Au/Ag:Au were fabricated by ultrasonic spray deposition method.
- The plasmonic nature of the metal/bimetal NPs is maintained in hybrid nanocolloids synthesized using low energy laser.
- XPS results validated the metallic and bimetallic nature of Ag, Au and Ag:Au NPs formed by PLAL as well as the purity of NPs formed by PLAL.

- The XRD, structural, optical studies and I-V measurements conducted in dark and light with photoresponse measurements support the observation that 400 ℃ annealed SnS:metallic/bimetallic hybrid thin films showed better performance compared to other annealing conditions.
- The photocurrent responses to various LEDs, continuous lasers and laser diodes were also measured.
- The device had good repeatability, sensitivity, responsivity and detectivity in the UV-Vis-NIR area of the spectrum.

Chapter 6

General Conclusions and Outlook

In this thesis work, the synthesis and characterization of tin sulfide (SnS) nanoparticles, their thin films as well as hybrid nanomaterials with Si, graphene and Ag/Au/Ag:Au is presented. SnS nanocolloids were prepared by laser assisted techniques like pulsed laser ablation in liquid (PLAL) and pulsed laser fragmentation in liquid (PLFL). The work was aimed towards the fabrication of nanostructured thin film photodetectors with extended wavelength range of absorption and high efficiency. Each of the materials chosen to form hybrids with SnS had completely different properties. The effects of silicon (Si), graphene and metallic/bimetallic nanoparticles (NPs) were presented with different characterizations and properties.

- The SnS NPs prepared by PLAL and PLIL exhibited morphology of spherical particles interconnected by small chains. The parameters such as laser wavelength, pulse energy, solvent selected, time of ablation/irradiation were varied and investigated. Though the morphology remained the same irrespective of the laser technique used for synthesis of SnS NPs, for laser ablation using wavelength of 532 nm, the average particle size of SnS NPs was 8.02 ± 1.33 nm and much larger particles were formed in the case of SnS NPs formed by PLFL. It was in the range of 17-23 ± 11.77 nm. For laser ablation using 1064 nm laser wavelength, the particle size was calculated as 12.27 ± 6.04 nm. Even the changes in the particles size with respect to different wavelengths and same conditions of experiment were mainly owing to the different photon energies. For particles generated by 532 nm laser, the high photon energy assists in bond breaking and ionization processes which leads to fragmentation causing the reduction in particle size.

- The thin films were fabricated using the nanocolloids by techniques like spin-coating and spray deposition. The nanocolloids in IPA was stable and due to the faster evaporation rate during spin-coating as well as spray deposition, the films were easy to achieve while using IPA than other solvents like DMF. The colloidal concentration, stability and morphology were found to be solvent dependent. There were noticeable effects on the film thickness, optical and electrical

characteristics depending on the method of film fabrication employed, supporting the part of the hypothesis that the method of thin film fabrication plays a significant role in altering the properties and consequently, the optoelectronic applications.

While the spin-coated films had bandgaps between 2-2.7 eV for as-prepared films, the spray-deposited films had substantially smaller bandgaps, around 1.7 eV. This obvious difference in bandgap can be attributed to the change in crystallinity, film growth and morphological differences that arise due to the different fabrication techniques. The annealing temperature and conditions were varied in different studies based on the hybrid for obtaining better crystallinity and therefore the bandgap of the annealed films cannot be compared directly.

- Ultra-small (~4-5 nm) NPs of monocrystalline and polycrystalline Si and their hybrids with SnS showed some interesting results with a detection of up to 1064 nm. The monocrystalline Si samples with SnS showed better photodetection performance than SnS:polycrystalline Si and this was due to the lesser grain boundaries in monocrystalline Si in comparison to polycrystalline Si that acted as trapping centers affecting the charge carrier mobility. Additionally, the visible light photocatalytic degradation study of methylene blue using SnS and SnS:Si hybrids demonstrates that it is a highly promising material for future studies, such as the removal of contaminants from water, air, or soil as well as for solar water splitting and hydrogen production.

- SnS:graphene hybrids demonstrated the best photodetection properties among all the hybrids studied. We could not only extend the wavelength of absorption of SnS with addition of graphene, but also could fabricate a photodetector which gives the same photocurrent value irrespective of the wavelength of illumination used. Raman analysis of graphene revealed its multilayer-like properties, which contributed to the enhancement of crystallinity and absorption of SnS films. While SnS served as the light-harvesting material, graphene promoted the quick transfer of charge carriers between the layers of SnS and graphene. This was mainly supported by the morphology of the spherical SnS NPs embellished on graphene layers confirmed by SEM analysis. The value of detectivity obtained for SnS:graphene films was in the order of 10^7 Jones. The photodetector works in photoconductive mode at low applied voltages under ambient conditions.

- Hybrid nanomaterials of metallic (Ag/Au) and bimetallic (Ag:Au) NPs incorporated into SnS with the aim of using wavelength specific detection corresponding to that of the plasmonic peaks could not exhibit the expected results. However, photodetectors did have detection in the entire UV-Vis-NIR range with detectivity of 10^5-10^7 Jones for different films fabricated.

Table 6.1 : A comparison of the photodetection properties of the hybrids developed in this thesis work.

Photodetector	NP synthesis	Thin film fabrication	Operating wavelength range (nm)	Responsivity (A/W)	Detectivity (Jones)
SnS	PLAL	Spin-coating	300-980	10^{-7} (5 V)	10^6 (5 V)
SnS:Si	SnS-PLFL Si-PLAL	Spin-coating	300-1064	10^{-7} (5 V)	10^6 (5 V)
SnS:Graphene	SnS-PLFL Gr-commercial powder	Spin-coating	300-980	10^{-4} (1 V)	10^7 (1 V)
SnS:Ag,Au,Ag-Au	PLAL	Spray-deposition	300-785	10^{-6} (5 V)	10^7 (5 V)

Investigation on hybrids of SnS combined with materials having unique features revealed how the structural or morphological interactions of the combining nanomaterials in the hybrid affects the overall optical/electrical properties. Additionally, a detailed study of the synthesis, structure, morphology, composition, optical, electrical properties and applications of hybrid nanomaterials synthesized by pulsed laser were well studied. A very simple and green method of laser assisted technique was employed for the synthesis of different nanocolloids. The film fabrication was also achieved by facile techniques such as spin-coating and spray deposition. A lot of SnS based photodetectors are well-documented in literatures which are prepared by different wet chemistry methods or physical methods but pulsed laser fragmentation to synthesize SnS NPs is reported for

the first time. Also, a combination of PLAL and spin coating has never been reported so far. With the exception of one or two investigations, most SnS thin films only demonstrate photodetection up to 860 nm, and the operational mode is difficult such as the phototransistor or photodiode mode. However, all the SnS hybrids we fabricated exhibit detection up to 980 nm or 1064 nm, and the photodetectors operate in a simple photoconductive mode thus validating our hypothesis of extending the wavelength range of detection by hybrid structures. The hybrid developed utilizing properties such asf indirect semiconducting (Si) nature, layered and highly conducting material (graphene) and plasmonic nanoparticles (Ag, Au and Ag:Au) can be extended to different materials for sensitive and spectrally distinct light detection as well as extended wavelength detection. This study opens the door for the material's use not only for photodetectors or photocatalytic applications but also in photovoltaic applications, batteries including lithium or sodium-ion batteries, as well as various electrochemical energy storage devices, sensors etc. which emphasizes the long-term goals of this thesis work.

References

[1] A.P. Alivisatos, Semiconductor Clusters, Nanocrystals, and Quantum Dots, Science (80-.). 271 (1996) 933–937. https://doi.org/10.1126/science.271.5251.933.

[2] G.C. Papaefthymiou, Nanoparticle magnetism, Nano Today. 4 (2009) 438–447. https://doi.org/10.1016/j.nantod.2009.08.006.

[3] D. Ma, Hybrid Nanoparticles, in: Noble Met. Oxide Hybrid Nanoparticles, Elsevier, 2019: pp. 3–6. https://doi.org/10.1016/B978-0-12-814134-2.00001-2.

[4] D.R. Boverhof, C.M. Bramante, J.H. Butala, S.F. Clancy, W.M. Lafranconi, J. West, S.C. Gordon, Comparative assessment of nanomaterial definitions and safety evaluation considerations, Regul. Toxicol. Pharmacol. 73 (2015) 137–150. https://doi.org/10.1016/j.yrtph.2015.06.001.

[5] J. Wong, T. Zou, A.H.C. Lee, C. Zhang, The potential translational applications of nanoparticles in endodontics, Int. J. Nanomedicine. 16 (2021) 2087–2106. https://doi.org/10.2147/IJN.S293518.

[6] S.Y. Lu, S.W. Chen, Deposition of nano-size titania-silica particles in a hot-wall CVD process, J. Am. Ceram. Soc. 83 (2000) 709–712. https://doi.org/10.1111/j.1151-2916.2000.tb01263.x.

[7] J. Wang, M. Nozaki, M. Lachab, R.S. Qhalid Fareed, Y. Ishikawa, T. Wang, Y. Naoi, S. Sakai, Formation and optical properties of InGaN/GaN nano-structures grown on amorphous Si substrates by MOCVD, J. Cryst. Growth. 200 (1999) 85–89. https://doi.org/10.1016/S0022-0248(98)00935-X.

[8] J. Huerta, M. López, O. Zelaya-Angel, Phase stability during molecular beam epitaxial growth of CdTe on InSb(111) substrates, J. Vac. Sci. Technol. B Microelectron. Nanom. Struct. 18 (2000) 1716. https://doi.org/10.1116/1.591459.

[9] C.B. Murray, C.R. Kagan, M.G. Bawendi, Synthesis and Characterization of Monodisperse Nanocrystals and Close-Packed Nanocrystal Assemblies, Annu. Rev. Mater. Sci. 30 (2000) 545–610. https://doi.org/10.1146/annurev.matsci.30.1.545.

[10] C.B. Murray, D.J. Norris, M.G. Bawendi, Synthesis and Characterization of Nearly Monodisperse CdE (E = S, Se, Te) Semiconductor Nanocrystallites, J. Am. Chem. Soc. 115 (1993) 8706–8715. https://doi.org/10.1021/ja00072a025.

[11] T.S. Ahmadi, Z.L. Wang, T.C. Green, A. Henglein, M.A. El-Sayed, Shape-Controlled Synthesis of Colloidal Platinum Nanoparticles, Science (80-.). 272 (1996) 1924–1925. https://doi.org/10.1126/science.272.5270.1924.

[12] N. Baig, I. Kammakakam, W. Falath, I. Kammakakam, Nanomaterials: A review of synthesis methods, properties, recent progress, and challenges, Mater. Adv. 2 (2021) 1821–1871. https://doi.org/10.1039/d0ma00807a.

[13] K. Huang, Y. Yan, K. Li, A. Khan, H. Zhang, X. Pi, X. Yu, D. Yang, High and Fast Response of a Graphene-Silicon Photodetector Coupled with 2D Fractal Platinum Nanoparticles, Adv. Opt. Mater. 6 (2018) 1700793. https://doi.org/10.1002/adom.201700793.

[14] C. Chen, H. Qiao, S. Lin, C. Man Luk, Y. Liu, Z. Xu, J. Song, Y. Xue, D. Li, J. Yuan, W. Yu, C. Pan, S. Ping Lau, Q. Bao, Highly responsive MoS2 photodetectors enhanced by graphene quantum dots, Sci. Rep. 5 (2015) 11830. https://doi.org/10.1038/srep11830.

[15] V. Amendola, I. Fortunati, C. Marega, A.L. Abdelhady, M.I. Saidaminov, O.M. Bakr, High-Purity Hybrid Organolead Halide Perovskite Nanoparticles Obtained by Pulsed-Laser Irradiation in Liquid, ChemPhysChem. 18 (2017) 1047–1054. https://doi.org/10.1002/cphc.201600863.

[16] P.D. Cozzoli, T. Pellegrino, L. Manna, Synthesis, properties and perspectives of hybrid nanocrystal structures, Chem. Soc. Rev. 35 (2006) 1195–1208. https://doi.org/10.1039/b517790c.

[17] M.R. Kim, Z. Xu, G. Chen, D. Ma, Semiconductor and metallic core-shell nanostructures: Synthesis and applications in solar cells and catalysis, Chem. - A Eur. J. 20 (2014) 11256–11275. https://doi.org/10.1002/chem.201402277.

[18] F. Yang, A. Skripka, A. Benayas, X. Dong, S.H. Hong, F. Ren, J.K. Oh, X. Liu, F. Vetrone, D. Ma, An Integrated Multifunctional Nanoplatform for Deep-Tissue Dual-Mode

Imaging, Adv. Funct. Mater. 28 (2018) 1706235. https://doi.org/10.1002/adfm.201706235.

[19] M. Lattuada, T.A. Hatton, Synthesis, properties and applications of Janus nanoparticles, Nano Today. 6 (2011) 286–308. https://doi.org/10.1016/j.nantod.2011.04.008.

[20] A. Benayas, F. Ren, E. Carrasco, V. Marzal, B. Del Rosal, B.A. Gonfa, Á. Juarranz, F. Sanz-Rodríguez, D. Jaque, J. García-Solé, D. Ma, F. Vetrone, PbS/CdS/ZnS Quantum Dots: A Multifunctional Platform for in Vivo Near-Infrared Low-Dose Fluorescence Imaging, Adv. Funct. Mater. 25 (2015) 6650–6659. https://doi.org/10.1002/adfm.201502632.

[21] L. Weng, H. Zhang, A.O. Govorov, M. Ouyang, Hierarchical synthesis of non-centrosymmetric hybrid nanostructures and enabled plasmon-driven photocatalysis, Nat. Commun. 5 (2014) 4792. https://doi.org/10.1038/ncomms5792.

[22] A.E. Saunders, I. Popov, U. Banin, Synthesis and characterization of organic-soluble Ag/AgBr dimer nanocrystals, Zeitschrift Fur Anorg. Und Allg. Chemie. 633 (2007) 2414–2419. https://doi.org/10.1002/zaac.200700290.

[23] V.C. Thipe, M. Thatyana, F.R. Ajayi, P.B. Njobeh, K. V. Katti, Hybrid nanomaterials for detection, detoxification, and management mycotoxins, in: Multifunct. Hybrid Nanomater. Sustain. Agri-Food Ecosyst., Elsevier, 2020: pp. 271–285. https://doi.org/10.1016/B978-0-12-821354-4.00012-1.

[24] H. Bhardwaj, M.K. Pandey, Rajesh, G. Sumana, Electrochemical Aflatoxin B1 immunosensor based on the use of graphene quantum dots and gold nanoparticles, Microchim. Acta. 186 (2019) 592. https://doi.org/10.1007/s00604-019-3701-5.

[25] J. Li, J.Z. Zhang, Optical properties and applications of hybrid semiconductor nanomaterials, Coord. Chem. Rev. 253 (2009) 3015–3041. https://doi.org/10.1016/j.ccr.2009.07.017.

[26] K. Dewangan, K. Shrivas, R. Kurrey, Hybrid nanomaterials as chemical sensors, in: Multifunct. Hybrid Nanomater. Sustain. Agri-Food Ecosyst., Elsevier, 2020: pp. 213–239. https://doi.org/10.1016/B978-0-12-821354-4.00009-1.

[27] R. Costi, A.E. Saunders, U. Banin, Colloidal hybrid nanostructures: A new type of functional materials, Angew. Chemie - Int. Ed. 49 (2010) 4878–4897. https://doi.org/10.1002/anie.200906010.

[28] T. Mokari, E. Rothenberg, I. Popov, R. Costi, U. Banin, Selective growth of metal tips onto semiconductor quantum rods and tetrapods, Science (80-.). 304 (2004) 1787–1790. https://doi.org/10.1126/science.1097830.

[29] A.E. Saunders, I. Popov, U. Banin, Synthesis of hybrid CdS-Au colloidal nanostructures, J. Phys. Chem. B. 110 (2006) 25421–25429. https://doi.org/10.1021/jp065594s.

[30] W. Shi, H. Zeng, Y. Sahoo, T.Y. Ohulchanskyy, Y. Ding, Z.L. Wang, M. Swihart, P.N. Prasad, A general approach to binary and ternary hybrid nanocrystals, Nano Lett. 6 (2006) 875–881. https://doi.org/10.1021/nl0600833.

[31] E. Shaviv, O. Schubert, M. Alves-Santos, G. Goldoni, R. Di Felice, F. Vallée, N. Del Fatti, U. Banin, C. Sönnichsen, Absorption Properties of Metal-Semiconductor Hybrid Nanoparticles, ACS Nano. 5 (2011) 4712–4719. https://doi.org/10.1021/nn200645h.

[32] C. Pacholski, A. Kornowski, H. Weller, Site-Specific Photodeposition of Silver on ZnO Nanorods, Angew. Chemie. 116 (2004) 4878–4881. https://doi.org/10.1002/ange.200453880.

[33] M. Achermann, Exciton−Plasmon Interactions in Metal−Semiconductor Nanostructures, J. Phys. Chem. Lett. 1 (2010) 2837–2843. https://doi.org/10.1021/jz101102e.

[34] X. Song, K. Vladislav, C. Liu, W. Xu, The preparation of anisotropic hybrid nanostructures based on CdSe and CdS by the ligand combination method, Nanoscale. 9 (2017) 3934–3940. https://doi.org/10.1039/c7nr00527j.

[35] E.S. Cho, N.E. Coates, J.D. Forster, A.M. Ruminski, B. Russ, A. Sahu, N.C. Su, F. Yang, J.J. Urban, Engineering Synergy: Energy and Mass Transport in Hybrid Nanomaterials, Adv. Mater. 27 (2015) 5744–5752. https://doi.org/10.1002/adma.201500130.

[36] W. Tian, H. Sun, L. Chen, P. Wangyang, X. Chen, J. Xiong, L. Li, Low-dimensional nanomaterial/Si heterostructure-based photodetectors, InfoMat. 1 (2019) 140–163. https://doi.org/10.1002/inf2.12014.

[37] M. Vemula, S. Veeralingam, S. Badhulika, Hybrid 2D/0D SnSe2-SnO2 vertical junction based high performance broadband photodetector, J. Alloys Compd. 883 (2021) 160826. https://doi.org/10.1016/j.jallcom.2021.160826.

[38] W. Tian, D. Liu, F. Cao, L. Li, Hybrid Nanostructures for Photodetectors, Adv. Opt. Mater. 5 (2017) 1600468. https://doi.org/10.1002/adom.201600468.

[39] H.A. Atwater, A. Polman, Plasmonics for improved photovoltaic devices, Nat. Mater. 9 (2010) 205–213. https://doi.org/10.1038/nmat2629.

[40] S. Linic, P. Christopher, D.B. Ingram, Plasmonic-metal nanostructures for efficient conversion of solar to chemical energy, Nat. Mater. 10 (2011) 911–921. https://doi.org/10.1038/nmat3151.

[41] J. Park, J.C. Hwang, G.G. Kim, J. Park, Flexible electronics based on one-dimensional and two-dimensional hybrid nanomaterials, InfoMat. 2 (2020) 33–56. https://doi.org/10.1002/inf2.12047.

[42] M. Zahid, N. Nadeem, N. Tahir, Farid-Un-Nisa, M.I. Majeed, Asim-Mansha, S.A.R. Naqvi, T. Hussain, Hybrid nanomaterials for water purification, in: Multifunct. Hybrid Nanomater. Sustain. Agri-Food Ecosyst., Elsevier, 2020: pp. 155–188. https://doi.org/10.1016/B978-0-12-821354-4.00007-8.

[43] D. Zhang, B. Gökce, S. Barcikowski, Laser Synthesis and Processing of Colloids: Fundamentals and Applications, Chem. Rev. 117 (2017) 3990–4103. https://doi.org/10.1021/acs.chemrev.6b00468.

[44] V. Amendola, D. Amans, Y. Ishikawa, N. Koshizaki, S. Scirè, G. Compagnini, S. Reichenberger, S. Barcikowski, Room-temperature laser synthesis in liquid of oxide, metal-oxide core-shells and doped oxide nanoparticles, Chem. – A Eur. J. 26 (2020) 9206. https://doi.org/10.1002/chem.202000686.

[45] J. Neddersen, G. Chumanov, T.M. Cotton, Laser ablation of metals: A new method for preparing SERS active colloids, Appl. Spectrosc. 47 (1993) 1959–1964. https://doi.org/10.1366/0003702934066460.

[46] M. Kim, S. Osone, T. Kim, H. Higashi, T. Seto, Synthesis of Nanoparticles by Laser

Ablation: A Review, KONA Powder Part. J. 34 (2017) 80–90. https://doi.org/10.14356/kona.2017009.

[47] M.N.R. Ashfold, F. Claeyssens, G.M. Fuge, S.J. Henley, Pulsed laser ablation and deposition of thin films, Chem. Soc. Rev. 33 (2004) 23–31. https://doi.org/10.1039/B207644F.

[48] V. Amendola, M. Meneghetti, What controls the composition and the structure of nanomaterials generated by laser ablation in liquid solution?, Phys. Chem. Chem. Phys. 15 (2013) 3027–3046. https://doi.org/10.1039/c2cp42895d.

[49] G.K. Yogesh, S. Shukla, D. Sastikumar, P. Koinkar, Progress in pulsed laser ablation in liquid (PLAL) technique for the synthesis of carbon nanomaterials: a review, Appl. Phys. A. 127 (2021) 810. https://doi.org/10.1007/s00339-021-04951-6.

[50] H. Zeng, X.W. Du, S.C. Singh, S.A. Kulinich, S. Yang, J. He, W. Cai, Nanomaterials via laser ablation/irradiation in liquid: A review, Adv. Funct. Mater. 22 (2012) 1333–1353. https://doi.org/10.1002/adfm.201102295.

[51] K.Y. Niu, J. Yang, S.A. Kulinich, J. Sun, H. Li, X.W. Du, Morphology control of nanostructures via surface reaction of metal nanodroplets, J. Am. Chem. Soc. 132 (2010) 9814–9819. https://doi.org/10.1021/ja102967a.

[52] F. Lin, J. Yang, S.H. Lu, K.Y. Niu, Y. Liu, J. Sun, X.W. Du, Laser synthesis of gold/oxide nanocomposites, J. Mater. Chem. 20 (2010) 1103–1106. https://doi.org/10.1039/b918945a.

[53] P. Liu, Y.L. Cao, H. Cui, X.Y. Chen, G.W. Yang, Micro- and nanocubes of silicon with zinc-blende structure, Chem. Mater. 20 (2008) 494–502. https://doi.org/10.1021/cm7027178.

[54] Q.A. Drmosh, M.A. Gondal, Z.H. Yamani, T.A. Saleh, Spectroscopic characterization approach to study surfactants effect on ZnO2 nanoparticles synthesis by laser ablation process, Appl. Surf. Sci. 256 (2010) 4661–4666. https://doi.org/10.1016/j.apsusc.2010.02.068.

[55] Z. Yan, D.B. Chrisey, Pulsed laser ablation in liquid for micro-/nanostructure generation,

J. Photochem. Photobiol. C Photochem. Rev. 13 (2012) 204–223. https://doi.org/10.1016/j.jphotochemrev.2012.04.004.

[56] M. Censabella, V. Torrisi, S. Boninelli, C. Bongiorno, M.G. Grimaldi, F. Ru, Applied Surface Science Laser ablation synthesis of mono- and bimetallic Pt and Pd nanoparticles and fabrication of Pt-Pd / Graphene nanocomposites, Appl. Surf. Sci. 475 (2019) 494–503. https://doi.org/10.1016/j.apsusc.2019.01.029.

[57] W. Guo, B. Liu, Liquid-Phase Pulsed Laser Ablation and Electrophoretic Deposition for Chalcopyrite Thin-Film Solar Cell Application, Appl. Mater. Interfaces. 4 (2012) 7036–7046. https://doi.org/10.1021/am3022976.

[58] A. Pyatenko, H. Wang, N. Koshizaki, T. Tsuji, Mechanism of pulse laser interaction with colloidal nanoparticles, Laser Photonics Rev. 604 (2013) 596–604. https://doi.org/10.1002/lpor.201300013.

[59] H. Wang, A. Pyatenko, K. Kawaguchi, X. Li, Z. Swiatkowska-, N. Koshizaki, Selective Pulsed Heating for the Synthesis of Semiconductor and Metal Submicrometer Spheres **, Angew. Chemie - Int. Ed. 49 (2010) 6361–6364. https://doi.org/10.1002/anie.201002963.

[60] M. Lau, Laser Fragmentation and Melting of Particles, Springer Fachmedien Wiesbaden, Wiesbaden, 2016. https://doi.org/10.1007/978-3-658-14171-4.

[61] A. De Giacomo, M. Dell'Aglio, A. Santagata, R. Gaudiuso, O. De Pascale, P. Wagener, G.C. Messina, G. Compagnini, S. Barcikowski, Cavitation dynamics of laser ablation of bulk and wire-shaped metals in water during nanoparticles production, Phys. Chem. Chem. Phys. 15 (2013) 3083–3092. https://doi.org/10.1039/c2cp42649h.

[62] F. Paquin, J. Rivnay, A. Salleo, N. Stingelin, C. Silva, Multi-phase semicrystalline microstructures drive exciton dissociation in neat plastic semiconductors, J. Mater. Chem. C. 3 (2015) 10715–10722. https://doi.org/10.1039/b000000x.

[63] H. Cai, N. Chaudhary, J. Lee, M.F. Becker, J.R. Brock, J.W. Keto, Generation of metal nanoparticles by laser ablation of microspheres, J. Aerosol Sci. 29 (1998) 627–636. https://doi.org/10.1016/S0021-8502(97)00465-5.

[64] L. V. Zhigilei, B.J. Garrison, Computer simulation study of damage and ablation of

submicron particles from short-pulse laser irradiation, Appl. Surf. Sci. 127–129 (1998) 142–150. https://doi.org/10.1016/S0169-4332(97)00624-7.

[65] S.S. Kanakkillam, S. Shaji, B. Krishnan, S. Vazquez-Rodriguez, J.A.A. Martinez, M.I.M. Palma, D.A. Avellaneda, Nanoflakes of zinc oxide:cobalt oxide composites by pulsed laser fragmentation for visible light photocatalysis, Appl. Surf. Sci. 501 (2020) 144223. https://doi.org/10.1016/j.apsusc.2019.144223.

[66] G.W. Yang, Laser ablation in liquids: Applications in the synthesis of nanocrystals, Prog. Mater. Sci. 52 (2007) 648–698. https://doi.org/10.1016/j.pmatsci.2006.10.016.

[67] W.T. Nichols, T. Sasaki, N. Koshizaki, Laser ablation of a platinum target in water. III. Laser-induced reactions, J. Appl. Phys. 100 (2006) 114913. https://doi.org/10.1063/1.2390642.

[68] A. Pyatenko, M. Yamaguchi, M. Suzuki, Synthesis of Spherical Silver Nanoparticles with Controllable Sizes in Aqueous Solutions, J. Phys. Chem. C. 111 (2007) 7910–7917. https://doi.org/10.1021/jp071080x.

[69] Y. Ishikawa, Q. Feng, N. Koshizaki, Growth fusion of submicron spherical boron carbide particles by repetitive pulsed laser irradiation in liquid media, Appl. Phys. A Mater. Sci. Process. 99 (2010) 797–803. https://doi.org/10.1007/s00339-010-5745-6.

[70] X. Li, J. Liu, X. Wang, M. Gao, Z. Wang, Preparation of silver spheres by selective laser heating in silver-containing precursor solution, Opt. Express. 19 (2011) 2846–2851. https://doi.org/10.1364/OE.19.002846.

[71] X. Li, A. Pyatenko, Y. Shimizu, H. Wang, K. Koga, N. Koshizaki, Fabrication of Crystalline Silicon Spheres by Selective Laser Heating in Liquid Medium, Langmuir. 27 (2011) 5076–5080. https://doi.org/10.1021/la200231f.

[72] H. Wang, M. Miyauchi, Y. Ishikawa, A. Pyatenko, N. Koshizaki, Y. Li, L. Li, X. Li, Y. Bando, D. Golberg, Single-Crystalline Rutile TiO 2 Hollow Spheres : Room-Temperature Synthesis, Tailored Visible-Light-Extinction, and Effective Scattering Layer for Quantum Dot-Sensitized Solar Cells, J. Am. Chem. Soc. 133 (2011) 19102–19109. https://doi.org/10.1021/ja2049463.

[73] X. Li, Y. Shimizu, A. Pyatenko, H. Wang, Tetragonal zirconia spheres fabricated by carbon-assisted selective laser heating in a liquid medium, Nanotechnology. 23 (2012) 115602. https://doi.org/10.1088/0957-4484/23/11/115602.

[74] H. Wang, K. Kawaguchi, A. Pyatenko, X. Li, Z. Swiatkowska-warkocka, Y. Katou, N. Koshizaki, General Bottom-Up Construction of Spherical Particles by Pulsed Laser Irradiation of Colloidal Nanoparticles : A Case Study on CuO, Chem. - A Eur. J. 18 (2012) 163–169. https://doi.org/10.1002/chem.201102079.

[75] K.S. Chung, J.C. Lee, H. Lee, S.Y. Eom, E.A. Yoo, Synthesis of highly concentrated TiO2 nanocolloids and coating on boron nitride powders, Colloids Surfaces A Physicochem. Eng. Asp. 313–314 (2008) 175–178. https://doi.org/10.1016/J.COLSURFA.2007.04.127.

[76] H. Wang, J.Z. Xu, J.J. Zhu, H.Y. Chen, Preparation of CuO nanoparticles by microwave irradiation, J. Cryst. Growth. 244 (2002) 88–94. https://doi.org/10.1016/S0022-0248(02)01571-3.

[77] G.G. Guillen, M.I. Mendivil Palma, B. Krishnan, D. Avellaneda Avellaneda, S. Shaji, Tin sulfide nanoparticles by pulsed laser ablation in liquid, J. Mater. Sci. Mater. Electron. 27 (2016) 6859–6871. https://doi.org/10.1007/s10854-016-4639-6.

[78] Y.M. Lvov, P. Pattekari, X. Zhang, V. Torchilin, Converting poorly soluble materials into stable aqueous nanocolloids, Langmuir. 27 (2011) 1212–1217. https://doi.org/10.1021/la1041635.

[79] A. Radoń, A. Drygała, Ł. Hawełek, D. Łukowiec, Structure and optical properties of Fe3O4 nanoparticles synthesized by co-precipitation method with different organic modifiers, Mater. Charact. 131 (2017) 148–156. https://doi.org/10.1016/J.MATCHAR.2017.06.034.

[80] A. Barhoum, M.L. García-Betancourt, J. Jeevanandam, E.A. Hussien, S.A. Mekkawy, M. Mostafa, M.M. Omran, M.S. Abdalla, M. Bechelany, Review on Natural, Incidental, Bioinspired, and Engineered Nanomaterials: History, Definitions, Classifications, Synthesis, Properties, Market, Toxicities, Risks, and Regulations, Nanomaterials. 12

(2022) 177. https://doi.org/10.3390/nano12020177.

[81] S. Shaji, V. Vinayakumar, B. Krishnan, J. Johny, S.S. Kanakkillam, J.M.F. Herrera, S.S. Guzman, D.A. Avellaneda, G.A.C. Rodriguez, J.A.A. Martinez, Copper antimony sulfide nanoparticles by pulsed laser ablation in liquid and their thin film for photovoltaic application, Appl. Surf. Sci. 476 (2019) 94–106. https://doi.org/10.1016/j.apsusc.2019.01.072.

[82] A.P. Sreekala, B. Krishnan, R.F.C. Pelaes, D.A. Avellaneda, M.I.M. Palma, S. Shaji, Tin sulfide thin films by spin coating of laser ablated nanocolloids for UV-Vis-NIR photodetection, Colloids Surfaces A Physicochem. Eng. Asp. 639 (2022) 128382. https://doi.org/10.1016/j.colsurfa.2022.128382.

[83] W. Guo, K. Hagedorn, B. Liu, Electrophoretic deposition of colloidal nanoparticles for synthesis of chalcopyrite thin films, in: 2011 37th IEEE Photovolt. Spec. Conf., IEEE, 2011: pp. 002715–002718. https://doi.org/10.1109/PVSC.2011.6186508.

[84] L. Besra, M. Liu, A review on fundamentals and applications of electrophoretic deposition (EPD), Prog. Mater. Sci. 52 (2007) 1–61. https://doi.org/10.1016/j.pmatsci.2006.07.001.

[85] A.R.B. James H. Dickerson, Electrophoretic Deposition of Nanomaterials, Springer New York, New York, NY, 2012. https://doi.org/10.1007/978-1-4419-9730-2.

[86] D.A.A. Leal, S. Shaji, D.A. Avellaneda, J.A.A. Martínez, B. Krishnan, In situ incorporation of laser ablated PbS nanoparticles in CH3NH3PbI3 films by spin-dip coating and the subsequent effects on the planar junction CdS/CH3NH3PbI3 solar cells, Appl. Surf. Sci. 508 (2020) 144899. https://doi.org/10.1016/j.apsusc.2019.144899.

[87] H.Z. Ye, X.Y. Liu, Review of recent studies in magnesium matrix composites, J. Mater. Sci. 39 (2004) 6153–6171. https://doi.org/10.1023/b:jmsc.0000043583.47148.31.

[88] J. Johny, S. Sepulveda-Guzman, B. Krishnan, D.A. Avellaneda, J.A. Aguilar Martinez, S. Shaji, Synthesis and Properties of Tin Sulfide Thin Films from Nanocolloids Prepared by Pulsed Laser Ablation in Liquid, ChemPhysChem. 18 (2017) 1061–1068. https://doi.org/10.1002/cphc.201601186.

[89] J.A. Saimon, R.O. Mahdi, K.S. Khashan, F.A. Abdulameer, Preparation of CuO NPs by

laser ablation in liquid for photodiodes, AIP Conf. Proc. 2213 (2020) 020312. https://doi.org/10.1063/5.0000118.

[90] R.A. Ismail, A.K. Ali, K.I. Hassoon, Preparation of a silicon heterojunction photodetector from colloidal indium oxide nanoparticles, Opt. Laser Technol. 51 (2013) 1–4. https://doi.org/10.1016/j.optlastec.2013.03.008.

[91] F. Omnes, Introduction to Semiconductor Photodetectors, in: Optoelectron. Sensors, ISTE, London, UK, 2010: pp. 1–14. https://doi.org/10.1002/9780470611630.ch1.

[92] Z. Lou, Z. Liang, G. Shen, Photodetectors based on two dimensional materials, J. Semicond. 37 (2016) 091001. https://doi.org/10.1088/1674-4926/37/9/091001.

[93] Z. Bielecki, K. Achtenberg, M. Kopytko, J. Mikołajczyk, J. Wojtas, A. Rogalski, Review of photodetectors characterization methods, Bull. Polish Acad. Sci. Tech. Sci. 70 (2022) 1–26. https://doi.org/10.24425/bpasts.2022.140534.

[94] P. Dardano, M.A. Ferrara, Integrated photodetectors based on Group IV and colloidal semiconductors: Current state of affairs, Micromachines. 11 (2020) 842. https://doi.org/10.3390/MI11090842.

[95] T.P. Pearsall, Photodetectors for Optical Communication, J. Opt. Commun. 2 (1981) 42–48. https://doi.org/10.1515/JOC.1981.2.2.42.

[96] F. Zhong, H. Wang, Z. Wang, Y. Wang, T. He, P. Wu, M. Peng, H. Wang, T. Xu, F. Wang, P. Wang, J. Miao, W. Hu, Recent progress and challenges on two-dimensional material photodetectors from the perspective of advanced characterization technologies, Nano Res. 14 (2021) 1840–1862. https://doi.org/10.1007/s12274-020-3247-1.

[97] R.A. Yotter, D.M. Wilson, A review of photodetectors for sensing light-emitting reporters in biological systems, IEEE Sens. J. 3 (2003) 288–303. https://doi.org/10.1109/JSEN.2003.814651.

[98] A. Parameswaran Sreekala, A. Nadukkandy, S. Shaji, D.A. Avellaneda, J.A. Aguilar-Martínez, B. Krishnan, AgSbS2-xSex thin films: Structure, composition, morphology and photodetection properties, Mater. Today Commun. 27 (2021) 102362. https://doi.org/10.1016/j.mtcomm.2021.102362.

[99] K. Kasirajan, A.N.A. Anasthasiya, O.M. Aldossary, M. Ubaidullah, M. Karunakaran, Structural, morphological, optical and enhanced photodetection activities of CdO films: An effect of Mn doping, Sensors Actuators A Phys. 319 (2021) 112531. https://doi.org/10.1016/j.sna.2020.112531.

[100] C.H. Kuo, J.M. Wu, S.J. Lin, W.C. Chang, High sensitivity of middle-wavelength infrared photodetectors based on an individual InSb nanowire, Nanoscale Res. Lett. 8 (2013) 327. https://doi.org/10.1186/1556-276X-8-327.

[101] X. Zhou, D. Yang, D. Ma, Extremely Low Dark Current, High Responsivity, All-Polymer Photodetectors with Spectral Response from 300 nm to 1000 nm, Adv. Opt. Mater. 3 (2015) 1570–1576. https://doi.org/10.1002/adom.201500224.

[102] S.T. Kassim, H.A. Hadi, R.A. Ismail, Fabrication and characterization of high photosensitivity CuS/porous silicon heterojunction photodetector, Optik (Stuttg). 221 (2020) 165339. https://doi.org/10.1016/j.ijleo.2020.165339.

[103] A. Parameswaran, A. Nadukkandy, S. Shaji, D. Avellaneda, J.A. Aguilar-martínez, B. Krishnan, AgSbS2-xSex thin films : Structure,composition, morphology and photodetection properties, Mater. Today Commun. 27 (2021) 102362. https://doi.org/10.1016/j.mtcomm.2021.102362.

[104] L. Shen, Y. Zhang, Y. Bai, X. Zheng, Q. Wang, J. Huang, A filterless, visible-blind, narrow-band, and near-infrared photodetector with a gain, Nanoscale. 8 (2016) 12990–12997. https://doi.org/10.1039/c6nr02902g.

[105] K.J. Norton, F. Alam, D.J. Lewis, A Review of the Synthesis, Properties, and Applications of Bulk and Two-Dimensional Tin (II) Sulfide (SnS), Appl. Sci. 11 (2021) 2062. https://doi.org/10.3390/app11052062.

[106] F. Li, M.M. Ramin Moayed, F. Gerdes, S. Kull, E. Klein, R. Lesyuk, C. Klinke, Colloidal tin sulfide nanosheets: Formation mechanism, ligand-mediated shape tuning and photo-detection, J. Mater. Chem. C. 6 (2018) 9410–9419. https://doi.org/10.1039/c8tc02559b.

[107] L. Li, Z. Lou, G. Shen, Flexible Broadband Image Sensors with SnS Quantum Dots/Zn2SnO4 Nanowires Hybrid Nanostructures, Adv. Funct. Mater. 28 (2018) 1705389.

https://doi.org/10.1002/adfm.201705389.

[108] Y.H. Zhou, H.N. An, C. Gao, Z.Q. Zheng, B. Wang, UV–Vis-NIR photodetector based on monolayer MoS2, Mater. Lett. 237 (2019) 298–302. https://doi.org/10.1016/j.matlet.2018.11.112.

[109] J. Jiang, J. Huang, Z. Ye, S. Ruan, Y.J. Zeng, Self-Powered and Broadband Photodetector Based on SnS2/ZnO1−xSx Heterojunction, Adv. Mater. Interfaces. 7 (2020) 2000882. https://doi.org/10.1002/admi.202000882.

[110] Z. Zheng, L. Gan, J.B. Zhang, F. Zhuge, T.Y. Zhai, An enhanced UV-Vis-NIR an d flexible photodetector based on electrospun Zno nanowire array/PbS quantum dots film heterostructure, Adv. Sci. 4 (2017) 1600316. https://doi.org/10.1002/advs.201600316.

[111] J.Z. Wu, M. Gong, Nanohybrid Photodetectors, Adv. Photonics Res. 2 (2021) 2100015. https://doi.org/10.1002/adpr.202100015.

[112] H. Wang, D.H. Kim, Perovskite-based photodetectors: Materials and devices, Chem. Soc. Rev. 46 (2017) 5204–5236. https://doi.org/10.1039/c6cs00896h.

[113] M. Kumar, H.S. Kim, D.Y. Park, M.S. Jeong, J. Kim, Wide channel broadband CH3NH3PbI3/SnS hybrid photodetector: breaking the limit of bandgap energy operation, RSC Adv. 8 (2018) 23206–23212. https://doi.org/10.1039/c8ra02825g.

[114] Z. Zhang, J. Yang, K. Zhang, S. Chen, F. Mei, G. Shen, Anisotropic photoresponse of layered 2D SnS-based near infrared photodetectors, J. Mater. Chem. C. 5 (2017) 11288–11293. https://doi.org/10.1039/c7tc02865b.

[115] X. Li, S. Ruan, H. Zhu, SnS Nanoflakes/Graphene Hybrid: Towards Broadband Spectral Response and Fast Photoresponse, Nanomaterials. 12 (2022) 2777. https://doi.org/10.3390/nano12162777.

[116] D. Kufer, I. Nikitskiy, T. Lasanta, G. Navickaite, F.H.L. Koppens, G. Konstantatos, Hybrid 2D-0D MoS2-PbS quantum dot photodetectors, Adv. Mater. 27 (2015) 176–180. https://doi.org/10.1002/adma.201402471.

[117] J.J. Wang, J.S. Hu, Y.G. Guo, L.J. Wan, Eco-friendly visible-wavelength photodetectors

based on bandgap engineerable nanomaterials, J. Mater. Chem. 21 (2011) 17582–17589. https://doi.org/10.1039/c1jm12173a.

[118] Z. Zheng, L. Gan, H. Li, Y. Ma, Y. Bando, D. Golberg, A Fully Transparent and Flexible Ultraviolet – Visible Photodetector Based on Controlled Electrospun ZnO-CdO Heterojunction Nanofi ber Arrays, Adv. Funct. Mater. 25 (2015) 5885–5894. https://doi.org/10.1002/adfm.201502499.

[119] Y. Tao, X. Wu, W. Wang, J. Wang, Flexible photodetector from ultraviolet to near infrared based on a SnS2 nanosheet microsphere film, J. Mater. Chem. C. 3 (2015) 1347–1353. https://doi.org/10.1039/c4tc02325k.

[120] M.S. Mahdi, K. Ibrahim, A. Hmood, N.M. Ahmed, F.I. Mustafa, S.A. Azzez, High performance near infrared photodetector based on cubic crystal structure SnS thin film on a glass substrate, Mater. Lett. 200 (2017) 10–13. https://doi.org/10.1016/j.matlet.2017.04.077.

[121] M. Khabbaz, M.H. Entezari, Simple and versatile one-step synthesis of FeS2 nanoparticles by ultrasonic irradiation, J. Colloid Interface Sci. 470 (2016) 204–210. https://doi.org/10.1016/j.jcis.2016.02.055.

[122] V.R. Minnam Reddy, S. Gedi, C. Park, M. R.w, R.R. Ramakrishna, Development of sulphurized SnS thin film solar cells, Curr. Appl. Phys. 15 (2015) 588–598. https://doi.org/10.1016/j.cap.2015.01.022.

[123] Z. Zainal, M.Z. Hussein, A. Kassim, A. Ghazali, Electrodeposited SnS thin films from aqueous solution, J. Mater. Sci. Lett. 16 (1997) 1446–1449. https://doi.org/10.1023/A:1018586000130.

[124] T.S. Reddy, M.C.S. Kumar, Co-evaporated SnS thin films for visible light photodetector applications, RSC Adv. 6 (2016) 95680–95692. https://doi.org/10.1039/c6ra20129f.

[125] G.H. Yue, L.S. Wang, X. Wang, Y.Z. Chen, D.L. Peng, Characterization and optical properties of the single crystalline SnS nanowire arrays, Nanoscale Res. Lett. 4 (2009) 359–363. https://doi.org/10.1007/s11671-009-9253-6.

[126] S.R. Suryawanshi, S.S. Warule, S.S. Patil, K.R. Patil, M.A. More, Vapor-liquid-solid

growth of one-dimensional tin sulfide (SnS) nanostructures with promising field emission behavior, ACS Appl. Mater. Interfaces. 6 (2014) 2018–2025. https://doi.org/10.1021/am405039j.

[127] J. Chao, Z. Xie, X. Duan, Y. Dong, Z. Wang, J. Xu, B. Liang, B. Shan, J. Ye, D. Chen, G. Shen, Visible-light-driven photocatalytic and photoelectrochemical properties of porous SnSx(x = 1,2) architectures, CrystEngComm. 14 (2012) 3163–3168. https://doi.org/10.1039/c2ce06586j.

[128] M.Y. Sun, J. Yang, T. Lin, X.W. Du, Facile synthesis of SnS hollow nanoparticles via laser ablation followed by chemical etching, RSC Adv. 2 (2012) 7824–7828. https://doi.org/10.1039/c2ra21112b.

[129] A.M. Mostafa, E.A. Mwafy, M.S. Hasanin, One-pot synthesis of nanostructured CdS, CuS, and SnS by pulsed laser ablation in liquid environment and their antimicrobial activity, Opt. Laser Technol. 121 (2020) 105824. https://doi.org/10.1016/j.optlastec.2019.105824.

[130] J. Johny, S. Sepulveda-Guzman, B. Krishnan, D.A. Avellaneda, J.A. Aguilar Martinez, S. Shaji, Synthesis and Properties of Tin Sulfide Thin Films from Nanocolloids Prepared by Pulsed Laser Ablation in Liquid, ChemPhysChem. 18 (2017) 1061–1068. https://doi.org/10.1002/cphc.201601186.

[131] S. Banu, S.J. Ahn, Y.J. Eo, J. Gwak, A. Cho, Tin monosulfide (SnS) thin films grown by liquid-phase deposition, Sol. Energy. 145 (2017) 33–41. https://doi.org/10.1016/j.solener.2016.12.013.

[132] A. De Kergommeaux, J. Faure-Vincent, A. Pron, R. De Bettignies, P. Reiss, SnS thin films realized from colloidal nanocrystal inks, Thin Solid Films. 535 (2013) 376–379. https://doi.org/10.1016/j.tsf.2012.11.068.

[133] B.P. Reddy, M.C. Sekhar, S.V.P. Vattikuti, Y. Suh, S.H. Park, Solution-based spin-coated tin sulfide thin films for photovoltaic and supercapacitor applications, Mater. Res. Bull. 103 (2018) 13–18. https://doi.org/10.1016/j.materresbull.2018.03.016.

[134] S.M. Arakelyan, V.P. Veiko, S. V Kutrovskaya, A.O. Kucherik, A. V Osipov, T.A.

Vartanyan, T.E. Itina, Reliable and well-controlled synthesis of noble metal nanoparticles by continuous wave laser ablation in different liquids for deposition of thin films with variable optical properties, J. Nanoparticle Res. 18 (2016) 155. https://doi.org/10.1007/s11051-016-3468-0.

[135] S. Basu, S.K. Ghosh, S. Kundu, S. Panigrahi, S. Praharaj, S. Pande, S. Jana, T. Pal, Biomolecule induced nanoparticle aggregation: Effect of particle size on interparticle coupling, J. Colloid Interface Sci. 313 (2007) 724–734. https://doi.org/10.1016/j.jcis.2007.04.069.

[136] N.D. Klein, K.R. Hurley, Z.V. Feng, C.L. Haynes, Dark field transmission electron microscopy as a tool for identifying inorganic nanoparticles in biological matrices, Anal. Chem. 87 (2015) 4356–4362. https://doi.org/10.1021/acs.analchem.5b00124.

[137] N. Patra, K. Akash, S. Shiva, R. Gagrani, H.S.P. Rao, V.R. Anirudh, I.A. Palani, V. Singh, Parametric investigations on the influence of nano-second Nd 3+ :YAG laser wavelength and fluence in synthesizing NiTi nano-particles using liquid assisted laser ablation technique, Appl. Surf. Sci. 366 (2016) 104–111. https://doi.org/10.1016/j.apsusc.2016.01.072.

[138] S.Z. Mortazavi, P. Parvin, A. Reyhani, A.N. Golikand, S. Mirershadi, Effect of laser wavelength at IR (1064 nm) and UV (193 nm) on the structural formation of palladium nanoparticles in deionized water, J. Phys. Chem. C. 115 (2011) 5049–5057. https://doi.org/10.1021/jp1091224.

[139] J. Kim, D. Amaranatha Reddy, R. Ma, T.K. Kim, The influence of laser wavelength and fluence on palladium nanoparticles produced by pulsed laser ablation in deionized water, Solid State Sci. 37 (2014) 96–102. https://doi.org/10.1016/j.solidstatesciences.2014.09.005.

[140] M. Procházka, Probing applications of laser-ablated Ag colloids in SERS spectroscopy: Improvement of ablation procedure and SERS spectral testing, Anal. Chem. 69 (1997) 5103–5108. https://doi.org/10.1021/ac970683+.

[141] Z. Chen, S. Wang, W. Liu, X. Gao, D. Gao, M. Wang, S. Wang, Morphology-dependent

performance of Co3O4 via facile and controllable synthesis for methane combustion, Appl. Catal. A Gen. 525 (2016) 94–102. https://doi.org/10.1016/J.APCATA.2016.07.009.

[142] W. Zhou, H.F. Greer, What Can Electron Microscopy Tell Us beyond Crystal Structures?, Eur. J. Inorg. Chem. 2016 (2016) 941–950. https://doi.org/10.1002/ejic.201501342.

[143] P. Sinsermsuksakul, L. Sun, S.W. Lee, H.H. Park, S.B. Kim, C. Yang, R.G. Gordon, Overcoming Efficiency Limitations of SnS-Based Solar Cells, Adv. Energy Mater. 4 (2014) 1400496. https://doi.org/10.1002/aenm.201400496.

[144] H.S. Desarkar, P. Kumbhakar, A.K. Mitra, Optical properties of tin oxide nanoparticles prepared by laser ablation in water: Influence of laser ablation time duration and laser fluence, Mater. Charact. 73 (2012) 158–165. https://doi.org/10.1016/j.matchar.2012.08.014.

[145] T. Tsuji, K. Iryo, N. Watanabe, M. Tsuji, Preparation of silver nanoparticles by laser ablation in solution: influence of laser wavelength on particle size, Appl. Surf. Sci. 202 (2002) 80–85. https://doi.org/10.1016/S0169-4332(02)00936-4.

[146] D. Zhang, B. Gökce, S. Barcikowski, B. Go, S. Barcikowski, Laser Synthesis and Processing of Colloids: Fundamentals and Applications, Chem. Rev. 117 (2017) 3990–4103. https://doi.org/10.1021/acs.chemrev.6b00468.

[147] M.S. Mahdi, K. Ibrahim, A. Hmood, N.M. Ahmed, S.A. Azzez, F.I. Mustafa, A highly sensitive flexible SnS thin film photodetector in the ultraviolet to near infrared prepared by chemical bath deposition, RSC Adv. 6 (2016) 114980–114988. https://doi.org/10.1039/c6ra24491b.

[148] P.K. Nair, M.T.S. Nair, R.A. Zingaro, E.A. Meyers, XRD, XPS, optical and electrical studies on the conversion of SnS thin films to SnO2, Thin Solid Films. 239 (1994) 85–92. https://doi.org/10.1016/0040-6090(94)90112-0.

[149] E. Guneri, C. Ulutas, F. Kirmizigul, G. Altindemir, F. Gode, C. Gumus, Effect of deposition time on structural, electrical, and optical properties of SnS thin films deposited by chemical bath deposition, Appl. Surf. Sci. 257 (2010) 1189–1195. https://doi.org/10.1016/j.apsusc.2010.07.104.

[150] Y. Qachaou, O. Daoudi, A. Raidou, M. Lharch, A. Qachaou, M. Fahoume, The influence of solution temperature of SnS thin films grown by successive ionic layer adsorption and reaction (SILAR) method, J. Phys. Conf. Ser. 1292 (2019). https://doi.org/10.1088/1742-6596/1292/1/012022.

[151] R. Mariappan, T. Mahalingam, V. Ponnuswamy, Preparation and characterization of electrodeposited SnS thin films, Optik (Stuttg). 122 (2011) 2216–2219. https://doi.org/10.1016/j.ijleo.2011.01.015.

[152] M. Sastry, Nanostructured thin films by self-assembly of surface modified colloidal particles, Curr. Sci. 78 (2000) 1089–1097. https://doi.org/http://www.jstor.org/stable/24103619.

[153] G. Greczynski, L. Hultman, X-ray photoelectron spectroscopy: Towards reliable binding energy referencing, Prog. Mater. Sci. 107 (2020) 100591. https://doi.org/10.1016/j.pmatsci.2019.100591.

[154] B.J. Lindberg, K. Hamrin, G. Johansson, U. Gelius, A. Fahlman, C. Nordling, K. Siegbahn, Molecular Spectroscopy by Means of ESCA II. Sulfur compounds. Correlation of electron binding energy with structure , Phys. Scr. 1 (1970) 286–298. https://doi.org/10.1088/0031-8949/1/5-6/020.

[155] G.H. Yue, W. Wang, L.S. Wang, X. Wang, P.X. Yan, Y. Chen, D.L. Peng, The effect of anneal temperature on physical properties of SnS films, J. Alloys Compd. 474 (2009) 445–449. https://doi.org/10.1016/j.jallcom.2008.06.105.

[156] F. Paquin, J. Rivnay, A. Salleo, N. Stingelin, C. Silva, Multi-phase semicrystalline microstructures drive exciton dissociation in neat plastic semiconductors, J. Mater. Chem. C. 3 (2015) 10715–10722. https://doi.org/10.1039/b000000x.

[157] J. Gao, S.C. Nguyen, N.D. Bronstein, A.P. Alivisatos, Solution-Processed, High-Speed, and High-Quantum-Efficiency Quantum Dot Infrared Photodetectors, ACS Photonics. 3 (2016) 1217–1222. https://doi.org/10.1021/acsphotonics.6b00211.

[158] M.S. Mahdi, K. Ibrahim, A. Hmood, N.M. Ahmed, F.I. Mustafa, S.A. Azzez, High performance near infrared photodetector based on cubic crystal structure SnS thin film on

a glass substrate, Mater. Lett. 200 (2017) 10–13. https://doi.org/10.1016/j.matlet.2017.04.077.

[159] J.D. Prades, R. Jimenez-Diaz, F. Hernandez-Ramirez, L. Fernandez-Romero, T. Andreu, A. Cirera, A. Romano-Rodriguez, A. Cornet, J.R. Morante, S. Barth, S. Mathur, Toward a systematic understanding of photodetectors based on individual metal oxide nanowires, J. Phys. Chem. C. 112 (2008) 14639–14644. https://doi.org/10.1021/jp804614q.

[160] O. Lopez-Sanchez, D. Lembke, M. Kayci, A. Radenovic, A. Kis, Ultrasensitive photodetectors based on monolayer MoS2, Nat. Nanotechnol. 8 (2013) 497–501. https://doi.org/10.1038/nnano.2013.100.

[161] Y. Fang, J. Huang, Resolving weak light of sub-picowatt per square centimeter by hybrid perovskite photodetectors enabled by noise reduction, Adv. Mater. 27 (2015) 2804–2810. https://doi.org/10.1002/adma.201500099.

[162] M. Patel, H.S. Kim, J. Kim, Wafer-scale production of vertical SnS multilayers for high-performing photoelectric devices, Nanoscale. 9 (2017) 15804–15812. https://doi.org/10.1039/c7nr03370b.

[163] H. Tian, C. Fan, G. Liu, S. Yuan, Y. Zhang, M. Wang, E. Li, Ultrafast broadband photodetector based on SnS synthesized by hydrothermal method, Appl. Surf. Sci. 487 (2019) 1043–1048. https://doi.org/10.1016/j.apsusc.2019.05.175.

[164] C.C. Huang, Y.J. Lin, C.Y. Chuang, C.J. Liu, Y.W. Yang, Conduction-type control of SnSx films prepared by the sol-gel method for different sulfur contents, J. Alloys Compd. 553 (2013) 208–211. https://doi.org/10.1016/j.jallcom.2012.11.134.

[165] F. Wang, Y. Zhang, Y. Gao, P. Luo, J. Su, W. Han, K. Liu, H. Li, T. Zhai, 2D Metal Chalcogenides for IR Photodetection, Small. 15 (2019) 1901347. https://doi.org/10.1002/smll.201901347.

[166] H. Qiu, T. Xu, Z. Wang, W. Ren, H. Nan, Z. Ni, Q. Chen, S. Yuan, F. Miao, F. Song, G. Long, Y. Shi, L. Sun, J. Wang, X. Wang, Hopping transport through defect-induced localized states in molybdenum disulphide, Nat. Commun. 4 (2013) 2642. https://doi.org/10.1038/ncomms3642.

[167] D. Gedamu, I.M. Asuo, D. Benetti, M. Basti, I. Ka, S.G. Cloutier, F. Rosei, R. Nechache, Solvent-Antisolvent Ambient Processed Large Grain Size Perovskite Thin Films for High-Performance Solar Cells, Sci. Rep. 8 (2018) 12885. https://doi.org/10.1038/s41598-018-31184-0.

[168] B. Li, J. Tian, L. Guo, C. Fei, T. Shen, X. Qu, G. Cao, Dynamic Growth of Pinhole-Free Conformal CH3NH3PbI3 Film for Perovskite Solar Cells, ACS Appl. Mater. Interfaces. 8 (2016) 4684–4690. https://doi.org/10.1021/acsami.5b11679.

[169] G. Su, V.G. Hadjiev, P.E. Loya, J. Zhang, S. Lei, S. Maharjan, P. Dong, P. M. Ajayan, J. Lou, H. Peng, Chemical vapor deposition of thin crystals of layered semiconductor SnS2 for fast photodetection application, Nano Lett. 15 (2015) 506–513. https://doi.org/10.1021/nl503857r.

[170] H. Yin, A. Akey, R. Jaramillo, Large and persistent photoconductivity due to hole-hole correlation in CdS, Phys. Rev. Mater. 2 (2018) 084602. https://doi.org/10.1103/PhysRevMaterials.2.084602.

[171] X. Zhou, L. Gan, Q. Zhang, X. Xiong, H. Li, Z. Zhong, J. Han, T. Zhai, High performance near-infrared photodetectors based on ultrathin SnS nanobelts grown via physical vapor deposition, J. Mater. Chem. C. 4 (2016) 2111–2116. https://doi.org/10.1039/c5tc04410c.

[172] N. Abhiram, D. Thangaraju, R. Marnadu, S. Gunasekaran, V. Santhana, J. Chandrasekaran, N.S.M.P.L. Devi, M. Shkir, S. AlFaify, Development of morphology tuned SnS hierarchical structures for enhanced photosensitive photodiode fabrication, Inorg. Chem. Commun. 129 (2021) 108623. https://doi.org/10.1016/j.inoche.2021.108623.

[173] M.S. Mahdi, H.S. Al-Arab, K.H. Latif, K. Ibrahim, M. Bououdina, Flexible and high-performance broadband nanoflowers tin sulfide photodetector, Appl. Phys. A Mater. Sci. Process. 126 (2020) 958. https://doi.org/10.1007/s00339-020-04144-7.

[174] D. Alagarasan, S. Varadharajaperumal, K.D.A. Kumar, R. Naik, S. Umrao, M. Shkir, S. AIFaify, R. Ganesan, Influence of nanostructured SnS thin films for visible light photo detection, Opt. Mater. (Amst). 121 (2021) 111489. https://doi.org/10.1016/j.optmat.2021.111489.

[175] R. Balakarthikeyan, A. Santhanam, A. Khan, A.M. El-Toni, A.A. Ansari, A. Imran, M. Shkir, S. AlFaify, Performance analysis of SnS thin films fabricated using thermal evaporation technique for photodetector applications, Optik (Stuttg). 244 (2021) 167460. https://doi.org/10.1016/j.ijleo.2021.167460.

[176] H. Öztürk, F. Aslan, Preparation of high-quality SnS thin films for self-powered photodetectors and solar cells using a low-temperature powder technique, Opt. Mater. (Amst). 131 (2022) 112755. https://doi.org/10.1016/J.OPTMAT.2022.112755.

[177] M.S. Mahdi, K. Ibrahim, N.M. Ahmed, A. Hmood, F.I. Mustafa, S.A. Azzez, M. Bououdina, High performance and low-cost UV–Visible–NIR photodetector based on tin sulphide nanostructures, J. Alloys Compd. 735 (2018) 2256–2262. https://doi.org/10.1016/j.jallcom.2017.10.203.

[178] M. Casalino, G. Coppola, R.M. De La Rue, D.F. Logan, State-of-the-art all-silicon sub-bandgap photodetectors at telecom and datacom wavelengths, Laser Photonics Rev. 10 (2016) 895–921. https://doi.org/10.1002/lpor.201600065.

[179] S. Yang, W. Cai, H. Zhang, X. Xu, H. Zeng, Size and structure control of Si nanoparticles by laser ablation in different liquid media and further centrifugation classification, J. Phys. Chem. C. 113 (2009) 19091–19095. https://doi.org/10.1021/jp907285f.

[180] R.W. Miles, O.E. Ogah, G. Zoppi, I. Forbes, Thermally evaporated thin films of SnS for application in solar cell devices, Thin Solid Films. 517 (2009) 4702–4705. https://doi.org/10.1016/j.tsf.2009.03.003.

[181] S. Cheng, G. Conibeer, Physical properties of very thin SnS films deposited by thermal evaporation, Thin Solid Films. 520 (2011) 837–841. https://doi.org/10.1016/j.tsf.2011.01.355.

[182] B.A. Hasan, I.H. Shallal, Structural and Optical Properties of SnS Thin Films, J. Nanotechnol. Adv. Mater. 2 (2014) 43–49. https://doi.org/10.12785/jnam/020201.

[183] K. Maniammal, G. Madhu, V. Biju, X-ray diffraction line profile analysis of nanostructured nickel oxide: Shape factor and convolution of crystallite size and microstrain contributions, Phys. E Low-Dimensional Syst. Nanostructures. 85 (2017)

214–222. https://doi.org/10.1016/J.PHYSE.2016.08.035.

[184] T. Garmim, S. Chahib, L. Soussi, R. Mghaiouini, Z. El Jouad, A. Louardi, O. Karzazi, M. El Jouad, E.K. Hlil, B. Hartiti, M. Monkade, Optical, electrical and electronic properties of SnS thin films deposited by sol gel spin coating technique for photovoltaic applications, J. Mater. Sci. Mater. Electron. 31 (2020) 20730–20741. https://doi.org/10.1007/s10854-020-04586-y.

[185] T.G. Ulusoy Ghobadi, A. Ghobadi, T. Okyay, K. Topalli, A.K. Okyay, Controlling luminescent silicon nanoparticle emission produced by nanosecond pulsed laser ablation: role of interface defect states and crystallinity phase, RSC Adv. 6 (2016) 112520–112526. https://doi.org/10.1039/C6RA24412B.

[186] F.A. Rustamov, N.H. Darvishov, V.E. Bagiev, M.Z. Mamedov, E.Y. Bobrova, H.O. Qafarova, Determination of size and bandgap distributions of Si nanoparticles from photoluminescence excitation and emission spectra in n-type stain etched porous silicon, J. Lumin. 154 (2014) 224–228. https://doi.org/10.1016/j.jlumin.2014.04.037.

[187] I. Umezu, H. Minami, H. Senoo, A. Sugimura, Synthesis of photoluminescent colloidal silicon nanoparticles by pulsed laser ablation in liquids, J. Phys. Conf. Ser. 59 (2007) 392–395. https://doi.org/10.1088/1742-6596/59/1/083.

[188] B. Xin, N. Alaal, S. Mitra, A. Subahi, Y. Pak, D. Almalawi, N. Alwadai, S. Lopatin, I.S. Roqan, Identifying Carrier Behavior in Ultrathin Indirect-Bandgap CsPbX 3 Nanocrystal Films for Use in UV/Visible-Blind High-Energy Detectors, Small. 16 (2020) 2004513. https://doi.org/10.1002/smll.202004513.

[189] J. Xu, Y. Yang, Z. Xie, Effect of vacuum annealing on the properties of Sputtered SnS thin films, Chalcogenide Lett. 11 (2014) 485–491.

[190] P. Jain, P. Arun, Influence of grain size on the band-gap of annealed SnS thin films, Thin Solid Films. 548 (2013) 241–246. https://doi.org/10.1016/j.tsf.2013.09.089.

[191] A. Parameswaran Sreekala, B. Krishnan, R. Fabian Cienfuegos Pelaes, D. Avellaneda Avellaneda, J. Amilcar Aguilar-Martínez, S. Shaji, Ultraviolet to near infrared wavelength independent SnS-graphene hybrid thin film photodetector from nanocolloids, Appl. Surf.

Sci. 609 (2023) 155277. https://doi.org/10.1016/j.apsusc.2022.155277.

[192] I.B. Kherchachi, A. Attaf, H. Saidi, A. Bouhdjer, H. Bendjedidi, Y. Benkhetta, R. Azizi, Structural, optical and electrical properties of SnxSy thin films grown by spray ultrasonic, J. Semicond. 37 (2016) 032001. https://doi.org/10.1088/1674-4926/37/3/032001.

[193] J. Xu, C. Wang, T. Wang, Y. Wang, Q. Kang, Y. Liu, Y. Tian, Mechanisms for low-temperature direct bonding of Si/Si and quartz/quartz: Via VUV/O3 activation, RSC Adv. 8 (2018) 11528–11535. https://doi.org/10.1039/c7ra13095c.

[194] B. Li, D. Yu, S. Zhang, Raman spectral study of silicon nanowires, Phys. Rev. B - Condens. Matter Mater. Phys. 59 (1999) 1645–1648. https://doi.org/10.1103/PhysRevB.59.1645.

[195] W.J. Lee, Y.H. Chang, Growth without postannealing of monoclinic VO2 thin film by atomic layer deposition using VCl4 as precursor, Coatings. 8 (2018) 431. https://doi.org/10.3390/coatings8120431.

[196] V.P. Jethwa, K. Patel, N. Som, V.M. Pathak, K.D. Patel, G.K. Solanki, P.K. Jha, Temperature-dependent vibrational properties of DVT grown orthorhombic SnS single crystals and their application as a self-powered photodetector, Appl. Surf. Sci. 531 (2020) 147406. https://doi.org/10.1016/j.apsusc.2020.147406.

[197] J. Yu, J. Gao, F. Xue, X. Yu, H. Yu, X. Dong, H. Huang, A. Ding, X. Quan, G. Cao, Formation mechanism and optical characterization of polymorphic silicon nanostructures by DC arc-discharge, RSC Adv. 5 (2015) 68714–68721. https://doi.org/10.1039/c5ra11738k.

[198] A. Takami, H. Kurita, S. Koda, Laser-Induced Size Reduction of Noble Metal Particles, J. Phys. Chem. B. 103 (1999) 1226–1232. https://doi.org/10.1021/jp983503o.

[199] S.C. Singh, S.K. Mishra, R.K. Srivastava, R. Gopal, Optical properties of selenium quantum dots produced with laser irradiation of water suspended Se nanoparticles, J. Phys. Chem. C. 114 (2010) 17374–17384. https://doi.org/10.1021/jp105037w.

[200] D. Sharma, N. Kamboj, K. Agarwal, B.R. Mehta, Structural, optical and photoelectrochemical properties of phase pure SnS and SnS2 thin films prepared by

vacuum evaporation method, J. Alloys Compd. 822 (2020) 153653. https://doi.org/10.1016/j.jallcom.2020.153653.

[201] H. Jadhav, S. Suryawanshi, M.A. More, S. Sinha, Pulsed laser deposition of tin oxide thin films for field emission studies, Appl. Surf. Sci. 419 (2017) 764–769. https://doi.org/10.1016/j.apsusc.2017.05.020.

[202] F.A. Stevie, C.L. Donley, Introduction to x-ray photoelectron spectroscopy, J. Vac. Sci. Technol. A. 38 (2020) 063204. https://doi.org/10.1116/6.0000412.

[203] I. Milošev, Ž. Jovanović, J.B. Bajat, R. Jančić-Heinemann, V.B. Mišković-Stanković, Surface Analysis and Electrochemical Behavior of Aluminum Pretreated by Vinyltriethoxysilane Films in Mild NaCl Solution, J. Electrochem. Soc. 159 (2012) C303–C311. https://doi.org/10.1149/2.042207jes.

[204] S. Kudryashov, A. Samokhvalov, A. Nastulyavichus, I. Saraeva, V. Mikhailovskii, A. Ionin, V. Veiko, Nanosecond-Laser Generation of Nanoparticles in Liquids: From Ablation through Bubble Dynamics to Nanoparticle Yield, Materials (Basel). 12 (2019) 562. https://doi.org/10.3390/ma12040562.

[205] W. Charee, V. Tangwarodomnukun, C. Dumkum, Laser ablation of silicon in water under different flow rates, Int. J. Adv. Manuf. Technol. 78 (2015) 19–29. https://doi.org/10.1007/s00170-014-6625-6.

[206] P.G. Kuzmin, G.A. Shafeev, V. V. Bukin, S. V. Garnov, C. Farcau, R. Carles, B. Warot-Fontrose, V. Guieu, G. Viau, Silicon nanoparticles produced by femtosecond laser ablation in ethanol: Size control, structural characterization, and optical properties, J. Phys. Chem. C. 114 (2010) 15266–15273. https://doi.org/10.1021/jp102174y.

[207] Q.X. Zhang, S.Y. Ma, R. Zhang, Y. Tie, S.T. Pei, Optimization ethanol detection performance manifested by SnS/SnS2 nanoparticles, Mater. Lett. 258 (2020) 126783. https://doi.org/10.1016/j.matlet.2019.126783.

[208] J.Y.W. Seto, The electrical properties of polycrystalline silicon films, J. Appl. Phys. 46 (1975) 5247–5254. https://doi.org/10.1063/1.321593.

[209] M.S. Mahdi, K. Ibrahim, A. Hmood, N.M. Ahmed, S.A. Azzez, F.I. Mustafa, A highly

sensitive flexible SnS thin film photodetector in the ultraviolet to near infrared prepared by chemical bath deposition, RSC Adv. 6 (2016) 114980–114988. https://doi.org/10.1039/c6ra24491b.

[210] A. Ajmal, I. Majeed, R.N. Malik, H. Idriss, M.A. Nadeem, Principles and mechanisms of photocatalytic dye degradation on TiO2 based photocatalysts: A comparative overview, RSC Adv. 4 (2014) 37003–37026. https://doi.org/10.1039/c4ra06658h.

[211] S. Na Phattalung, S. Limpijumnong, J. Yu, Passivated co-doping approach to bandgap narrowing of titanium dioxide with enhanced photocatalytic activity, Appl. Catal. B Environ. 200 (2017) 1–9. https://doi.org/10.1016/j.apcatb.2016.06.054.

[212] C. Yang, W. Wang, Z. Shan, F. Huang, Preparation and photocatalytic activity of high-efficiency visible-light-responsive photocatalyst SnSx/TiO2, J. Solid State Chem. 182 (2009) 807–812. https://doi.org/10.1016/j.jssc.2008.12.018.

[213] X. Hu, G. Song, W. Li, Y. Peng, L. Jiang, Y. Xue, Q. Liu, Z. Chen, J. Hu, Phase-controlled synthesis and photocatalytic properties of SnS, SnS 2 and SnS/SnS2 heterostructure nanocrystals, Mater. Res. Bull. 48 (2013) 2325–2332. https://doi.org/10.1016/j.materresbull.2013.02.082.

[214] A.M.M. and S.I. Preeti Singh, Role of Nanomaterials and their Applications as Photo-catalyst and Senors : A Review, Nano Res. Appl. 2:1 (2016) 1–10.

[215] A.E. Oluwalana, P.A. Ajibade, Tin sulfide nanoparticles as photocatalysts for the degradation of organic dyes, J. Sulfur Chem. 43 (2022) 95–116. https://doi.org/10.1080/17415993.2021.1979975.

[216] G. Liao, C. Li, X. Li, B. Fang, Emerging polymeric carbon nitride Z-scheme systems for photocatalysis, Cell Reports Phys. Sci. 2 (2021) 100355. https://doi.org/10.1016/j.xcrp.2021.100355.

[217] Q. Xu, L. Zhang, B. Cheng, J. Fan, J. Yu, S-Scheme Heterojunction Photocatalyst, Chem. 6 (2020) 1543–1559. https://doi.org/10.1016/j.chempr.2020.06.010.

[218] S.S. Mohtar, F. Aziz, A.F. Ismail, N.S. Sambudi, H. Abdullah, A.N. Rosli, B. Ohtani, Impact of Doping and Additive Applications on Photocatalyst Textural Properties in

Removing Organic Pollutants: A Review, Catalysts. 11 (2021) 1160. https://doi.org/10.3390/catal11101160.

[219] S.S. Hegde, B.S. Surendra, V. Talapatadur, P. Murahari, K. Ramesh, Visible light photocatalytic properties of cubic and orthorhombic SnS nanoparticles, Chem. Phys. Lett. 754 (2020) 137665. https://doi.org/10.1016/j.cplett.2020.137665.

[220] Y. Qu, X. Duan, Progress, challenge and perspective of heterogeneous photocatalysts, Chem. Soc. Rev. 42 (2013) 2568–2580. https://doi.org/10.1039/c2cs35355e.

[221] A. López, D. Acosta, A. I. Martínez, J. Santiago, Nanostructured low crystallized titanium dioxide thin films with good photocatalytic activity, Powder Technol. 202 (2010) 111–117. https://doi.org/10.1016/j.powtec.2010.04.025.

[222] P. Geim, A. K.; Novoselov, K. S, The rise of graphene, Nat. Mater. 6 (2007) 183–191. https://doi.org/10.1038/nmat1849.

[223] F. Bonaccorso, Z. Sun, T. Hasan, A.C. Ferrari, Graphene photonics and optoelectronics, Nat. Photonics. 4 (2010) 611–622. https://doi.org/10.1038/nphoton.2010.186.

[224] W. Zhang, C.P. Chuu, J.K. Huang, C.H. Chen, M.L. Tsai, Y.H. Chang, C. Te Liang, Y.Z. Chen, Y.L. Chueh, J.H. He, M.Y. Chou, L.J. Li, Ultrahigh-Gain Photodetectors Based on Atomically Thin Graphene-MoS2 Heterostructures, Sci. Rep. 4 (2014) 3826. https://doi.org/10.1038/srep03826.

[225] G. Konstantatos, M. Badioli, L. Gaudreau, J. Osmond, M. Bernechea, F.P.G. De Arquer, F. Gatti, F.H.L. Koppens, Hybrid graphene-quantum dot phototransistors with ultrahigh gain, Nat. Nanotechnol. 7 (2012) 363–368. https://doi.org/10.1038/nnano.2012.60.

[226] N.O. Weiss, H. Zhou, L. Liao, Y. Liu, S. Jiang, Y. Huang, X. Duan, Graphene: An emerging electronic material, Adv. Mater. 24 (2012) 5782–5825. https://doi.org/10.1002/adma.201201482.

[227] L. Gao, C. Chen, K. Zeng, C. Ge, D. Yang, H. Song, J. Tang, Broadband, sensitive and spectrally distinctive SnS2 nanosheet/PbS colloidal quantum dot hybrid photodetector, Light Sci. Appl. 5 (2016) e16126. https://doi.org/10.1038/lsa.2016.126.

[228] H. Tabata, M. Fujii, S. Hayashi, Laser ablation of diamond particles suspended in ethanol: Effective formation of long polyynes, Carbon N. Y. 44 (2006) 522–529. https://doi.org/10.1016/j.carbon.2005.08.007.

[229] H. Tabata, M. Fujii, S. Hayashi, Synthesis of polyynes by laser ablation of diamond nanoparticles suspended in solution, Eur. Phys. J. D. 34 (2005) 223–225. https://doi.org/10.1140/epjd/e2005-00147-0.

[230] H. Tabata, M. Fujii, S. Hayashi, Laser ablation of diamond nanoparticles suspended in solvent: Synthesis of polyynes, Chem. Phys. Lett. 395 (2004) 138–142. https://doi.org/10.1016/j.cplett.2004.07.063.

[231] R.M. Altuwirqi, Graphene Nanostructures by Pulsed Laser Ablation in Liquids: A Review, Materials (Basel). 15 (2022) 5925. https://doi.org/10.3390/ma15175925.

[232] M.A. Dar, D. Govindarajan, G.N. Dar, Facile synthesis of SnS nanostructures with different morphologies for supercapacitor and dye-sensitized solar cell applications, J. Mater. Sci. Mater. Electron. 32 (2021) 20394–20409. https://doi.org/10.1007/s10854-021-06550-w.

[233] A.P. Sreekala, B. Krishnan, R.F.C. Pelaes, D.A. Avellaneda, M.I.M. Palma, S. Shaji, Tin sulfide thin films by spin coating of laser ablated nanocolloids for UV–Vis–NIR photodetection, Colloids Surfaces A Physicochem. Eng. Asp. 639 (2022) 128382. https://doi.org/10.1016/j.colsurfa.2022.128382.

[234] S.A. Kazmi, S. Hameed, A.S. Ahmed, M. Arshad, A. Azam, Electrical and optical properties of graphene-TiO2 nanocomposite and its applications in dye sensitized solar cells (DSSC), J. Alloys Compd. 691 (2017) 659–665. https://doi.org/10.1016/j.jallcom.2016.08.319.

[235] S.S. Hegde, A.G. Kunjomana, P. Murahari, B.K. Prasad, K. Ramesh, Vacuum annealed tin sulfide (SnS) thin films for solar cell applications, Surfaces and Interfaces. 10 (2018) 78–84. https://doi.org/10.1016/j.surfin.2017.12.003.

[236] J. Kang, V.K. Sangwan, H.S. Lee, X. Liu, M.C. Hersam, Solution-Processed Layered Gallium Telluride Thin-Film Photodetectors, ACS Photonics. 5 (2018) 3996–4002.

https://doi.org/10.1021/acsphotonics.8b01066.

[237] H. Wang, Y.H. Hu, Effect of oxygen content on structures of graphite oxides, Ind. Eng. Chem. Res. 50 (2011) 6132–6137. https://doi.org/10.1021/ie102572q.

[238] G. Mohan Kumar, X. Fu, P. Ilanchezhiyan, S.U. Yuldashev, D.J. Lee, H.D. Cho, T.W. Kang, Highly Sensitive Flexible Photodetectors Based on Self-Assembled Tin Monosulfide Nanoflakes with Graphene Electrodes, ACS Appl. Mater. Interfaces. 9 (2017) 32142–32150. https://doi.org/10.1021/acsami.7b09959.

[239] M. Dogrusoz, R. Demir-Cakan, Mechanochemical synthesis of SnS anodes for sodium ion batteries, Int. J. Energy Res. 44 (2020) 10809–10820. https://doi.org/10.1002/er.5735.

[240] H.C. Tao, X.L. Yang, L.L. Zhang, S.B. Ni, One-step in situ synthesis of SnS/graphene nanocomposite with enhanced electrochemical performance for lithium ion batteries, J. Electroanal. Chem. 728 (2014) 134–139. https://doi.org/10.1016/j.jelechem.2014.07.004.

[241] A. Debataraja, R.V. Manurung, L.A.T.W. Asri, B. Yuliarto, Nugraha, B. Sunendar, Synthesis and characterization of nanocomposites of tin oxide-graphene doping Pd using polyol method, Indones. J. Chem. 18 (2018) 344–348. https://doi.org/10.22146/ijc.26660.

[242] S. Sagadevan, Z.Z. Chowdhury, M.R. Bin Johan, R.F. Rafique, F.A. Aziz, One pot synthesis of hybrid ZnS–Graphene nanocomposite with enhanced photocatalytic activities using hydrothermal approach, J. Mater. Sci. Mater. Electron. 29 (2018) 9099–9107. https://doi.org/10.1007/s10854-018-8937-z.

[243] F. Tao, Y. Zhang, B. Wang, F. Zhang, X. Chang, R. Fan, L. Dong, Y. Yin, Graphite powder/semipermeable collodion membrane composite for water evaporation, Sol. Energy Mater. Sol. Cells. 180 (2018) 34–45. https://doi.org/10.1016/j.solmat.2018.02.014.

[244] Y.H. Lee, S. Park, Y. Won, J. Mun, J.H. Ha, J.H. Lee, S.H. Lee, J. Park, J. Yeom, J. Rho, H. Ko, J.H. Oh, Flexible high-performance graphene hybrid photodetectors functionalized with gold nanostars and perovskites, NPG Asia Mater. 12 (2020) 79. https://doi.org/10.1038/s41427-020-00260-1.

[245] X. Chen, X. Wang, D. Fang, A review on C1s XPS-spectra for some kinds of carbon materials, Fullerenes, Nanotub. Carbon Nanostructures. 28 (2020) 1048–1058.

https://doi.org/10.1080/1536383X.2020.1794851.

[246] J. Park, W.C. Mitchel, S. Elhamri, L. Grazulis, J. Hoelscher, K. Mahalingam, C. Hwang, S.K. Mo, J. Lee, Observation of the intrinsic bandgap behaviour in as-grown epitaxial twisted graphene, Nat. Commun. 6 (2015) 5677. https://doi.org/10.1038/ncomms6677.

[247] D. Shao, M. Yu, H. Sun, T. Hu, J. Lian, S. Sawyer, High responsivity, fast ultraviolet photodetector fabricated from ZnO nanoparticle-graphene core-shell structures, Nanoscale. 5 (2013) 3664–3667. https://doi.org/10.1039/c3nr00369h.

[248] Z. Gao, Z. Jin, Q. Ji, Y. Tang, J. Kong, L. Zhang, Y. Li, Crumpled graphene prepared by a simple ultrasonic pyrolysis method for fast photodetection, Carbon N. Y. 128 (2018) 117–124. https://doi.org/10.1016/J.CARBON.2017.11.082.

[249] Z. Chen, Z. Cheng, J. Wang, X. Wan, C. Shu, H.K. Tsang, H.P. Ho, J. Bin Xu, High Responsivity, Broadband, and Fast Graphene/Silicon Photodetector in Photoconductor Mode, Adv. Opt. Mater. 3 (2015) 1207–1214. https://doi.org/10.1002/adom.201500127.

[250] Q. Guo, Z. Zheng, H. Gao, J. Ma, X. Qin, SnO2/graphene composite as highly reversible anode materials for lithium ion batteries, J. Power Sources. 240 (2013) 149–154. https://doi.org/10.1016/j.jpowsour.2013.03.116.

[251] P. Li, B. Zhu, P. Li, Z. Zhang, L. Li, Y. Gu, A facile method to synthesize CdSe-reduced graphene oxide composite with good dispersion and high nonlinear optical properties, Nanomaterials. 9 (2019) 957. https://doi.org/10.3390/nano9070957.

[252] Y.C. Lin, D.C. Tsai, Z.C. Chang, F.S. Shieu, Ultrasonic chemical synthesis of CdS-reduced graphene oxide nanocomposites with an enhanced visible light photoactivity, Appl. Surf. Sci. 440 (2018) 1227–1234. https://doi.org/10.1016/j.apsusc.2018.01.305.

[253] Q. Xiang, B. Cheng, J. Yu, Graphene-Based Photocatalysts for Solar-Fuel Generation, Angew. Chemie - Int. Ed. 54 (2015) 11350–11366. https://doi.org/10.1002/anie.201411096.

[254] W. Wang, K.K. Leung, W.K. Fong, S.F. Wang, Y.Y. Hui, S.P. Lau, Z. Chen, L.J. Shi, C.B. Cao, C. Surya, Molecular beam epitaxy growth of high quality p-doped SnS van der Waals epitaxy on a graphene buffer layer, J. Appl. Phys. 111 (2012) 093520.

https://doi.org/10.1063/1.4709732.

[255] D. Chao, C. Zhu, P. Yang, X. Xia, J. Liu, J. Wang, X. Fan, S. V. Savilov, J. Lin, H.J. Fan, Z.X. Shen, Array of nanosheets render ultrafast and high-capacity Na-ion storage by tunable pseudocapacitance, Nat. Commun. 7 (2016) 12122. https://doi.org/10.1038/ncomms12122.

[256] L. Wang, X. Li, Z. Jin, Z. Liang, X. Peng, X. Ren, B. Gao, G. Feng, P.K. Chu, K. Huo, Spatially controlled synthesis of superlattice-like SnS/nitrogen-doped graphene hybrid nanobelts as high-rate and durable anode materials for sodium-ion batteries, J. Mater. Chem. A. 7 (2019) 27475–27483. https://doi.org/10.1039/c9ta08945d.

[257] V.A. Zuñiga-Ibarra, S. Shaji, B. Krishnan, J. Johny, S. Sharma Kanakkillam, D.A. Avellaneda, J.A.A. Martinez, T.K.D. Roy, N.A. Ramos-Delgado, Synthesis and characterization of black TiO2 nanoparticles by pulsed laser irradiation in liquid, Appl. Surf. Sci. 483 (2019) 156–164. https://doi.org/10.1016/j.apsusc.2019.03.302.

[258] S. Sharma Kanakkillam, B. Krishnan, S. Sepulveda Guzman, J. Amilcar Aguilar Martinez, D. Avellaneda Avellaneda, S. Shaji, Defects rich nanostructured black zinc oxide formed by nanosecond pulsed laser irradiation in liquid, Appl. Surf. Sci. 567 (2021) 150858. https://doi.org/10.1016/j.apsusc.2021.150858.

[259] S. Kunwar, S. Pandit, R. Kulkarni, R. Mandavkar, S. Lin, M.Y. Li, J. Lee, Hybrid device architecture using plasmonic nanoparticles, graphene quantum dots, and titanium dioxide for UV photodetectors, ACS Appl. Mater. Interfaces. 13 (2021) 3408–3418. https://doi.org/10.1021/acsami.0c19058.

[260] F. Yang, H. Cong, K. Yu, L. Zhou, N. Wang, Z. Liu, C. Li, Q. Wang, B. Cheng, Ultrathin Broadband Germanium-Graphene Hybrid Photodetector with High Performance, ACS Appl. Mater. Interfaces. 9 (2017) 13422–13429. https://doi.org/10.1021/acsami.6b16511.

[261] V. Krishnamurthi, H. Khan, T. Ahmed, A. Zavabeti, S.A. Tawfik, S.K. Jain, M.J.S. Spencer, S. Balendhran, K.B. Crozier, Z. Li, L. Fu, M. Mohiuddin, M.X. Low, B. Shabbir, A. Boes, A. Mitchell, C.F. McConville, Y. Li, K. Kalantar-Zadeh, N. Mahmood, S. Walia, Liquid-Metal Synthesized Ultrathin SnS Layers for High-Performance Broadband

Photodetectors, Adv. Mater. 32 (2020) 2004247. https://doi.org/10.1002/adma.202004247.

[262] W.Y. Lee, S. Ha, H. Lee, J.H. Bae, B. Jang, H.J. Kwon, Y. Yun, S. Lee, J. Jang, High-Detectivity Flexible Near-Infrared Photodetector Based on Chalcogenide Ag2Se Nanoparticles, Adv. Opt. Mater. 7 (2019) 1900812. https://doi.org/10.1002/adom.201900812.

[263] X. Yu, Y. Li, X. Hu, D. Zhang, Y. Tao, Z. Liu, Y. He, M.A. Haque, Z. Liu, T. Wu, Q.J. Wang, Narrow bandgap oxide nanoparticles coupled with graphene for high performance mid-infrared photodetection, Nat. Commun. 9 (2018) 4299. https://doi.org/10.1038/s41467-018-06776-z.

[264] C. Zhou, X. Wang, X. Kuang, S. Xu, High performance flexible ultraviolet photodetectors based on TiO2/graphene hybrid for irradiation monitoring applications, J. Micromechanics Microengineering. 26 (2016) 75003. https://doi.org/10.1088/0960-1317/26/7/075003.

[265] Y. Chen, Y. Wu, J. Ben, K. Jiang, Y. Jia, S. Zhang, H. Zang, Z. Shi, B. Duan, X. Sun, D. Li, A high-response ultraviolet photodetector by integrating GaN nanoparticles with graphene, J. Alloys Compd. 868 (2021) 159281. https://doi.org/10.1016/j.jallcom.2021.159281.

[266] M.K. Thakur, A. Gupta, M.Y. Fakhri, R.S. Chen, C.T. Wu, K.H. Lin, S. Chattopadhyay, Optically coupled engineered upconversion nanoparticles and graphene for a high responsivity broadband photodetector, Nanoscale. 11 (2019) 9716–9725. https://doi.org/10.1039/c8nr10280e.

[267] J. Wu, Z. Yang, C. Qiu, Y. Zhang, Z. Wu, J. Yang, Y. Lu, J. Li, D. Yang, R. Hao, E. Li, G. Yu, S. Lin, Enhanced performance of a graphene/GaAs self-driven near-infrared photodetector with upconversion nanoparticles, Nanoscale. 10 (2018) 8023–8030. https://doi.org/10.1039/c8nr00594j.

[268] V.Q. Dang, T.Q. Trung, D. Il Kim, L.T. Duy, B.U. Hwang, D.W. Lee, B.Y. Kim, L.D. Toan, N.E. Lee, Ultrahigh Responsivity in Graphene-ZnO Nanorod Hybrid UV Photodetector, Small. 11 (2015) 3054–3065. https://doi.org/10.1002/smll.201403625.

[269] K. Charipar, H. Kim, A. Piqué, N. Charipar, ZnO nanoparticle/graphene hybrid photodetectors via laser fragmentation in liquid, Nanomaterials. 10 (2020) 1648. https://doi.org/10.3390/nano10091648.

[270] Y. Lee, J. Kwon, E. Hwang, C.H. Ra, W.J. Yoo, J.H. Ahn, J.H. Park, J.H. Cho, High-performance perovskite-graphene hybrid photodetector, Adv. Mater. 27 (2015) 41–46. https://doi.org/10.1002/adma.201402271.

[271] J. Jiang, Y. Wen, H. Wang, L. Yin, R. Cheng, C. Liu, L. Feng, J. He, Recent Advances in 2D Materials for Photodetectors, Adv. Electron. Mater. 7 (2021) 2001125. https://doi.org/10.1002/aelm.202001125.

[272] J. Zhang, Y. Wang, D. Li, Y. Sun, L. Jiang, Engineering Surface Plasmons in Metal/Nonmetal Structures for Highly Desirable Plasmonic Photodetectors, ACS Mater. Lett. 4 (2022) 343–355. https://doi.org/10.1021/acsmaterialslett.1c00768.

[273] A. Samir, H.M. Abd El-salam, S.W. Harun, T. Mohamed, The effects of different parameters and interaction angles of a 532 nm pulsed Nd: YAG laser on the properties of laser-ablated silver nanoparticles, Opt. Commun. 501 (2021) 127366. https://doi.org/10.1016/j.optcom.2021.127366.

[274] B.W. Boote, H. Byun, J.H. Kim, Silver-gold bimetallic nanoparticles and their applications as optical materials, J. Nanosci. Nanotechnol. 14 (2014) 1563–1577. https://doi.org/10.1166/jnn.2014.9077.

[275] R.A. Ganeev, M. Baba, A.I. Ryasnyansky, M. Suzuki, H. Kuroda, Characterization of optical and nonlinear optical properties of silver nanoparticles prepared by laser ablation in various liquids, Opt. Commun. 240 (2004) 437–448. https://doi.org/10.1016/j.optcom.2004.06.049.

[276] T.T. Ha Pham, N.D. Dien, X.H. Vu, Facile synthesis of silver/gold alloy nanoparticles for ultra-sensitive rhodamine B detection, RSC Adv. 11 (2021) 21475–21488. https://doi.org/10.1039/d1ra02576g.

[277] V.K. Arepalli, T.D. Nguyen, J. Kim, Influence of Ag thickness on the structural, optical, and electrical properties of the SnS/Ag/SnS trilayer films for solar cell application, Curr.

Appl. Phys. 20 (2020) 438–444. https://doi.org/10.1016/j.cap.2020.01.002.

[278] S. Sebastian, S. Vinoth, K.H. Prasad, M.S. Revathy, S. Gobalakrishnan, P.K. Praseetha, V. Ganesh, S. AlFaify, Quantitative analysis of Ag-doped SnS thin films for solar cell applications, Appl. Phys. A Mater. Sci. Process. 126 (2020) 1–12. https://doi.org/10.1007/s00339-020-03959-8.

[279] J. Johny, S. Sepulveda-Guzman, B. Krishnan, D.A. Avellaneda, J.A. Aguilar Martinez, M.R. Anantharaman, S. Shaji, Tin sulfide: Reduced graphene oxide nanocomposites for photovoltaic and electrochemical applications, Sol. Energy Mater. Sol. Cells. 189 (2019) 53–62. https://doi.org/10.1016/j.solmat.2018.09.025.

[280] D. Zhang, W. Choi, K. Yazawa, K. Numata, A. Tateishi, S.-H. Cho, H.-P. Lin, Y.K. Li, Y. Ito, K. Sugioka, Two Birds with One Stone: Spontaneous Size Separation and Growth Inhibition of Femtosecond Laser-Generated Surfactant-Free Metallic Nanoparticles via ex Situ SU-8 Functionalization, ACS Omega. 3 (2018) 10953–10966. https://doi.org/10.1021/acsomega.8b01250.

[281] P. Nancy, A.K. Nair, R. Antoine, S. Thomas, N. Kalarikkal, In Situ Decoration of Gold Nanoparticles on Graphene Oxide via Nanosecond Laser Ablation for Remarkable Chemical Sensing and Catalysis, Nanomaterials. 9 (2019) 1201. https://doi.org/10.3390/nano9091201.

[282] K. Jia, M.Y. Khaywah, Y. Li, J.L. Bijeon, P.M. Adam, R. Déturche, B. Guelorget, M. François, G. Louarn, R.E. Ionescu, Strong improvements of localized surface plasmon resonance sensitivity by using Au/Ag bimetallic nanostructures modified with polydopamine films, ACS Appl. Mater. Interfaces. 6 (2014) 219–227. https://doi.org/10.1021/am403943q.

[283] G. Kaur, S. Tanwar, V. Kaur, R. Biswas, S. Saini, K.K. Haldar, T. Sen, Interfacial design of gold/silver core–shell nanostars for plasmon-enhanced photocatalytic coupling of 4-aminothiophenol, J. Mater. Chem. C. 9 (2021) 15284–15294. https://doi.org/10.1039/D1TC03733A.

[284] N.K. Reddy, K.T.R. Reddy, SnS films for photovoltaic applications: Physical

investigations on sprayed SnxSy films, Phys. B Condens. Matter. 368 (2005) 25–31. https://doi.org/10.1016/j.physb.2005.06.032.

[285] M.S. Mahdi, K. Ibrahim, N.M. Ahmed, A. Hmood, S.A. Azzez, Growth and Characterization of Tin Sulphide Nanostructured Thin Film by Chemical Bath Deposition for Near-Infrared Photodetector Application, Solid State Phenom. 290 (2019) 220–224. https://doi.org/10.4028/www.scientific.net/SSP.290.220.

[286] S.K. Shaikh, S.I. Inamdar, V. V. Ganbavle, K.Y. Rajpure, Chemical bath deposited ZnO thin film based UV photoconductive detector, J. Alloys Compd. 664 (2016) 242–249. https://doi.org/10.1016/j.jallcom.2015.12.226.

Annexure -1

Pyrite (FeS_2) nanoparticles by pulsed laser ablation in liquid and its thin films for photodiodes

A.1 Introduction

Pyrite (FeS_2) is one of the earth-abundant and non-toxic semiconductors possessing a promising role in optoelectronic applications. FeS_2 has a narrow band gap (0.95 eV), high light absorption coefficient (~10^5 cm^{-1}), excellent properties in photoelectric conversion and has enormous potential as an efficient photodetector system [1,2]. Pyrite has been identified as a promising material for effectively removing environmental contaminants in the earth's near-surface environment including toxic heavy metals and metalloids, radionuclides and organic pollutants [3]. This is in addition to the benefits mentioned above as semiconductor. This opens our possibility of tuning the material for various applications using its nanostructures and thin films. Pulsed laser ablation in liquid (PLAL), has been adopted for successfully synthesizing pyrite (FeS_2) nanoparticles. In this study, we synthesized FeS_2 nanoparticles in different solvents by laser ablation using Nd:YAG laser output of 532 nm wavelength. Morphology was identified by transmission electron microscopy (TEM) and these nanoparticles have different morphologies in the solvents used in PLAL. For thin film fabrication from nanocolloid, we present a simple and convenient method combining electrophoretic deposition (EPD) and spin-coating. FeS_2 nanoparticles in IPA were deposited on n-type silicon (Si) substrate by EPD followed by spin-coating of FeS_2 (NPs in IPA and DMF) on the surface of these films for surface morphological modification and to enhance thickness of the films. Photodiode configurations of n-Si/p-FeS_2 is achieved using the nanocolloids in IPA and DMF. Annealing of these structures is also done in vacuum at different temperatures. The optical properties of the colloids and films were evaluated using UV-Visible spectroscopy. The surface morphologies were studied using scanning electron microscopy (SEM) and the crystalline structure of the films was characterized by X-ray diffraction (XRD) analyses. We report the photodetection properties of a p-n junction based on these FeS_2 nanoparticles and the results of different studies on light sensing parameters evaluated are also presented.

A.2 Methodology

A.2.1 Synthesis of FeS_2 nanoparticles

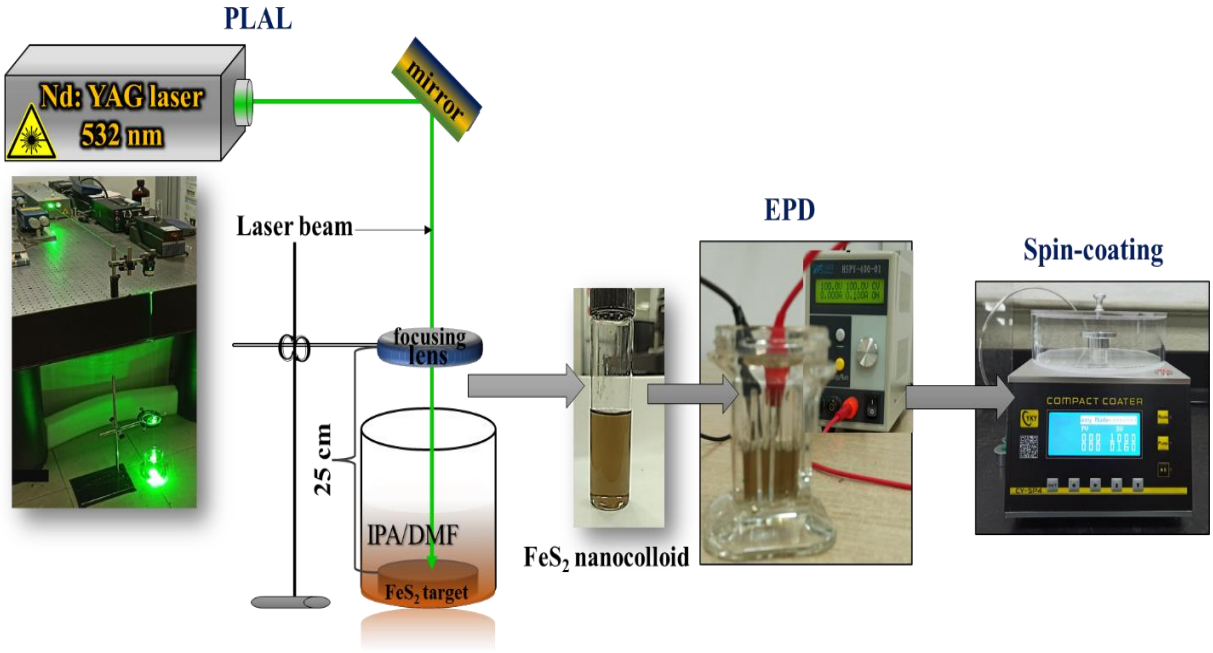


Fig. A.1: Methodology for the synthesis and fabrication of FeS_2 nanoparticles and their thin films.

The schematic representation of the methodology is given in Fig. A.1. Iron sulfide (FeS_2) nanoparticles were synthesized using pulsed laser ablation in liquid (PLAL) process. For laser ablation, the target (99.9% pure, Beijing Goodwill Metals, China) was placed in a 250 mL beaker with 25 mL solvents (isopropyl alcohol (IPA), ethanol, methanol, dimethyl formamide (DMF) and acetone, all from Fermont, 99.9% pure analytical-grade). Each time, the FeS_2 target was polished and washed with the respective solvent used for ablation to get rid of any surface impurities. A second harmonic output of 532 nm wavelength was employed to irradiate the FeS_2 target positioned in the beaker in a vertical configuration of the experiment. For the ablation, a pulsed Nd:YAG laser (Model LQ 629, Solar laser system) with pulse width 10 ns and pulse repetition frequency of 100 Hz was used. 90 mJ/pulse of laser energy were produced using a 100 Hz laser. In each solvent, laser ablation was carried out for 10 minutes with the aid of a focusing lens kept at 25 cm distance from the target. With the use of a lens, the laser fluence was adjusted. Images of the colloids obtained in different solvents are shown below in the inset of Fig. A.2. FeS_2 nanocolloids in IPA and DMF were used for the film-fabrication process and the NPs of FeS_2 in IPA are referred to as FIPA and those in DMF as FDMF.

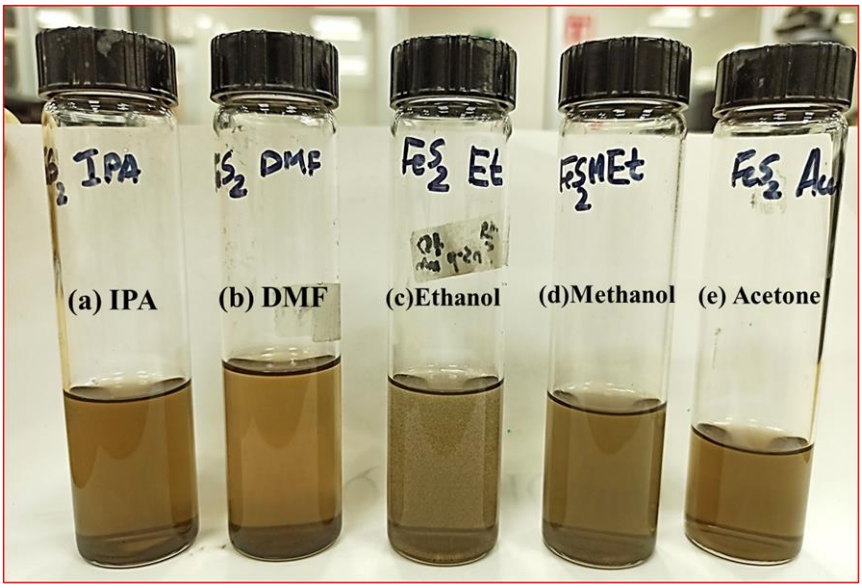


Fig. A.2: Images of the FeS_2 nanocolloids prepared in different solvents.

A.2.2 Electrophoretic deposition of FeS_2 nanoparticles

Using hot probe method [4], the p-type nature of FeS_2 was identified. Based on this a n type Si (n-Si) substrate was chosen to achieve the photodiode structure. Electrophoretic deposition **(**EPD) process was used for thin film fabrication. Due to its ease of use, capability for large-scale deposition, and the fact that its performance depends on the applied parameters, electrophoretic deposition is one of the known synthesis processes that is particularly intriguing. A n-type silicon (Si) substrate was used as the anode and the cathode. With a 4.5 mm gap between them, the electrodes were positioned parallel to one another and immersed in 12.5 mL FeS_2 nanocolloid (FIPA) kept at a constant temperature during EPD. A steady current of 2 mA and a potential difference of 400 V were applied. The deposition was carried out for 1 h. The positive electrode was coated with nanoparticles.

A.2.3 Spin-coating of FeS_2 nanoparticles

Following EPD, FeS_2 nanocolloids in IPA and DMF were individually spin-coated onto the films for seeded growth, improved thickness and to avail use of the morphological characteristics of FeS_2 nanoparticles in both solvents. A spin rate of 400 rpm, an acceleration speed of 20 rpm/s and a 20 s spin time were the conditions used for spin-coating. The films formed by combing EPD and spin-coating were annealed at 250 and 350 ℃ for 30 min in vacuum. The films under as-prepared and annealed conditions are given in Fig. A.3. The FIPA that was electrophoretically deposited and then spin coated with FeS_2 NPs in DMF is indicated on the figure

as "FIPA+DMF A250." As-prepared film is referred to as AP, and annealing temperature is referred to as A250. A photodiode structure of form p-FeS_2/n-Si was fabricated successfully.

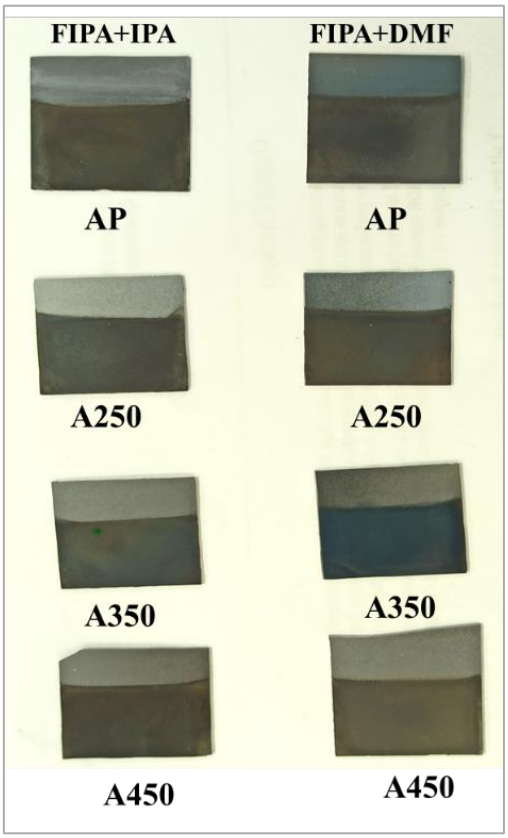


Fig. A.3: As-prepared and annealed films of FeS_2 fabricated by combining EPD and spin-coating.

A.3 Results

A.3.1 TEM and SEM analysis of NPs

The TEM and SEM analyses of the NPs of pyrite in different solvents like IPA, DMF, ethanol, methanol and acetone is provided below. The TEM images, HRTEM, STEM and SAED patterns are also provided. From HRTEM images, the lattice fringes were indexed to that of cubic phase of FeS_2 (ICDD#042-1340) and hexagonal phase of FeS (ICDD#029-0725). From the diffraction spots of the SAED images as well, both these phases were identified. The SEM and TEM images of FIPA is shown in Fig. A.4 (a-f). FIPA (FeS_2 NPs in IPA) showed spherical and long rod like particles in SEM analysis. In the images, the long rod like particles are marked in red oval shapes. The SEM images at a scale of 3 µm, 1 µm and 500 nm are shown below.

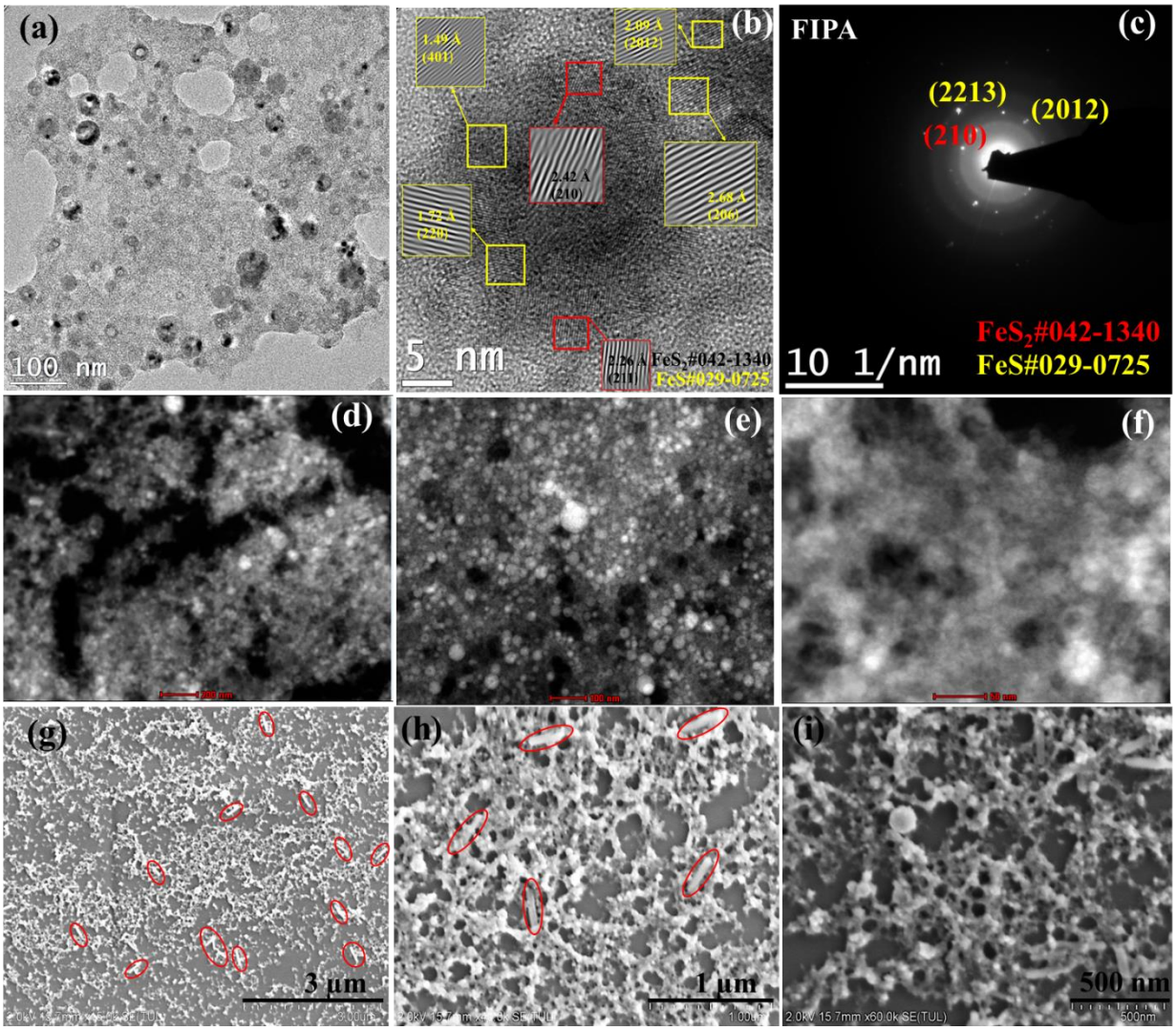


Fig. A.4: (a) TEM (b) HRTEM (c) SAED (d-f) STEM and (g-i) SEM images of FeS_2 NPs in isopropyl alcohol (IPA).

In the case of NPs in DMF also, the SAED patterns showed mixed phases of FeS_2 and FeS. In comparison to IPA, a completely different type of morphology was observed from SEM. Only spherical particles and distributed rice like morphology were seen in DMF. There was no presence of the rod shaped particles at all. The images are shown in Fig. A.5 (a-f).

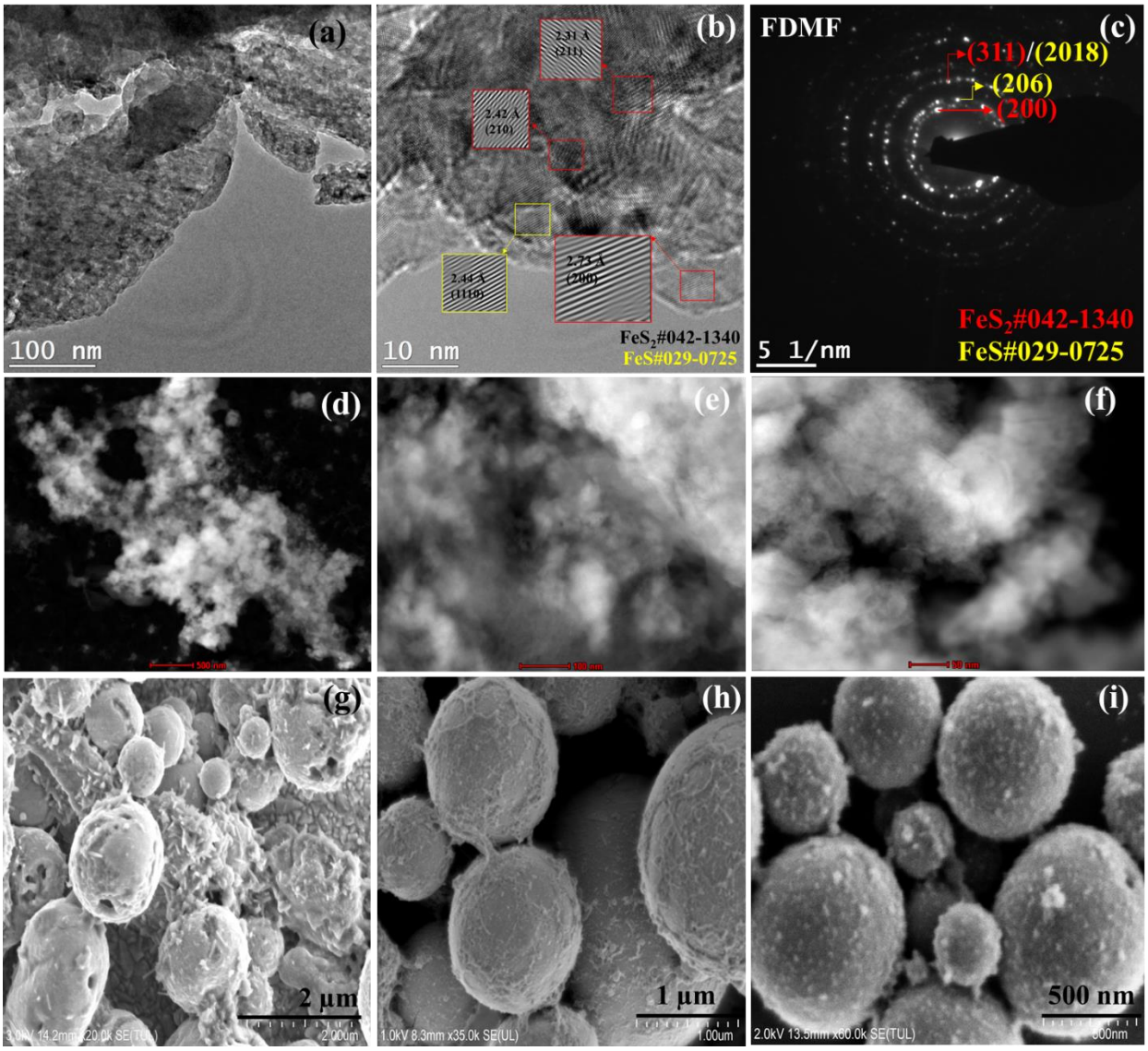


Fig. A.5: (a) TEM (b) HRTEM (c) SAED (d-f) STEM and (g-i) SEM images of FeS_2 NPs in dimethyl formamide (DMF).

For NPs in ethanol, methanol and acetone, spherical interconnected particles were observed. The images are given in Fig. A.6, A.7 and A.8 respectively. In all the cases, the scanning transmission electron micrographs are also included. In the case of STEM images of NPs in DMF, the majority of the analyzed regions are amorphous. This maybe because of the effect of solvent i.e. the higher boiling point of DMF so it takes long time to evaporate which may have led to agglomeration. On the other hand, as alcohol and acetone evaporates much more quickly, the

influence of the solvent was significantly reduced in the case of the samples made in those solvents. As a result, the morphology from STEM images are not discernible for NPs in DMF.

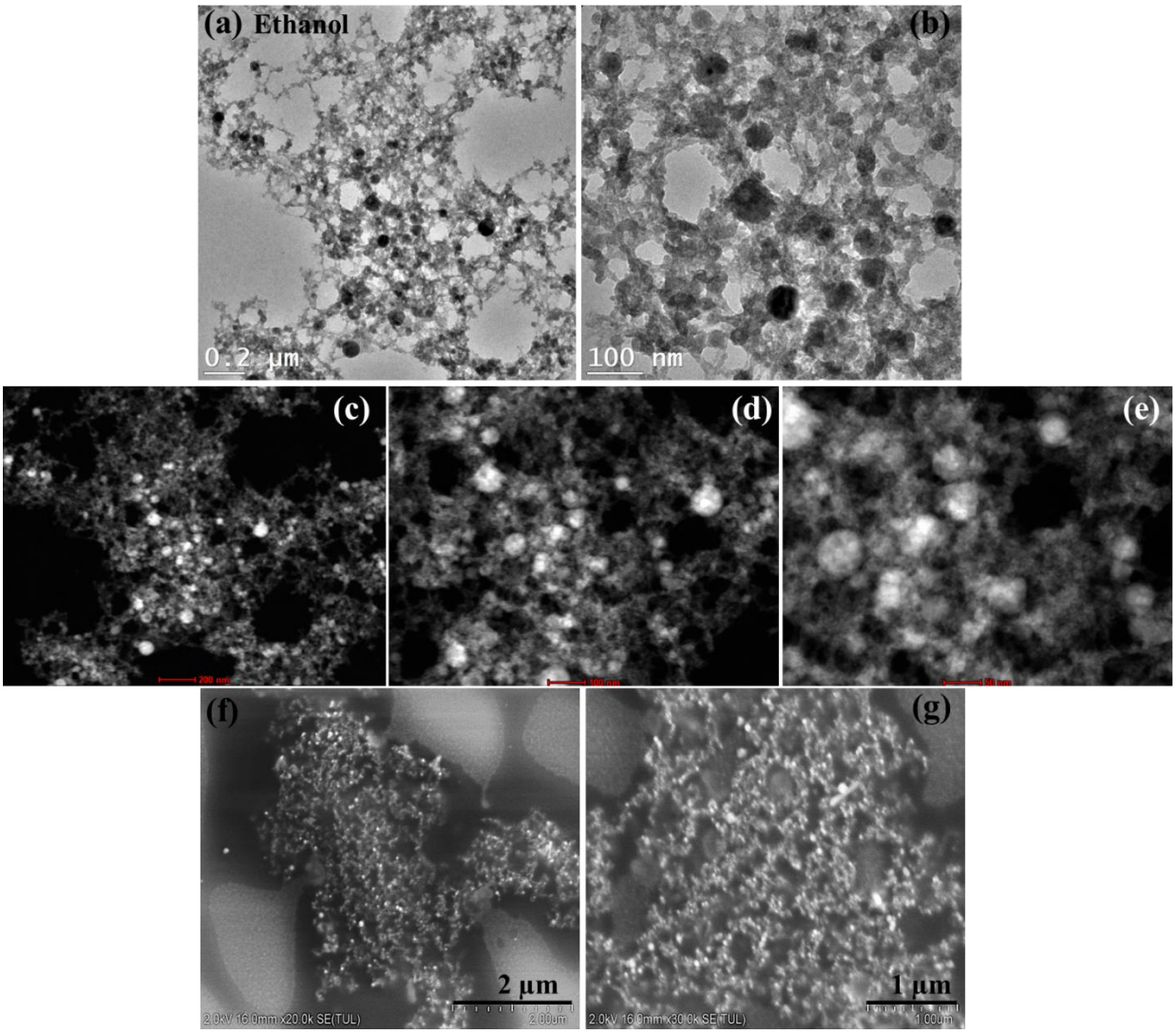


Fig. A.6: (a, b) TEM (c-e) STEM and (f, g) SEM images of FeS_2 NPs in ethanol.

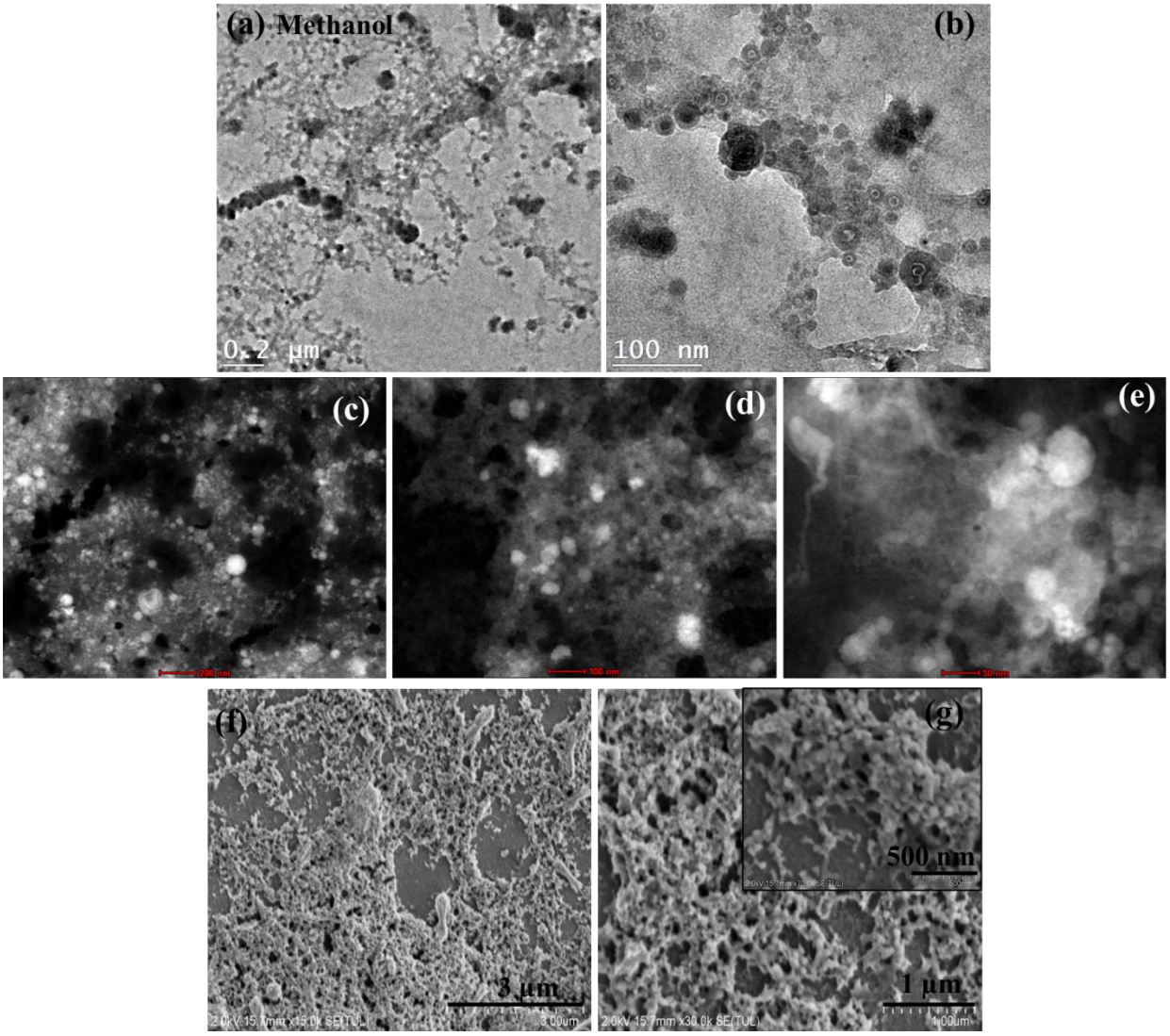


Fig. A.7: (a, b) TEM (c-e) STEM and (f, g) SEM images of FeS_2 NPs in methanol.

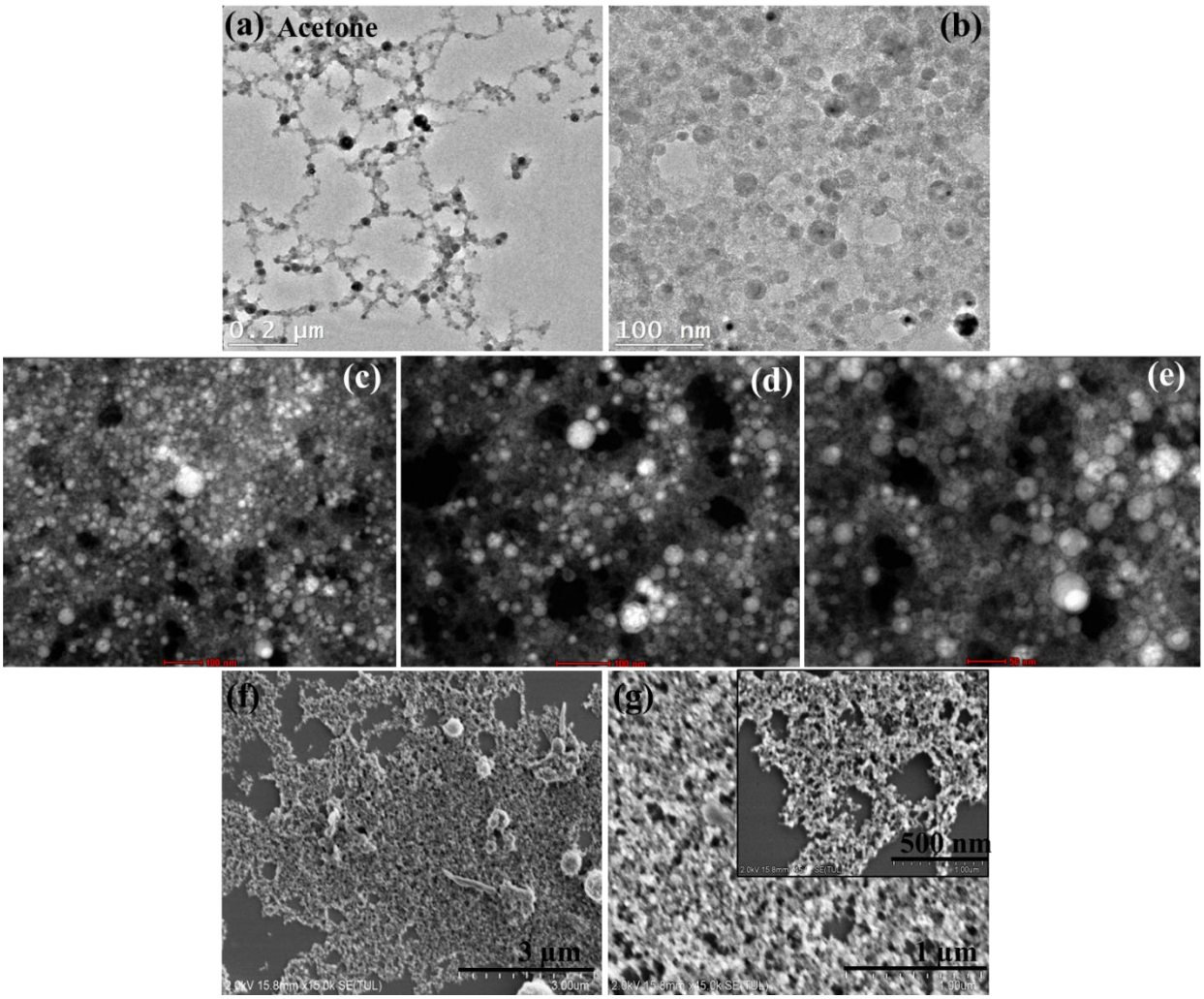


Fig. A.8: (a, b) TEM (c-e) STEM and (f, g) SEM images of FeS_2 NPs in acetone.

A.3.2 X-ray Photoelectron Spectroscopy (XPS) of NPs

By dropcasting the NPs onto FTO substrates and analyzing them using XPS, the elemental composition of the particles in all the solvents was identified. The high-resolution spectra of Fe 2p and S 2p after etching is provided in Fig. A.9. The Fe 2p spectra of pyrite NPs in all the solvents (Fig. A.9 (a-e)) show two major peaks of Fe $2p_{3/2}$ and Fe $2p_{1/2}$ at around 709 and 722 eV respectively which denotes the Fe^{2+} bulk peak [5]. The interval energy of Fe $2p_{3/2}$ and Fe $2p_{1/2}$ was maintained as 13.1 eV. A small peak around 713-714 eV is associated to Fe(II)–S bond of FeS [6]. The S 2p peaks in all the samples were deconvoluted to S $2p_{3/2}$ and S $2p_{1/2}$ whose intensity was maintained at 2:1 with a binding energy difference of 1.18 eV between the peaks (Fig. A.9 (f-j)). The peaks at 161 eV (S $2p_{3/2}$a) and 162 eV (S $2p_{1/2}$a) are the contributions of the S 2p spin orbital of S^{2-} in FeS [7]. The bulk core level of S bound as a disulfide group (S_2^{2-}) in iron pyrite, S $2p_{3/2}$b

and S $2p_{1/2}$b, respectively, was centered around 162 eV and 164 eV. To form S-S dimers, each S atom forms a tetrahedrally coordinated bond with three Fe^{2+} and one other S atom [8–10].

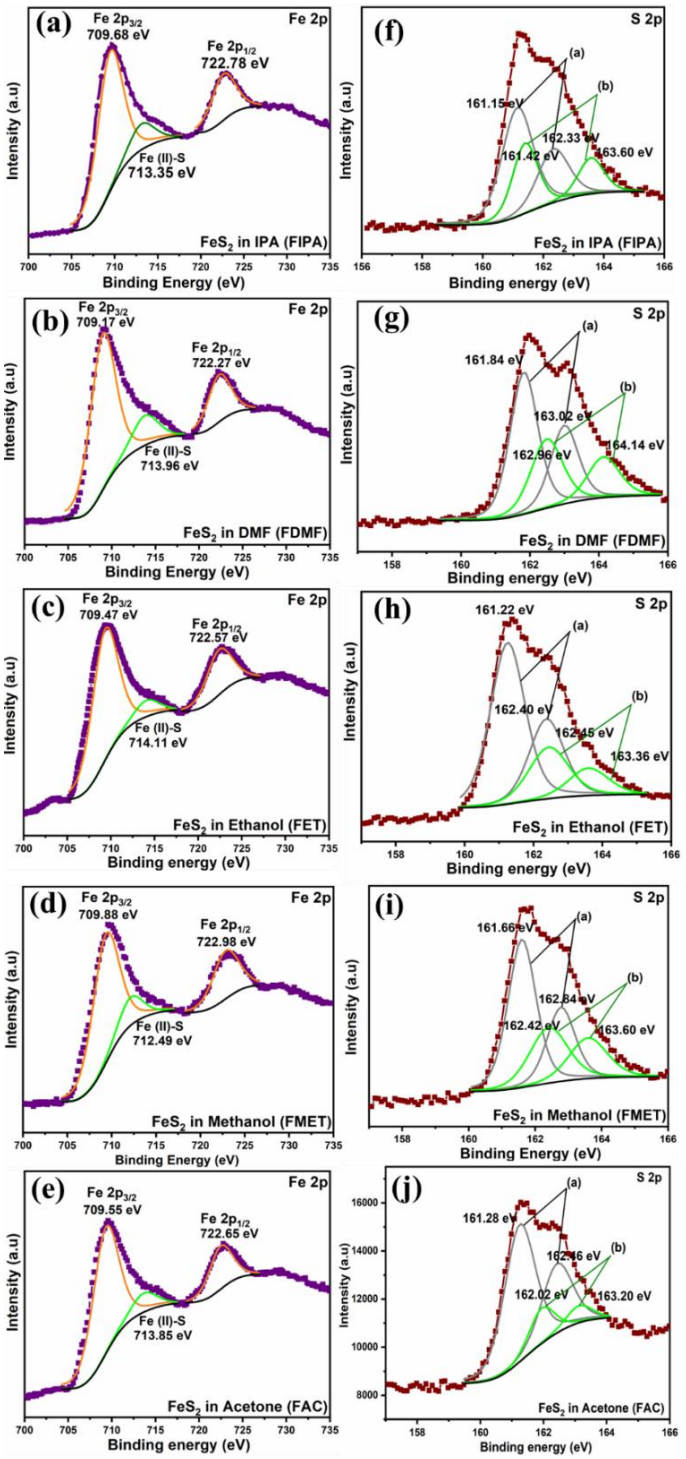


Fig. A.9 High resolution XPS spectra of (a-e) Fe 2p and (f-j) S 2p of the FeS_2 NPs in different solvents.

A.3.3 UV-Vis studies of NPs

Fig. A.10 (a) shows the UV-Vis spectra of the FeS_2 nanoparticles in different solvents. The absorption edges of the NPs were around 400 nm except for NPs in ethanol and acetone. For NPs in ethanol, the colloid was less stable and started precipitating within a few minutes of ablation and during the synthesis of NPs in acetone, the solvent started evaporating faster. This is why the absorption is blue shifted in these cases. During the trial experiments, the nanoparticles in IPA were synthesized with and without the use of a focusing lens. The images of the nanocolloids and its corresponding absorption spectra are given in Fig. A.10 (b). The absorption and concentration of the nanocolloids were lower when laser ablation was done without a lens and therefore the experiments were continued with the use of lens.

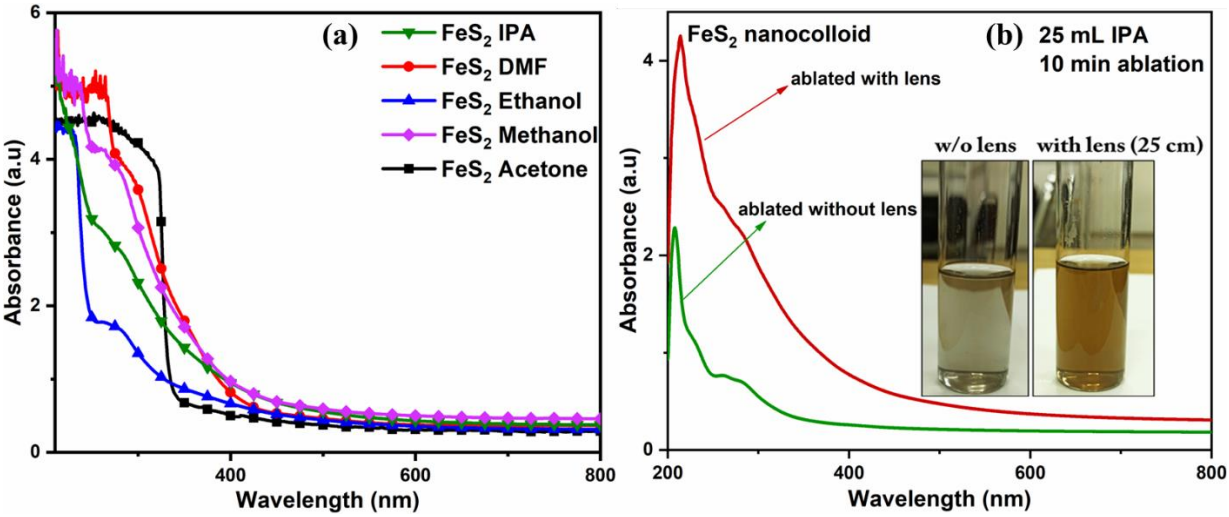


Fig. A.10: The absorption spectra of (a) FeS_2 nanoparticles synthesized by PLAL in different solvents (b) FeS_2 nanoparticles in IPA synthesized with and without the use of focusing lens.

A.3.4 X-ray Diffraction (XRD) of the films

XRD was utilized to characterize the phases of the FeS_2 target that was used for laser ablation as well as the films fabricated on n-Si by EPD and spin-coating. The cubic phase of pyrite (FeS_2) and the hexagonal phase of pyrrhotite (FeS) could be used to index all the diffraction peaks of the target, which is consistent with the value provided in the standard cards, ICDD# 042-1340 and 029-0725 respectively. The refined scale-factors are used to directly determine the phase abundances in the target and were calculated as 84.3 and 14.5 % for pyrite and FeS respectively. In the case of the films as well, we observed that most of the phases identified are those of FeS. Peak of silicon dioxide (SiO_2) is also observed which is from the substrate. The XRD pattern of

the target is given in Fig. A.11 (a) and the films on n-Si are given in Fig. A.11 (b). To confirm whether FeS is formed during laser ablation, the nanocolloids obtained after laser ablation in IPA and DMF (FIPA and FDMF) were dropcasted onto FTO substrates and the XRD was analyzed, as shown in Fig. A.11 (c). FeS_2 and FeS phases were identified in the cases of dropcasted FIPA and FDMF films also. Other peaks observed match those of the FTO substrate that was utilized for dropcasting. It has to be presumed that the conversion of pyrites to FeS happens during the process of laser ablation. The presence of FeS along with FeS_2 was also identified from the results of XPS and the XRD results validate it. A plausible mechanism is suggested for the formation of FeS. First, the FeS_2 target may effectively absorb the laser light upon ablation, reach a high temperature, and split into Fe^{2+} and S_2^{2-} ions. The presence of FeS in the target is also another reason for favoring this phase change. In the meantime, the surrounding solution (IPA or DMF, the solvent used) is rapidly heated and causes the partial reduction of S^{1-} (in S_2^{2-}) to S^{2-}. The ions in the high-temperature bubble might have reacted quickly to form FeS nanoparticles. Zhou et al. explains a similar mechanism while describing the formation of $Cu_{1.4}S$ from Cu $(acac)_2$ by laser ablation in liquid. In that case, the ions S^{2-} formed from the decomposition of organic solvent (DMSO), Cu^{2+} (formed by breaking down of Cu $(acac)_2$ and Cu^{+} (reduction of Cu^{2+} in ethanol) reacted to form $Cu_{1.4}S$ NPs [11].

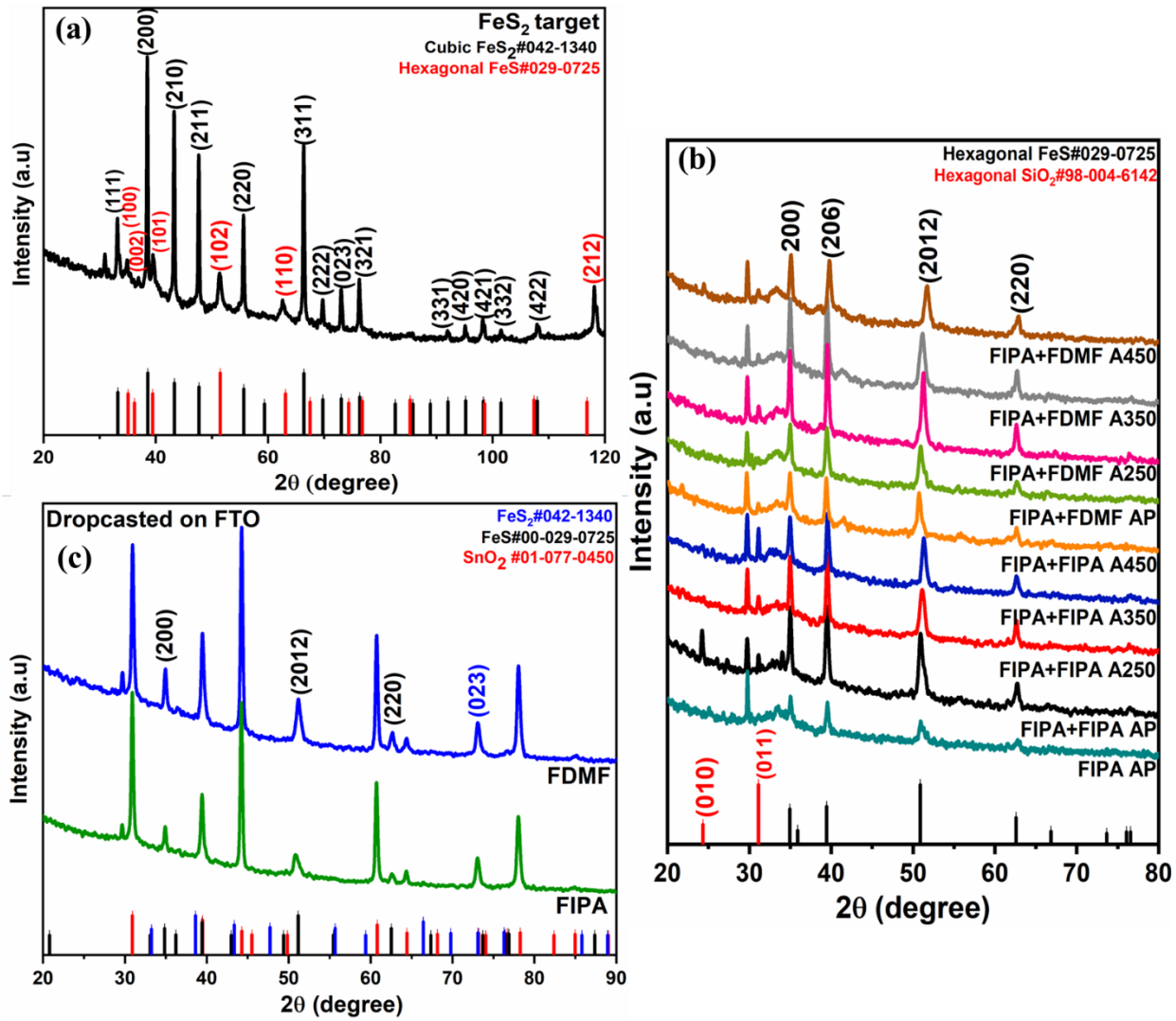


Fig. A.11: XRD patterns of the (a) Pyrite target used for PLAL (b) thin films of FeS_2 fabricated on n-Si by EPD and spin-coating (c) films of FIPA and FDMF dropcasted on FTO substrates.

For obtaining phase pure FeS_2 films, we tried sulfurization method. At different sulfurization temperatures (from 200 to 300 ℃) and amounts of sulfur powder (5 to 20 mg), we optimized the best condition for the formation of pure FeS_2 phase. Using 5 mg sulfur powder at 300 ℃, most of phases were converted to FeS_2. For the experiment, FDMF was dropcasted onto FTO substrates (2.5 × 2 × 0.1 cm) and the film was annealed for 1 hour at 300 ℃ in the sulfur environment. In a semi-cylindrical glass container (12 × 2.5 cm), 5 mg of sulfur powder was added, and samples were maintained on top of the powder. Aluminum foil was used to wrap the sample and glass vessel before they were introduced into the quartz tube furnace (Lindberg/Blue MTM

Mini-Mite Tube Furnace). At a very low-pressure, high-quality nitrogen gas was passed through the tubular furnace. The presence of nitrogen flow prevented the samples from oxidizing or being contaminated during sulfurization. Using the temperature controller programmer of the furnace, the tube furnace was heated to the necessary temperature and maintained there for 1 hour. The heated samples were cooled down to room temperature gradually. Throughout the experiment, the flow of nitrogen gas was kept steady. Upon sulfurization, the color of the films turned grey. Fig. A.12 (a) and (b) show the XRD patterns of the films following sulfurization at various temperatures and sulfur concentrations, respectively.

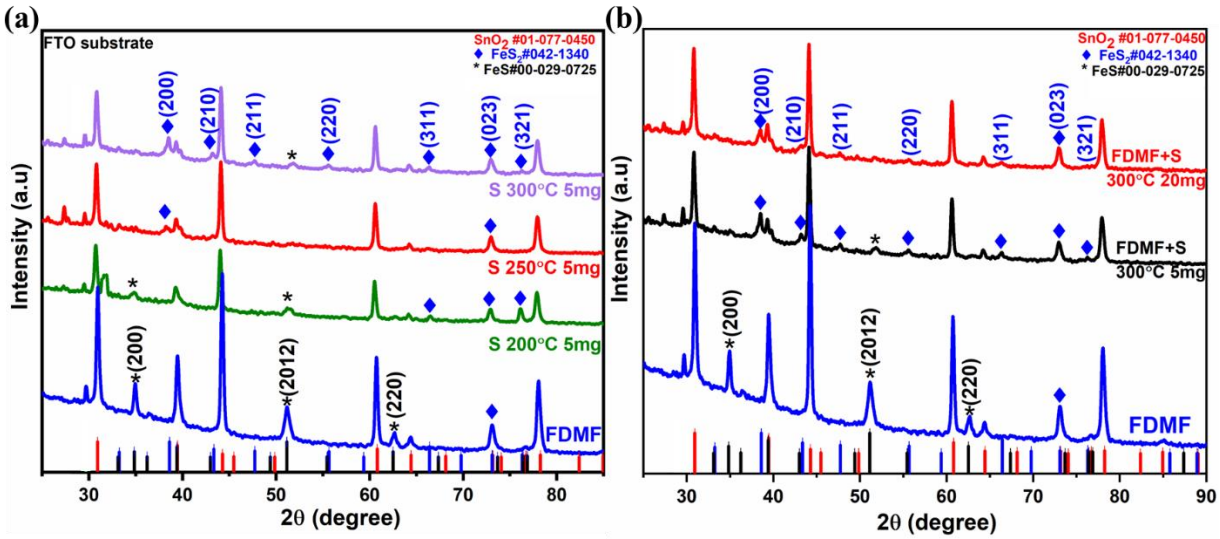


Fig. A.12: XRD of FDMF films on FTO under sulfurization at different (a) annealing temperatures (b) sulfur concentrations.

A.3.5 SEM of FeS_2 films

The surface morphological analysis of the EPD and spin-coated films resulted in same type of morphology which is similar to that of the pyrite NPs in IPA and DMF. Spherical and long rod-shaped particles were evident in FIPA spin-coated films, but only spherical particles with randomly distributed rice-shaped morphology were seen in DMF. Fig. A.13 shows the micrographs of FIPA spin-coated films and Fig. A.14 shows the FDMF-coated samples under as-prepared and annealed conditions.

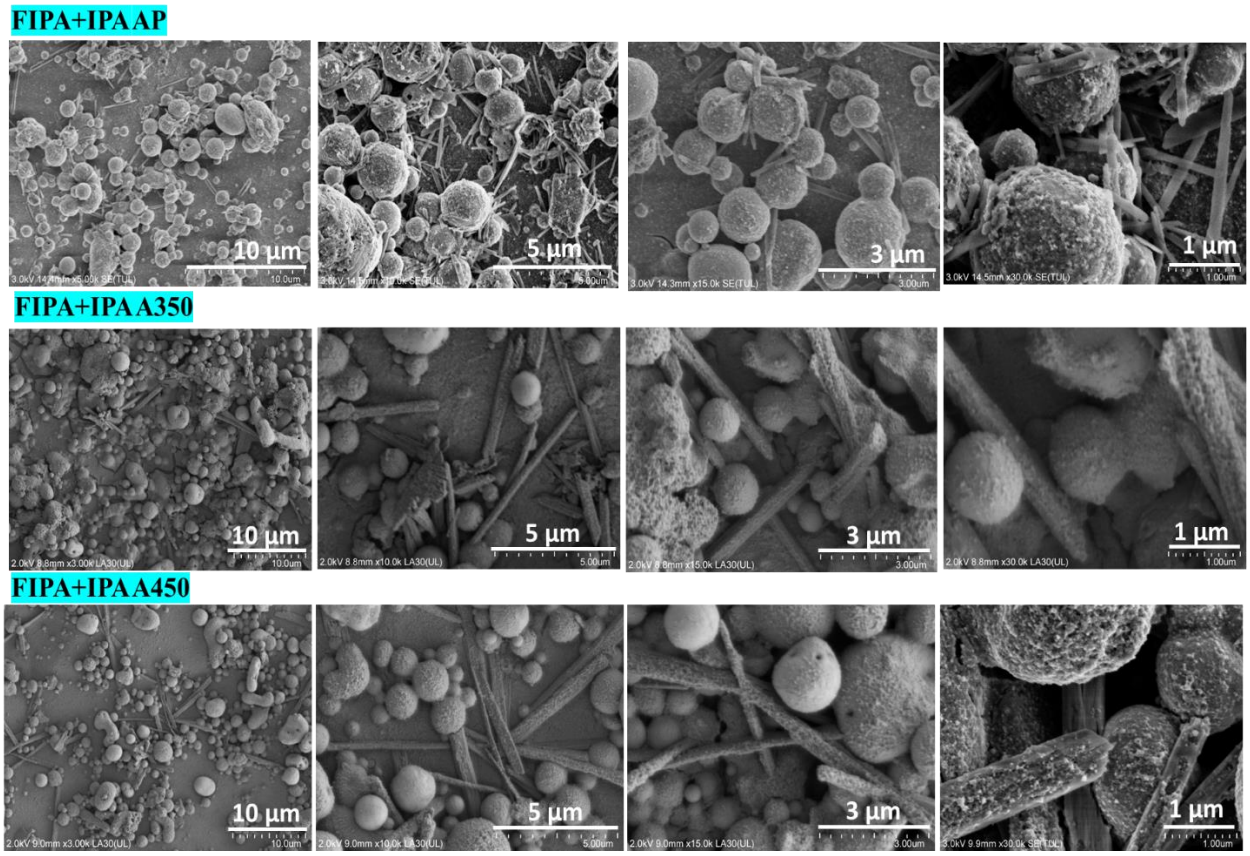


Fig. A.13: SEM images of the as-prepared and annealed thin films fabricated on n-Si by EPD above which FeS_2 NPS in IPA (FIPA) are spin-coated.

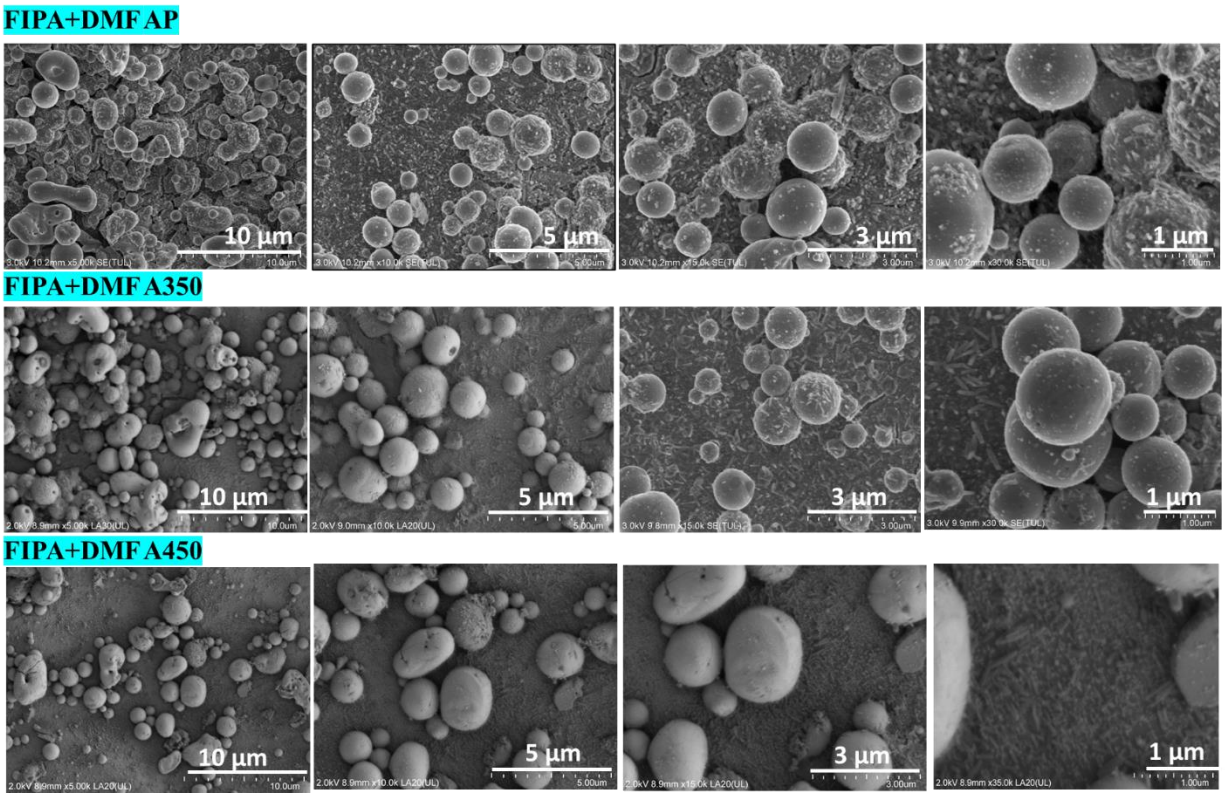


Fig. A.14: SEM images of the as-prepared and annealed thin films fabricated on n-Si by EPD above which FeS_2 NPS in DMF (FDMF) are spin-coated.

A.3.6 Optical Studies of FeS_2 films

As the films were fabricated on n type Si substrate which has a very reflective surface, the percentage reflectance was measured and is given in Fig. A.15.

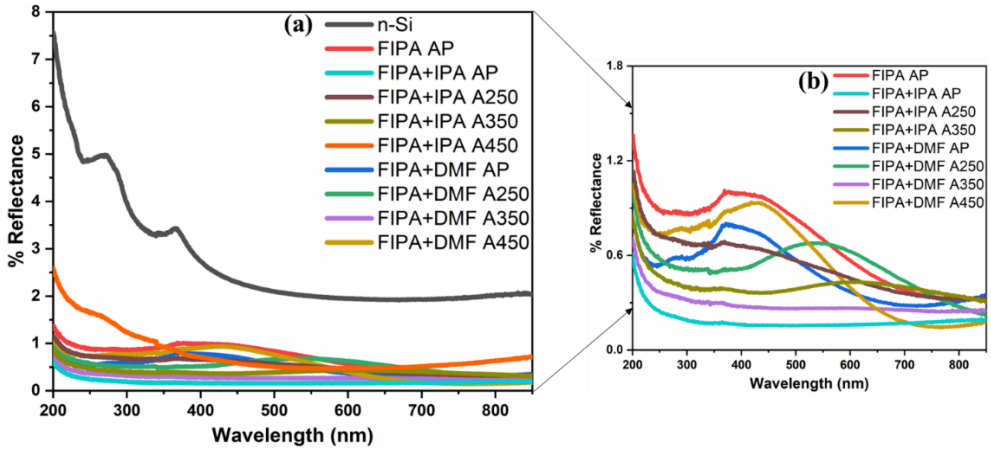


Fig. A.15: (a) % Reflectance of the as-prepared and annealed films (b) zoomed image of the % reflectance of the films.

A.3.7 I-V characteristics and Photoresponse measurements

It is important to note that all of the diodes fabricated exhibit fast photo-response under light, as illustrated in Fig. A.16. Additionally, the exponentially sharp increase in current values with respect to the applied voltage and illumination also suggests that p-FeS_2/n-Si diodes are photoconductive in nature. As there was not much change in the value of current obtained for films annealed at 250 ℃ when compared to the as-prepared films, those samples were not included in further studies.

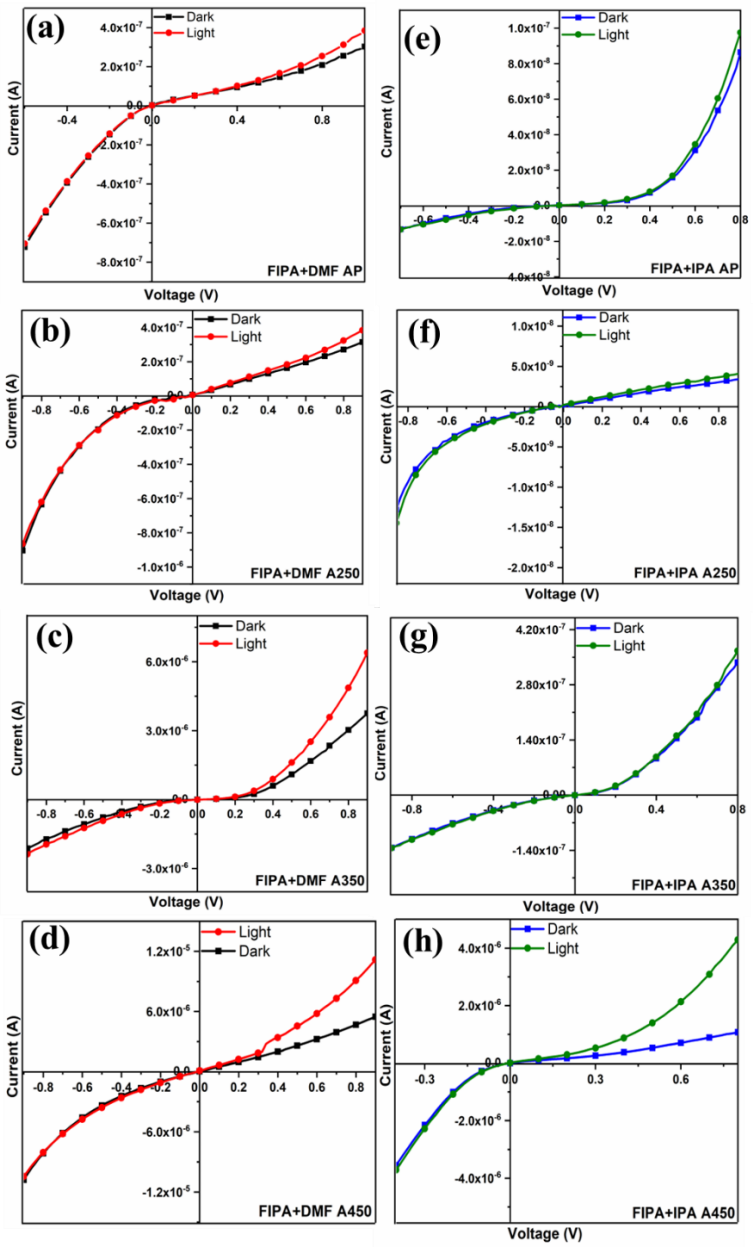


Fig. A.16: I-V characteristics of the p-FeS_2/n-Si photodiode.

Fig. A.17 (a) illustrates the ON/OFF behavior of the p-FeS_2/n-Si diode device using an illumination from tungsten (W) at a bias voltage of 0.5 V. The data were collected for cyclic measurements as well (Fig. A.17 (b)) for 160 s at a 10 s ON/OFF interval. In contrast to the dark condition, under illumination, the diode generates its maximum amount of charge carriers, which increases the photocurrent value. Based on these findings, the fabricated p-FeS_2/n-Si diode has an excellent photosensitive nature and it may well be employed for optoelectronic applications. To achieve high photodetection properties, other alterations and development of this photodiode are also ongoing. The morphological variations between the two sets of spin-coated films are primarily responsible for the variance in photocurrents between them. In the case of FIPA spin-coated films, charge recombination at the grain boundaries because of the spherical and rod-shaped surface may be the cause for comparatively reduced photocurrent. Additionally, it has been noted that the electron mobility of spherical and rice-shaped nanoparticles exhibits comparable values and is greater than that of rod-shaped particles. The combination of rice-like shaped particles with sphere-like particles as in FDMF spin-coated films are intriguing because the rice-shaped NPs probably have a less dense capping layer at the sharp apex, which makes carrier transfer easier [12].

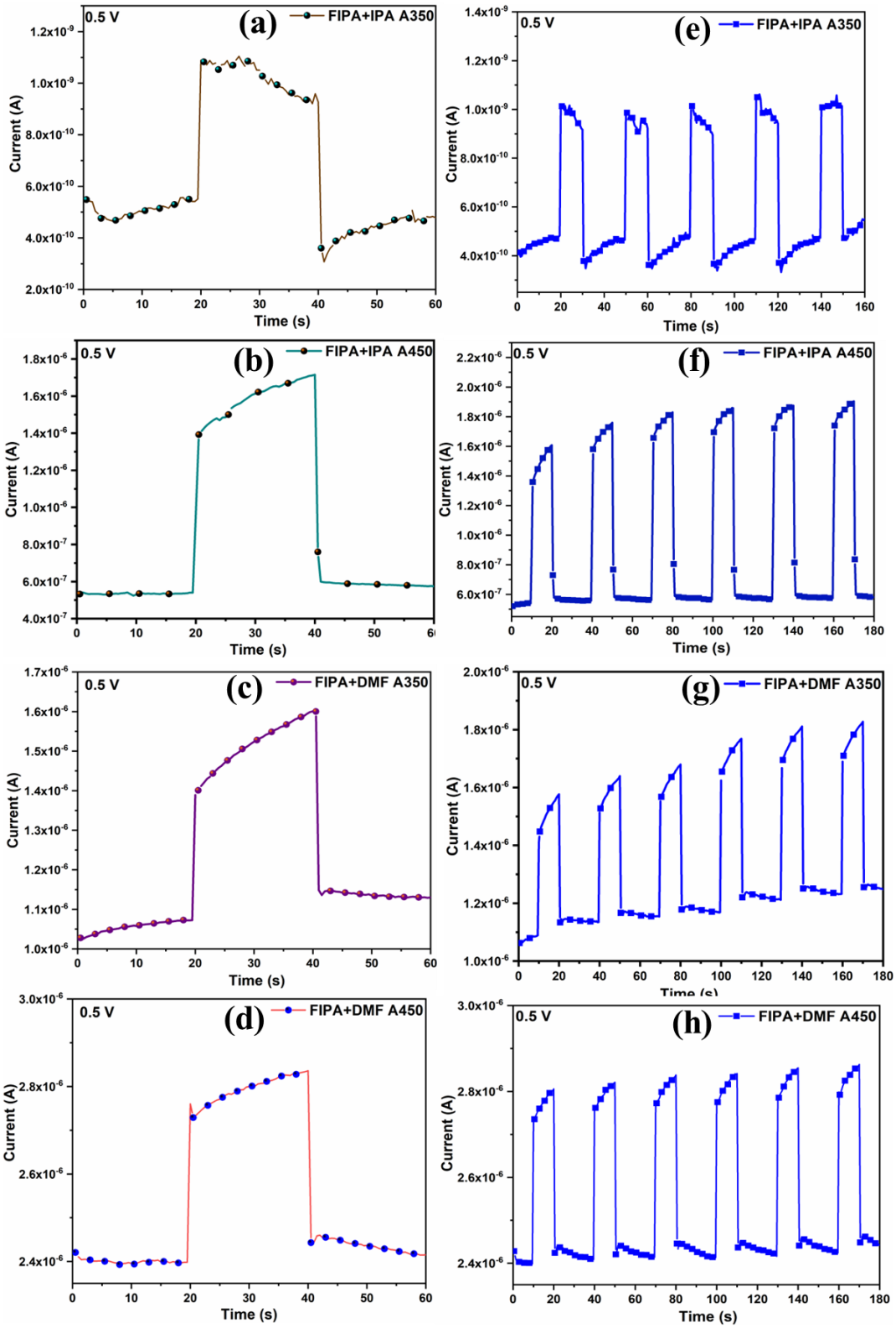


Fig. A.17: Time-dependent photoresponse measurements of p-FeS_2/n-Si photodiode under illumination using tungsten lamp and a bias voltage of 0.5 V.

Due to their benefits of high sensitivity, extremely small size and low power consumption, self-powered photodetectors, which have numerous uses in the military and for civilian reasons, have been increasingly popular in recent years [13]. This greatly interested us in this area and motivated to further look into its possibilities. The fabricated diodes were illuminated using W lamp, different wavelegths of LEDs without applying any voltage and all the diodes showed excellent reponse (Fig. A.18). In the self-powered mode, spikes and overshoots can be seen in the transient photocurrent response of FIPA+IPA A350 film, which are typically interpreted as indicators of surface recombination. Peter et al. has explained this mechanism in semiconductor photoanodes [14]. When the light is turned on, there is an apparent "instantaneous" photocurrent that results from the rapid separation of photogenerated electron hole pairs in the space charge region. The subsequent photocurrent decay is then attributed to the accumulation of photogenerated minority carriers at or near the interface, which results in an escalating flow of electrons (i.e., a negative current) into the surface as a result of recombination and causes the photocurrent to decay. After a while, a steady state is reached where the rate of holes entering the interface is precisely balanced by the rate at which they are being consumed by charge transfer and recombination. As a result, the photocurrent becomes constant and equal to the current flowing across the semiconductor interface. When the light is turned off, the hole flux quickly stops, revealing just the electron flux. As the electron flux decays, any leftover holes are consumed by recombination and charge transfer, causing the current to return to zero with a negative overshoot. This justification suggests that since both the instantaneous negative spike and the reduction in photocurrent up until the point of light switch-off measure the recombination current, they should be of similar magnitude. The steady-state photocurrent (as in other films), in contrast, is the flux of holes that successfully enter the interface without coming into contact with any surface electrons [15].

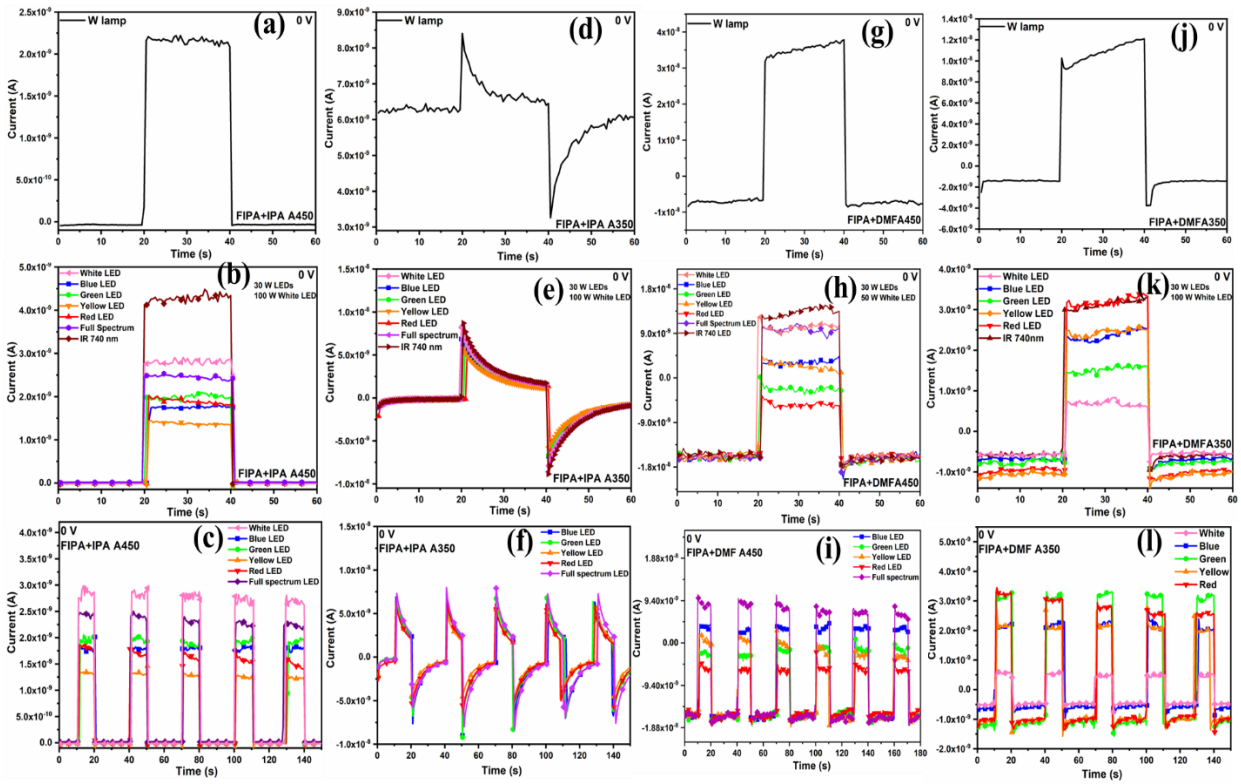


Fig. A.18: Photoresponse measurements of p-FeS_2/n-Si photodiode under illumination using different wavelengths of LEDs under self-powered mode.

The effect of light intensities was also investigated while illuminating using 532 and 785 nm continuous laser source with various light powers ranging from 20 to 100 mW. The power of the source was changed from 20 to 100 mW in all cases for the 785 nm continuous laser, and the applied voltages in each sample are also shown in Fig. A.19 (a). With the exception of FIPA spin-coated film that was annealed at 350 °C, all other samples were illuminated with a 532 nm laser, and the power was adjusted to range from 20 to 50 mW with a 10 mW increment every time. The increament for FIPA+IPA A350 was 20 mW each time. Fig. A.19 (b) shows the graph of the measurement.

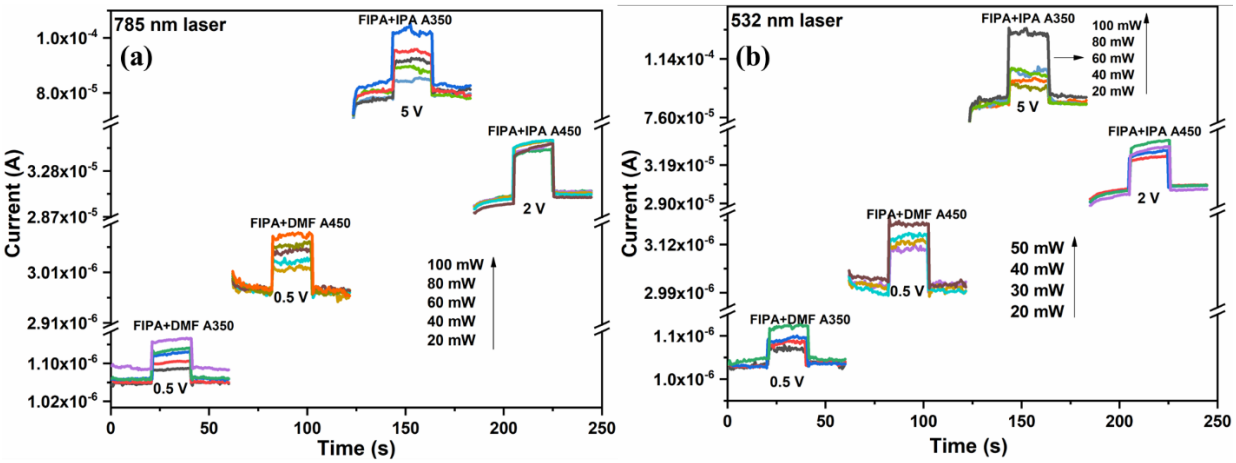


Fig. A.19: Photoresponse curves of p-FeS_2/n-Si photodiode under illumination using continuous lasers of wavelength (a) 785 nm (b) 532 nm.

The evaluation of specific detectivity, D* calculated by illuminating the photodiode using 785 nm laser is given below in Fig. A.20. The values of detectivity were in the order of 10^8 Jones for FIPA spin-coated films and for FDMF coated films, it was in the order of 10^6-10^7 Jones. The results we got are comparable to the reports by Zebarjad et al. on pyrite-based photodetectors. The detectors were developed by electrochemical deposition utilizing chemical precursors, where they stated FeS as the main phase and carried out sulphurization to obtain phase pure FeS_2. A photodetector with detectivity of around 10^8 Jones was reported [16]. Mohsin et al. reported an external magnetic field–assisted laser ablation in liquid technique to prepare FeS_2 nanoparticles [17]. They also reported fabricating FeS_2 NPs/p-Si photodetectors using dipping technique, which demonstrated a detectivity of 10^{11} Jones.

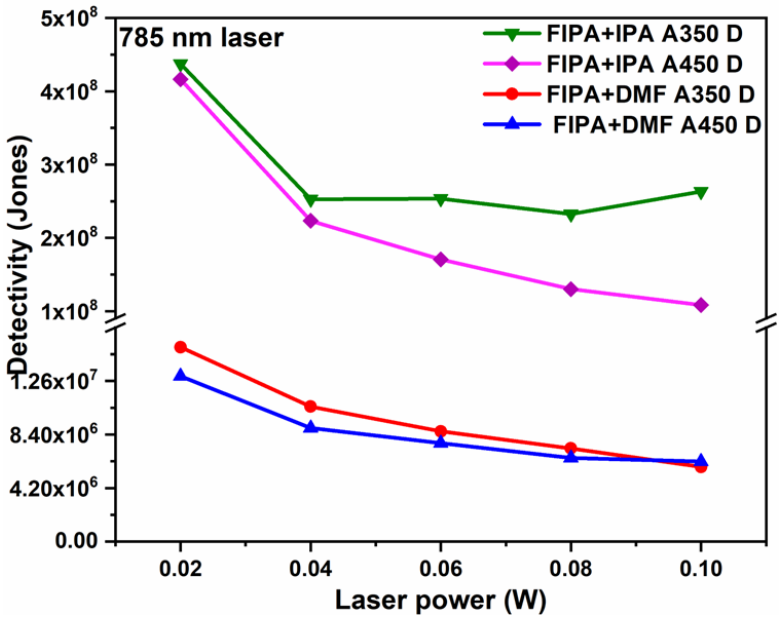


Fig. A.20: Detectivity of p-FeS_2/n-Si photodiode under illumination using continuous laser of wavelength 785 nm.

A.4 Conclusions

- ❖ This is the first report of FeS_2 NPs synthesized using PLAL in different solvents.
- ❖ Synthesis of NPs in different solvents resulted in different morphologies.
- ❖ By a combination of EPD and spin-coating technique, photodiodes were fabricated on n type silicon substrate.
- ❖ Spherical NPs with distributed rice-like morphology in FDMF spin-coated films demonstrated a greater response than spherical and rod-shaped particles in FIPA coated films. The primary causes of this are the carrier mobility and recombination effects in various surface morphologies.
- ❖ The photodiode showed a detectivity of 10^8 Jones.

References

[1] M. Gong, A. Kirkeminde, Y. Xie, R. Lu, J. Liu, J.Z. Wu, S. Ren, Iron Pyrite (FeS2) Broad Spectral and Magnetically Responsive Photodetectors, Adv. Opt. Mater. 1 (2013) 78–83. https://doi.org/10.1002/adom.201200003.

[2] B. Yuan, W. Luan, S.T. Tu, J. Wu, One-step synthesis of pure pyrite FeS2 with different morphologies in water, New J. Chem. 39 (2015) 3571–3577. https://doi.org/10.1039/c4nj02243b.

[3] X. Nie, S. Luo, M. Yang, P. Zeng, Z. Qin, W. Yu, Q. Wan, Facile hydrothermal synthesis of nanocubic pyrite crystals using greigite fe3s4 and thiourea as precursors, Minerals. 9 (2019) 273. https://doi.org/10.3390/min9050273.

[4] G. Golan, A. Axelevitch, B. Gorenstein, V. Manevych, Hot-Probe method for evaluation of impurities concentration in semiconductors, Microelectronics J. 37 (2006) 910–915. https://doi.org/10.1016/j.mejo.2006.01.014.

[5] S. Seefeld, M. Limpinsel, Y. Liu, N. Farhi, A. Weber, Y. Zhang, N. Berry, Y.J. Kwon, C.L. Perkins, J.C. Hemminger, R. Wu, M. Law, Iron pyrite thin films synthesized from an Fe(acac)3 Ink, J. Am. Chem. Soc. 135 (2013) 4412–4424. https://doi.org/10.1021/ja311974n.

[6] Z. Wang, C. Liu, G. Shi, G. Wang, H. Zhang, Q. Zhang, X. Jiang, X. Li, F. Luo, Y. Hu, K. Yi, Preparation and electrochemical properties of electrospun FeS/carbon nanofiber composites, Ionics (Kiel). 26 (2020) 3051–3060. https://doi.org/10.1007/s11581-020-03455-2.

[7] H. Ning, Z. Liu, Y. Xie, H. Huang, CoS2 Coatings for Improving Thermal Stability and Electrochemical Performance of FeS2 Cathodes for Thermal Batteries, J. Electrochem. Soc. 165 (2018) A1725–A1733. https://doi.org/10.1149/2.0321809jes.

[8] T.K. Trinh, N.T.N. Truong, V.T.H. Pham, H. Kim, C. Park, Effect of sulfur annealing on the morphological, structural, optical and electrical properties of iron pyrite thin films formed from FeS2 nano-powder, Korean J. Chem. Eng. 35 (2018) 1525–1531. https://doi.org/10.1007/s11814-018-0060-6.

[9] K. Wang, W. Guo, S. Yan, H. Song, Y. Shi, Hierarchical Co-FeS2/CoS2 heterostructures as a superior bifunctional electrocatalyst, RSC Adv. 8 (2018) 28684–28691. https://doi.org/10.1039/c8ra05237a.

[10] T. Van Nguyen, N.T.N. Truong, P. Ho, T.K. Trinh, J.H. Kim, C. Park, Green and simple preparation of carbon-coated iron pyrite thin films for solar cells application, J. Mater. Sci. Mater. Electron. 30 (2019) 19752–19759. https://doi.org/10.1007/s10854-019-02340-7.

[11] Y. Zhou, H. Liu, J. Yang, J. Mao, C.K. Dong, T. Ling, X.W. Du, Scalable synthesis of cubic Cu1.4S nanoparticles with long-term stability by laser ablation of salt powder, Chem. Commun. 52 (2016) 811–814. https://doi.org/10.1039/c5cc08656f.

[12] X. Zhang, G. Guo, C. Ji, K. Huang, C. Zha, Y. Wang, L. Shen, A. Gupta, N. Bao, Efficient

Thermolysis Route to Monodisperse Cu2ZnSnS4 Nanocrystals with Controlled Shape and Structure, Sci. Rep. 4 (2014) 5086. https://doi.org/10.1038/srep05086.

[13] Z.M. Wei, J.B. Xia, Recent progress in polarization-sensitive photodetectors based on low-dimensional semiconductors, Acta Phys. Sin. 68 (2019) 393–411. https://doi.org/10.7498/aps.68.20191002.

[14] L.M. Peter, A.B. Walker, T. Bein, A.G. Hufnagel, I. Kondofersky, Interpretation of photocurrent transients at semiconductor electrodes: Effects of band-edge unpinning, J. Electroanal. Chem. 872 (2020) 114234. https://doi.org/10.1016/j.jelechem.2020.114234.

[15] H.K. Dunn, J.M. Feckl, A. Müller, D. Fattakhova-Rohlfing, S.G. Morehead, J. Roos, L.M. Peter, C. Scheu, T. Bein, Tin doping speeds up hole transfer during light-driven water oxidation at hematite photoanodes, Phys. Chem. Chem. Phys. 16 (2014) 24610–24620. https://doi.org/10.1039/c4cp03946g.

[16] M. Zebarjad, F. Jamali-Sheini, R. Yousefi, Nanostructured FeS2 films: Influence of effective parameters on electrochemical deposition and characterization of physical properties, Ceram. Int. 47 (2021) 21969–21981. https://doi.org/10.1016/j.ceramint.2021.04.215.

[17] M.H. Mohsin, R.A. Ismail, R.O. Mhadi, Preparation of nanostructured FeS2/Si heterojunction photodetector by laser ablation in water under effect of an external magnetic field, Appl. Phys. A Mater. Sci. Process. 127 (2021) 214. https://doi.org/10.1007/s00339-021-04369-0.

List of Figures

Fig. 1.1: A conceptual illustration of nanomaterials and their uses. *Reproduced with permission from RSC [12].* 16

Fig. 1.2: Different kinds of hybrid nanostructures. *Reproduced with permission from [3].* 17

Fig. 1.3: Statistics information on the number of articles published on hybrid nanomaterials between 2000 and 2022 (September) *(Data Source: SciFinder).* 18

Fig. 1.4: Advantages of LSPC techniques. 24

Fig. 1.5: Fundamental laser ablation in liquid laboratory setup. 25

Fig. 1.6: Sketch of the techniques used so far for the investigation of LAL. *Reproduced with permission from* [48]. 26

Fig. 1.7: Setup for laser melting and fragmentation experiments in liquid. 28

Fig. 1.8: Word cloud illustrating LSPC-NP uses mentioned in the literature. The word size in the figure is proportional to its mentions in the literature. *Reproduced with permission from* [43]... 30

Fig. 1.9: Schematic of the most used techniques for thin film fabrication from nanocolloids. 32

Fig. 1.10: Structure of photoconductive photodetector 33

Fig. 1.11: Structure of photodiode 34

Fig. 2.1: Images of the (a) SnS nanocolloids produced by PLAL using laser of wavelength (i) 532 nm (ii) 1064 nm; (b) as well as their thin films fabricated by spin coating (I, II) SnS as-prepared (AP), (III, IV) annealed at 350 ℃, (V, VI) annealed at 450 ℃ (© from Elsevier 2022)……45

Fig. 2.2: (a, b) TEM, (c) HRTEM and (d) SAED patterns of SnS NPs produced with a laser output of 1064 nm wavelength in isopropyl alcohol (© from Elsevier 2022). 48

Fig. 2.3: (a, b) TEM, (c) HRTEM and (d) SAED patterns of SnS NPs produced with a laser output of 532 nm wavelength in isopropyl alcohol (© from Elsevier 2022). 49

Fig. 2.4: Scanning electron micrographs of SnS colloid on ITO prepared using (a, b) 532 nm (c, d) 1064 nm colloid (© from Elsevier 2022). 50

Fig. 2.5: Scanning electron micrographs of SnS films (a, d) as-prepared (b, e) annealed at 350 ℃ (c, f) annealed at 450 ℃ (inset: 1 μm scale images of the films) (© from Elsevier 2022). 51

Fig. 2.6: Cross-sectional SEM images of S1064 and S532 films on glass substrate for thickness measurements. 51

Fig. 2.7: A comparison of the GIXRD patterns of the SnS films annealed at 350 and 450 °C (© from Elsevier 2022). 53

Fig. 2.8: (a) Absorption spectra of SnS NPs in IPA obtained by 5 min ablation using laser of wavelength 532 nm (S532) and 1064 nm (S1064) (© from Elsevier 2022) (b) Photos of the SnS nanocolloids prepared by PLAL using 532 and 1064 nm wavelength laser for different ablation

times (c, d) Comparison of absorption spectra of SnS NPs in IPA obtained by laser ablation at different ablation times using 532 and 1064 nm wavelength. 54

Fig. 2.9: (a) Absorption of SnS films under various conditions (as-prepared and annealed at 350/450 ℃) (© from Elsevier 2022) (b) % Transmittance and % Reflectance of SnS thin films, (c) Bandgap calculations using Tauc plot. 56

Fig. 2.10: XPS survey scan spectra of SnS films annealed at various conditions with Sn, S, O, and C line marked (a) before etching (b) after etching (© from Elsevier 2022). 58

Fig. 2.11: High resolution XPS images of (a, b, e, f) Sn 3d, (c, d, g, h) S 2p of SnS nanocolloids (S532 and S1064) deposited on titanium (Ti) substrate (before and after etching) (© from Elsevier 2022). 59

Fig. 2.12: High resolution XPS images of SnS films annealed at various conditions (a, c, e, g) Sn 3d, (b, d, f, h) S 2p s (after etching) (© from Elsevier 2022). 59

Fig. 2.13: High resolution XPS images of SnS films annealed under various conditions (a, c, e, g) Sn 3d, and (b, d, f, h) S 2p (before etching). 60

Fig. 2.14: (a) I-V graphs for SnS films measured from −5 to +5 V in the dark and under light (© from Elsevier 2022). 61

Fig. 2.15: Measurements of the photoresponse of the SnS films (S1064 A450, S1064 A350, and S532 A450) illuminated with (a-c) LEDs of wavelengths 465, 520, 590 and 620 nm at a bias voltage of 5 V, (d-f) tungsten lamp at a bias voltage of 0.5, 1, and 5 V (© from Elsevier 2022). 62

Fig. 2.16: Photoresponse of (a, b) S532 annealed at 450℃ (c, d) S1064 sample annealed at 350℃ and (e, f) S1064 annealed at 450℃ to varying powers of 532 nm (4-24 mW) and 785 nm (10-60 mW) continuous laser, (g, h) cyclic photoresponse of SnS films for 10 mW and 60 mW continuous lasers operating at 532 nm and 785 nm, respectively, at an applied voltage of 5 V (© from Elsevier 2022). 64

Fig. 2.17: Photocurrent of the samples in response to (A) 405, (B) 840 and (C) 980 nm diode lasers with an applied voltage of 5 V (© from Elsevier 2022). 66

Fig. 2.18: Sensitivity, responsivity and detectivity plotted against laser power density for the films determined using the continuous lasers of wavelength (a, b) 532 nm and (c, d) 785 nm (© from Elsevier 2022). 67

Fig. 3.1: Images of (a) different amounts of SnS powder dispersed in IPA (b) laser irradiated nanocolloids (c) Absorption spectra of the nanocolloids in image (b) (d) Absorption spectra of 100 mg SnS dispersed nanocolloids at different irradiation time……74

Fig. 3.2: Absorption spectra of (a) monocrystalline Si colloids (b) polycrystalline Si colloids obtained for different ablation times (Inset : Images of nanocolloids after ablation). 75

Fig. 3.3: Images of the SnS and SnS-Si films (AP refers to the as-prepared films and A450 refers to the films annealed at 450 ℃). 76

Fig. 3.4: Depiction of SnS and Si nanocolloid synthesis and device fabrication using these nanocolloids. 76

Fig. 3.5: (a, b) TEM images (c) size distribution chart and (d) HRTEM image of SnS NPs after laser irradiation. 77

Fig. 3.6: TEM and HRTEM images of (a, b, c) monocrystalline Si NPs (d, e, f) polycrystalline Si NPs. 78

Fig. 3.7: STEM images, EDX quantification and average size distribution of monocrystalline Si. 80

Fig. 3.8: STEM images, EDX quantification and average size distribution of polycrystalline Si. 80

Fig. 3.9: (a-c) TEM and (d) HRTEM images of hybrid SnS NPs and monocrystalline Si NPs... 81

Fig. 3.10: XRD patterns of SnS and SnS-Si films at as-prepared and annealed condition. 82

Fig. 3.11: XRD of SnS films synthesized using nanocolloids from a low energy laser output and spin-coated afterwards. 83

Fig. 3.12: Absorbance of (a) SnS NPs in the nanocolloid (Inset: Absorbance of Si NPs) (b) SnS and SnS:Si hybrid films, (c) Bandgap calculation of the films by Tauc plot (d) % Transmittance and reflectance of the films. 85

Fig. 3.13: Raman spectrum of (a) Si targets (Inset: Zoomed image of the Raman spectra of Si targets) (b) SnS and SnS:Si films annealed at 450 ℃. 87

Fig. 3.14 SEM images of SnS powder (a, b) before laser irradiation (c, d) after laser irradiation. 88

Fig. 3.15 SEM images of moncrystalline Si NPs deposited on (a, b) ITO and (c) Ti substrates; and SEM images of polycrystalline Si NPs on (d, e) ITO and (f) Ti substrate. 89

Fig. 3.16: SEM images of as-prepared and annealed (a, b, c) SnS (d, e, f) SnS:m-Si (g, h, i) SnS:p-Si films. 90

Fig. 3.17: Cross-section SEM for thickness measurements of (a, b) SnS (c, d) SnS:m-Si (e, f) SnS:p-Si films. 91

Fig. 3.18: (a-f) XPS survey scan spectra of the as-prepared and annealed SnS and SnS-Si films. 92

Fig. 3.19: High resolution XPS spectra of (a, b, c) Sn 3d, (d, e, f) S 2p and (g, h) Si 2p of SnS and SnS-Si as-prepared films. 94

Fig. 3.20: High resolution XPS spectra of (a, b, c) Sn 3d, (d, e, f) S 2p and (g, h) Si 2p of SnS and SnS-Si annealed films. 95

Fig. 3.21: I-V plot of (a) SnS and SnS:Si hybrid annealed films (b) SnS:p-Si annealed film..... 96

Fig. 3.22: Photoresponse behavior of the annealed (a) SnS (b) SnS:m-Si (c) SnS:p-Si films to illumination using W lamp and different wavelength of LEDs. 97

Fig. 3.23: Photoresponse of the annealed SnS and SnS:Si hybrid films to (a, c) varying powers of 532 nm and 785 nm (10-60 mW) continuous laser (b, d) 532 nm and 785 nm continuous laser operated at 60 mW and 50 mW respectively at an applied voltage of 5 V..... 99

Fig. 3.24: Plot of sensitivity and responsivity vs laser power density for the films estimated using (a, b) 532 nm and (c, d) 785 nm continuous laser..... 100

Fig. 3.25: Plot of detectivity vs laser power density for the films estimated using (a) 785 nm and (b) 532 nm continuous laser..... 101

Fig. 3.26: Photoresponse of the annealed SnS and SnS:Si hybrid films to laser diodes of wavelength (a) 840 nm (f) 980 nm and (c) 1064 nm at an applied voltage of 5 V..... 103

Fig. 3.27: (a, b) Absorbance plot of SnS:m-Si films at different annealing and RTP conditions; Absorption, % Transmittance and % Reflectance of (c, d) SnS:m-Si and (e, f) SnS:p-Si films. 104

Fig. 3.28: Dye decay absorption studies of the as-prepared SnS and SnS:Si hybrid films (two cycles). 106

Fig. 3.29: Dye decay absorption studies of the annealed SnS and SnS:Si hybrid films (two cycles). 106

Fig. 3.30: Photocatalytic results of SnS and SnS:Si hybrid films (as-prepared and annealed). . 107

Fig. 3.31: (a) Schematic representation of the mechanism of photocatalysis (b) Dye decay vs time plot for cyclic photocatalysis of SnS and SnS:Si hybrid films. 109

Fig. 3.32: SEM images of the as-prepared SnS and SnS:Si hybrid films before and after catalysis. 110

Fig. 3.33: SEM images of the annealed SnS and SnS:Si hybrid films before and after catalysis. 111

Fig. 4.1: (a) Nanocolloids of graphene synthesized by laser irradiating graphene powder at different ablation times. Absorbance plot of graphene nanocolloids in (b) IPA and (c) DMF…...116

Fig. 4.2: Different experimental paths for the synthesis of SnS:graphene hybrid films..... 117

Fig. 4.3: (a) Absorption of the SnS nanocolloids before and after laser irradiation in liquid; and graphene incorporated SnS nanocolloid (b) UV-Vis spectra of the as-prepared and annealed SnS and GPS films (c) Tauc graph for calculating the bandgap in SnS and GPS films (d) %Transmittance and %Reflectance of the films (© from Elsevier 2022). 119

Fig. 4.4: TEM, particle size distribution and high resolution-TEM (a-c) SnS NPs (Set I and III) (d-f) TEM and HRTEM images of Graphene (Set III), (g-i) TEM images of the hybrid nanocolloid of SnS-graphene recorded for various magnifications (Set III) (© from Elsevier 2022). 121

Fig. 4.5: TEM and HRTEM images of (a-c) graphene after irradiation (Set I and II) (d-f) Graphene:SnS NPs i.e.; nanoparticles synthesized by SnS powder in graphene colloid (25 minutes) and irradiating afterwards (Set II). 122

Fig. 4.6: SEM images of (a, b) Graphene (c) SnS powder prior to laser irradiation (d) SnS powder after laser irradiation (A voltage of 2 kV and a current of 10 µA were used to capture the images) (© from Elsevier 2022). 123

Fig. 4.7: SEM images of Graphene (a) before irradiation (b) after 25 min irradiation (G25); (c) SnS powder dispersed in graphene colloid (G25) prior to laser irradiation (d) laser irradiated colloid of SnS dispersed in G25..... 124

Fig. 4.8: SEM micrographs of (a, d) as-prepared (b, e) annealed at 350 ℃ (c, f) annealed at 450 ℃ films of GPS and SnS (© from Elsevier 2022). 125

Fig. 4.9: Cross-sectional SEM images of (a) SnS (b) GPS films (© from Elsevier 2022). 126

Fig. 4.10: SEM of SnS and graphene:SnS films fabricated by Set I and II experimental routes. 127

Fig. 4.11: XRD of (a) Graphene powder (b) SnS and GPS films at various annealing conditions. 128

Fig. 4.12: Raman spectrum of GPS and SnS films (© from Elsevier 2022). 129

Fig. 4.13: XPS survey spectra of SnS and GPS films..... 130

Fig. 4.14: (a) XPS survey spectra of graphene (b) High resolution C 1s spectra of graphene. .. 131

Fig. 4.15: High resolution XPS spectra of (a, d, g) Sn 3d, (b, e, h) S 2p and (c, f, i) C 1s of GPS films at different conditions (© from Elsevier 2022). 132

Fig. 4.16: XPS mapping of SnS and GPS films (a, c) as-prepared (b, d) annealed at 450 ℃ (© from Elsevier 2022). 133

Fig. 4.17: I-V plot of (a) SnS and SnS:graphene hybrids prepared by Set I and II routes (b) annealed films of GPS (The axis in red (left y-axis) represents the current values for GPS films) and SnS (The axis in blue (right y-axis) represents those for SnS films) (© from Elsevier 2022). 134

Fig. 4.18: Photoresponse behavior of the films under illumination using (a) W lamp (b-e) different wavelength of LEDs (© from Elsevier 2022). 136

Fig. 4.19: Photoresponse behavior of SnS and GPS films to illumination using continuous-wave laser of wavelengths (a) 532 (b) 785 nm at different laser powers (c, d) Cyclic photoresponse behavior at constant laser powers (© from Elsevier 2022). 137

Fig. 4.20: (a) Photoresponse behavior of GPS and SnS films to illumination using laser diodes of wavelength 840 and 980 nm (b) Energy band alignment and charge carrier transport mechanism in SnS:graphene films (© from Elsevier 2022). 139

Fig. 4.21: I_{light} vs wavelength plot of GPS and SnS films annealed at 350 and 450 ℃ (© from Elsevier 2022). 140

Fig. 4.22: Sensitivity(S) (represented using ★), responsivity(R) (represented using ●) and detectivity plots for annealed GPS and SnS films calculated from photoresponse curves obtained from illumination using (a, c) 785 nm and (b, d) 532 nm laser source..... 142

Fig. 5.1: Schematic representation of the (a) experimental methodology for the synthesis of SnS, Ag, Au and Ag:Au nanocolloids and (b) film fabrication from these nanocolloids using ultrasonic spray deposition technique……...148

Fig. 5.2: Hybrid films of (a) SnS (532 and 1064 nm) with metallic/bimetallic NPs synthesized using nanocolloids from high energy laser (b) SnS:Ag fabricated in glass substrates placed at different substrate temperatures (c) SnS (under as prepared and annealed condition) with metallic/bimetallic NPs synthesized using nanocolloids from low energy laser. 149

Fig. 5.3: (a, d) TEM images (b, e) STEM images and (c, f) HRTEM images of S532 and S1064 NPs. 150

Fig. 5.4: (a, d, g) TEM images (b, e, h) STEM images and (c, f, i) average size distribution chart of Ag, Au and Ag:Au NPs. 151

Fig. 5.5: (a, e, i) TEM images (b, f, j) STEM images (c, g, k) HRTEM images and (d, h, l) EDX of S532 NPs with Ag, Au and Ag:Au NPs. 152

Fig. 5.6: (a, e, i) TEM images (b, f, j) STEM images (c, g, k) HRTEM images and (d, h, l) EDX of S1064 NPs with Ag, Au and Ag:Au NPs. 153

Fig. 5.7: The absorption plots of (a) Ag, (b) Au and (c) Ag:Au NPs in IPA for different ablation times varying from 30 s to 20 min. 154

Fig. 5.8: Absorption spectra of (a, c) monometallic and bimetallic NPs (b, d) Hybrid colloid of SnS: Ag, Au and Ag:Au NPs synthesized using high energy and low energy lasers. 155

Fig. 5.9: (a, b) Absorption spectra (c, d) Tauc plot (e, f) % Transmittance and (g, h) % Reflectance of S532 and S1064 as-prepared and annealed hybrid films. 157

Fig. 5.10: (a) Absorption spectra of SnS hybrid films prepared using colloids from low energy laser and their (b) % Transmittance and % Reflectance (c, d) Absorption spectra, % Transmittance and % Reflectance of the SnS:Ag hybrid films annealed at different temperatures. 158

Fig. 5.11: XRD patterns of the SnS:Ag hybrid films annealed at 350, 375 and 400 ℃ for 1 h. 159

Fig. 5.12: SEM images of S532 hybrid films with Ag, Au and Ag:Au annealed at 400 ℃..... 160

Fig. 5.13: SEM images of S1064 hybrid films with Ag, Au and Ag:Au annealed at 400 ℃..... 161

Fig. 5.14 : XPS spectra of (a-c) Sn 3d (d-f) S 2p (g, h) Ag 3d and (i, j) Au 4f in the hybrid SnS films (before etching)..... 162

Fig. 5.15: XPS spectra of (a-c) Sn 3d (d-f) S 2p (g, h) Ag 3d and (i, j) Au 4f in the hybrid SnS films (after etching)..... 163

Fig. 5.16: I-V plots of (a) S532 hybrid films (b) S1064 hybrid films under dark and under illumination using W lamp..... 164

Fig. 5.17: Cyclic photoresponse of the SnS:Ag hybrid films annealed at different temperatures. 165

Fig. 5.18: Photoresponse measurement of S532:metallic/bimetallic hybrid films to W lamp at increasing applied voltages. 166

Fig. 5.19: Photoresponse measurement of S1064:metallic/bimetallic hybrid films to W lamp at increasing applied voltages. 166

Fig. 5.20: Photoresponse measurements of different SnS hybrid films (S1064 and S532 with Ag, Au and Ag:Au) illuminated using UV, Blue, Green and Yellow LEDs of wavelengths 395, 465, 520 and 590 nm respectively. 168

Fig. 5.21: Photoresponse behavior of S532 and S1064 hybrid films to illumination using continuous-wave laser of wavelengths (a, b) 532 (c, d) 785 nm at different laser powers..... 169

Fig. 5.22: (a, b) Photoresponse behavior of S532 and S1064 films to illumination using laser diodes of wavelengths 405, 840 and 980 nm. 170

Fig. 5.23: Sensitivity (S) calculated from photoresponse curves obtained from illumination using (a) 532 nm and (b) 785 nm laser source (c-h) The dependence of photocurrent on illumination using 785 nm laser. 171

Fig. 5.24: Responsivity (represented using ★) and detectivity (represented using ●) plots calculated from photoresponse curves obtained from illumination using (a) 532 nm and (b) 785 nm laser source. 172

Fig. A.1: Methodology for the synthesis and fabrication of FeS_2 nanoparticles and their thin films…….213

Fig. A.2: Images of the FeS_2 nanocolloids prepared in different solvents. 214

Fig. A.3: As-prepared and annealed films of FeS_2 fabricated by combining EPD and spin-coating. 215

Fig. A.4: (a) TEM (b) HRTEM (c) SAED (d-f) STEM and (g-i) SEM images of FeS_2 NPs in isopropyl alcohol (IPA)..... 216

Fig. A.5: (a) TEM (b) HRTEM (c) SAED (d-f) STEM and (g-i) SEM images of FeS_2 NPs in dimethyl formamide (DMF). 217

Fig. A.6: (a, b) TEM (c-e) STEM and (f, g) SEM images of FeS_2 NPs in ethanol..... 218

Fig. A.7: (a, b) TEM (c-e) STEM and (f, g) SEM images of FeS_2 NPs in methanol..... 219

Fig. A.8: (a, b) TEM (c-e) STEM and (f, g) SEM images of FeS_2 NPs in acetone. 220

Fig. A.9 High resolution XPS spectra of (a-e) Fe 2p and (f-j) S 2p of the FeS_2 NPs in different solvents. 221

Fig. A.10: The absorption spectra of (a) FeS_2 nanoparticles synthesized by PLAL in different solvents (b) FeS_2 nanoparticles in IPA synthesized with and without the use of focusing lens. 222

Fig. A.11: XRD patterns of the (a) Pyrite target used for PLAL (b) thin films of FeS_2 fabricated on n-Si by EPD and spin-coating (c) films of FIPA and FDMF dropcasted on FTO substrates. 224

Fig. A.12: XRD of FDMF films on FTO under sulfurization at different (a) annealing temperatures (b) sulfur concentrations. 225

Fig. A.13: SEM images of the as-prepared and annealed thin films fabricated on n-Si by EPD above which FeS_2 NPS in IPA (FIPA) are spin-coated. 226

Fig. A.14: SEM images of the as-prepared and annealed thin films fabricated on n-Si by EPD above which FeS_2 NPS in DMF (FDMF) are spin-coated. 227

Fig. A.15: (a) % Reflectance of the as-prepared and annealed films (b) zoomed image of the % reflectance of the films. 227

Fig. A.16: I-V characteristics of the p-FeS_2/n-Si photodiode. 228

Fig. A.17: Time-dependent photoresponse measurements of p-FeS_2/n-Si photodiode under illumination using tungsten lamp and a bias voltage of 0.5 V. 230

Fig. A.18: Photoresponse measurements of p-FeS_2/n-Si photodiode under illumination using different wavelengths of LEDs under self-powered mode. 232

Fig. A.19: Photoresponse curves of p-FeS_2/n-Si photodiode under illumination using continuous lasers of wavelength (a) 785 nm (b) 532 nm. 233

Fig. A.20: Detectivity of p-FeS_2/n-Si photodiode under illumination using continuous laser of wavelength 785 nm. 234

List of Table

Table 1.1: Comparison of key parameters of different hybrid nanostructure-based photodetectors. 39

Table 2.1: NEP values for the SnS photodetectors for 532 and 785 nm……...68

Table 2.2: Rise and decay times of the SnS films under various illumination conditions. (© from Elsevier 2022). 69

Table 2.3: Results of our SnS photodetector compared to those of SnS photodetectors reported in literatures. 69

Table 3.1: Crystalline size calculated from XRD for the as-prepared and annealed SnS and SnS:Si films……...83

Table 3. 2: Binding energy values from high resolution spectra of Sn 3d, S 2p and Si 2p of the as-prepared and annealed SnS and SnS:Si films..... 93

Table 3.3: The rise time and decay time calculated for the annealed SnS and SnS:Si hybrid films. 102

Table 4.1: Key device performance metrics of photodetection devices based on graphene-semiconductor nanoparticles……143

Table 5. 1: Binding energies of Sn, S, Ag and Au in the hybrid SnS films after etching……163

Table 6.1 : A comparison of the photodetection properties of the hybrids developed in this thesis work…….176

Curriculum Vitae

Fields of Interest

- Nanomaterials
- Thin films
- Optoelectronics
- Pulsed laser ablation
- Semiconductors
- Photocatalysis



Akshana Parameswaran Sreekala

+52 8119928889
+91 8281552925

Monterrey, Mexico

akshana.parameswaransr@uanl.edu.mx
akshana2770@gmail.com

linkedin.com/in/akshana-ps-0246b61ab/

EDUCATION

2019 - Present	PhD in Materials Engineering Universidad Autónoma de Nuevo León- México
2018	CSIR-UGC NET IN CHEMICAL SCIENCES
2015 - 2017	M.Sc. In Chemistry National Institute of Technology- Tiruchirappalli
2013 - 2014	Diploma in Computer Applications Centre for Development of Imaging Technology- Trivandrum
2012 - 2015	B.Sc. In Chemistry HHMSPBNSS College for Women-Trivandrum
2011 - 2012	XII Standard St. Thomas Residential School- Trivandrum
2009 - 2010	X Standard St. Thomas Residential School- Trivandrum

EXPERIENCES

- Worked as Research Intern, University of Hyderabad, India on 'Synthesis of Cadmium Sulphide Nanoparticles and its Effect on Cr(VI) Reduction.'
- Project student, National Institute of Technology, Trichy on 'Synthesis of quinolinyl derivatives and determination of cations and anions at trace level.'

REFERENCES

Dr. Sadasivan Shaji
Facultad de Ingeniería Mecánica y Eléctrica
Cubículo #69, 2do piso CIDET
Universidad Autónoma de Nuevo León.
sadasivan.shaji@uanl.edu.mx

Dr. David Avellaneda Avellaneda
Facultad de Ingeniería Mecánica y Eléctrica
Cubículo #8, 2do piso CIDET
Universidad Autónoma de Nuevo León.
david.avellanedavl@uanl.edu.mx

PROFESSIONAL DEVELOPMENT

- **Oral Presentation** of the work "*Pyrite (FeS2) nanoparticles by pulsed laser ablation in liquid and its thin films for photodiodes*" in thin films symposium of the XV International Conference on Surfaces, Materials and Vacuum, held in **Puerto Vallarta, Jalisco from Sept 26 - Sept 30, 2022**.
- **Oral Presentation** of the work "*Hybrid nanostructured thin films of noble metal/bimetallic nanoparticles with tin monosulphide for wavelength extended photodetection*" in symposium Materials for nanoelectronics and nanophotonics at the European Materials Research Society, held in **Strasbourg, France from May 31 - June 3, 2022**.
- **Oral Presentation** of the work "*Nanostructured thin films of SnS-Si and SnS-Graphene hybrids for photodetetction in extended wavelengths*" in symposium Nanostructured Materials and Nanotechnology: Synthesis, Properties, and Theory at the XXIX International Materials Research Congress, held in **Cancun from August 15 - 20, 2021**.
- **Oral presentation** of the work "*Synthesis of SnS-Si hybrid thin films by pulsed laser irradiation/ablation in liquid for photodetection*" in the International Virtual Conference, Progress and Promises in Chemical Sciences (PPCS-2021) organized by Department of Chemistry, CHRIST (Deemed to be University), **Bengaluru held from 22 March 2021 to 28 March 2021.**
- **Poster presentation** titled "*SnS nanocolloids by pulsed laser ablation in liquid technique and fabrication of thin films by spin coating for optoelectronics*" in the International Virtual Conference, Progress and Promises in Chemical Sciences (PPCS-2020) organized by Department of Chemistry, CHRIST (Deemed to be University), **Bengaluru held from 15 February 2020 to 15 March 2020.**
- **Plenary talk** on the topic "*Nanostructured thin films of tin sulphide for photodetector applications from pulsed laser ablated nanocolloids"* in the VII Leopoldo Garcia—Colin Mexican Meeting on Mathematical and Experimental Physics in Laser Ablation Symposium of the Meeting held in **Mexico City from February 17-21, of 2020.**

PUBLICATIONS

- **Akshana P. S.,** B. Krishnan, R. Fabian, C. Pelaes, D. Avellaneda, J.A. Aguilar-martínez, S. Shaji. *Applied Surface Science Ultraviolet to near infrared wavelength independent SnS-graphene hybrid thin film photodetector from nanocolloids*, **Appl. Surf. Sci. 609 (2023) 155277**. https://doi.org/10.1016/j.apsusc.2022.155277.

- **Akshana P. S**, B. Krishnan, R.F.C. Pelaes, D.A. Avellaneda, M.I.M. Palma, S. Shaji. *Tin sulfide thin films by spin coating of laser ablated nanocolloids for UV-Vis-NIR photodetection, Colloids Surfaces A Physicochem*, **Eng. Asp. 639 (2022) 128382.** https://doi.org/10.1016/j.colsurfa.2022.128382.

- **Akshana P. S.,** A. Nadukkandy, S. Shaji, D.A. Avellaneda, J.A. Aguilar-Martínez, B. Krishnan, *$AgSbS_{2-x}Se_x$ thin films: Structure, composition, morphology and photodetection properties,* **Mater. Today Commun. 27 (2021) 102362.** https://doi.org/10.1016/J.MTCOMM.2021.102362

TECHNICAL EXPERTISE

- ✓ Scanning Electron Microscopy, SEM
- ✓ Transmission Electron Microscopy, TEM
- ✓ X-ray Photoelectron spectroscopy, XPS
- ✓ X-ray Diffraction, XRD
- ✓ Raman spectroscopy
- ✓ UV-Vis-NIR Spectroscopy
- ✓ Electrical measurements using Keithley Source Measuring Unit
- ✓ Fluorescence
- ✓ FT-IR spectrometer

SKILLS

- ✓ Research analysis
- ✓ Meticulous organization
- ✓ Analysis & problem-solving
- ✓ Effective written & oral communication
- ✓ Interpersonal skill
- ✓ Technical know-how